Observations and Modelling of the Chromosphere During Solar Flares

Graham Stewart Kerr, M.Sci. (Hons.)

Astronomy and Astrophysics Group
School of Physics and Astronomy
Kelvin Building
University of Glasgow
Glasgow, G12 8QQ
Scotland, U.K.

Presented for the degree of
Doctor of Philosophy
The University of Glasgow
September 2016

This thesis is my own composition except where indicated in the text. No part of this thesis has been submitted elsewhere for any other degree or qualification.

28th September 2016

"... Make the Universe your companion, always bearing in mind the true nature of things – mountains and rivers, trees and grasses, and humanity – and enjoy the falling blossoms and the scattering leaves ... "

Learn From the Pine,
Matsuo Bashō

"WHEN I heard the learn'd astronomer;
When the proofs, the figures, were ranged in columns before me;
When I was shown the charts and the diagrams, to add, divide, and measure them;
When I, sitting, heard the astronomer, where he lectured with much applause in the lecture-room,
How soon, unaccountable, I became tired and sick;
Till rising and gliding out, I wander'd off by myself,
In the mystical moist night-air, and from time to time,
Look'd up in perfect silence at the stars. "

When I Heard the Learn'd Astronomer, Leaves of Grass
Walt Whitman, 1900

Acknowledgements

During my PhD studies I have received much help, support and encouragement from colleagues, friends and family, for which I am immensely grateful. First and foremost, many thanks are due to my supervisor, Prof. Lyndsay Fletcher, who's patience, enthusiasm, knack for asking the right questions, and ability to cut through the quagmire to identify the salient details has immeasurably helped guide my research and is much appreciated.

The University of Glasgow's Astronomy & Astrophysics group has been a very rewarding environment in which to do a PhD. In addition I must also express my thanks to colleagues based elsewhere. Without exception the A&A group and my external colleagues have patiently answered my many questions. In particular I would like to thank Joel Allred, Adam Kowalski, & Mats Carlsson for sharing (and helping me understand!) the powerful `RADYN` code. I have enjoyed working closely with (and getting help from) Paulo Simões, Hugh Hudson, Ryan Milligan, Alex Russell, Jiong Qiu, Petr Heinzel, Dave Graham, Alasdair Wilson, Duncan Stackhouse, and many others. A research visit to Montana State University (M.S.U.), hosted by Prof. Qiu, allowed me to learn from the accomplished solar physicists who work there. I very much enjoyed my time in Big Sky Country, and hope to visit again soon.

I would, of course, be remiss if I did not mention my fellow students and friends from 604 (and 614), who helped to keep me (somewhat) grounded during my PhD - I will miss 4pm coffee time and the regular trips to the Chip!

I would also be remiss if I did not acknowledge the College of Science and Engineering at the University of Glasgow, who awarded the research scholarship that enabled me to undertake my PhD, and the travel support to visit M.S.U.

Finally, my sincerest thanks to Mum, Dad, Douglas *et al*, for their love and support in getting to this stage, and to Mikey, who brilliantly put with up the stress, distraction, crankiness, and almost hermit-like nature that came with the final stretch.

Abstract

Solar flares release an enormous amount of energy (up to $\sim 10^{32}$ erg) which is transported through the Sun's atmosphere until it is deposited in the chromosphere, resulting in a broadband enhancements to the solar radiative output. The bulk of the flare radiative output originates from the chromosphere. Despite the importance of the chromosphere we do not yet have a comprehensive understanding of the radiation produced there following flare energy deposition, and the diagnostic potential of radiation from this layer of the atmosphere has not been fully exploited. Additionally, there is evidence that the standard model of flare energy transport via non-thermal electron beams might not be the complete scenario. Chromospheric radiation will be crucial in discriminating between the standard model and alternative energy transport mechanisms. Through near-UV spectroscopy, optical imaging, and radiation hydrodynamic modelling using both the electron beam model and energy transport via Alfvén waves, the chromospheric response to flare energy input was investigated.

One of the first detailed analyses of the response of the Mg II h & k spectral lines to flare energy input is presented. These are strong, optically thick, lines formed in multiple locations of the chromosphere. In addition to showing a strong intensity enhancement, the lines were redshifted, showed a blue wing asymmetry in the most intense sources, and were substantially broadened. The lines were also single peaked during the flare, in contrast to their double peaked, centrally-reversed structure in the non-flaring Sun. Despite this, the analysis suggested they remained optically thick during the flare.

Using snapshots from radiation hydrodynamic flare simulations in combination with a radiation transfer code capable of modelling partial redistribution effects, the Mg II h & k line formation properties during flares were analysed. These simulations showed the same qualitative behaviour as observations, but instead of being single

peaked they contained a shallow central reversal. Additionally the lines were too narrow, suggesting the lower chromosphere was too cool in the simulations. Line core Doppler shifts were well-correlated with atmospheric velocity. The lines were formed lower than in the quiet Sun, with source functions (and therefore emergent intensities) that were more strongly coupled to the Planck function during the flare - that is, they reflected the local conditions to a greater degree. While the lines did indeed remain optically thick during the flare, some optically thin contributions resulted in asymmetries. However, the strongest blue wing asymmetries were the result of a stationary component to the line profile when the line core was redshifted.

Optical continuum enhancements are amongst the strongest emission during solar flares, though are relatively rare to observe. Understanding the emission mechanism responsible is important for models of flare energy transport, but there remains debate as to the dominant mechanism. This emission may originate from the heated photosphere, or from an overionised region of the chromosphere. Imaging in three optical passbands during a strong flare was used to analyse the temperature enhancement and luminosity of optical sources were under the assumption of two simple models. This was in an effort to determine the most likely emission mechanism. The models were a photospheric (blackbody) model and a chromospheric model with enhanced recombination radiation. Observations were most consistent with the photospheric origin, although some evidence that both mechanisms play a role is discussed. Additionally, initial analysis of observations of a flare in which both the optical continuum and near-UV continuum were observed is presented.

Finally, a radiation hydrodynamic numerical model was adapted to include flare energy transport via the dissipation of Alfvén waves. Some representative simulations surveying the parameter space are discussed. Additionally, a detailed comparison is presented between a simulation using the standard model of energy transport via non-thermal electron beams, and a simulation using Alfvén wave dissipation. Both the hydrodynamic response is compared, as well as the radiative response of the Ca II 8542Å and Mg II k line. It was found that Alfvén waves are able to sufficiently heat the chromosphere during flares, making them a viable candidate for energy transport, and that there is the potential for discriminating between energy transport models using observations of chromospheric radiation.

Contents

List of Figures

Chapter 1

Introduction

On September 1st 1859 Richard Carrington was observing a sunspot group on the Sun's surface when, quite unexpectedly,"two patches of intensely bright and white light" appeared at the edge of the sunspot group (Carrington 1859). In an effort to share this (at the time) unique and startling occurrence, Carrington hastily left to fetch a witness. Upon returning within one minute he "was mortified to find that it was already much changed and enfeebled", with the last vestiges of the brightening disappearing over the next several minutes. This weaker continuing emission showed discrete sources moving rapidly through the field of view, travelling around 35,000 miles in a span of 5 minutes. These observations were independently confirmed by Richard Hodgson (Hodgson 1859).

Seventeen hours and 40 minutes later, a severe geomagnetic storm was recorded by the magnetometer at Kew Observatory (Stewart 1861) and at other locations around the World (as noted in Tsurutani et al. 2003). Intense aurorae were visible at low latitude, reaching to within 23° north and south of the equator. Reports recorded originally by E. Loomis in a series of articles from 1859-1861, and which were later compiled by Shea & Smart (2006), and discussed by Kimball (1960), included those from a ship at sea 23° north of the equator and from Santiago, Chile. In addition, across Europe and the U.S.A there were reports of fires being started by currents induced in telegraph wires.

It was recognised that Carrington's observation was possibly related to, and potentially the cause of, the severe geomagnetic activity (Stewart 1861), though Carrington himself was careful not to draw too many conclusions and it took several years for the scientific community to reach a consensus. We know now that the brightening

Carrington witnessed was the first recorded observation of a solar flare (and was an extremely powerful example of one), and that the subsequent geomagnetic storm was the result of coronal mass ejection (CME), which are events commonly associated with flares. This particular flare is commonly referred to as the 'Carrington Event'. Both the flare and the geomagnetic storm are thought to be most energetic yet observed (Tsurutani et al. 2003; Cliver & Dietrich 2013), and represent one of the most extreme examples of the effects of space weather on the Earth.

The fortuitous observation of the first solar flare shortly before the largest geomagnetic storm on record, coupled with the recent discovery of the 11-year sunspot cycle, in phase with recorded geomagnetic storms (e.g Sabine 1852; Cliver 2006, and references therein), helped to kick-start the research field of solar-terrestrial physics. That is, the study of the Sun, the solar atmosphere, solar flares, space weather, and the Sun-Earth connection. Today this research falls under the umbrella term of heliophysics which encompasses all aspects of how the Sun interacts with the rest of the Solar System.

Stars are often referred to as the building blocks of the Universe, but with the exception of the Sun we are limited to studying them as distant point sources. The Sun is a fairly average G-type star, but its proximity allows us to spatially resolve features. Knowledge gained from our study of the Sun can be applied to further understand stars (for example the complementary fields of solar and stellar flares). At its most basic level the Sun is an example of an astrophysical plasma. Since the majority of the visible Universe exists as a plasma, observing plasma processes on the Sun can provide illustrations of similar processes occurring in other astrophysical plasmas. Understanding the physics at play in solar flares therefore presents both an interesting problem in its own right, as well as a useful tool to elucidate related processes on other astrophysical objects.

Perhaps a more relatable, and more practical, example of the importance of solar flare research is the role solar flares play in space weather. While flares and CMEs as extreme as those that led to the geomagnetic storms of 1859 are rare, strong flares and Earth-directed CMEs are reasonably common, and have the potential to have substantial technological impact. Effects include disruption of the power grid, to global positioning systems (GPS), global satellite communications, and high frequency radio communications. Additionally, satellites can be damaged or lost, and there is a

risk of increased radiation exposure on certain flight routes. These issues result from heating of the ionosphere from flares, high energy radiation and particles from flares & CMEs, and rapid variations in the Earth's magnetic field following a CME impact. Given how dependent modern society is to communications technology a space weather event on the level of the Carrington Event could have severe consequences. Even smaller geo-effective space weather events can have strong technological (and economic) impacts. Recently the U.K. Government recognised the risk that space weather poses, adding it to the National Risk Register of Civil Emergencies and creating the Met Office Space Weather Operations Centre (MOSWOC)[1]. Flares are a fundamental component of space weather, and so understanding them is an essential part of research in Solar-Terrestrial physics.

During solar flares energy is released in the corona (the outer layer of the Sun's atmosphere), and is transported down to the lower-lying chromosphere where it is deposited. The bulk of the flare radiative output then originates from the chromosphere (e.g Fletcher et al. 2007, 2011), but despite the importance of the flaring chromosphere we still do not have a comprehensive understanding of the radiation produced there following flare energy deposition. This thesis presents research that focuses on furthering our understanding of the flaring chromosphere and lower atmosphere. Observational research was performed via imaging of the optical continuum, and via spectroscopy of the optically thick Mg II h & k spectral line emission. The observational analysis was supported by numerical simulations that investigated the formation of Mg II h & k lines and the viability of novel energy transport mechanisms to heat the chromosphere during flares.

Routine observations of the Mg II h & k spectral lines during flares have only been available since the launch of the Interface Region Imaging Spectrograph (IRIS) satellite in June 2013 and so presented a new opportunity to study the chromospheric response to flares (only one flare observation of Mg II h & k lines by Lemaire et al. 1984 had been reported before the launch of IRIS). However, since they are optically thick, extracting the information they carry about the flaring chromosphere can be complicated, requiring radiation transfer simulations to forward model the lines. Despite the challenges associated with the interpretation of optically thick radiation in comparison to optically thin radiation, the Mg II h & k lines were studied in

[1] http://www.metoffice.gov.uk/publicsector/emergencies/space-weather

this thesis. This was because not only are they among the few routine space-based spectroscopic observations of the chromosphere in flares, with a flare response that had not yet been studied in detail, but they potentially carry information about the whole flaring chromosphere since different components of the line form throughout the chromosphere from the upper chromosphere to the temperature minimum region (see Chapter 3 for more details).

The remainder of this chapter introduces the solar atmosphere and solar flares, while Chapter 2 introduces the numerical codes and related physics, and the solar observatories used. Chapter 3 discusses new observations of the Mg II h & k lines in flares and Chapter 4 details the formation properties of those lines during flares via numerical simulations. Chapter 5 then investigates the hydrodynamic and radiative response of the chromosphere to flare energy input via Alfvén waves. Finally, Chapter 6 concludes the thesis with a discussion of flare optical continuum enhancements.

1.1 The Sun's Atmosphere

The Sun's atmosphere spans several orders of magnitude in temperature, electron density, mass density, pressure, ionisation fraction and plasma beta (β; the ratio of gas pressure to magnetic pressure), making it a complex environment. High resolution images have shown that it is inhomogeneous with a dynamic small-scale spatial structure (features can vary on time-scales of a few seconds to several days or longer). The Sun's four main atmospheric layers are the photosphere, the chromosphere, the transition region, and the corona. Individually, each of these layers displays rich and complex physics leading to the formation of features such as the granulation pattern, plage, sunspots, active regions, spicules and prominences, and to the formation of radiation. Observations of the radiative output allows us to probe, and diagnose, the Sun's atmosphere. It is difficult to think about these layers in isolation, since the interface between them, as well as the layers themselves, governs how energy and mass are transported through the solar atmosphere. This is of particular importance during violent events such as flares, so that models and numerical simulations usually must include the full atmosphere, to some degree. Since these parameters vary by many orders of magnitude, this can be a non-trivial task.

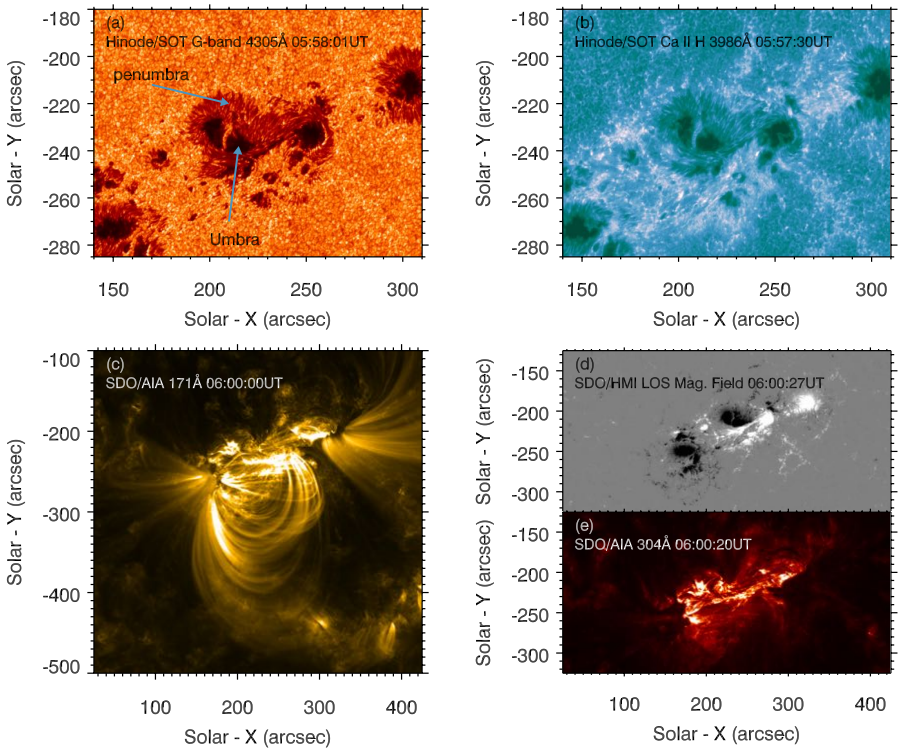

Figure 1.1: *An active region viewed at different wavelengths on 2011-Feb-15th. Panel (a) shows the photosphere using 4305Å G-band observations from the Hinode Solar Optical Telescope (SOT). Granulation cells, sunspots, umbra, and penumbra and pores are visible. Panel (b) shows observations of the Ca II H line from the SOT. This wide filter observes line core and wings so that the chromosphere and temperature minimum region are sampled. The brighter regions surrounding the sunspot are plage. Panel (c) shows the transition region/corona using the 171 Å filter from the Solar Dynamics Observatory's Atmospheric Imaging Assembly (SDO/AIA). Temperatures in the transition region are several hundred thousand kelvin, and in the corona are in excess of $T \sim 1-2$ MK. Loop structures are clear. Panel (d) shows a line of sight magnetogram from SDO, where white is positive field and black is negative. Panel (e) shows the active region using the 304Å filter from SDO/AIA which samples the top of the chromosphere and transition region. Note that the SOT and SDO images have not been aligned so there is a pointing offset.*

1.1.1 Description of the Sun's Atmospheric Layers

The Photosphere and Active Regions: The Sun's pseudo-surface is the photosphere. Here the optical depth of the visible part of the electromagnetic (EM) spectrum is

such that photons are able to escape and be observed. Formally, it is usually defined as the height at which the optical depth at 5000 Å is unity ($\tau_{5000} = 1$). The dominant source of opacity in the photosphere is H^- bound-free opacity (Foukal 1990), where an electron is captured by weak electrostatic attraction to a neutral hydrogen atom. Photoionisations then take place by photons with wavelengths $\lambda < 1.65$ μm. The H^- opacity at the photosphere begins to decrease sufficiently so that radiation is able to escape, carrying an energy flux of $\sim 6.5 \times 10^{10}$ erg s^{-1} cm^{-2} (Zirin 1988).

The photosphere can be assumed to be in local thermodynamic equilibrium (LTE), so that population levels are defined by Saha-Boltzmann statistics (Gray 1992), with a source function equal to a blackbody with temperature 5780 K. Sources of opacity (e.g. from singly ionised metals) result in an emergent intensity that departs from a perfect blackbody curve. Temperature and density decrease with height through the upper photosphere to the temperature minimum region (TMR; $T \sim 4400$ K), at which point the chromosphere begins. At the photosphere the number density is around $\sim 10^{17}$ cm^{-3} and falling to $\sim 10^{15}$ cm^{-3} at the TMR.

A granulation pattern is obvious when observing the photosphere. What appears to be a smooth surface is actually filled with irregular polygons, each a few hundred km in size with lifetimes of a few minutes (Zirin 1988). This pattern is caused by convection below the photosphere, where hot plasma rises (appearing brighter in cell centres) and cooler plasma falls resulting in dark intergranular lanes.

The photosphere is a high-β plasma, where gas pressure exceeds magnetic pressure, so that the magnetic field is pushed around by fluid motions. Magnetic flux tubes can buoyantly rise through the convection zone (the layer beneath the photosphere), forming active regions (AR) when they emerge through the photosphere (see a recent review by van Driel-Gesztelyi & Green 2015). Faculae are patches of brighter material that form in active regions, seen mostly at the limb, where magnetic field concentrations reduce the density allowing us to see slightly deeper, where the atmosphere is hotter (Foukal 1990; Foukal et al. 2006). If the magnetic flux is sufficiently strong then it can appear as a magnetic pore. Pores are areas where the flux emergence has inhibited convective flows resulting in dark, cooler, patches on the photosphere. These can grow and merge to form larger features known as sunspots, where the footpoints of flux tubes are rooted (e.g Solanki 2003; van Driel-Gesztelyi & Green 2015). Sunspots are recognised by the presence of a dark 'umbra' ($T \sim 3900 - 4800$ K) roughly in the centre and a brighter 'penumbra'

($T \sim 5400 - 5500$ K) surrounding it that has a fibril structure, whereas pores do not have a penumbra (Solanki 2003). Figure 1.1(a,d) shows an AR as it seen in the photosphere. These images contain a sunspot, and show the line of sight magnetic field strength in the field of view. Energy is stored in the stressed magnetic field of AR. This energy can be released in small amounts, leading to small scale brightenings, but when a significant amount of energy is released we refer to this as a solar flare. Sunspots (and flares) follow an observed cycle of activity, going from a period of low activity (solar minimum) to a period of maximum activity (solar maximum) every 11 years or so (e.g van Driel-Gesztelyi & Green 2015). We are currently descending from the maximum of Solar Cycle 24.

The Chromosphere: Above the TMR is the relatively thin chromosphere which extends for $\sim 2000 - 3000$ km to the transition region. Through the chromosphere the temperature increases outward from ~ 4400 K at the TMR to $\sim 20 - 30,000$ K at the base of the transition region. At the same time the number density drops from $\sim 10^{15}$ cm^{-3} at the TMR, to $\sim 10^{11}$ cm^{-3} at the transition region. The gas pressure drops off faster than the magnetic pressure so the plasma-β varies with height and the magnetic field begins to dominate the dynamics. High temperatures mean that the chromosphere is partially ionised, and is, mostly, optically thin to radiation though not at all wavelengths. Certain atomic species produce photons to which the chromosphere is optically thick due to the relatively large abundance of that species that can absorb or scatter those photons (examples include H, He, Mg and Ca, with abundances on the logarithmic abundance scale[2] of 12, 10.93, 7.60 and 6.34 respectively Asplund et al. 2009). This is also a function of the ionisation state of that species. For example, the chromosphere is optically thick for the h & k transitions of Mg II, but at transition region or coronal temperatures Mg is typically in the Mg III state meaning that those parts of the atmosphere are optically thin to h & k photons. Density enhancements in some chromospheric features might also change the opacity structure. For clarity, an optically thin spectral line transition (or continuum) is one in which the emitted photon can escape the Sun's atmosphere to be observed without first being absorbed or going through any scattering events. An optically

[2]The logarithmic scale for atomic abundances is defined such that the hydrogen abundance is $\log \epsilon_H = 12$. For a species X the abundance relative to hydrogen is $\log \epsilon_X = \log(n_X/n_H) + 12$, where n_H is the number density of hydrogen and n_X is the number density of species X.

thick transition is one in which the emitted photons are absorbed and re-emitted, or otherwise scattered, before escaping the atmosphere (sometimes through multiple absorption or scattering events).

The chromosphere is bright in ultraviolet (UV) lines and continua which reach optical depth unity ($\tau_\lambda = 1$) there, and in certain optical & infrared (IR) lines of ionised species, including the Ca II H & K resonance lines, Hα, Lyα, and the Mg II h & k resonance lines. Due to the low density the chromosphere is no longer in LTE, and instead we must consider a non-LTE (NLTE) plasma, where the population density of atomic levels can depart from the Saha-Boltzmann LTE description (Mihalas 1978). As a result the radiation temperature (the temperature that a blackbody would be if it were to emit the observed intensity) is usually lower than the gas temperature at the radiation formation height. The radiation field is non-local (it is not set solely by local temperature and density) and can have a complex opacity structure such that strong lines of certain abundant elements (like Ca or Mg) can form over a range of heights in the chromosphere. Additionally, the dynamics and history of the chromosphere is important since dynamical effects can occur on timescales shorter than the ionisation/recombination relaxation time (e.g Carlsson & Stein 2002), which means that the ionisation equilibrium value is not reached.

Observations of the chromosphere show that it is dynamic. For example, observations of the Ca II H & K lines show short lived ($t < 100$ s, brightenings that are periodic on timescales of 2 – 5 minutes (e.g. Rutten & Uitenbroek 1991), and features such as spicules that have lifetimes around 3 – 12 minutes (e.g Tsiropoula et al. 2012). The magnetic field governs dynamics in the chromosphere, with several common features including the chromospheric network (bright patches that outline the boundaries of supergranulation cells), the internetwork (weaker emission from granulation cell centres), spicules (cool magnetically bound material that extend far into the outer atmosphere, appearing as thin, wispy structures), and fibrils or mottles that appear both bright or dark depending on density, orientation and altitude (see e.g. Heinzel et al. 1992; Zirin 1988; Foukal 1990).

In AR, the chromosphere appears bright in UV lines and continua. Plage are the patches of bright, hot, chromospheric material in AR, shown in Figure 1.1(b). They are typically sites where the magnetic field is unipolar, where the field lines emerge from the photosphere. Flare energy release in the corona is transported down flux tubes, and deposited in the chromosphere where significant heating and ionisation

takes place.

The Transition Region: The transition region (TR) is the almost vanishingly small layer only a few ×100 km thick joining the chromosphere to the lower corona. Through the TR temperatures climb two orders of magnitude from $\sim 25,000$ K to $1-2$ MK, and densities drop precipitously to 10^{8-9} cm^{-3}. The TR is almost completely ionised, and is observed using far-UV (FUV) and extreme-UV (EUV) emission lines of ionised elements such as O IV, C II,III,IV, and Si IV, as well Fe lines such as Fe IX,X.

Observations, including those from the Interface Region Imaging Spectrograph (IRIS; De Pontieu et al. 2014) have revealed that, like the chromosphere, the TR is dynamic and inhomogeneous. Features visible in the chromosphere, such as the network and AR also appear in the TR. Energy and mass is transported through the TR during flares, and so emission from this region is an important testing ground for flare models. Figure 1.1(e) shows observations of an AR using He II 304Å which samples material at the base of the TR, showing the small scale brightenings and complex environment.

The Corona: The outermost layer of the Sun's atmosphere is the corona. The 'closed' coronal magnetic field extends for several solar radii, while the 'open' coronal field extends out to the heliopause in the outer Solar System. It is a diffuse (with density 10^{8-9} cm^{-3}), ionised plasma with temperatures in excess of 1-2 MK as indicated by EUV observations of emission lines from highly excited atomic species (such as Fe and Ca), and from X-ray observations. Radiation from this region of the atmosphere is often analysed under the assumption, that the radiation field is dominated by collisionally excited, radiatively de-excited, optically thin lines (often referred to as the 'coronal approximation').

The plasma-β is $<< 1$, so magnetic fields dominate. Magnetohydrodynamics (MHD) can successfully model the dynamics of the coronal plasma (see, e.g. Priest 1982). A feature of this is the 'frozen-in-condition' whereby the plasma is forced along field lines and is unable to cross the magnetic field. Above an AR, closed magnetic field lines confine the plasma in hot loops, which can be seen in Figure 1.1(c). As well as coronal loops, coronal streamers can form which are larger scale closed loops that trap plasma, creating locally denser regions in the corona. Streamers can

become pointed due to interactions with the escaping slow solar wind (a constant stream of charged particles escaping from 'open' field lines between the streamers). The fast solar wind originates from coronal holes, which are much larger areas of open magnetic field lines (usually near the poles) .

The coronal loops that form above AR are thought to be the source of flare energy release, as discussed in § 1.2, so that all layers of the Sun's atmosphere play a role during flares.

1.1.2 Semi-Empirical Model Atmospheres

Semi-empirical model solar atmospheres have been developed and widely used to help interpret solar observations. These are typically 1D plane-parallel hydrostatic models. The most commonly discussed are the VAL & FAL models, named after their authors: Vernazza, Avrett & Loeser and Fontenla, Avrett & Loeser. Of these atmospheres, VALC (Vernazza et al. 1981) and FALC (Fontenla et al. 1993) describe the mean quiet Sun. Others exist that describe other atmospheric features, such as plage. The temperature, hydrogen density, and electron density stratification with height in the FALC model atmosphere are shown in Figure 1.2, illustrating the 'average' quiet chromosphere. Models like VALC and FALC are created by taking an assumed temperature-height distribution and solving the equations of hydrostatic equilibrium along with the radiation transfer and statistical equilibrium equations for numerous atomic species. Comparing spatially and temporally averaged observations of optical, UV and EUV lines and continua to the emergent intensity from the simulations allows the temperature structure to be varied iteratively to achieve the closest match to observations. The physics involved in these models can be complex, and the reader is encouraged to consult Vernazza et al. (1981) and Fontenla et al. (1993).

While semi-empirical atmospheres can be useful to investigate the general physics at play in the chromosphere, it is uncertain how well such models actually represent the true chromosphere. The chromosphere is so dynamic, with many spatially inhomogeneous features, that it is difficult (and perhaps even somewhat misguided) to interpret or discuss an average chromosphere like the VAL or FAL models. Those atmospheres describe the average chromospheric stratification based on observations of a number of strong lines and continua. However, some observations of CO

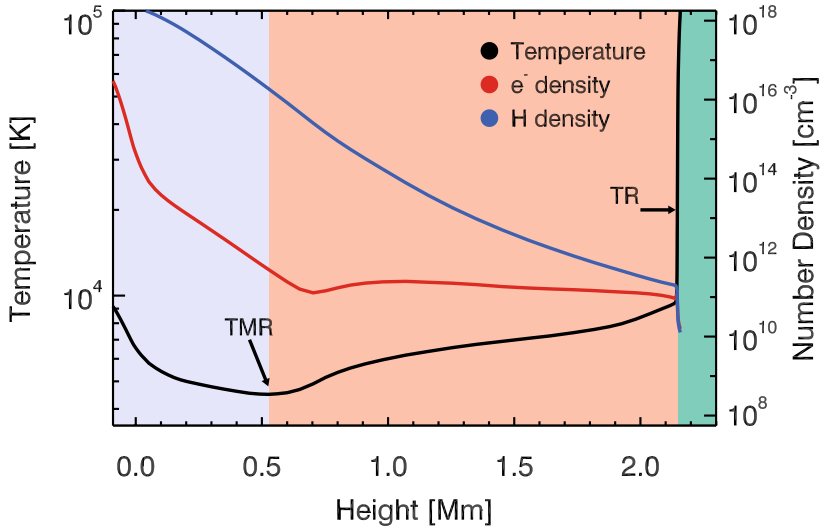

Figure 1.2: *The FALC semi-empirical atmosphere (Fontenla et al. 1993). Temperature (black line), electron density (red line), and hydrogen density (blue line) stratification as a function of height are shown. The temperature minimum region (TMR) and transition region (TR) are indicated. Background shading indicates the photosphere (light purple), chromosphere (orange), and inner TR (green). The upper TR and corona are not shown. The data to make this plot was included with the RH GitHub distrubution (https://github.com/tiagopereira/rh).*

molecules suggest that the temperature might drop below that of the classical TMR, to $T \sim 3700$ K (e.g Noyes & Hall 1972; Uitenbroek 2000). Further, numerical experiments using a time-dependent radiation hydrodynamics code (RADYN), by Carlsson & Stein (1995, 1997), successfully reproduced the observed evolution of the Ca II K line but their chromosphere showed a mean temperature *decrease* with height rather than the increase suggested by semi-empirical atmospheres. As discussed by Uitenbroek (2000), it is perhaps better to forward model radiative transfer calculations through dynamic models in an effort to understand the observed radiation. More colourfully, Carlsson & Stein (1999) state: "The very essence of the chromosphere lies in the dynamics. To study the chromosphere with a mean model is as meaningful as taking the mean of Beethoven's 9th symphony."

Clearly the chromosphere has an overall temperature rise and density decrease that takes the atmosphere from photospheric conditions through to the corona. However, the temperature as a function of height in any given spatial element or feature is the complex result of chromospheric dynamics which should be borne

in mind when discussing an 'average' chromosphere. This thesis uses the dynamic RADYN code to simulate flares, but references are also made to semi-empirical models.

1.2 Solar Flares

Solar flares are enormous energy release events in the solar corona where the magnetic field reconfigures (thought to be via magnetic reconnection) releasing up to 10^{32} ergs over the span of a few tens of minutes (Fletcher et al. 2011). This energy is transported along newly reconnected field lines and deposited at loop footpoints in the chromosphere, where it results in plasma heating, ionisation and large scale mass motions. Flares are characterised by a broadband enhancement to the solar radiative output, from γ-rays and X-rays, through UV, optical, intra-red (IR) and radio. Emissions show different morphologies and are produced via a variety of mechanisms and from different atmospheric locations. Flares typically occur in ARs, and can have associated CMEs, which carry a large amount of plasma with an average mass of a few $\times 10^{12}$ kg (e.g Webb & Howard 2012), and magnetic field into interplanetary space. To illustrate the following discussion, Figure 1.3 shows a flare observed in four different UV filters originating from different atmospheric layers.

1.2.1 Solar Flare Overview: GOES Classes, The Impulsive Phase, and Enhanced Radiation Output

In this section an overview of the enhanced emissions during flares, the main phases of a flare, and the GOES classification system is given. For a comprehensive review the reader is encouraged to consult Fletcher et al. (2011).

Flares vary in strength, with the strength originally classified in terms of the brightness and spatial extent of Hα emission (see, e.g. Švestka 1966). They were described by a number from 0 – 4 defined by the area of enhanced Hα emisssion where 0 is a sub-flare and 4 is a large event, and by a letter that qualifies the brightness: faint 'F', normal 'N' or brilliant 'B'. For example, a large and intense flare would be a 4B class event, equivalent to an X-class flare. This definition of flare strength (mostly) appears in older literature. The modern standard method of assigning a quantitative measure of flare strength is the GOES class. This is measured by the strength of emission as

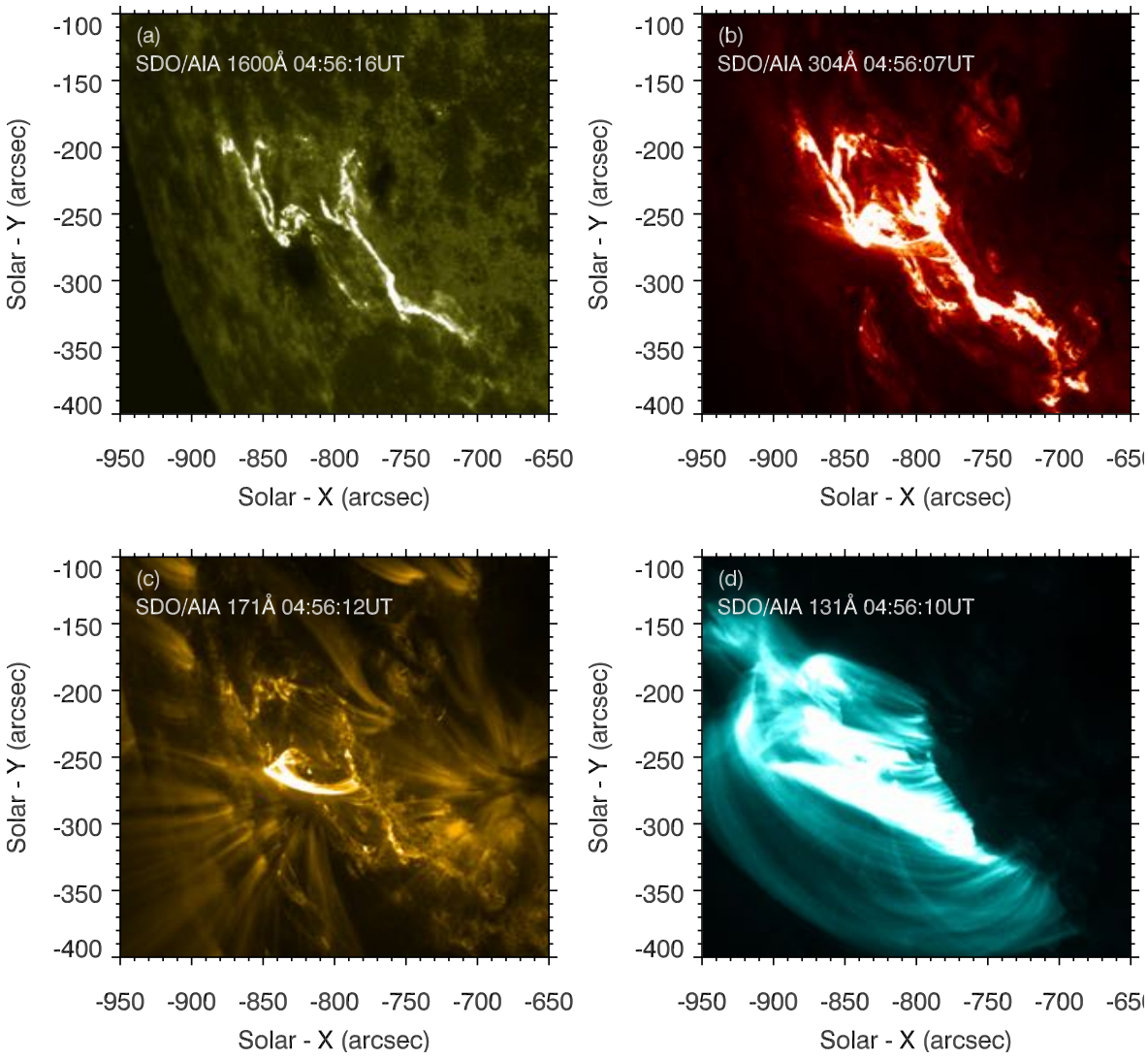

Figure 1.3: *A solar flare from 2014-Oct-19th viewed at different wavelengths using observations from the SDO/AIA. Panel (a) shows 1600Å emission from the chromosphere and transition region where the UV ribbon structure is illustrated. Panel (b) shows 304Å emission from the upper chromosphere and transition region. While the ribbon structures are similar there are also some hot loops. Panel (c) shows 171Å emission, which samples MK plasma in the corona. A flare loop is in the centre of the image, the footpoints of which lie along the cooler ribbons. Panel (d) shows 10 MK plasma from the 131Å filter, where the hot coronal loops overlying the AR are visible.*

detected in the 1-8 Å soft X-ray (SXR) channel of the Geostationary Orbiting Environmental Satellites. An X-class flare is one in which the 1-8 Å energy flux at the Earth

is greater than 1×10^{-4} W m^{-2}. The classification from weakest to strongest is A, B, C, M, & X-class, where the energy flux decreases in decades from X-class. M-class flares are flares in excess of 1×10^{-5} W m^{-2}, and so on. Within each class, flares can be subdivided with a number from 1-9, numbers increasing logarithmically until the next class. This is not the case for X-class flares, where numbering continues past X10. Flare size follows an approximate power-law (extending down to microflares and possibly to nanoflares; Hannah et al. 2011), with fewer X-class flares compared to M-class, and so on. To illustrate the prevalence of smaller events compared to larger flares, between 1976 and 2000 there were 359 X-class flares (with only a handful ≥X10 Hannah et al. 2011), 4709 M-Class, and 32784 C-class flares (Veronig et al. 2002). For context, the Carrington event has been estimated as being X45±5 (Cliver & Dietrich 2013). The next strongest flare on record occurred on 2003-November-4th (part of the "Hallowe'en" series of flares) was estimated as being X35±5 (Cliver & Dietrich 2013), deduced from other observations since this event saturated the GOES SXR detector.

The flare impulsive phase is defined by the rapid rise of the hard X-ray (HXR) emission following initial energy deposition, during which the radiative output of the Sun is greatly enhanced. It can be as short as a few tens of seconds, or extend to a few tens of minutes. In this phase radiation from the chromosphere and transition region is seen to be enhanced, both continua and lines. Hot EUV lines exhibit blueshifts indicating fast upflows in excess > 100 km s^{-1} and redshifts in cooler lines indicating downflows (e.g Acton et al. 1982; Ding et al. 1995; Milligan et al. 2006a). These upflows have become known as chromospheric evaporation, and downflows as chromospheric condensations. Mass motions carry hot chromospheric material into the corona.

The impulsive phase is followed by the gradual phase, where SXR and EUV coronal loops are observed as a result of chromospheric evaporation as well as some *in situ* heating. Coronal temperatures in the AR can exceed 10-20 MK. As loops cool by conduction and radiative losses they can be observed in cooler lines. Optical and UV emission generally take several minutes to decay to pre-flare intensity.

Flare X-ray emission appears as SXR ($E \lesssim 10$ keV) or hard X-rays ($E \gtrsim 10$ keV), with the SXR mostly appearing as thermal emission at the top of heated flare loops following chromospheric evaporation. Some SXR emission during the impulsive phase is

present, resulting from *in situ* heating. HXR emission generally appears as compact double-footpoint sources in the chromosphere, with a non-thermal power-law photon energy spectrum resulting from bremsstrahlung radiation (e.g Holman et al. 2011). The presence of a non-thermal HXR bremsstrahlung spectrum unambiguously points to accelerated electrons during flares. The observed photon spectrum can be used to find the parent electron distribution, and using the collisional thick-target model (CTTM; Brown 1971), the electron flux can be calculated. The thick-target in this model is the chromosphere, with the model assumption that the ambient thermal plasma has an energy significantly lower than the accelerated electron distribution valid in the solar chromosphere.

While HXRs are only a small contribution to the total radiative output during solar flares compared to the dominant UV & optical emission (e.g Woods et al. 2006; Kretzschmar 2011; Fletcher et al. 2011), electrons are thought to be important for flare energy transport. Only a small fraction of the electron energy is lost via bremsstrahlung ($\sim 10^{-5}$), and the bulk of the energy contained within the electrons is deposited via Coulomb interactions which heat the chromospheric plasma and ionises hydrogen via non-thermal collisions. Computing the energy in electrons under the assumptions of the CTTM reveals they carry a significant proportion of flare energy, with estimates of around 10 – 50 % of the total flare energy (e.g Lin & Hudson 1976; Emslie et al. 2012). This is discussed further in § 1.2.2.

Conjugate HXR footpoint sources are typically observed to appear on either side of the polarity inversion line (PIL; the line along which the sign of the vertical magnetic field flips) and move over the field of view during the flare. They are largely co-spatial with UV & optical emissions, suggesting a common source of energy input, though do not always follow the more ordered pattern that those emissions exhibit (though this is at least in part due to the difficulty of imaging in HXR). HXRs are often used as an indication of the locations of energy deposition into the chromosphere.

The heated and overionised chromosphere and TR give rise to enhanced EUV, UV, optical and IR emission, with different emission mechanisms and originating from different locations in the atmosphere. EUV emission ($\sim 100 - 1200$Å) has been extensively exploited as a diagnostic tool of the hot flare plasma. Typically, EUV emission is from optically thin lines of highly excited ions, from $\sim 100,000$ K to in excess of 10 MK. They can originate from the heated chromosphere, TR or corona.

Note that the statement regarding optically thin radiation is a generalisation, as some lines at this temperature range may still be optically thick, and conversely, some lines in this wavelength range can be emitted from cooler plasma and still be optically thin. The continua in the EUV can also be enhanced during flares (e.g Milligan et al. 2014). EUV optically thin emission lines can be used to diagnose the temperature, density and velocity structure of the flare plasma, and for differential emission measure (DEM) analysis. Flare EUV emission can appear as a hot loop structure (a few hundred thousand to in excess of one million kelvin), as shown in Figure 1.3(c,d). For reviews of the solar EUV/UV spectrum consult Doschek & Feldman (2010) and Feldman et al. (1988). For a recent review focussing on solar flare EUV emission see Milligan (2015).

Flares enhance both the continuum and line emission at optical & UV wavelengths. Some of the earliest flare work was performed using ground based observations of optical lines such as the Hα and Ca II H & K lines, as well as higher order Balmer lines (see a review by Švestka 1966). Chromospheric lines can be optically thick, and species with a large abundance (e.g. H, He, Ca, Mg) can have different parts of the line (i.e line core and line wings) forming in different atmospheric locations. Observations of these lines enable us to probe multiple layers of the flaring chromosphere. This adds extra complexity and it is often necessary to forward model optically thick lines using radiation transfer simulations in order to understand their flare response. UV and optical radiation provides a way to test models of flare heating, where the output of flare simulations can be compared to observations. The Hα line has historically been one of the most exploited in terms of flare observations but the space-based era has seen it mostly replaced by UV & EUV lines. Despite the importance of the chromosphere to flare energy transport, the diagnostic potential of flare emissions in some strong chromospheric and transition region UV lines (such as Mg II h & k, C II & Si IV) has not been fully exploited due to a lack of observations. In fact it is only fairly recently, with the launch of IRIS that we can now routinely study the flare response of these lines.

The optical continuum enhancements have been rare to observe (due in part to the bright photospheric background that makes detecting contrasts of only a few percent difficult, and in part due to the lack of broadband optical spectroscopy), though recent evidence is suggesting that, despite the rarity of the observations, they are present in a significant fraction of flares (e.g. Kretzschmar 2011; Matthews et al. 2003;

Hudson et al. 2006). Events with an optical continuum component are referred to as white light flares (WLFs). The Carrington event was a WLF, but it is very unusual to see as high a contrast as in that flare. Optical continuum enhancement have become somewhat enigmatic because of the prevailing mystery of their emission mechanisms, and the constraints they could set on flare energy transport mechanisms. Some observations suggest that heating is required at low depths to help explain WLF emission, since the optical continuum is consistent with enhanced H^- emission from below the TMR or even in the photosphere (e.g Neidig 1989; Hiei 1982). A more in-depth discussion is given in Chapter 6.

With the exception of the Ca II infrared line triplet and the He I 10830Å line, flare IR emissions have been rare. Some examples include observations by Xu et al. (2004) pointing to heating near the opacity minimum region, and the results of Penn et al. (2016) who studied observed IR ribbons concluding they originated via free-free mechanism from a relatively cooler but strongly ionised and dense region in the chromosphere.

EUV, UV, optical & IR emission tends to appear in the form of flare ribbons, which are more extended structures compared to the HXR footpoints (and can be seen clearly in Figure 1.3(a,b)), with lengths of a few tens of arcseconds. They are relatively narrow, with sub-arcsecond structure. A bright and sharp 'leading edge' with weaker, more diffuse, emission behind can be seen in high-resolution images (e.g Isobe et al. 2007), with the interpretation that the brightest part of the ribbon is the site of energy deposition into newly brightened footpoints. In this way ribbon motion maps the motion of energy release sites in the chromosphere. In two-ribbon flares, one ribbon forms on each side of the PIL, and follow a somewhat ordered motion relative to the PIL (e.g. Fletcher & Hudson 2002; Qiu et al. 2002; Cheng et al. 2012). Ribbons show elongation parallel to the PIL and expansion away from it. While the two ribbon structure is common, it is also usual for flares to show more than two ribbons or to have smaller bright kernels alongside the ribbons (similar to HXR footpoint sources). WLF sources also appear as kernels or footpoints. In general HXR footpoints and optical/UV ribbons are spatially associated, and can have a shared motion to a certain degree. HXR footpoints tend to move along flare ribbons, and are often co-spatial with the brightest ribbon locations.

There has not been a discussion of γ-ray, radio or microwave observations here since

the focus of this thesis is on the chromospheric UV/optical response to flares, but these emissions allow diagnostics of particle acceleration and flare energy release, making them of significant interest to the solar flare community. For recent reviews of solar flare radio emission see Pick & Vilmer (2008); Reid & Ratcliffe (2014). Of particular recent excitement is the opportunity to observe solar flares using millimetre and submillimetre wavelengths via the Atacama Large Millimetre/Submillimetre Array (ALMA). ALMA has the potential to probe the chromosphere with excellent spatial and time resolution, using a largely un-explored part of the solar spectrum. See Wedemeyer et al. (2016) for a review of the possible solar science with ALMA.

1.2.2 The *Standard Model* of Solar Flares

Elements of the *standard model* of solar flares have been mentioned above when discussing observational characteristics of flares. Namely, the formation of ribbons and footpoints in the hot chromospheric plasma, non-thermal HXR footpoints indicating electron acceleration, chromospheric evaporation and chromospheric condensation. The mechanism by which flare energy is transported from the release site to the dense chromosphere has so far been left unmentioned. In this section the standard model is presented. A vast amount of research has been performed to elucidate, build upon, and improve this model, which for the sake of brevity is largely omitted. The standard model is discussed in outline, but the reader is encouraged to consult Fletcher et al. (2011), Holman et al. (2011) & Kontar et al. (2011) for recent reviews on the observational characteristics of flares and particle acceleration, and commentary on how these observations fit into our theoretical framework. Priest & Forbes (2002) also provides a good theoretical overview of flare physics from an MHD perspective, and Sweet (1969) discusses a review of the early work in the mechanisms of solar flares.

In the corona, above AR, the sheared and stressed magnetic field stores a significant amount of energy, and can have a complex geometry (in excess of 10^{32} erg Priest & Forbes 2002). These fields become unstable and the magnetic topology reconfigures to a more stable, relaxed state via a process that is thought to be magnetic reconnection. Reconnection occurs in a diffusion region, where field lines are forced together and where the MHD frozen-in-condition breaks down and particles are able

to cross the magnetic field (Priest 1982). This can occur spontaneously due to some instability, or as a result of some external perturbation (such as the eruption of a filament). Whatever the reason for the field to reconfigure, during the process a large amount of energy is released. Some of this energy heats the plasma *in situ* at the loop top, but the bulk is transported down along newly reconnected field lines to footpoints in the lower atmosphere.

Given the observations of a power-law bremsstrahlung spectrum from HXR footpoint sources in the chromosphere, and the interpretation from the CTTM that these observations imply an energetic population of non-thermal electrons (Brown 1971), a leading candidate for the flare energy transport mechanism is downward propagating non-thermal particle beams (e.g Brown 1972; Hudson 1972; Brown 1973). Electrons are the leading candidate, but protons and ions can also be accelerated (Brown et al. 1990). In the solar flare literature the term CTTM has become synonymous with 'non-thermal electron beams', but the CTTM itself just describes a situation where non-thermal electrons (i.e. those accelerated out of the thermal population) lose their energy collisionally, and makes no assumptions about the geometry (Brown et al. 2009), so that the CTTM does not stipulate that the electrons are accelerated from the corona.

Following energy release, electrons (or ions) are accelerated out of the thermal background to energies greater than $E \sim 20$ keV up to a few $\times 100$ keV, or even to MeV energies. The acceleration mechanism is not yet confirmed, and is not discussed here, with some candidates described in Holman et al. (2011). Note that the lower energy bound quoted is simply an estimate, based on HXR observations, and represents where the non-thermal HXR spectrum joins the thermal background spectrum. This is a notoriously hard quantity to measure and so the energies may extend lower. Electrons precipitate down the flux tube where they encounter the dense thick-target of the chromosphere, losing a tiny fraction ($\sim 10^{-5}$) of their energy to bremsstrahlung, producing the compact footpoints, and the majority of their energy via Coulomb interactions. The depth to which electrons are able to penetrate and the energy flux they deposit in the chromosphere is a function of the electron energy distribution. This can be inferred from HXR observations. A typical energy flux might be on the order of $1 \times 10^{10-11}$ erg cm^{-2} s^{-1}, with a spectral index δ that describes the 'hardness' of the power-law spectrum above a low-energy cutoff energy, E_c. A lower $\delta \sim 3-6$ (a harder spectrum) means that there is a higher proportion of high-energy electrons in

the distribution, compared to higher $\delta \geq 7$ (a softer spectrum) where there is a lower proportion of high-energy electrons.

Coulomb interactions heat the plasma in the chromosphere and transition region, which becomes overionised following heating and direct collisions with the beam. This results in the enhanced EUV, UV, optical and IR radiative output discussed above, and flare ribbons form. As new field lines reconnect the energy deposition site changes, heating new atmospheric locations, and the brightest emission appears to move across the field of view, leading to the apparent motion of the ribbons. If the energy flux is large enough then radiative losses become unable to balance energy input, and the plasma temperature explosively increases driving high velocity flows (chromospheric evaporation and condensations). Upflows carry chromospheric material into the flux tube, increasing the density (and pressure) and creating the flare loops observed in hot EUV lines (e.g. Figure 1.3(c)) and SXR, which then cool through the gradual phase forming an arcade of loops. There is a rich literature presenting and interpreting observations of these processes including (but not limited to!) the following: Doschek et al. (1980), Antonucci & Dennis (1983), Canfield et al. (1987), Culhane et al. (1994), Schmieder et al. (1995), Doschek et al. (1996), Yokoyama et al. (2001), Brosius & Phillips (2004), Milligan et al. (2006a), Milligan et al. (2006b), Milligan & Dennis (2009), Graham & Cauzzi (2015).

During flares the ribbons spread apart, and extend along the PIL, and coronal loops increase in height (e.g. Martin 1979). This is not due to bulk plasma motions (e.g Martin 1979; Schmieder et al. 1987) but is instead a consequence of the geometry of flare energy release as reconnection occurs between new field lines, and the reconnection site propagates (e.g. Priest & Forbes 2002). Motion along the PIL occurs as newly reconnected loops deposit energy, while the spreading away from the PIL and increase in height of SXR loops happens when the reconnection site moves higher in the atmosphere (Priest & Forbes 2002).

Following tradition, a cartoon of a flaring loop is shown in Figure 1.4, that attempts to illustrate the standard model (for a treasure trove of additional flare cartoons see Dr. H. Hudson's 'Grand Archive'[3]). This cartoon shows a single flare loop, with the energy release site in the corona and the locations of HXR and UV sources (modified from an image provided by N. Jeffrey, *private communication*). Whilst only being a cartoon representation, observations reported by, for example,

[3] http://solarmuri.ssl.berkeley.edu/~hhudson/cartoons/

Su et al. (2013) and Yokoyama et al. (2001) look remarkably similar to this picture.

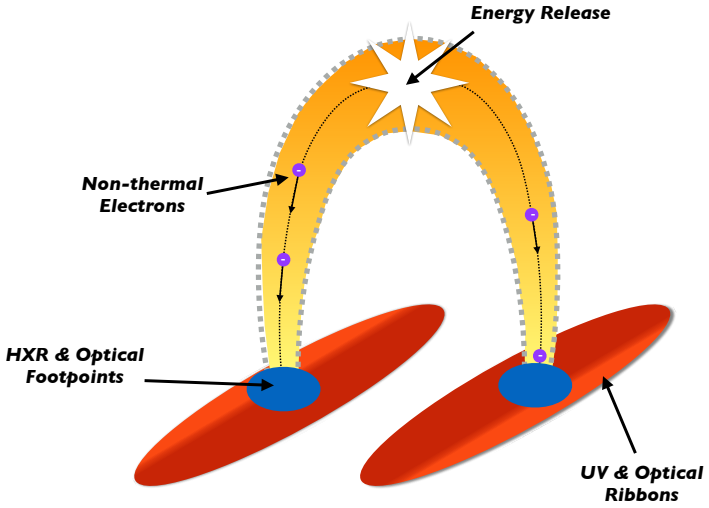

Figure 1.4: *A cartoon model of a flare loop. Non-thermal electrons transport energy from the energy release site in the corona to the chromosphere. This energy is deposited, resulting in compact HXR & optical footpoints, and more extended UV and optical ribbons. Ribbons usually have a bright leading edge. Over time the reconnection site propagates, forming a rising arcade of new loops which results in ribbon separation. Image has been adapted from a cartoon provided by Dr. N. Jeffrey (private communication).*

1.2.3 Beyond a Simplified Description

Observations interpreted under the electron beam model imply a large flux of electrons of up to 10^{36} electrons s^{-1} (e.g. Hoyng et al. 1976; Holman et al. 2003). For a coronal density of 10^9 cm^{-3} this is equivalent to accelerating all of the electrons with a coronal volume of $(10{,}000\text{ km})^3$ every second. A continual resupply mechanism is required to avoid quickly exceeding the available electrons. A return current of electrons streaming in the opposite direction of the beam (e.g. Hoyng et al. 1976; Knight & Sturrock 1977; Hoyng et al. 1978; Brown & Melrose 1977; Holman et al. 2011), produced by an electron field created from the flow of electrons in the beam, could be the resupply mechanism. However, as discussed by Fletcher & Hudson

(2008) and Krucker et al. (2011), some HXR observations suggest the beam density is a significant fraction of the ambient coronal density. In situations where this is the case the requirement of a dilute beam are not met. In such circumstances the beam return current speed is comparable to the beam speed and plasma waves can be produced, such as ion-accoustic waves (e.g Brown & Melrose 1977; Hoyng et al. 1978; Melrose 1990). This may in turn dissipate energy from the electron beam (e.g Lee et al. 2008; Karlický & Kontar 2012) and could result in the acceleration of electrons to energies higher than the injected energy. Research into the energy losses and acceleration due to plasma instabilites is a complex but active area of research.

HXR source heights have been studied by numerous authors (e.g Aschwanden et al. 2002; Kontar et al. 2008, 2010; Battaglia et al. 2012), and are typically in the range 700 – 1200 km, varying with electron energy. In the simulations of Battaglia et al. (2012), the source heights were in the range $\sim$ 600 km to several thousand km above the photosphere, depending on various parameters including the ambient density, pitch angle distribution and electron energy. The assumed density structure of the atmosphere had a strong impact on source height, as did the energy of the electrons, and the pitch angle distribution (see Figures 2 & 7 in Battaglia et al. 2012). Krucker et al. (2015) analysed RHESSI and HMI observations of three flares located at the solar limb, finding that HXR and WL sources to be largely co-spatial at a height of $\sim$ 800 – 1000 km above the photosphere. Based on the simulations of Battaglia et al. (2012), Krucker et al. (2015) state that if high density models are excluded then the source height range for the energies they consider in their flares (> 30 keV) should be $\sim$ 800 – 1500 km. The lower bound is based on highly beamed models, and the upper from an isotropic distrbution. Their analysis found that the HXR source heights were $\sim$ 800 – 1000 km, in the lower range of the simulations of Battaglia et al. (2012). Krucker et al. (2015) noted that in order to be consistent with the standard model, electrons would have to be strongly beamed into footpoints of low ambient density. However, a statistical study of the albedo of solar flare HXR footpoints Dickson & Kontar (2013) shows little evidence for beam anisotropy (so that electrons are not strongly beamed and are instead largely isotropic). Kane et al. (1998) found similar results. It is possible that modifications to the standard model, such as re-acceleration of electrons could act to decrease the source height (e.g Varady et al. 2014).

There exists one observation of a limb flare that shows a significantly lower HXR

source height than has been previously (or since) observed. Martínez Oliveros et al. (2012) analysed STEREO, HMI and RHESSI observations to deduce that the HXR sources were observed at a height only 305 ± 170 km above the photosphere. If accurate, these observations would place considerable contraint on the standard model. However, it should be noted that Krucker et al. (2015) studied the same event and found a source height ~ 800 km. Also, collisional losses increase with density, so with decreasing height towards the photosphere. This makes it more difficult to accelerate electrons. At a height of ~ 300 km the required energy to accelerate the electrons may be too great.

The electron beam model is attractive in that it neatly describes the heating of the chromosphere, the co-spatial optical & HXR footpoints, and the observed particle acceleration (albeit with some details to fill in regarding the acceleration mechanism). However, as mentioned above, the analysis of Krucker et al. (2015) would require electrons to be strongly beamed to be consistent with the simulations of Battaglia et al. (2012), but this is not observed. Additionally, the TMR has been observed to show temperature enhancements of up to a few hundred kelvin during flares (e.g Machado & Linsky 1975; Machado et al. 1978; Metcalf et al. 1990), and similarly there is evidence to suggest that WLF emission originates between the photosphere and upper photosphere (e.g Hiei 1982; Watanabe et al. 2013). Electrons require energies in excess of 350 keV to reach the TMR, and closer to 900 keV to penetrate to the upper photosphere (Machado et al. 1989; Neidig 1989). From HXR observations, there does not appear to be enough power in these high-energy electrons to deposit sufficient energy at these depths (Metcalf et al. 1990).

Given these observations it is prudent, and interesting, to also investigate alternative mechanisms of energy transport, which might either act in tandem with non-thermal electron beams, or alone. One such mechanism is the resistive dissipation of downward propagating Alfvén waves, modelled by Emslie & Sturrock (1982) as a means for heating the TMR during flares. Recently, this idea has been revisited as a potential candidate for delivering all of the flare energy to the chromosphere (Fletcher & Hudson 2008; Russell & Fletcher 2013; Reep & Russell 2016). Alfvén waves are an example of an MHD wave and since a flare is, fundamentally, a large scale restructuring of the coronal magnetic field then the production of MHD waves is likely. In this model, downward propagating Alfvén waves are launched from the

coronal energy release site, and are dissipated in the chromosphere where they heat the plasma. This energy transport mechanism is discussed in detail in Chapter 5.

1.3 Simulations of Solar Flares

Solar flares have been investigated theoretically, both from a radiation and hydrodynamic perspective that seeks to determine the structure of the flare atmosphere, and from an MHD & reconnection perspective that aims to identify how fields lines store and then release their energy. A summary of some noteable investigations of the former is given here, since this thesis concerns the response of the flare chromosphere to energy input.

As discussed in Ricchiazzi & Canfield (1983) and Hawley & Fisher (1994) there are two approaches to determine the flare atmospheric structure. One is to use the semi-empirical approach described in § 1.1.2, but this method makes it difficult to study the physics behind different flare heating mechanisms in any great detail. A second, but more computationally difficult, approach is to prescribe a flare heating function from a flare model, and to solve the equations of hydrostatics (or dynamics), level populations, and radiation transport, including the flare heating rate in the energy equation. This self-consistently returns a flare atmospheric structure and radiative output of transitions solved in detail by the simulation. In this way, the effects of changing the flare heating function on the resulting atmospheric evolution can be determined. The radiation produced by these models can be compared to observations to judge the validity of the prescribed heating and model assumptions. These models have included both static and hydrodynamic solutions, and are typically 1D.

The work of Ricchiazzi & Canfield (1983) and Canfield et al. (1984) were the amongst the first detailed theoretical investigations that used this second method (that they dubbed the 'synthetic' approach) to model flares, and they were the first to include detailed radiative losses that are crucial for energy balance. They solved the 1D plane-parallel hydrostatic equilibrium, energy balance, radiation transport and statistical equilibrium equations (see Chapter 2). Important transitions of H, Ca and Mg were solved in detail to compute their radiative losses and EUV and X-ray losses were computed under an optically thin assumption. Importantly, they included the effects of H ionisation from collisions with the non-thermal electron beam. Ricchiazzi

& Canfield (1983) investigated the relative importance of non-thermal electron beams versus enhanced thermal conduction for flare heating, finding that only beams could carry energy below the TR. For low pressure coronae (1 dyne cm^{-2} in their model), enhanced conduction had an effect on the TR location during the flare, but not so for the higher pressure case (10^2 dyne cm^{-2}) . The hydrogen ionisation fraction was seen to depend on collisions with the electron beam, which subsequently affected the atmospheric temperature structure. These models were limited by the fact that it was assumed hydrostatic equilibrium was achieved (unlikely in the impulsive phase of flares). In a follow up work (Canfield et al. 1984) these were compared to static 'impulsive' atmospheres, where energy balance has been achieved but the density structure has not had time to respond (so is unchanged from the pre-flare state). Canfield et al. (1984) studied the effect on synthetic Hα profiles of varying the coronal pressure and electron beam heating parameters. It was found that a higher pressure corona (> 100 dyne cm^{-2}) reduced the size of the central absorption feature of Hα, since the higher pressure results in a higher collisional rate at the top of the line forming region, and only heating with an energy flux of high energy electron $> 1 \times 10^{10}$ erg cm^{-2} s^{-1} produces the observed line width.

Fisher et al. (1985c,b,a) performed radiation hydro*dynamic* simulations, which attempted to capture the coupling between radiation transport and the hydrodynamic evolution of the atmosphere. This coupling is important since the radiation field is set by the thermodynamic state of the atmosphere via the dependence of the population rates on temperature and density. But since radiation losses then affect the energy balance (and therefore thermodynamic state) these are coupled. These simulations also captured non-equilibrium ionisation by computing the rate equations instead of statistical equilibrium (they considered the 'history' of the atmosphere on the level populations state). Their main finding was that the energy flux into the atmosphere dictated the type of mass flows that were generated. A flux $< 1 \times 10^{10}$ erg cm^{-2} s^{-1} will produce only modest upflows of a few $\times 10$ km s^{-1}, which has become known as 'gentle evaporation.' On the other hand, an energy flux greater than this threshold will result in 'explosive evaporation' where velocities can be > 100 km s^{-1}. Chromospheric condensations (dense, cool downflows) were only associated with explosive evaporation. The explosive evaporation was caused by a thermal instability, where radiative losses were unable to balance energy input and temperature rapidly increased. The resulting overpressure at the heating site drove

the high velocity flows into the corona. Since the mass density increases with depth into the chromosphere the downflows were of significantly lower magnitude than the upflows

These synthetic approaches have proven to be very useful in our understanding of the important physics at work during the atmospheric response to flare energy input. However, in order to make the numerical simulations tractable they used an escape probability formalism when solving the radiation transport problem. In this method the probability of a photon escaping from a particular location is given as a function of the optical depth at that location. If the photon escapes then it contributes towards radiative losses. If not then it is essentially immediately re-absorbed at that location (an example of the *on-the-spot-approximation*). In reality photons emitted in one location can be re-absorbed at a distant location (before eventually escaping), depending on the opacity of the atmosphere. They thus contribute towards radiative heating at that location. If the photon is absorbed at a deeper point in the atmosphere than it was emitted we refer to the process as backwarming. This is the non-local nature of the transport problem, and is something that escape probability does not capture (see, e.g. Hubeny 2001). Instead, to properly capture radiative loss and heating during flares, the full angle and frequency dependent transfer equation should be solved.

Hawley & Fisher (1994) improved upon the static Ricchiazzi & Canfield (1983) by solving the full transport equation to account for radiative heating and loss for H, Ca II and Mg II. They also incorporated optically thin backwarming of coronal X-rays into the chromosphere and optically thin losses of elements not included in detail. They modelled two scenarios similar to Canfield et al. (1984) where a static impulsive atmosphere in energy balance but not in hydrostatic balance was modelled, and an equilibrium atmosphere where both energetic and hydrostatic balance is achieved. To reproduce the observed broad Hα profiles ether a low coronal pressure or an additional source of energy flux was required. The Hα flux decreased with time as evaporation increased the coronal density and pressure, reducing the ability of the beam to heat the chromosphere.

Building upon these previous efforts, Abbett & Hawley (1999) simulated the flare response by solving the full transport equation rather than relying on escape probabilities, but also considered the hydrodynamical response, so that a full 1D radiative hydrodynamics treatment was implemented. This was achieved by modifying the

RADYN code of Carlsson & Stein (1995, 1997) to model the injection of a beam of non-thermal electrons, including the X-ray irradiation and optically thin losses of Hawley & Fisher (1994) and capturing the effects of mass motions. They confirmed the result of explosive versus gentle evaporation, showing the effect of gradients on the emergent line profiles. Additionally, they investigated the formation of Hα and optical continuum, noting that non-equilibrium ionisation effects were important. Allred et al. (2005, 2006, 2015) made further improvements to RADYN to include a better treatment of backwarming and electron beam heating, as detailed in Chapter 2. The flare version of RADYN is a powerful resource with which to investigate the complex radiative and thermodynamic response to flares. Flare simulations presented in this thesis use the RADYN code.

Finally, colleagues at Ondřejov Observatory have developed a modular radiation hydrodynamics flare code (FLARIX; Kašparová et al. 2009; Varady et al. 2010), with particular attention paid to the non-thermal collisional rates with hydrogen and other species. Their code, described by Kašparová et al. (2009), is the combination of three coupled modules. The first is a test-particle code that simulates the propagation, scattering and thermalisation of a beam of non-thermal electrons (Karlicky 1990; Karlicky & Henoux 1992), from which flare heating and non-thermal collisional rates are calculated. The second is a 1D hydrodynamic code that uses the VALC or other atmosphere as an initial state. The third is a time-dependent non-LTE radiative transfer code, which computes time-dependent ionisation and optically thick radiatives losses from various elements. Using short-pulse beam heating Kašparová et al. (2009) noted that while there were clear fast line intensity variations, which were well correlated with time variations in beam flux, they were unable to determine unambiguous diagnostics of non-thermal electrons from individual Balmer lines. This code has been further developed since Kašparová et al. (2009) and Varady et al. (2010) and is now being used to study the physics of the chromosphere during solar flares. Recent experiments to compare RADYN and FLARIX have shown remarkably close agreement (Mats Carlsson and Petr Heinzel, *private communication*, 2016).

Chapter 2

Numerical Codes and Observational Data

Research presented in this thesis made use of two numerical codes: the radiation hydrodynamics (RHD) code, RADYN, and the radiation transfer (RT) code, RH. Both of these codes were written and developed by others, who kindly shared these useful resources and assisted with their use. They are described below (§ 2.1), but the reader is encouraged to consult the references indicated for an in-depth description of the codes. In addition to numerical simulations, observations of solar flares using spectroscopic and imaging data are presented. The instruments from which this data originated are described in § 2.2.

2.1 Description of the Numerical Codes: RADYN and RH

2.1.1 RADYN

The RHD code RADYN was originally written by Carlsson & Stein (1995, 1997) to investigate the formation of Ca II of bright grains in the chromosphere, and the dynamics of acoustic shocks in the chromosphere. Since then it has become a well established resource for studying the dynamics and radiation from the chromosphere, including during solar flares. Abbett & Hawley (1999) adapted RADYN to model the atmospheric response to a energy deposition from a beam of non-thermal electrons, which included adding a transition region and corona to the radiative equilibrium atmosphere from Carlsson & Stein (1997) (see § 2.1.1.2 for a description of the initial

atmospheres). Later modifications were made by Allred et al. (2005, 2015), improving both the treatment of the non-thermal electron beam and radiation heating terms.

Below is an outline of the code, a description of heating terms used in flare simulations, and a description of the initial atmospheres. For full details about the code and method of solution the reader is directed towards Carlsson & Stein (1997), Abbett & Hawley (1999), and Allred et al. (2005, 2015).

2.1.1.1 RADYN Outline

Mass motions of up to a few hundred km s^{-1} present in solar flares create density and temperature variations that affect the strength of radiative losses, and the population density of atomic levels. Radiative heating and cooling in turn affect the temperature and density structure of the atmosphere. To model this, the equations of hydrodynamics (the conservation of mass, the conservation of momentum, and the conservation of energy) must be coupled with the equations of radiation transport (the radiative transfer equation and the time-dependent level population equation). RADYN solves the plane-parallel, coupled, non-local, non-linear equations of hydrodynamics, radiation transfer, and atomic level populations along a 1D flux tube, extending from the sub-photosphere to the corona.

The equations of radiative hydrodynamics are solved implicitly on an adaptive grid (Dorfi & Drury 1987) with 191 grid points, so that shocks and steep gradients can be adequately resolved. As described in Allred et al. (2015), higher weighting is given to resolving gradients in temperature, velocity and atomic level populations.

The equation of internal energy conservation includes terms for the conductive flux, and the radiative flux. The radiative flux is found by integrating the radiation transfer equation over frequency and solid angle. The conductive heating flux is the classical Spitzer conductive flux, but in order to avoid unphysical values of the flux in locations of steep temperature gradient (such at the transition region), the Spitzer form is adjusted as in Fisher et al. (1985c), which tends to a saturation limit when dT/dz is large. Recent work by Bian et al. (2016) has investigated the effect of including turbulent suppression of thermal conduction in an effort to explain the discrepancy between the predicted cooling rate of flare loops compared to observations (see, e.g.,Ryan et al. 2013). In their analytic study, Bian et al. (2016) found that in order to obtain a cooling rate similar to observations turbulence must be incorporated and, further, that collisionally-dominated conduction plays only

a limited role. By not including this effect in RADYN we may be overestimating the conductive cooling rate.

Sources of non-radiative and non-conductive heating are included in the internal energy conservation as an additional terms, Q, which can include heating via non-thermal electron beams, Q_{beam}, heating from backwarming associated with flare enhanced temperature Q_{back}, and time-dependent heating Q_{TD} which allows the user to input model independent heating as a function of height and time. In Chapter 5 an approximated form of Alfvén wave heating is added Q_{AW}.

Elements important for energy balance (due to strong radiative losses) in the chromosphere are solved in non-LTE (NLTE). Transitions solved in NLTE are referred to as the 'detailed transitions.' For a full list of transitions solved in detail see Tables 1 & 2 in Allred et al. (2015). In summary, RADYN solves the atomic level population equation and radiation transfer equation for a six-level-with-continuum hydrogen atom, a nine-level-with-continuum helium atoms, a six-level-with-continuum Ca II ion, and a four-level-with-continuum Mg II ion. Up to 100 frequency grid points and 5 angular points are solved by the radiative transfer equation for each transition. For atomic species not computed in detail, the Uppsala opacity package of Gustafsson (1973) is used to include their opacity as a background source as a function of temperature, density and frequency (in LTE). Radiation from detailed transitions can contribute to radiative heating non-locally. That is, the radiation can propagate either to escape, or to some location where it is absorbed and contributes to heating at that location.

All detailed transitions are computed under the assumption of complete redistribution (CRD). This assumes that the frequency of any absorbed photon is uncorrelated with the frequency of the emitted photon due to collisions that occur during the lifetime of the excited state. However, in the low density solar chromosphere there may be insufficient elastic collisions before the line de-excites. The frequency of an emitted photon would therefore be correlated to the absorbed photon via the redistribution function. This situation is called partial redistribution (PRD), and is not yet implemented in RADYN in order to keep the numerical solution tractable. Differences between CRD and PRD are discussed further in § 2.1.2.2 and Chapter 4 but in short, CRD results in a frequency independent line source function, whereas in PRD the source function is frequency dependent. Flare simulations with RADYN are already computationally expensive to run, with some simulations taking weeks

to complete just a few seconds or minutes of solar time. Including PRD radiative transfer, where the source function would explicitly depend on the radiation field in addition to the level populations, would further increase the computational cost significantly. The effects of PRD have been shown to be important for chromospheric lines, including the Lyα line (Milkey & Mihalas 1973), the Ca II H & K lines (e.g Uitenbroek 2002) and the Mg II h & k lines (e.g Milkey & Mihalas 1974). While PRD effects are mimicked for the Lyman lines by truncating them at 10 Doppler widths, they are not for the other lines. For an in-depth description of PRD consult Hubeny & Mihalas (2014).

In addition to radiative losses from the detailed transitions, RADYN computes losses from other species under the assumption that they are optically thin. It is assumed that radiation produced by species not treated in detail is able to escape without absorption (if it is directed upwards), so that this contributes towards local radiative losses. These optically thin losses are found by summing the emissivities as a function of temperature from the transitions in the CHIANTI atomic database (Dere et al. 1997; Landi et al. 2013), excluding the transitions already treated in detail by RADYN.

Previously Abbett & Hawley (1999) considered heating by soft X-rays (SXR), which was updated by Allred et al. (2005) to consider backwarming by SXR and extreme-ultraviolet (EUV) radiation (together referred to as XEUV). Allred et al. (2015) updated XEUV backwarming to self-consistently include enhanced photoionisations resulting from an increase in XEUV backwarming during flares. The product of the emission measure from the coronal and transition region portion of the loop, and the emissivities from numerous transitions from CHIANTI (as a function of frequency and temperature), are integrated to compute the XEUV spectrum. This is included as a downward-directed incident radiation when solving the NLTE radiation transfer and ionisation equations.

2.1.1.2 Initial Atmosphere

The pre-flare atmosphere consists of one half of semi-circular 1D flux tube that models one half of a symmetric flaring loop, anchored in the sub-photosphere and extending to the corona, initially created by Abbett & Hawley (1999) by adding a transition region and corona to the radiative equilibrium (RE) model of Carlsson & Stein (1997). It is assumed that this flux tube is a vertical cylinder of constant

cross-section, but the circular geometry is considered for gravitational acceleration (Abbett & Hawley 1999). Semi-empirical model atmospheres such as the well known VALC (Vernazza et al. 1981) and FALC (Fontenla et al. 1993) atmospheres were produced by finding an atmospheric structure that successfully reproduced spatially and temporally averaged observations. Radiative equilibrium atmospheres differ in that the computed atmospheric structure is a result of balance between radiative heating and losses, computed by solving the equations of radiation hydrodynamics. The temperature, density and pressure structure, and radiative output, approximates the actual atmosphere within the confines of the 1D RHD equations.

It is non-trivial to produce a stable starting atmosphere, but the process is to iteratively build towards a non-LTE converged solution to the RHD equations. Starting from a solution that is close to the expected result (e.g. the VALC atmosphere), the steps, in outline, to produce the RE atmosphere are: (1) solve the static version of RADYN for H in LTE to obtain the H populations and the electron density (2) vary the grid weighting on each variable to move the grid to locations where high resolution is required, (3) one-by-one include the other elements to be treated in detail, repeating the previous steps to obtain their LTE population densities, (4) solve for the NLTE populations of H, (5) one-by-one find the NLTE populations of the other elements, (6) using this static, NLTE solution, the dynamic version of RADYN is run with non-radiative heating applied to keep the upper and lower boundaries at a fixed temperature, (7) the atmosphere is allowed to evolve and reach a state of radiative equilibrium.

The initial atmospheres used in this thesis were provided by Dr. J. Allred (*private communication*), and are shown below in Figure 2.1. Using the nomenclature from Allred et al. (2015) atmospheres were defined by the loop length, photospheric temperature (at $\tau_{5000} = 1$) and coronal temperature as QS:SL:LT (quiet Sun photosphere at 5800 K, short loop of 10 Mm, low temperature corona at 1 MK) and QS:SL:HT (quiet Sun photosphere at 5800 K, short loop of 10 Mm, high temperature corona at 3 MK). The QS:SL:LT was used for the most part here, but one simulation (the 'reference flare simulation' provided by Dr J. Allred) used the QS:SL:HT initial atmosphere.

Figure 2.1 shows the structure of the initial atmospheres alongside the FALC semi-empirical atmosphere. Panel (a) shows the temperature, panel (b) shows the electron density and panel (c) shows the neutral hydrogen density. The main differences

between the RADYN atmospheres are that the QS:SL:LT atmosphere with lower coronal temperature has a correspondingly lower coronal density (electron and hydrogen), and a transition region located at a higher geometrical height. On a column mass scale the transition region in the QS:SL:LT atmosphere is located at a lower column mass. There are some differences in the mid-lower chromosphere and photosphere but these are small. Comparing to the FALC atmosphere, then both RADYN atmospheres have transition regions located at smaller geometrical heights, but while the QS:SL:LT has a transition region a lower column mass than FALC, QS:SL:HT's transition region is located at a greater column mass (resulting from the increased hydrogen density in the QS:SL:HT corona). The chromospheric temperature and electron density is higher in the FALC atmosphere.

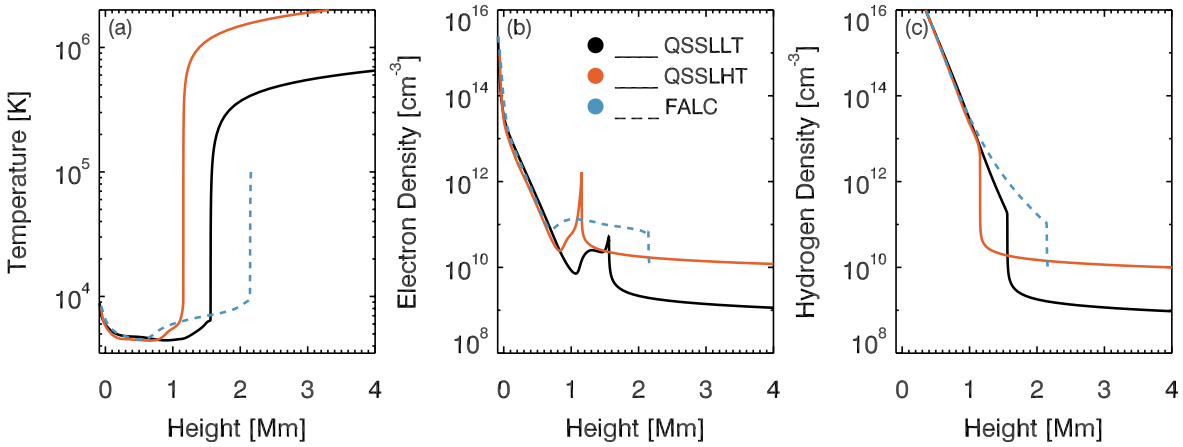

Figure 2.1: *The pre-flare RADYN atmospheres, QS:SL:LT (black, solid line) and QS:SL:HT (orange, solid line) and FALC semi-empirical atmosphere (blue, dashed line; Fontenla et al. 1993). Panel (a) shows temperature, panel (b) shows electron density, and panel (c) shows hydrogen density.*

2.1.1.3 Flare Simulations

In RADYN flare simulations, flare energy flux is injected at the apex of the loop, in the corona, where it then propagates downwards. Typically this flare energy deposition is via a non-thermal particle beam (usually electrons though a beam of protons or ions can also be injected), which deposits the bulk of its energy in the chromosphere. Energy deposition heats and ionises the plasma, leading to enhanced

radiative output (which in turns heats certain locations of the atmosphere), mass motions and increased XEUV backwarming. It is assumed that the beam impacts a 'cold target' (the chromosphere), where the ambient thermal energy of the plasma is significantly lower than the energy of electrons within the beam.

Different treatments of non-thermal particle beam heating have been incorporated. Abbett & Hawley (1999) used a beam-heating function based on Hawley & Fisher (1994) to compute the heating rate as a function of column depth. This follows the analytic formulation of the heating rate as a function of column depth from Emslie (1978), and using a non-uniform ionisation fraction. The heating rate at each depth point in the atmosphere is computed from an electron energy distribution above a low energy cutoff energy E_c with a single power law, δ, and non-thermal electron energy flux injected at the loop apex, F. The user defines δ, E_c, and F as a function of time. Informally, this implementation is referred as to as the 'Emslie Beam' treatment. Allred et al. (2005, 2006) modified RADYN to also allow an injected electron spectrum that has a double power law distribution. In this scenario, as well as specifying F and E_c, the user also defines the break energy E_B where the power law shifts from the lower spectral index δ_l to the upper spectral index δ_u. These parameters can be derived from HXR observations, for example from RHESSI (e.g. Holman et al. 2003), if a specific flare is to be simulated.

Finally, Allred et al. (2015) modified RADYN to use the Fokker-Planck method to obtain the electron distribution function, and from that the beam heating rate. This is a more realistic treatment of particle beam heating, which includes the pitch angle of the beam (set to unity in the 'Emslie Beams'), pitch angle diffusion, and synchrotron losses. The electron beam can set up a return current electric field (e.g Hoyng et al. 1976; Holman 2012), which results in a current of electrons in the opposite direction from the downward propagating beam. This current can heat the atmosphere through Joule dissipation. Based on the return current heating rates derived by Holman (2012), return current heating has been included as an optional additional non-radiative heating term in the energy equation. For full details of the Fokker-Planck and return current implementation Allred et al. (2015) should be consulted.

2.1.1.4 The Contribution Function

RADYN allows an investigation of both the atmospheric evolution during flares, and the radiative output of spectral lines and continua. A useful quantity when investigating the formation of radiation is the contribution function to the emergent intensity, $C_I(x)$, where x describes a layer of the Sun's atmosphere, defined on a suitable depth scale (Magain 1986; Carlsson & Stein 1997; Carlsson 1998). That is, the contribution to the emergent intensity originating from a layer x. From the contribution function, and related quantities, the depth and conditions of line formation can be determined as a function of frequency.

In a 1D plane-parallel atmosphere the equation for radiation transfer along a path length ds can be written as in Gray (1992):

$$\mathrm{d}I_\nu = (-\kappa_\nu \rho I_\nu + j_\nu \rho)\mathrm{ds}. \tag{2.1}$$

In Eq 2.1, κ_ν is the mass absorption coefficient, j_ν is the emission coefficient, ρ is the mass density and I_ν is the specific intensity at frequency ν. Defining this on a geometric height scale, z:

$$\mu\, \mathrm{d}I_{\nu,\mu} = (-\kappa_\nu \rho I_{\nu,\mu} + j_\nu \rho)\mathrm{dz}, \tag{2.2}$$

where the specific intensity now has an explicit dependence on the cosine of the angle between the ray and the normal to the surface $\mu = \cos\theta$. Further, defining the ratio of emission to absorption as the source function $S_\nu = j_\nu/\kappa_\nu$, and using the standard optical depth (τ_ν) scale d$\tau_\nu = -\kappa_\nu \rho \mathrm{dz}$, the transfer equation can be rewritten in the standard form as

$$\mu \frac{\mathrm{d}I_{\nu,\mu}}{\mathrm{d}\tau_\nu} = I_{\nu,\mu} - S_\nu. \tag{2.3}$$

The formal solution to this radiation transfer equation is

$$I_{\nu,\mu}(0) = \int_0^\infty \frac{1}{\mu} S_\nu \mathrm{e}^{-\tau_\nu/\mu} \mathrm{d}\tau_\nu, \tag{2.4}$$

where $I_{\nu,\mu}(0)$ is the specific intensity at $\tau_\nu = 0$, also called the emergent intensity.

Defining the emergent intensity on a depth scale x, the contribution function to that intensity can be defined as the integrand of Equation 2.4:

$$I_{\nu,\mu}(0) = \int C_I(x)\mathrm{d}x. \tag{2.5}$$

Defining on the optical depth scale as in Eq 2.4, the Contribution Function is

$$C_I(\tau_\nu) = \frac{1}{\mu} S_\nu e^{-\tau_\nu/\mu} \tag{2.6}$$

Transforming to a geometric height, via $C_I(\tau_\nu)d\tau_\nu = C_I(z)dz$

$$C_I(z) = \frac{1}{\mu} S_\nu e^{-\tau_\nu/\mu} \chi_\nu, \tag{2.7}$$

where χ_ν is the monochromatic opacity per volume, ($\chi_\nu = \kappa_\nu \rho$). Integrating over the whole atmosphere will result in the emergent intensity $I_{\nu,\mu}$.

A common approach is to follow the example of Carlsson & Stein (1994) and Carlsson & Stein (1997), who rewrote the formal solution to the transfer equation in a 1-D, plane-parallel, semi-infinite atmosphere as:

$$I_{\nu,\mu} = \int_z \frac{1}{\mu} S_\nu \, \tau_\nu e^{-\tau/\mu} \, \frac{\chi_\nu}{\tau_\nu} dz, \tag{2.8}$$

where the integrand is the contribution function, $C_I(z)$, and $0 < \mu < 1$.

The contribution function analysis can, of course, be applied to the output of similar radiation transport codes, such as RH. Separating the components of $C_I(z)$ in the manner of Equation 2.8 allows the formation properties to be visualised, in addition to $C_I(z)$. It has become common in the RADYN, RH, and related literature to represent this analysis as a four-panel diagram showing the components of the contribution function alongside the contribution function itself (introduced by Carlsson & Stein 1994, and discussed further in Chapter 4). The $\tau_\nu e^{-\tau_\nu/\mu}$ term describes the attenuation of the source function, and peaks when $\tau_\nu = 1$. The χ_ν/τ_ν term is high at locations of high particle density at low optical depth (because the opacity is proportional to the density of emitting particles). This picks out velocity gradients in the atmosphere. The source function is dependent on frequency across the line profile if partial redistribution is used (as in RH), and is independent of frequency if complete redistribution is assumed (as in RADYN).

For a line to be described as optically thick, the emergent intensity originates from around the $\tau_\nu = 1$ surface. In this case the theoretical line core can be defined as the wavelength position corresponding to that at which the height of the $\tau_\nu = 1$ surface is greatest (e.g Rathore et al. 2015). That is, the part of the line formed highest in the atmosphere (assuming optically thick emission dominates). If there is significant emission from heights where $\tau << 1$ then the line is considered to be optically thin.

As will be seen, the line can be mostly optically thick but mass motions and other flare related effects can result in optically thin contributions.

2.1.2 RH

As will be discussed in Chapter 4, radiative transfer with partial redistribution (PRD) is required to accurately model the Mg II h & k lines. Therefore, the well-established and publicly available radiative transfer code RH (Uitenbroek 2001) which employs PRD was used with snapshots of RADYN flare atmospheres to simulate the response of the Mg II h & k lines to flare energy input. This is a stationary, time-independent, code that requires a prescribed atmospheric structure to be input, so that unlike RADYN there is no feedback between the radiation field and the atmospheric structure. The radiation and associated heating and losses have no effect on the atmospheric structure which is pre-defined and does not vary in the simulation. Only the atomic level populations vary. By producing Mg II profiles from a sequence of RADYN snapshots we are in essence capturing the dynamics, but with the caveat of statistical equilibrium (see discussion below).

2.1.2.1 RH Outline

RH is a numerical radiative transfer code originally written by Uitenbroek (2001, 2002) and based on the Multi-Level Accelerated Lambda Iteration (MALI) methods of Rybicki & Hummer (1991, 1992) which allows overlapping transitions and the use of both CRD or PRD. Those authors should be consulted for an in-depth discussion of both the theory behind PRD, the numerical schemes and the code architecture.

The equations of statistical equilibrium and radiative transfer are solved for atmospheres that can be one of four geometries, 1D plane-parallel, 2D cartesian, 3D cartesian, and a 1D spherically symmetric geometry. Combinations of multiple atoms and molecules can be solved in NLTE, with numerous transitions per species.

The research presented in this thesis used the 1D plane-parallel version of RH, called `rhf1d`. The input atmospheres to RH require: the temperature (T in K), the electron density (n_e in cm^{-3}), the atmospheric velocity (v in km s^{-1}), the turbulent velocity ($v_{\rm turb}$ in km s^{-1}) and the hydrogen population densities of levels 1-5 plus the density of ionised hydrogen (n_{1-5} & n_p in cm $^{-3}$). These are described on either a height (z in km), log column mass ($\log C_{\rm mass}$ in g cm^{-2}), or optical depth (τ) scale. The

number of depth grid points is not fixed, and can be varied provided the parameters listed above are defined at each gridpoint. Internally, these units are converted to S.I. and code outputs are in S.I.

To use a RADYN flare atmosphere as input to RH then the atmospheres must be converted to this format. Since RH is a stationary code, multiple individual snapshots from a RADYN simulation must be created and input to separate RH simulations to compute the spectra produced as a function of time. See the RH documentation[1] and atmosphere files[2] included in the GitHub distribution for examples of the atmosphere files required.

Individual input files contain information about the atoms or molecules including the transitions, wave numbers, oscillator strengths, photoionisation cross sections, and collisional rates. The method of solution (for example partial redistribution, Voigt etc.,), whether the spectrum should be symmetric or asymmetric, and the number of wavelength points to sample can be varied. Other than the method of solution the atom files were not changed for this work.

Atoms to be included are listed in an input file, where they are set to 'active' for atoms where the non-LTE level populations and radiation transport are to be computed, and 'passive' for atoms where only the contribution to the background opacity is required. In the latter case, the populations are calculated at their LTE values. Typically it is better to include as many atoms as possible (in passive or active mode) as the background opacities will affect the level populations of the species computed in detail. Hydrogen must always be included. For the simulations presented here 14 atoms were included, unless specified otherwise. Molecules can also be included, but for this work they were included in passive mode only. Atoms and molecules used in simulations were:

Atoms/ions: H I, C I, O I, Si I & Si II, Al I & Al II, Ca II, Fe I & Fe II, He I & He II, Mg II, N I & N II, Na I & Na II, S I & S II, Ba II, Ni I. These were either included in the GitHub distribution or provided by Dr. Fatima Rubio da Costa (*private communication*, 2015), apart from the Mg II atom file that was provided by Dr. Jorrit Leenaarts (*private communication*, 2015). Atoms listed as both neutral and singly ionised were input as a single file with transitions from both ionisation states included. This list

[1] https://github.com/tiagopereira/rh/blob/master/doc/rhmanual_v2.pdf
[2] https://github.com/tiagopereira/rh/tree/master/Atmos

was recommended by Dr. J. Leenaarts (*private communication*, 2015) to account for the background opacity.

Molecules: H_2, H_2+, C_2, N_2, O_2, CH, CO, CN, NH, NO, OH, H_2O. These were all included in the GitHub distribution.

Opacity and emissivity from Thomson and Rayleigh scattering, hydrogen bound-free and free-free scattering, H^- bound-free and free-free scattering, are included.

A keyword input file tells RH the particular settings for a simulation. These include pointing to the location of the atmosphere, abundances, atom and molecule input files, and setting limits on iterations. The maximum number of iterations can be set, or alternatively, the minimum allowable value of change in populations can be set. Additionally, the angle dependence of the PRD calculation can be specified as either angle-independent, angle-dependent, or as angle-approximated (the hybrid scheme of Leenaarts et al. 2012). In any atmosphere with a non-zero plasma velocity the PRD scheme should be set to either angle-dependent or angle-approximated. These different schemes, and their applicability to the flaring scenario is discussed further in Chapter 4 § 4.2.

Once a particular simulation is set up RH solves the non-LTE radiative transfer for the lines specified, with a typical simulation of a single flare atmosphere snapshot taking several hours to complete (on a machine with a 3.8 GHz Intel Xenon processor and 8Gb memory) when several atoms are included in the active set. Since each flare RH run takes several hours to complete it is not feasible to produce synthetic spectra for *every* RADYN timestep (which can number in the thousands for long or particularly intensive simulations). Instead it is more practical to choose snapshots at every Δt s or for specific times of interest.

2.1.2.2 Partial Redistribution

Since there has been mention of PRD and CRD in a qualitative sense, it is worth also briefly introducing these concepts in a more quantitive manner. However, no attempt is made here to fully discuss the mathematical description of PRD, and what is presented is simply intended to give the reader an illustration of how the source function varies between CRD and PRD. For a more complete description Uitenbroek (2001) provides a very clear explanation of the theory, and Hubeny & Mihalas (2014)

provides a detailed discussion of redistribution functions.

As described in Milkey & Mihalas (1973) and Uitenbroek (2001) (and references therein) the line emission profile, $\psi_{i,j}(\nu, \mathbf{n})$ for upper level j and lower level i, emitted frequency at ν and in ray direction $\mathbf{n}$, is dependent on the radiation field. The emission profile is a function of the absorption profile, $\phi_{i,j}(\nu, \mathbf{n})$, upper and lower level populations, Einstein coefficient for radiative excitation, total rate out of the upper level, line intensity, and, crucially, the general redistribution function, R (in the observer's frame of reference). R describes the conditional probability distribution that if a photon is absorbed at some frequency ν' at angle $\mathbf{n}'$, then it is re-emitted at frequency ν and angle $\mathbf{n}$. See Equation 6, and related discussions, in Uitenbroek (2001). Often, instead of computing the emission profile directly, the ratio of emission to absorption profile is computed, $\rho_{i,j}(\nu, \mathbf{n}) = \psi_{i,j}(\nu, \mathbf{n})/\phi_{i,j}(\nu, \mathbf{n})$. Note that the expression for $\rho_{i,j}$ still contains an additional dependence on the absorption profile through a term involving the redistribution function (Equation 14 in Uitenbroek 2001).

The redistribution function for resonance lines can be written as in Milkey & Mihalas (1973): $R(\nu', \nu) = \gamma R^{II}(\nu', \mathbf{n}'; \nu, \mathbf{n}) + (1 - \gamma)\phi_\nu \phi_{\nu'}$. Here γ is known as the coherency fraction that describes how important PRD effects are to the line (i.e how coherent the emitted radiation is to the absorbed radiation), ν' is the frequency of absorbed photons, the ϕ terms are the absorption profiles of emitted and absorbed frequencies and R^{II} is the angle-dependent redistribution function (see, for example, Leenaarts et al. 2012, Eq. 2 for an expression for R^{II}). The coherency fraction is given by:

$$\gamma = \frac{P_j}{P_j + Q_j^E}, \tag{2.9}$$

where P_j is the total rate of the upper level j, and Q_j^E is the rate of elastic collisions with atoms, ions and electrons (e.g Uitenbroek 2001). The total rate is the sum of collisional and radiative rates.

The source function is:

$$S_{i,j}(\nu, \mathbf{n}) = \frac{n_j A_{j,i} \rho_{i,j}(\nu, \mathbf{n})}{n_i B_{i,j} - n_j B_{j,i} \rho_{i,j}(\nu, \mathbf{n})}, \tag{2.10}$$

where n_i is the population of the lower level, n_j is the population of the upper level, $A_{j,i}$ is the Einstein coefficient for spontaneous de-excitation, $B_{i,j}$ is the Einstein

coefficient for radiative excitation, and $B_{j,i}$ is the Einstein coefficient for induced de-excitation.

In the CRD regime the number of collisions is large so that $\gamma = 0$, and the redistribution function reduces to $R(\nu', \nu) = \phi_\nu \phi_{\nu'}$. In turn, from Equation 14 in Uitenbroek (2001), $\rho_{i,j} = 1$ and the emission profile is equal to the absorption profile. From Equation 2.10 the line source function is independent of frequency. In the PRD regime $\gamma > 0$, and $\rho_{i,j} \neq 1$. The source function is then a function of frequency as in Equation 2.10.

2.1.2.3 Statistical Equilibrium versus Non-Equilibrium Ionisation

Although the radiative transfer in RH offers the inclusion of PRD, representing an 'improvement' over RADYN, it assumes statistical equilibrium when computing population densities. Since RADYN is a time-dependent code, however, it computes the population densities using the population rate equation, which allows the consideration of time dependent processes. Non-equilibrium ionisation is thus taken into account. The population rate equation is:

$$\frac{\partial n_i}{\partial t} + \frac{\partial n_i v}{\partial z} - \left(\sum_{j \neq i}^{N'} n_j P_{j,i} - n_i \sum_{j \neq i}^{N'} P_{i,j} \right) = 0, \tag{2.11}$$

where v is the atmospheric velocity, N' is the total number of states, t is time, z is the height in the atmosphere, $P_{i,j}$ describes the total rates (collisional plus radiative) from i to j, and $P_{j,i}$ is the total rate from j to i. In the dynamic RADYN simulations the transition rates are functions of the local atmospheric conditions (including energy input) which vary with time. If the local thermodynamic state of the atmosphere or the radiation field vary faster than the timescale for ionisation and recombination then there is not enough time for the atmosphere to reach equilibrium and the populations are time dependent - the 'history' of the atmosphere becomes important. If the ionisation and recombination timescales are sufficiently fast then the populations can be approximated by statistical equilibrium (setting $\partial n_i / \partial t$ and $\partial n_i v / \partial z$ to zero in Equation 2.11).

The chromosphere is dynamic, especially during solar flares. Carlsson & Stein (1999, 2002) demonstrated, from RADYN simulations of propagating acoustic waves, that the ionisation and recombination timescale ($\tau \sim 10^3 - 10^5$ s) for hydrogen is long compared to the dynamical timescale, and that if statistical equilibrium is assumed

then the ionisation fraction is underestimated by several orders of magnitude in certain locations of the atmosphere. They did note that during shocks where the enhanced temperature and density shortened the timescale. Inputting RADYN atmospheres into RH eliminates the history of the atmosphere and so runs the risk of underestimating the ionisation of atomic species. Consequently there may be errors in the population densities of atomic states.

Leenaarts et al. (2013a) investigated whether or not non-equilibrium ionisation was important for magnesium. They concluded that whenever the temperature was large enough to produce significant amounts of Mg III the relaxation time was short, and that using statistical equilibrium was appropriate. Of course flares are dynamic and so the conclusions of Leenaarts et al. (2013a) might not apply in flaring conditions. While it is not known exactly how good an approximation statistical equilibrium is for simulating Mg II in flares, the effects of assuming statistical equilibrium for hydrogen, and the effects this assumption have on the output Mg II profiles, are shown in Chapter 4 § 4.2.4

2.2 Solar Flare Observations

Solar flare observations from the *Hinode* Solar Optical Telescope (SOT; Tsuneta et al. 2008), the Interface Region Imaging Spectrograph (IRIS; De Pontieu et al. 2014), the Solar Dynamics Observatory's Atmospheric Imaging Assembly (SDO/AIA; Pesnell et al. 2012; Lemen et al. 2012), and the Reuven Ramaty High-Energy Solar Spectroscopic Imager (RHESSI; Lin et al. 2002) were used in this thesis. The bulk of the research utilised data from IRIS and *Hinode*/SOT, with SDO/AIA and RHESSI observations mainly used for context. These are all space-based observatories with open data policies. The data reduction and analysis of these observations made use of instrument specific software, part of the SolarSoftWare (SSW; Freeland & Handy 1998) integrated library written in the Interactive Data Language IDL. More details of data reduction of observations from each instrument are provided in the relevant chapters. Below are brief overviews of the instruments and their capabilities.

2.2.1 Interface Region Imaging Spectrograph

IRIS is a NASA small explorer mission, launched in June 2013, that observes the Sun's chromosphere and transition region using two instruments to record images and spectra in several near-ultraviolet (NUV; from 2783 – 2835Å) and far-ultraviolet (FUV; from 1332 – 1407Å) wavelengths. Both instruments, the Slit-Jaw Imager (SJI) and the Spectrograph (SG), share the same optical path, featuring a 19 cm primary mirror and an effective focal length of 6.895 m. The SJI provides broadband filtered images of the field of view surrounding the SG slit, which provides high resolution spectra from a number of important chromospheric and transition region lines.

Images are available sampling the transition region at 1330Å and 1400Å, with a 55Å passband. These filters are dominated by the C II and Si IV lines at 1334 Å/1335 Å, and 1394 Å/1403 Å, respectively. Continuum and wing emission is likely to contribute also, and the C II filter may also contain a contribution from the Fe XXI line during flares. The chromosphere is sampled using two 4 Å wide filters, one centred on the Mg II k line (2796 Å), and one in the quasi-continuum near at 2832 Å. As is shown in Chapter 6 the continuum filter contains a substantial amount of contribution from line emission during flares. These images have a maximum field of view of 175" × 175", with a pixel scale of 0.1679" pixel^{-1} in the NUV and 0.1656" pixel^{-1} in the FUV. The spatial resolution is 0.33"(FUV) – 0.4"(FUV). On-board summing can increase the pixel scaling. Different combinations of SJI images are available depending on the observational set up but typically one image is taken per SG exposure.

The SG provides high resolution spectra in three channels, each with their own CCD: FUV-short (FUVS; 1332 – 1358 Å), FUV-long (FUVL; 1389 – 1407 Å), and NUV (2783 – 2835 Å). Lines covered by FUVS include the C II resonance lines, an O I line, and two iron lines (Fe XII and Fe XXI, the latter during flares) and lines covered by FUVL include the Si IV resonance lines, and the O IV 1400 Å and 1401 Å lines. The NUV channel includes the Mg II h & k resonance lines. In addition to these noted lines there are several tens of other lines, some of which have not been identified (see the IRIS webpages for line lists). The SG slit is 0.33" wide, and has a maximum length of 175". Dispersion in the FUVS is 12.98 mÅ pixel^{-1}, FUVL is 12.72 mÅ pixel^{-1}, and NUV is 25.46 mÅ pixel^{-1}. As with the SJI, on-board summing in both space and wavelength can occur. The spectral resolution is 26 mÅ (FUV) and 52 mÅ (NUV).

IRIS can perform a variety of observational modes, from long duration sit-and-stare where the spacecraft tracks a particular location, to sparse, coarse or dense rasters in which the slit positions steps in spatial location (from 2-step up to 64-step raster scans). There is also flexibility in terms of which parts of the spectrum to read out (the full FUV and NUV spectral range is not usually recorded, but portions are set by each observing plan). Depending on the choice of exposure times, line lists, and observing mode the repeat cadence from any one spatial location is variable.

Observing flares with an instrument such as IRIS can be tricky due to the transient nature of the event which requires not only that IRIS be pointed in the correct general location on the Sun, but additionally that the slit has good coverage at important spatial locations (i.e. along the flare ribbons). Fortunately IRIS has now successfully observed many flares, with a large database of events[3] and a flare list maintained by Dr. K. Reeves and Dr. H. Tian[4]. One of the first well observed flares is the focus of Chapter3.

2.2.2 Hinode/Solar Optical Telescope

Hinode is a JAXA spacecraft carrying JAXA, U.K. and U.S. instruments, launched in 2006, that observes the Sun using three instruments: the X-ray Telescope (XRT), the EUV imaging Spectrometer (EIS), and the Solar Optical Telescope (SOT). The XRT images the corona, at temperatures from $\sim 1-30$ MK, and EIS provides spectral observations from a range of lines between $170-210$ Å and $250-290$ Å. Lines within the wavelength range of EIS cover temperatures at $T \sim [0.04, 0.25, 1-20]$ MK, meaning that the transition region and coronal plasma can be investigated. The SOT is a 50-cm diffraction-limited Gregorian telescope that consists of the narrowband filtergraph (NFI), the broadband filtergraph (BFI) and the Stokes Spectro-Polarmieter (SP). The NFI produces Dopplergrams, filtergrams, and longitudinal and vector magnetograms from ten spectral lines between 5170 Å and 6570 Å. The SP observes the magnetically sensitive Fe I 6302.5 Å and 6301.5 Å lines, allowing high-resolution Stokes IQUV polarimetry. For the flare studied here only SOT/BFI observations were available, and so only the BFI is described in detail here.

The BFI observes the photosphere and lower chromosphere using six broadband

[3] http://iris.lmsal.com/search/

[4] https://docs.google.com/document/d/1TAUfuErPioQQ7aW_KoKL1EzUttGsAyAvN5eVBWHe8CM/edit

filters, which are recorded on a 4k × 2k CCD. These filters and widths are: the CN bandhead at [3883 ± 3.5] Å, the Ca II H line at [3968.5 ± 1.5] Å, the g-band at [4305.0±4] Å which includes the CH line, and three continuum filters at [4504.5±2]Å, [5550.5 ± 2] Å, and [6684.0 ± 2] Å. These continuum filters are known as the the red, green and blue (RGB) filters. Images have a maximum pixel scale of 0.0541" pixel^{-1} with a maximum field of view of 218" × 109". Exposure times are on the order 0.03 – 0.8 s, depending on the filter used. Cadence varies depending on the observational mode, but is typically on the order of 20 s during flares (assuming four filters are observed in sequence, with a readout time ranging from ∼ 0.9 – 3.4 s dependent on on-board summing, and a time to change filters of < 2.5 s). On-board summing can be set for certain observing modes, where pixels are averaged 2 × 2 or 4 × 4, which results in smaller field of view and a reduced pixel scale.

Flare observations using the SOT RGB continuum filters are relatively rare, with Ca II H line and g-band flare observations being more common. There have, however, been several flares observed in RGB using the flare observation mode. A flare trigger set by the XRT sends the coordinates to SOT, and if the flare is within the SOT field of view then observations are made with a minimum field of view of 108.5" × 108.5" with 2 × 2 pixel on-board summing so that the pixel scale is 0.108" pixel^{-1}. The RGB and Ca II H line filters are used with a cadence of ∼ 20 s. Typically the trigger only lasts a few minutes so that the decay phase is not observed. SOT tracks the flaring region, which can result in sudden pointing changes between successive frames, as well as spacecraft jitter.

Data is downloaded as a level-0 product with units of Data Numbers (DN), or counts, so requires corrections for flat-fielding, dark currents etc., using standard `SSW` routines and calibration to physical units as described in Chapter 6.

2.2.3 Solar Dynamics Observatory

The SDO is a NASA spacecraft launched in 2010 that provides high-resolution full disk images of the Sun in a number of passbands using its Atmospheric Imaging Assembly (AIA). AIA has four 20 cm telescopes, shared by ten filters which record images onto a 4096 × 4096 pixel CCD. Each filter observes a different primary ion or portion of the continuum so that AIA samples a range of temperatures covering the photosphere to the corona.

The coronal and transition region filters cover several Fe lines at wavelengths and characteristic temperatures of: 131 Å ($T \sim 0.4$ MK, $T \sim 10$ MK in flares), 94 Å ($T \sim 6$ MK), 335 Å ($T \sim 2.5$ MK), 211 Å ($T \sim 2$ MK), 193 Å ($T \sim 1.5$ MK), and 171 Å ($T \sim 0.6$ MK). The He II 304Å line samples the transition region and upper chromosphere at $T \sim 50,000$ K. The 1600 Å filter observes the continuum but also has contributions from the C IV line so samples both transition region and the upper photosphere. The 1700 Å filter observes the continuum from the temperature minimum region and photosphere near 5000 K. Finally, the photosphere is sampled infrequently using the 4500 Å continuum filter. Each of the filters are broad, and have a complex temperature response due to contributions from different spectral lines in addition to the primary ion, particularly during flares, so the temperatures quoted are the peak responses.

Coronal and transition region filters have a typical observational cadence of ~ 12 s and the 1600 Å and 1700 Å filters have a typical cadence of ~ 24 s (the reduced cadence is because telescope 3 observes both the UV filters and the 171 Å filter, whereas the other telescopes only observe two filters each). The 4500 Å filter has a significantly longer cadence of ~ 1 hour meaning it is of little use for flares. Exposure times are generally $\sim 0.5 - 3$ s. Images are recorded on a 4096×4096 CCD, with a pixel scale that varies slightly for each filter but which is ~ 0.6" pixel^{-1}.

As well as being used for investigations in their own right, AIA images are an excellent resource to give the wider context to solar flares observations from other instruments which is how they are used in this thesis.

2.2.4 Reuven Ramaty High Energy Solar Spectroscopic Imager

RHESSI is a NASA Small Explorer mission launched in 2002 to study X-rays during solar flares. It uses nine germanium detectors, each behind a rotating modulation collimator (RMC), sensitive to an energy range 3 keV to 17 MeV. The energy resolution is < 1 keV at $3 - 100$ keV, increasing with higher energy (~ 5 keV at energies of 3 MeV). Observations are full Sun, but spacecraft rotation allows spatial information to be obtained, with a resolution of ~ 2.3" at $3 - 100$ keV, 7" at $100 - 400$ keV and 36" at 400 keV -15 MeV. Thick and thin attenuators can be put in place when count rates exceed certain thresholds to absorb lower energy photons.

Analysis of RHESSI data to obtain images or fits to the photon spectrum (and

from that the electron distribution), is complex. Since analysis of RHESSI data was not the focus of this thesis, with results from RHESSI presented in Chapter 3 provided by Dr. P. Simões, only a basic outline is given here. There is a wealth of literature that can be consulted for detailed discussions of RHESSI capabilities and data analysis (see reviews by Kontar et al. 2011; Holman et al. 2011). From the count spectrum and knowledge of RHESSI's instrumental response, the photon spectrum (photons s^{-1} keV^{-1}) can be obtained. The photon spectrum is related to the non-thermal electron spectrum (e.g Brown 1971) so fitting the photon spectrum with a thermal component and non-thermal component (usually a power law, or a broken power law) ultimately allows the electron spectrum to be determined, with typical parameters being P, the power in non-thermal electrons, where dividing by source area yields the energy flux F, δ the spectral index (the power law index of the non-thermal part of the spectrum), and E_c the cutoff energy which is the lowest non-thermal electron energy consistent with the data, so that the electron distribution is defined $F \propto (E/E_c)^{-\delta}$. At low energies the thermal contribution to the photon spectrum from the hot plasma dominates, making the cutoff energy notoriously difficult to measure. The energy flux is therefore a lower limit on the true flux. Assuming the standard model of flares, these electron spectrum fit parameters can be used as input in flare simulations which model energy deposition by non-thermal particle beams.

Imaging of X-ray sources is possible via reconstruction techniques using the modulation of the count rate with roll angle from the nine RMCs, since RHESSI spins on its axis 15 times per minute. An introduction to RHESSI source imaging, and to some of the imaging algorithms, is provided by Hurford et al. (2002).

RHESSI imaging and spectroscopy provides information about the sites of flare energy deposition in the chromosphere, providing valuable complimentary context when interpreting ultraviolet and optical flare emission.

Chapter 3

Mg II Flare Observations: 2014-Feb-13th Solar Flare

The research discussed in this chapter was published in Kerr et al. (2015).

3.1 Introduction

Routine observations of the chromosphere have largely been confined to optical and infrared lines accessible from the ground, such as H α, the Ca II H & K resonance lines, the Ca II IR triplet and the He I triplet near 10830Å. However, the chromosphere emits strongly in several UV lines, of which there have been much fewer observations, with a particular paucity during transient events, including solar flares.

An important set of lines are the Mg II h & k resonance lines and the subordinate triplet, that all emit in the near ultraviolet (NUV), around 2800 Å. These lines have not been exploited as diagnostics of the chromosphere nearly as often as other lines, and have only been observed spectroscopically once during a solar flare (to my knowledge) prior to the launch of the Interface Region Imaging Spectrograph (IRIS) spacecraft. With IRIS we are now in a position to routinely observe these strong lines during solar flares, with high resolution, opening a new window on the flaring chromosphere. This chapter describes the first detailed observations of the response of the Mg II NUV spectrum to flare energy input since the observations of Lemaire et al. (1984). Shortly after the present work was completed (Kerr et al. 2015) two more studies of Mg II in flares were published (Liu et al. 2015; Matthews et al. 2015), the results of which are summarised here also.

The Mg II h & k lines are the $3s-3p$ transitions to the ground state of single ionised magnesium from excited upper levels that are close in energy ($3s\ ^2S_{1/2} - 3p\ ^2P_{1/2}$ & $3s\ ^2S_{1/2} - 3p\ ^2P_{3/2}$, for the h & k lines respectively), so that they are only a few angstroms apart. They are optically thick absorption lines with an emission component in the line core, and outer wings that extend quite far before reaching the continuum level. They form over a large range of heights in the chromosphere, and show a complex line profile. The line core appears as an emission line (k2), with two emission peaks (k2r & k2v), flanking a central reversal (k3). From this point forward, statements about the central emission or central reversal will refer to only the line centre feature, and not to the emission line as a whole. Similarly, statements about the line core will refer to the core of the emission line, whether it is centrally reversed (k3) or single peaked, and statements about the emission peaks will refer to the k2r and k2v peaks.

The line core is typically centrally reversed, and with the k3 component formed at the top of the chromosphere. The two emission peaks that flank the line core are the k2r and k2v peaks for the red and blue side of the line respectively, which are formed in the mid-chromosphere. Finally the k1r and k1v components are intensity minima located on the red and blue side of the line core, and formed near the temperature minimum region (TMR). The h line has the same naming convention. The vacuum line centre wavelengths are 2803.5209Å & 2796.3509Å, for h & k respectively.

In addition to the resonance lines, the Mg II subordinate line triplet (the $3p-3d$ transitions) also forms in the NUV, close to the resonance lines, so that all five lines can be easily observed simultaneously. The subordinate lines are transitions from excited upper states to the h & k upper levels, with wavelengths of 2796.10Å, 2798.75Å, and 2798.82Å (the $3p^2P_{1/2} - 3d^2D_{3/2}$, $3p^2P_{3/2} - 3d^2D_{3/2}$, & $3p^2P_{3/2} - 3d^2D_{5/2}$ transitions, respectively). These lines have not been studied in detail with the exception of observational work by Doschek & Feldman (1977) and Feldman & Doschek (1977), and recent modelling work by Pereira et al. (2015). Usually the triplet appears as absorption features in the h & k line outer wings, with the 2798.75Å, and 2798.82Å blended. They are formed deeper in the atmosphere than the h & k lines. However, above the limb, or when there is a sufficient temperature gradient (based on simulations), these lines can be in emission in the non-flaring atmosphere. This gradient must be at least ~ 1500 K and must be located in a region with electron density of at least 10^{12} cm^{-3} based on the simulations of Pereira et al.

(2015).

Modelling of the h & k lines (mostly in quiet Sun and plage) has been performed for many decades. The basic formation properties in the quiet Sun are outlined here, but discussed in detail in Chapter 4, in which references can also be found. Note that there has been a lack of flare modelling of these lines, so the formation may be different in flares. The h & k lines form at multiple layers in the atmosphere, sampling from the top of the chromosphere to the temperature minimum region. This is because opacity is a function of wavelength. Line core photons are preferentially absorbed compared to line wings photons, so that photons at line wing wavelengths can escape more easily and are thus formed deeper in the atmosphere. The h & k line cores form around 200 km below the transition region, and the emission peaks form in the mid-chromosphere. Due to their different opacities (the k-line has twice the opacity of the h-line) they reach their $\tau_\nu = 1$ surface at different heights, separated by a few $\times 10$ km (k-line is formed highest). The higher opacity also results in stronger coupling to the local gas temperature and so the k-line is more intense than the h-line. Modelling has also revealed that partial redistribution (PRD) is required to explain the source function behaviour, and that complete redistribution (CRD) is not sufficient. The main difference is that the source function is frequency dependent in PRD, which means the emergent intensity is a result of not only how the source function varies with height, but how it varies across the line profile, as a function of temperature, density and velocity.

The distinctive central reversal is caused by the variation of the line core source function with height in the atmosphere. The optical depth for the k2 component photons reaches unity ($\tau_\nu = 1$) in the mid-chromosphere, meaning they can escape and be observed. Near this height, the source functions have a maximum for k2 wavelengths, and having only partially decoupled from the Planck function at this height, still respond to the chromospheric temperature rise. The k3 $\tau_\nu = 1$ height is located higher in the atmosphere. The k3 source function decreases with height past the maximum, and has completely decoupled from the local temperature by the time the $\tau_\nu = 1$ height is reached. Thus, the intensity is lower than the k2 component intensity, and the line core appears reversed.

Temperature and velocity diagnostics of the quiet Sun were recently developed by Leenaarts et al. (2013a,b), and Pereira et al. (2013, 2015), exploiting the formation height differences between the various line components. However, given the lack

of a central reversal in flares and the likelihood that their formation properties are different, it is not known how applicable these diagnostics are.

While observations of the h & k lines, and the subordinate lines, have been rare in comparison to other strong spectral lines such as the Ca II H & K lines or Hα, there have been several past missions that have successfully observed a variety of solar features. A balloon launch by Lemaire & Skumanich (1973), and rocket launch by Kohl & Parkinson (1976) observed the Mg II spectrum found that the core was centrally reversed everywhere, but that there were strong intensity variations of up to 2 – 3× depending on the feature observed. Additionally there was a variation in the separation between the k2 emission peaks which varied between 0.3 – 0.36Å). The Mg II lines showed stronger fluctuations than Ca II H & K. Profiles showed a blue peak asymmetry, where the k2v component was more intense than k2r. The k:h line intensity ratio was 1.14 at disk centre and 1.21 at $\mu = 0.23$. This ratio is an indicator of optical depth. If the ratio were equal to 2 (the ratio of the lines' oscillator strengths) then they would be optically thin. A value less than 2 means that the lines are optically thick (see § 3.6.2 for a more in-depth discussion of this point).

The NRL slit spectrograph onboard *Skylab* (Bartoe et al. 1977) was used by Doschek & Feldman (1977) and Feldman & Doschek (1977) to investigate the Mg II spectra over active regions and quiet Sun, both on disk and above the limb (albeit with a lower spectral resolution of 120 mÅ). Approaching the limb, the profiles became wider, and central reversals deeper, due to the increased line of sight opacity. The central reversal disappeared by 6" above the limb and by 12" the k:h ratio was 2:1, suggesting that the lines were effectively optically thin. Results from active regions were similar. The continuum level was increased by 1.5×, and the ratio of peak intensity to continuum was between 3 – 5× (in the quiet Sun the peak intensity was approximately equal to the continuum intensity).

Using observations from the RASOLBA balloon-borne spectrograph (Samain & Lemaire 1985) some general properties of average non-flaring spectra were identified by Staath & Lemaire (1995): (1) that there is an overall blue-red asymmetry, with a stronger blue peak (k2v,h2v) than red (k2r,h2r), attributed to velocity fields in the upper atmosphere (2) intensity variations, and variations in the line shape, are present on small spatial scales (~ 3 – 5"), where the intensity could vary between 1-3× (3) the k:h ratio shows scatter around 1.24-1.43 but is not well correlated with

either k-line or h-line intensity (4) the h-line is less intense and slightly narrower than the k-line, with a full width at half maximum (FWHM) of 0.51Å for the h-line and 0.54Å for the k-line.

Umbral profiles of Mg II h & k lines are single peaked and less intense than the quiet Sun (Kneer et al. 1981). Despite being single peaked, the k:h ratio (which did not vary significantly between umbra, penumbra, or quiet Sun) indicated that they remained optically thick. In plage the integrated intensity was greater than in quiet Sun by up to a factor of 5, and profiles are wider at the base (1.42Å for plage compared to 1.30Å for quiet Sun), but narrower in the line core (smaller k2 separation, with 30Å for plage and 34Å for quiet Sun) and the depth of the central reversal is much reduced (e.g Lemaire et al. 1981; Schmit et al. 2015). Schmit et al. (2015) showed using a full Sun mosaic of IRIS data that plage profiles showed greater variation than the network or internetwork profiles.

Before the launch of IRIS there had been only one reported flare in which the Mg II h & k lines were observed spectroscopically. The Laboratoire de Physique et Planetaire (LPSP) instrument on board the Orbiting Solar Observatory 8 (OSO-8; Artzner et al. 1977; Bonnet et al. 1978) provided simultaneous observations of H I Lyα & Lyβ, Ca II H & K, and Mg II h & k. However, as noted by Lites & Hansen (1977) there was an "extremely low level of activity during the OSO-8 mission", so only one flare was observed (Lemaire et al. 1984). The Mg II h & k line intensities were significantly enhanced ($\sim 3\times$ in the line core) and broadened (FWHM rose from 0.56 Å to 0.93Å). It was unclear if central reversals were present or not. The profiles shown appeared quite jagged in appearance, and a small central reversal may have been present but the authors state that the spectral sampling meant it was not possible to ascertain (the spectral resolution was 0.09 Å). The subordinate triplet lines were in emission during the flare. There was a large amount of variation of the k:h ratio in the pre-flare and post-flare, with values ranging 0.9-1.5, but during the flare the ratio remained stable at a value of 1.1. This indicated that the lines remained optically thick throughout. Contrasting this with the Ca II H & K lines, the K:H ratio increased from 1 to 1.2 at flare peak before slowly decreasing. Flare effects on the ratios of lines of the same element, and ratios with lines of different elements, reduced within ~ 200 s, but the decay time for intensity overall was ~ 700 s. From a survey of line ratios and lightcurves the authors concluded that the lines of each element brightened in sequence indicating downward propagation of flare

energy during the event. Although a redshift was inferred from Ca II observations of ~ 12 km s^{-1} no mention was made of Mg II line shifts.

Flare profiles of Ca II H & K analysed by McKim Malville et al. (1968) were qualitatively similar to the flaring Mg II profiles (as might be expected due to their similar formation properties). Some profiles showed no central reversal, whereas others showed a much reduced reversal or a 'hybrid' core with multiple peaks. The peak separation was observed to decrease as K2 intensity increased, in a continuum from plage to flare intensities.

In addition to the work presented in this chapter, there have been two other reported spectroscopic observations of Mg II h & k during a flare, both using the IRIS spacecraft. Liu et al. (2015) studied the h & k lines during the well-observed 2014-Mar-29th X class flare. IRIS was operating with an 8-step raster program with 75 s repeat cadence. RHESSI observations showed that a non-thermal HXR footpoint source was co-spatial with the southern ribbon. Focusing on sources from that vicinity, Liu et al. (2015) noted that the line intensity became enhanced, the lines were substantially broadened (with a FWHM up to ~ 2Å), and that the lines showed redshifts up to several tens of km s^{-1}, all largely co-temporal with the HXR emission. The lines appeared asymmetric with broader red wings relative to the blue wing. Some sources showed the largest asymmetry and width occurring a short time after the peak emission. The k:h ratio was ~ 1.1, the same as noted by Lemaire et al. (1984). The lines were not all centrally reversed, with a tendency to appear single-peaked towards the peak of the event, and in the vicinity of the HXR sources. Liu et al. (2015) also carried out some preliminary modelling using semi-empirical flare atmospheres but were unable to match both the core and wing intensity to observations in a single simulation. Increasing microturbulence only acted to increase the core width, and did not significantly broaden line wings. A more in-depth discussion of flare modelling is presented in Chapter 4.

The same flare contained seismic sources, leading Matthews et al. (2015) to investigate the observational link between flares and sunquakes. They presented observations of the Mg II spectra contrasting those near the seismic source (the south ribbon profiles in Liu et al. 2015) to those without a seismic source (the northern ribbon). In general they agreed with the findings of Liu et al. (2015). They noted that while both the northern and southern Mg II h & k profiles initially decayed from flare peak in a similar fashion, a large red asymmetry and associated enhanced line width

appeared sometime after the flare peak, present only in the southern ribbon. This was co-spatial with an acoustic source that peaked at a similar time as the asymmetry and line width. Profiles were mostly single peaked. Finally, the k:h ratio showed a couple of interesting properties. In the southern sources it varied between ~ 1.1 and ~ 1.16 during the flare but rose to ~ 1.3 shortly after the flare peak before falling back to pre-flare values. In the northern ribbon pre-flare values were similar until a sharp rise to ~ 1.37 shortly before the flare peak, and decrease to ~ 1 at flare peak (~ 2 minutes later), before slowly rising back to pre-flare values. No explanation was apparent for this behaviour but it did show that the ratio can vary in response to atmospheric conditions.

This chapter presents one of the first detailed studies of the response of the Mg II lines to flare energy deposition. The temporal and spatial evolution of the lines are presented, covering both the general behaviour of the line shape and intensity, and some detailed metrics that analyse the centroid shifts, asymmetries, line widths and intensity ratios.

3.2 Observations

On the 2014-Feb-13th, NOAA active region 11974 produced an M1.8 class solar flare (SOL2014-02-13T01:40) beginning at ≈01:32 UT, peaking at ≈01:40 UT, and located at $\sim [140, -90]$". This event was accompanied by a failed filament eruption. Observations were available from IRIS, SDO and RHESSI.

The 2014-Feb-13th flare was chosen for an analysis of the Mg II h & k lines due to the good coverage of the event by both IRIS and RHESSI. The IRIS slit passed over most of the northern flare ribbon, with adequate cadence, and RHESSI HXR observations allow for the presence of non-thermal footpoint sources to be identified. From those observations the electron beam parameters used to drive radiation hydrodynamic flare simulations can be derived. Although a faster repeat cadence would be preferred, this was the best candidate at the time of selection (both in terms of slit coverage and the availability of joint RHESSI observations).

3.2.1 IRIS Observations

During this event IRIS was observing with no on-board summing so that the spectral pixel scale in the NUV was 25.46 mÅ pixel^{-1}, and spectrograph (SG) spatial scale in the y-direction was 0.167" pixel^{-1}. The slit width in the x-direction was 0.33" pixel^{-1}. For the slit-jaw imager (SJI) observations the plate scale was 0.167" pixel^{-1} in x & y. IRIS was observing with an 8-step raster program, where SJI images observed with a cadence of $\sim$ 5.4 s over a field of view 119" $\times$ 119". Exposures alternated between the 1330 Å and 1400 Å filters so that each filter had a repeat cadence of $\sim$ 11 s. Spectra were observed in an 8-step sequence, stepping 2.01" between exposures, so that the FOV per raster was 16" $\times$ 119". Four slit positions were observed simultaneous with the 1400 Å images, and four with the 1330 Å images (that is, one at a time, but observations alternated between SJI filters with each step of the raster), so that the cadence between the slit positions in a single raster was $\sim$ 5.4 s. The repeat cadence for the slit to return to the same location on the Sun was $\sim$ 43 s. The SG exposure time was $\sim$ 4s, and did not vary in response a the flare trigger. This exposure time provided a high count rate, while limiting saturation of the strong lines (Mg II and C II).

Figure 3.1 shows a 1330Å SJI image from near flare peak. The flare ribbon in the north of the field of view (labelled 'NR') was chosen as the focus of the study since the failed filament eruption further south obscures the other flare ribbon. A zoom-in on the ribbon is also shown. The red dotted lines show the IRIS slit locations, and their coverage along most of the ribbon. Green pixels at the bottom of the image were quiet Sun, and used to study non-flaring sources.

3.2.1.1 Level 2 IRIS data

Level 2 data products were downloaded from the IRIS Lockheed Martin Solar and Astrophysics Laboratory website[1]. This is the recommended data product (De Pontieu et al. 2014). Data reduction from level 1 to level 1.5 includes: corrections for cosmic ray spikes, removal of dark currents and pedestals, corrections for flat-fielding, and a geometric calibration and (as of the April 2014 pipeline, through which this data was re-processed) a wavelength calibration for the SG data. The resulting data is on a common spatial and spectral plate scale. Level 1.5 to level 2 involves re-formatting

[1] http://iris.lmsal.com/search/

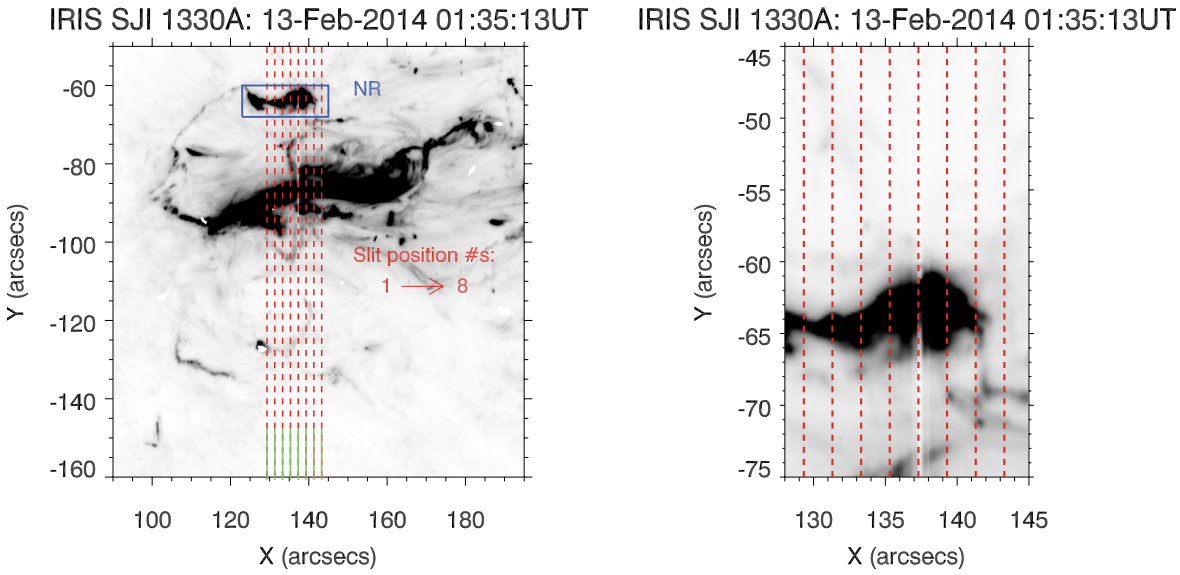

(a) **(b)**

Figure 3.1: *A snapshot of the flare observed at 1330Å by the SJI. The SG slit positions are overlaid in red dashed lines for illustrative purposes. In panel (a) the northern ribbon structure is outlined by a blue box, and the quiet Sun pixels discussed in § 3.4 are in green. Panel (b) shows a zoomed in view of the northern ribbon that is the focus of this chapter.*

the data and header files into rasters.

The wavelength calibration is to correct for the spacecraft velocity, as well as small variations that occur during the orbit due to temperature changes that flex the instrument. The spacecraft velocity is combined with thermal variations to find the overall wavelength correction, which is applied in the pipeline processing from level 1 to level 1.5. There are some residual thermal variations that persist in the level 2 data which, though small, were corrected for using the IRIS SSW routine `iris_orbitvar_corr_l2.pro`. In this routine the Ni I 2799.474Å line (a strong photospheric line with an intrinsic velocity 1 km s^{-1} or less that appears between the h & k lines) is fitted with a single Gaussian function, and the variation of the line centroid measured over the course of the orbit. A spline function is fitted to the variation, after smoothing over 5 minute periods to remove the 5 minute photospheric oscillation. This additional correction was applied to the level 2 wavelength array.

Intensity data were initially in terms of counts, or data numbers (DN $pixel^{-1}$), but were converted to a count rate (DN s^{-1} $pixel^{-1}$) by dividing by the exposure time.

The exposure time was fixed for the SG during the course of the observations, apart from small fluctuations. For the SJI images the exposure time was variable. In the pre-flare the exposure time was $\tau_{\rm exp} \sim 4$ s. During the flare $\tau_{\rm exp} \sim 1.199$ s. Post-flare exposure time was $\tau_{\rm exp} \sim 2.399$ s.

3.2.1.2 Intensity Errors

For an intensity measured in DN $I_{\rm DN}$, we can convert to the intensity in photons counts: $I_\gamma = \frac{g}{\eta} I_{\rm DN}$ photons. Here g is the gain of the detector, which is the number of electrons required to result in a single DN count (electrons DN^{-1}), and η is the yield, or number of electrons released by a photon (electrons photon^{-1}). The gain of the NUV SG detector is $g = 18$ electrons DN^{-1}, and at NUV wavelengths one photon results in one electron-hole pair so that the yield is $\eta = 1$ electrons photon^{-1} (De Pontieu et al. 2014), giving $g/\eta = 18$ photons DN^{-1}.

Assuming Poisson noise, the error on the photon counting is $\sigma_\gamma = \sqrt{I_\gamma}$. We must also consider the readout noise/dark current uncertainty that is quoted as $\sigma_{\rm rn} = 1.2$ DN by De Pontieu et al. (2014). Combining these errors (in terms of photons) gives the fractional error on the photon counts as

$$f_{\rm err} = \frac{\sigma_\gamma}{18\ I_{\rm DN}} = \frac{\sqrt{18\ I_{\rm DN} + (18\ \sigma_{\rm rn})^2}}{18\ I_{\rm DN}}. \tag{3.1}$$

Using $f_{\rm err}$, the error on intensity measured in DN, in DN s^{-1}, or physical units is simply $\sigma_{\rm int} = f_{\rm err}\ I$ (for I in the appropriate units).

3.2.1.3 Radiometric Calibration

Most of the analysis discussed in this chapter was completed before the IRIS intensity calibration was well established with only the pre-launch effective areas available. It was decided to work in DN s^{-1} px^{-1} units, until the calibration was better known. Updates were provided by the IRIS instrument team in March 2015. J. P. Wuelser[2] computed the time-dependent effective areas by cross-calibrating with the UV irradiance data from the SOLSTICE instrument onboard the SORCE spacecraft (McClintock et al. 2005) and through monitoring the throughput of IRIS data since launch. These up-to-date effective areas are available via the IRIS SSW routine

[2] http://iris.lmsal.com/itn26/itn26.pdf

`iris_get_response.pro`, where the observation date can be specified (though it was noted in the IRIS analysis guide that this calibration is preliminary).

Using the new effective areas, the line intensities and lightcurves are presented here in physical units, but the results from characterising the line profiles were obtained from analysing the data in count rate units (since this analysis was completed pre-March 2015). As is demonstrated here, the differences in calibration across the line profiles, and between the h & k lines, after radiometric calibration are small and so results regarding line characterisation would not change appreciably if the data were instead analysed with the newer calibration.

To convert from intensity expressed as a count rate I_{CR} [DN s^{-1} px^{-1}] to intensity in physical units I [erg s^{-1} cm^{-2} sr^{-1} Å^{-1}], the following relation can be used, where intensity is a function of wavelength:

$$I(\lambda) = I_{\mathrm{CR}} \frac{g}{\eta} \frac{hc}{\lambda} \frac{10^7}{\delta\lambda A_{\mathrm{eff}} \Omega}. \tag{3.2}$$

In this expression g and η are as described in § 3.2.1.2, and $g/\eta = 18$ photons DN^{-1}. Planck's constant, h [J s], the speed of light, c [m s^{-1}] and the wavelength, λ [m], together give the energy per photon [J photon^{-1}]. The power is then divided by the spectral dispersion, $\delta\lambda$ [mÅ px^{-1}], the solid angle subtended by an IRIS pixel, Ω, and the effective area, A_{eff} [cm^2]. We then multiply by 10^7 to convert from J to ergs. When no on-board summing is performed $\delta\lambda = 25.46$ mÅ px^{-1}. The effective areas are provided as a function of wavelength, so must be interpolated to the corrected wavelength array being used.

The effective area as a function of wavelength for the NUV SG is shown in Figure 3.2(a), where the up-to-date value is shown as a black solid line and the pre-launch as a black dotted line. The k & h-line centres ±1.5Å are highlighted by a red and blue band respectively. There is quite a large difference between the two effective areas, with the up-to-date values being some $\sim 15-20\%$ larger. The k-line shows a larger range across the profile than the h-line. Dividing Eq 3.2 by I_{CR} gives a conversion factor that is plotted in Figure 3.2(b), where the variation of effective area results in variation to the conversion factor. Again, the k-line shows a bigger range than the h-line, but that said the k-line only varies by $\sim 0.83\%$ across the line, and is only $\sim 1.28\%$ larger than the h-line. The differences between the h & k lines that arise when performing the radiometric calibration are slight, and so it is justified to use DN s^{-1} for analysis.

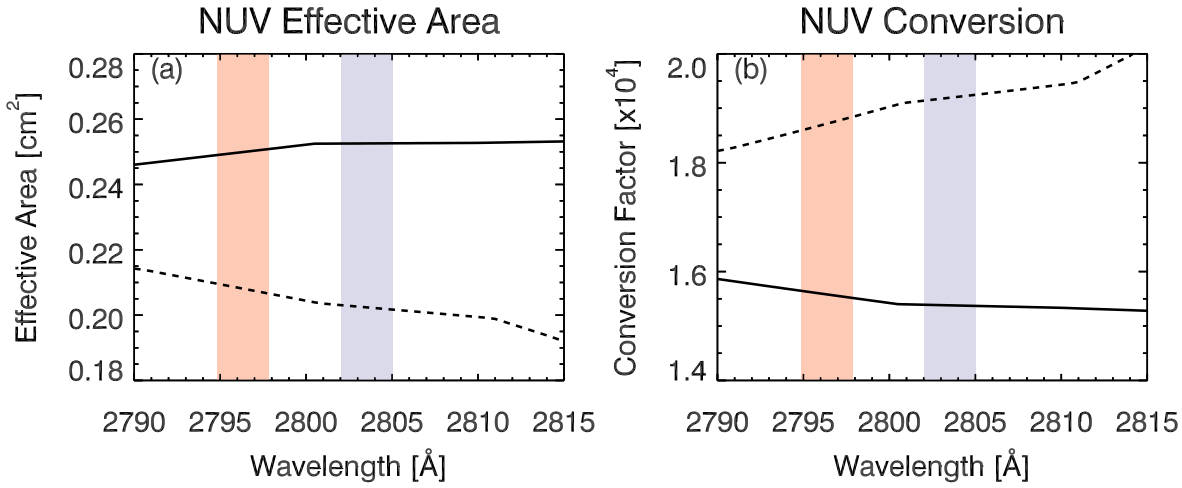

Figure 3.2: *Panel (a) shows the IRIS SG effective area in the NUV. The black solid line is the up-to-date effective area (computed for the 2014-Feb-13th observations) and the dotted line is pre-launch. The red band shows* ±1.5*Å around the k-line core, and the blue band is* ±1.5*Å around the h-line. Panel (b) shows the conversion factor to go from DN s^{-1} to* erg s^{-1} cm^{-2} sr^{-1} Å^{-1}*, for the 2014-Feb-13 observations (solid line) and the pre-launch (dotted line).*

3.2.1.4 Line Core Depth Statistic

A near ubiquitous feature of the Mg II h & k resonance lines is the central reversal, the depth of which is variable depending on the source type. This variation makes it a useful measure, providing information about the behaviour of the source function with height in the atmosphere. A shallower reversal suggests a core that is formed closer in height to one or both of the emission peaks than those profile with deeper reversals. Single peaked profiles, which are common in sunspots and reasonably common in plage, indicate regions where the source function increases with height through the k3 optical depth unity height (where the line is formed). It is useful, then, to have a measure of the depth of reversal, and to ascertain the variability during flares.

A simple peak finding algorithm was used to identify the locations of the peaks and minima of each profile:

(1) For each of the h & k lines, the line was isolated around the nominal rest wavelengths ±1.5Å and interpolated to a finer resolution of 300 pixels in wavelength space which for the 3Å range gave 0.001Å px^{-1}.

(2) The IDL routine `lclxtrem.pro` (written by Dr. M. Buie, and available from the IRIS SSW tree[3]) was used to identify local maxima and minima across the line. The width of the search zone is specified so that maxima and minima closer than this width are discounted.

(3) The location of the largest maximum was identified (λ_{Imax}), and assumed to either be one of the k2r or k2v emission peaks, or the line centroid of a single peaked profile. Any maxima and minima located outside $\lambda_{\mathrm{Imax}} \pm 0.4$Å were discarded since the region of interest was the line core. The number of remaining maxima and minima were counted.

(4) If there were no minima then the line was taken to be single peaked. The k3 wavelength was set to the wavelength position of the maximum.

(5) If there were more minima than maxima then the central maximum was chosen as as the k3 wavelength.

(6) If the number of maxima exceeded the number of minima then the k3 wavelength was set to the lowest minima between the largest maxima - that is, the largest central depression flanked by the largest emission peaks. The k2r and k2v wavelengths were set to the positions of the largest emission peaks.

The depth statistic was then calculated using the intensity of the emission peaks and line core as

$$D_{\mathrm{c}} = 1 - \frac{2I_{\mathrm{k3}}}{I_{\mathrm{k2v}} + I_{\mathrm{k2r}}} \tag{3.3}$$

where I_{k3}, I_{k2v} and I_{k2r} are the k3, k2v and k2r intensities. This is the same statistic used by Schmit et al. (2015). Single peaked profiles have a value $D_{\mathrm{c}} = 0$ (for the calculation of D_{c} when the line was single peaked, I_{k2v} and I_{k2r} were set equal to I_{k3}). Profiles with $D_{\mathrm{c}} \approx 0$ have shallow reversals, and profiles $D_{\mathrm{c}} > 0$ have clear reversals. A larger D_{c} means deeper reversal. The general behaviour of the reversal depth in quiet Sun, pre-flare and flaring sources are commented on later in this chapter. Note that this peak-finding algorithm and the depth statistic were only used as an illustrative tool to show the general behaviour of the reversal depth, and presence of single peaked profiles in different sources.

[3] `/ssw/iris/idl/uio/utils/lclxtrem.pro`

3.2.2 SDO Observations

To provide context to the flare at different temperatures, images from the SDO/AIA were downloaded from the Virtual Solar Observatory (VSO; Hill et al. 2009). Level 1 AIA data already include corrections for readout noise, dark currents, flat-fielding, and cosmic ray hits. Images were rotated, translated and scaled to a common plate scale (that of the 1600Å data) using the standard SSW routine `aia_prep.pro`. The field of view was reduced to the flaring region and this region was tracked to account for solar rotation.

IRIS and AIA pointing was offset by several arcseconds. Similar features are visible in the 1330Å SJI images and 1600Å AIA images, so these were used to cross-correlate the data and correct the IRIS pointing. First, the closest in time 1600Å images were co-registered and re-scaled to the 1330Å maps. Then the images offsets were found by cross-correlation, and the IRIS maps shifted to match AIA pointing (using the SSW routine `coreg_map.pro`).

3.2.3 RHESSI Observations

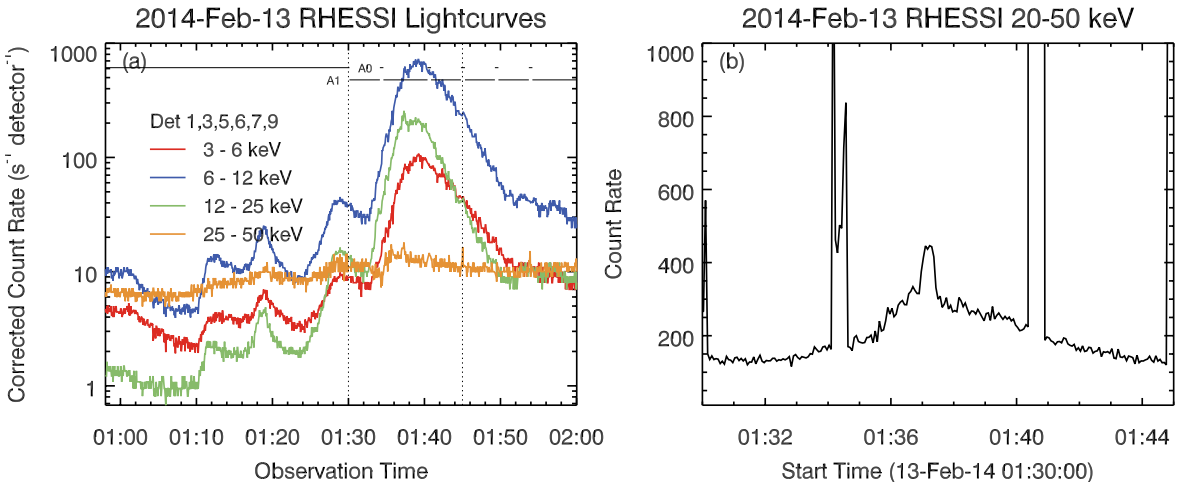

Figure 3.3: *RHESSI lightcurves from the 2014-Feb-13th flare. Panel (a) shows the count rates per detector, corrected for attenuator changes. Dotted lines show the zoomed portion in panel (b), which shows the 20-50 keV count rate summed over the detectors, not corrected for attenuator changes, where the small non-thermal flare peak between ~01:35:30-01:38:00 UT is visible.*

Table 3.1: RHESSI Fit Parameters

Time	Parameters			
	δ	E_c [keV]	Flux [10^{35} elec. s^{-1}]	P [erg s^{-1}]
01:34:52 UT+36s	9.3	19.6	0.46	1.62×10^{27}
01:35:36 UT+36s	8.6	19.5	0.75	2.69×10^{27}
01:36:16 UT+40s	9.8	20.6	1.02	3.77×10^{27}
01:37:00 UT+44s	8.9	20.1	1.26	4.62×10^{27}

RHESSI was observing during the rise phase, peak and the start of the decay phase of the flare. Figure 3.3(a) shows RHESSI lightcurves, separated into different energy bins as indicated. These are the corrected count rates per detector, taking into account changes in attenuator state (attenuators are used when there is a large count rate, and during the flare the 'A1' detector was used). The flare peak is clear in the lower energy bins (3-6 keV, 6-12keV and 12-25 keV) but only a weak flare signal is observed in the 25-50 keV bin. Typically, 3-25 keV x-rays could be considered thermal, and 25-50 keV non-thermal so the lightcurves suggest only a weak non-thermal emission. Figure 3.3(b) shows the 20-50 keV count rate summed over the detectors (not corrected for attenuator state). There is a small peak that could be considered non-thermal at ~01:37 UT. Note that the high count rates on either side of the peak are due to the attenuator state changing.

RHESSI spectral analysis and imaging was performed by Dr. P. Simões, with the results summarised here. Using the standard OSPEX software (Schwartz et al. 2002) the HXR spectrum was fit with an isothermal plus thick-target model. Under the assumption that the non-thermal electron distribution was a single power-law, the thick-target model parameters were obtained. These parameters were the electron flux, F_e, which is the total electron rate above the low energy cutoff E_c, and the spectral index, δ which describes the slope of the power law. E_c is notoriously hard to determine: in these fits E_c is the highest energy that is consistent with the spectrum, meaning that the electron flux is a lower limit on the true electron flux. The total power in the electron distribution was also calculated. Fitting was performed for the time intervals listed in Table 3.1, where the fit results are also listed. The spectral

index of ~ 9indicates a soft spectrum with weak non-thermal emission. Images were constructed using the MEM NJIT algorithm (Schmahl et al. 2007), integrating over 38 s time intervals near the flare peak, in the following energy ranges: 6-9 keV, 15-20 keV, 20-25 keV, 20-50 keV. These images are discussed in § 3.3.

Note that these spectra could alternatively be fitted by two thermal components, one at ~ 16 MK and one at ~ 40 MK, instead of an isothermal plus non-thermal power law. The thermal component at ~ 40 MK would make this a 'super-hot' flare. That is, a flare with temperature > 30 MK (e.g Caspi et al. 2014). Caspi et al. (2014) reported some statistics of 'super-hot' flares, showing that, generally, temperatues > 30 MK were only present in high-M or X-class flares, while the event reported here is an M1.8 class flare. That does not, of course, rule out this scenario. However, microwave observations from the Nobeyama Radio Observatory (NRO; Nakajima et al. 1994) and the USAF Radio Solar Telescope Network (RSTN) indicate the presence of non-thermal particles, supporting the isothermal plus non-thermal power law scenario (P. Simões, *private communication*).

3.3 Flare Overview

HXR lightcurves (see Figure 3.3) show that the rise phase of the flare begins at ~01:32UT, and peaks at ~01:40UT in the lower energy channels, but slightly earlier in the higher energy channels (20-50 keV emission peaks at ~01:37:50 UT). Several smaller pre-flare peaks are present in the lower energy channels, at ~01:11UT, ~01:19UT, and ~01:28UT. Concurrently there are brightenings in hot loops the coronal 131Å and 193Å AIA images. Imaging the RHESSI 6-9 keV emission reveals sources that are co-spatial with the enhancements in AIA, shown in Figure 3.4(a,c,d). The 1330Å images (which show significantly cooler material that that observed in the 131Å images) contained a source that brightened at the same time as the hot loops, co-spatial with the stronger RHESSI sources at ~ [145, −80]" (Figure 3.4(b)). The 1330Å 1400Å 1600Å & 304Å images all show an active region filled with short-lived brightenings.

The flare ribbons begin to form at ~01:28UT, including the 131Å images. The onset of the ribbons is at the time of the third, and largest, pre-flare peak in the HXR lightcurves. The main flare starts a short time later (2 minutes) with the northern ribbon (NR) clearly visible in all passbands by 01:32 UT. As the flare proceeds to the

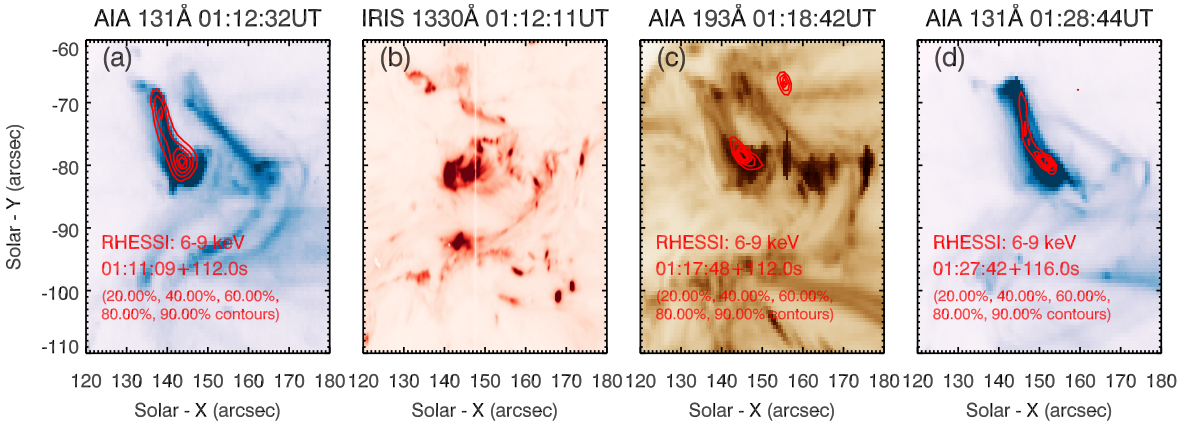

Figure 3.4: *AIA and SJI images showing the pre-flare brightenings. Panels (a),(c) & (d) have RHESSI 6-9 keV HXR contours overlaid. The white vertical line in panel (b) is the IRIS slit location. Images are inverse colour (bright is more intense).*

peak the ribbon expands northwards and eastwards, with a bright front (the 'outer ribbon'), leaving a less intense wake that decays gradually as it moves on (the 'inner ribbon'). The southern ribbon is obscured by an erupting filament. Figure 3.5(a,b,c) shows a sequence of SJI images. Figure 3.5(d,e,f) shows RHESSI X-ray sources overlaid on the AIA UV images. RHESSI sources were manually shifted by 2" east. The non-thermal 20–50keV sources are only spatially associated with the NR source at ~01:36:18 UT. Before this point, and afterwards, strong non-thermal emission is not present near flaring ribbons. At ~01:37:01 UT, 20–25 keV emission is no longer spatially associated with the NR source, though 6–9keV footpoint sources are, however, spatially associated with the UV ribbons.

Finally, at ~01:31UT, a filament is clearly seen in absorption in the 131Å, 171Å, 193Å & 304Å passbands, and as a bright source in the SJI and 1600Å. It begins to erupt at ~01:33:30UT, with the eruption and expansion of the filamentary material occurring over several minutes. The filament expands over the north half of the region, eventually obscuring the northern flare ribbon (starting at ~01:40UT and by ~01:47UT the ribbon is completely obscured). Figure 3.6 shows the filament progression in several passbands. It is difficult to separate the flare and filament sources in the southern part of the flare region, so the northern ribbon is the focus to avoid confusion.

In the following sections the behaviour of the Mg II profiles during the flare is analysed, and contrasted with quiet Sun and pre-flare sources.

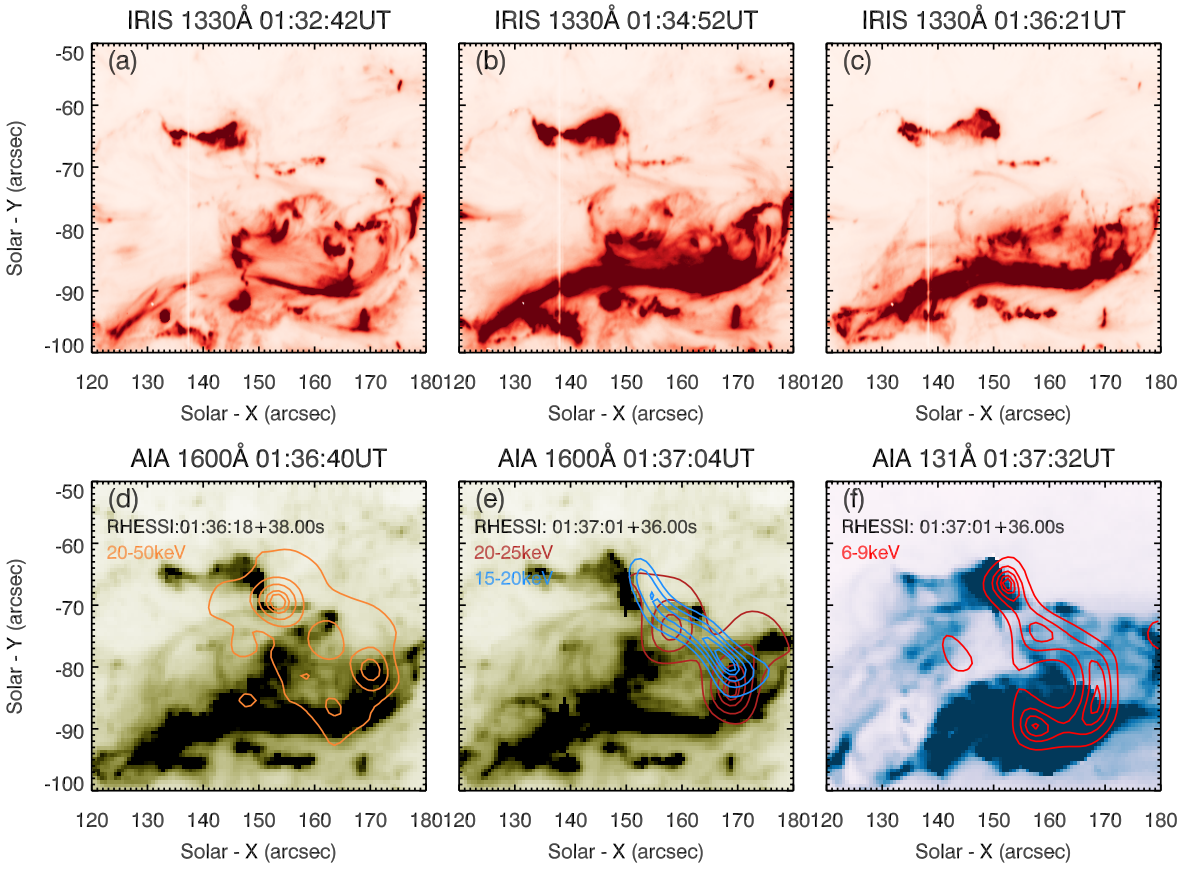

Figure 3.5: *AIA and SJI images during the flare. The first row shows a sequence of 1330Å images. The northern flare source is the focus of analysis due to the complex mix of filament and flare sources in the south. The second row shows a sequence of AIA images with RHESSI sources overlaid. Panel (d) shows a non-thermal source in the vicinity of the northern flare source. This is no longer co-spatial a short time later in panel (e). Panel (f) shows 6 – 9 keV footpoint source co-spatial with the northern flare source. Images are inverse scale.*

3.4 Mg II Quiet Sun Profiles

An overview of the quiet Sun profiles in the IRIS field of view is presented in this section, to set the flaring profiles in context. Non-flaring Mg II h & k line profiles have been analysed by a number of authors, including a comprehensive statistical study of the h-line by Schmit et al. (2015), and so the reader is directed there for a detailed discussion on the variability of the line with source type.

From SJI & AIA (mainly the 1600Å and 1700Å filters) observations a patch of

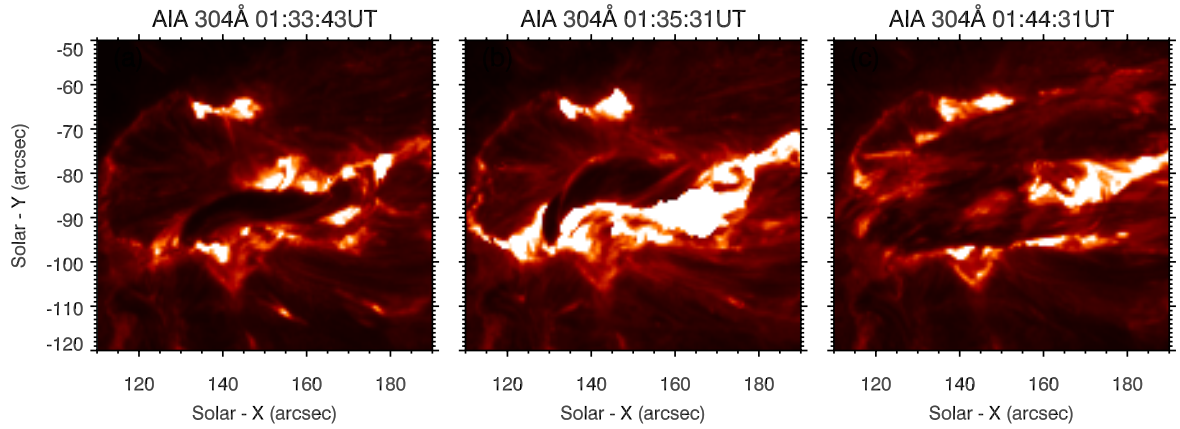

Figure 3.6: *A sequence of AIA 304Å images showing the failed filament eruption (dark material) that obscures the field of view.*

quiet Sun was identified containing only small or short-lived variations. This patch is shown as green pixels in Figure 3.1. Figure 3.7 gives an example of the full spectrum from a quiet Sun pixel, with error bars showing the typical size of uncertainty on the data. The h & k lines, and subordinate lines are indicated.

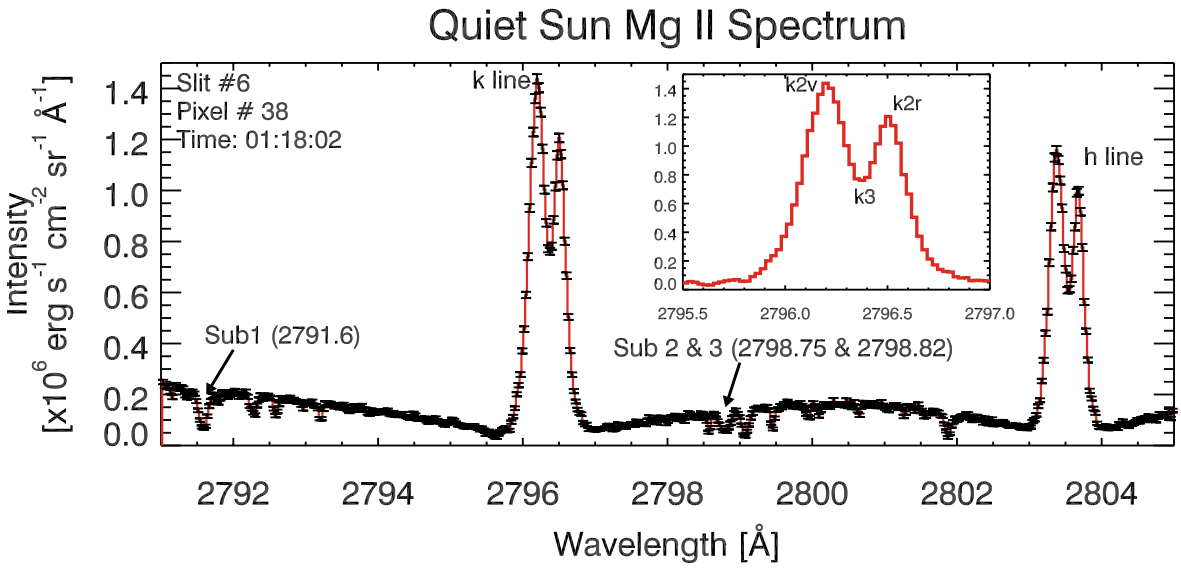

Figure 3.7: *A typical quiet Sun Mg II profiles, with the k-line, h-line, and subordinate lines indicated. The subordinate lines labelled 'sub 2 & 3' are blended. An inset shows the k-line, with the emission peaks labelled k2v and k2r for the blue and red side of line core respectively, and the the centrally reversed line core is labelled k3.*

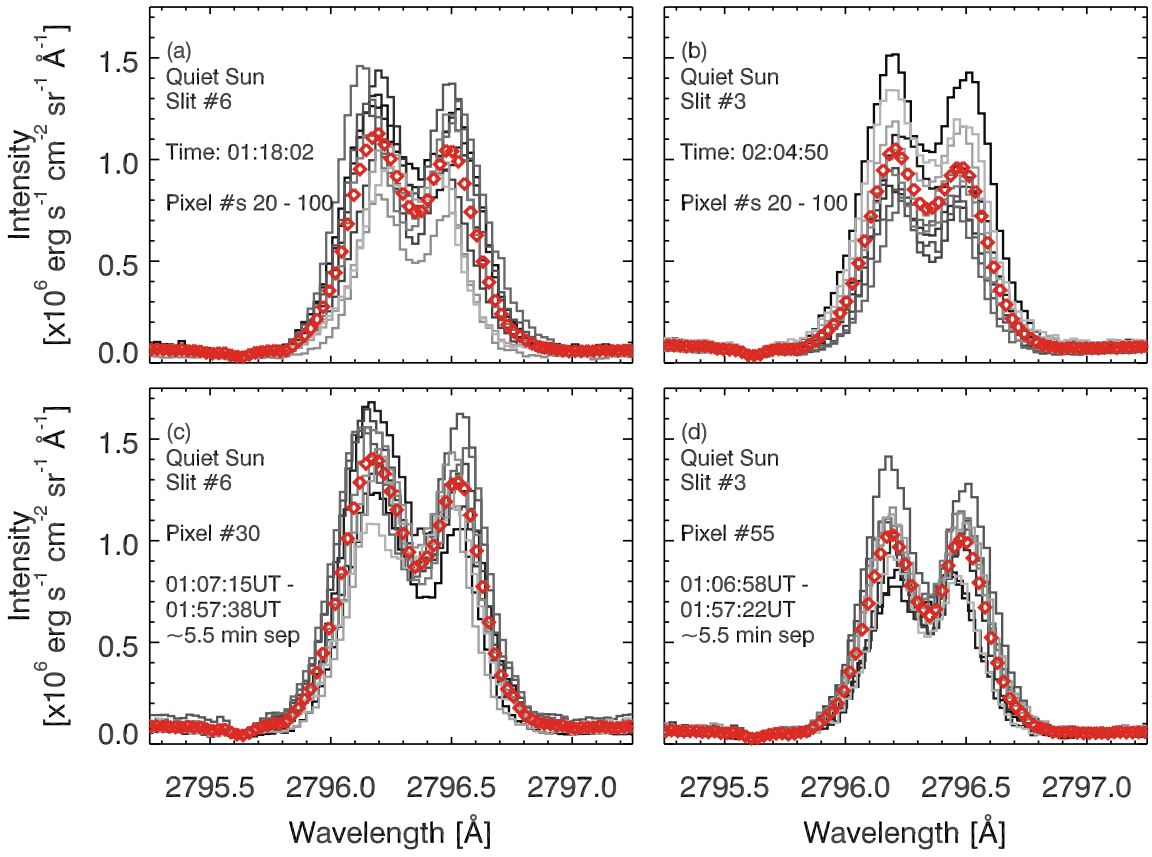

Figure 3.8: *A representative sample of quiet Sun profiles in greyscale and the average of the profiles in each panel overlaid as red diamonds. Panel (a) shows profiles in steps of 9 pixels (≈ 1.5″) from y-position 20 to 100 along slit position 6 at 01:18:02 UT. Panel (b) shows profiles in steps of 9 pixels (≈ 1.5″) from y-position 20 to 100 along slit position 3 at 02:04:50 UT. Panel (c) shows profiles from y-position 30 along slit position 6 at from 01:07:15 UT - 01:57:38 UT in steps of ≈ 5.5 min. Panel (d) shows profiles from y-position 55 along slit position 3 at from 01:06:58 UT - 01:57:22 UT in steps of ≈ 5.5 min.*

A larger sampling of representative k-line profiles from the quiet Sun is shown in greyscale in Figure 3.8, with the average of those profiles overlaid in red diamonds. Panels (a,b) show profiles from various cuts along a single slit positions and time. Panels (c,d) show profiles from a single pixel as a function of time. Profiles show variations in the depth of the central reversal, peak separation, and peak asymmetry with spatial location and time, but all of the profiles shown (and indeed the majority of the pixels in the quiet Sun patch) do have the usual line

shape with two emission peaks and a centrally reversed line core. The typical peak intensity is $\approx [0.8-1.5]\times10^6$ erg s^{-1} cm^{-2} sr^{-1} Å^{-1}, and typical core intensity is $\approx [0.5-1]\times10^6$ erg s^{-1} cm^{-2} sr^{-1} Å^{-1}. These intensities are somewhat higher (by $\approx 2-4\times$) than the quiet Sun intensity reported in Liu et al. (2015) . A single exposure along slit position 6 is shown in Figure 3.9, giving a wider view of the variations in the quiet Sun profiles. In this image the wavelength is along the x-axis, position along the slit (i.e. position on the Sun) is on the y-axis, and intensity is represented by colour. The k-line, h-line and 2791.6Å subordinate line are shown from 01:18:02 UT. The h & k-lines behave similarly, with the same variations in peak separation, reversal depth, peak intensity and base width as each other. The subordinate line is in absorption at all locations in the quiet Sun.

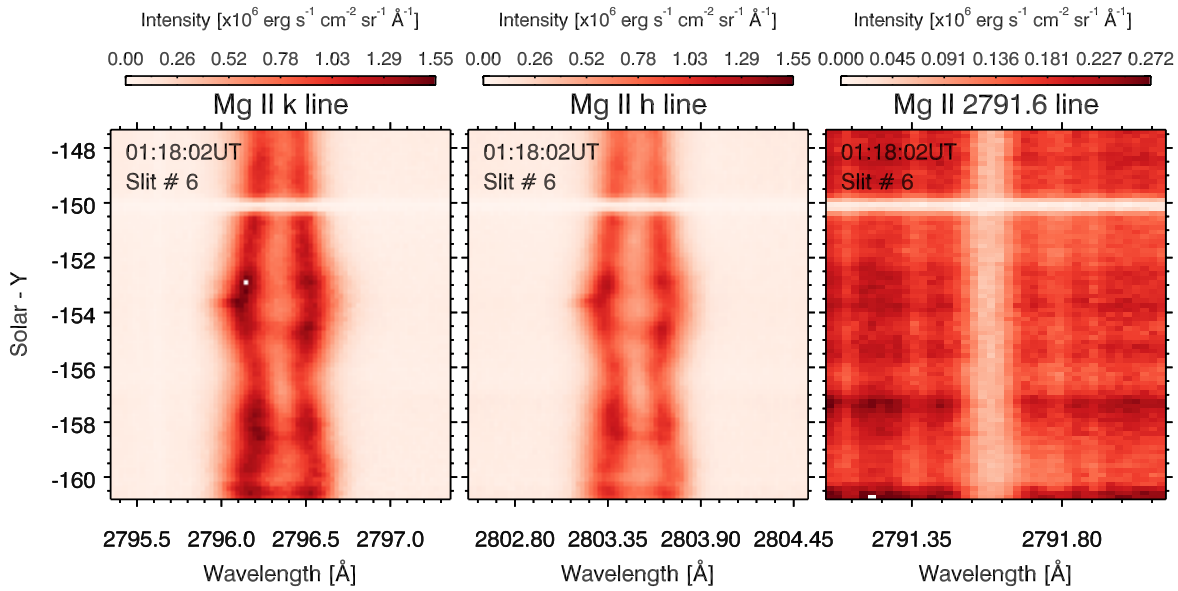

Figure 3.9: *The k-line, h-line, and 2791.6 Å subordinate line exposures from the quiet Sun patch, along slit position 6. The small variations in depth of the reversal, peak positions, and intensity in the resonance lines are clear. The subordinate line are in absorption at all times in the quiet Sun. Note that the images are inverse scale, and not normalised to a common intensity scale. The bright band near −150″ is the lower fiducial mark.*

Figure 3.10 shows the integrated intensity of the k-line (integrated over 2796.3509± 1.3)Å. There is little variation in time, but some spatial variation is present. However, the majority of the emission is weaker (between $[0.3-0.9]\times10^6$ erg s^{-1} cm^{-2} sr^{-1}),

with only a few small areas showing higher intensity. Additionally, compared to the enhancement in flares sources, these differences are small.

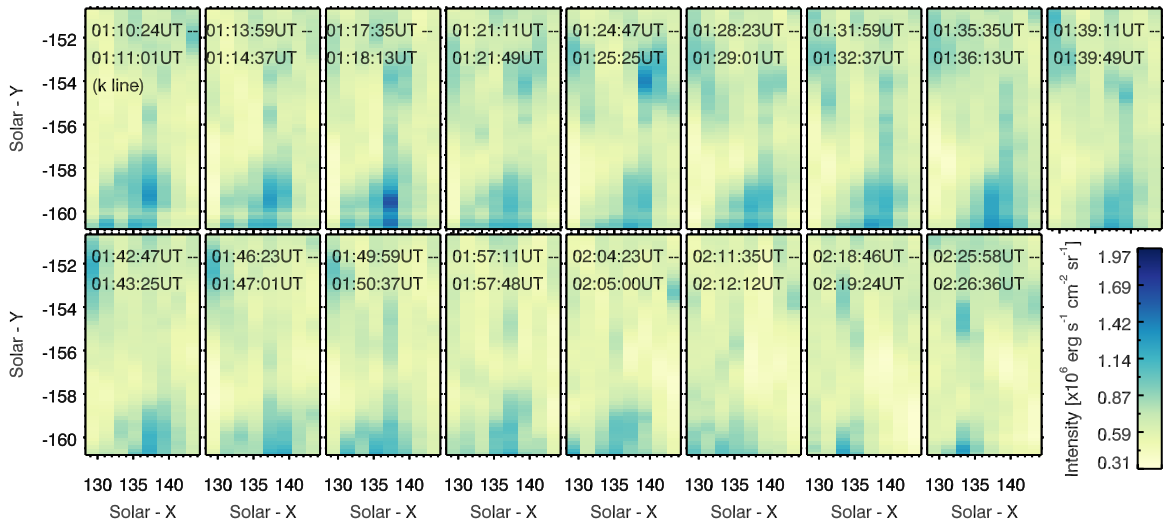

Figure 3.10: *The k-line integrated intensity (2796.3509 ± 1.3) for the quiet Sun patch. Each panel is a different raster. It takes approximately 5 s between exposures so that each raster is imaged over ∼ 40 s. Also, there is a 2" spacing between slit positions, which is not reproduced here - instead the pixels in the x-axis are stretched to fill the gap.*

Finally, the depth statistic, D_c, described in § 3.2.1.4 was used to find the typical depth of central reversal in the quiet Sun, shown in Figure 3.11. Recall that for this measure $D_c = 0$ for a single peaked profile (set to blue in the Fig. 3.11), $D_c \approx 0$ for a weakly reversed profiles, and $D_c > 0$ for profiles with clear reversals. The lines in the majority of pixels have a clear reversal with $D_c \lesssim 0.5$ though a few do have deeper cores (consistent with the survey of Schmit et al. 2015). There are a number of single peaked profiles within this region, some of which are likely to have been flagged inappropriately as single peaked. Since this is only used as a relative comparison between quiet Sun, pre-flare and flare profiles a few incorrect flags are acceptable.

The rest wavelengths of the h & k lines were measured in using the quartiles method described later in § 3.6.3. Line centroids for the pixels in the quiet Sun patch were measured as a function of time and averaged spatially and temporally, giving rest wavelengths of $\lambda_{\text{rest,k}} = 2796.3292$ Å and $\lambda_{\text{rest,h}} = 2803.5181$Å. Converting the standard deviation of the line centroids into velocity gave a $1-\sigma$ confidence level of

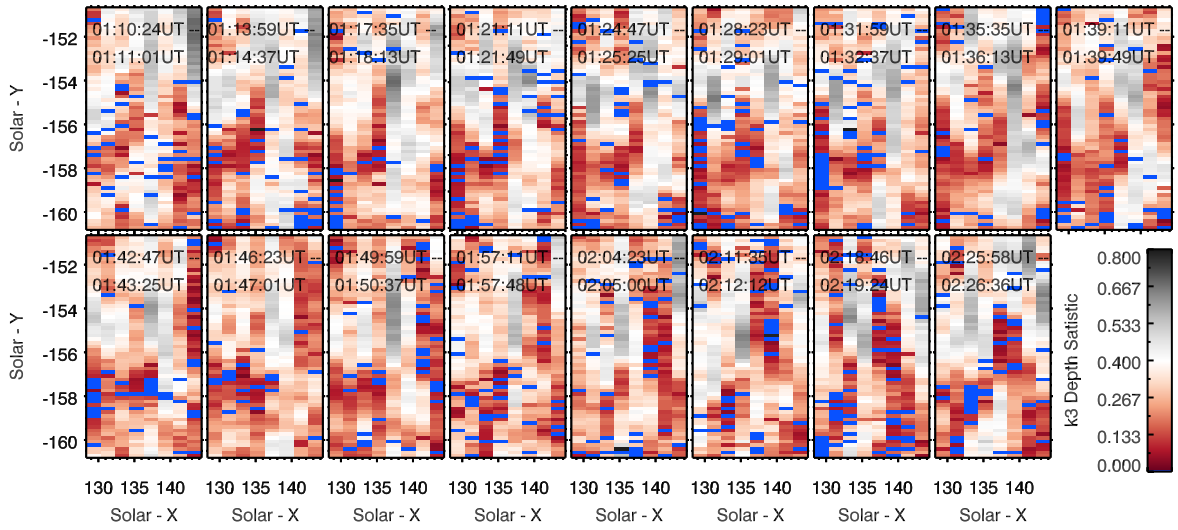

Figure 3.11: *The k3 depth statistic in a quiet-Sun patch as a function of time. Colour is as indicated on the colourbar, apart from $D_c = 0$ (single peaked profiles) where the pixels are shown in blue.*

the k-line centre position of ±0.64 km s^{-1}, and of the h-line centre of ±0.77 km s^{-1}.

3.5 Mg II Pre-Flare Profiles

Focussing on the northern flare sources, the behaviour of the pre-flare region was analysed to find the general profile shape and the integrated intensity variations. Figure 3.12 shows a pre-flare profile, from around 20 minutes before the flare peak. The profile appears narrower, single-peaked, and lacking the central reversal present in the quiet Sun profiles. It is more intense than the typical quiet Sun profiles, and shows a small asymmetry in the red wing. Note also that the subordinate lines are in emission in this pixel (not true of every pre-flare profile). Figure 3.13 shows several more pre-flare k-line profiles. These are from slit position 5 and 6 (panels (a) & (b) respectively). The lines in grey are a sampling of k-line profiles along the slit in steps of ∼ 0.33", showing that there is some variation in the line intensity and also line shape. This is more evident in panel (b) where the line core is not as clearly single peaked. In fact, some profiles do contain a weak reversal or appear as flat-topped (e.g. the averaged profile in panel (a)).

From AIA 1700Å images the pre-flare region appears to be plage on the border of a small pore. Pre-flare profiles are similar to the plage profiles shown in Carlsson

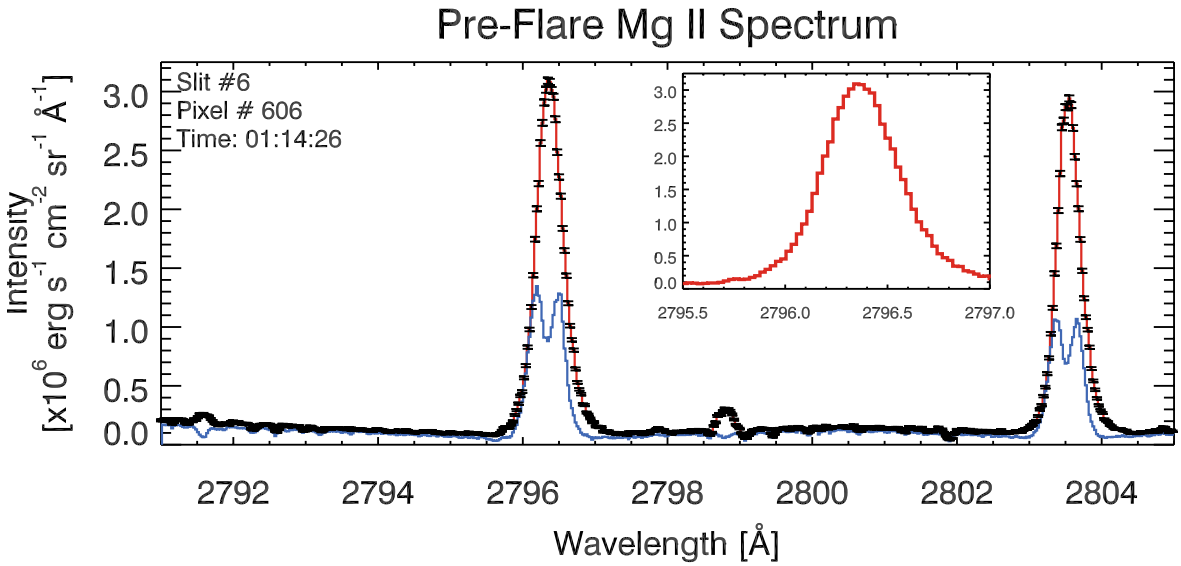

Figure 3.12: *A typical pre-flare Mg II spectrum (red line), with the k-line, h-line, and subordinate lines. An inset shows the k-line in detail. The spectrum in blue is a quiet Sun profile for comparison. Note that the central reversal is filled in, and intensity increased over the quiet Sun profiles.*

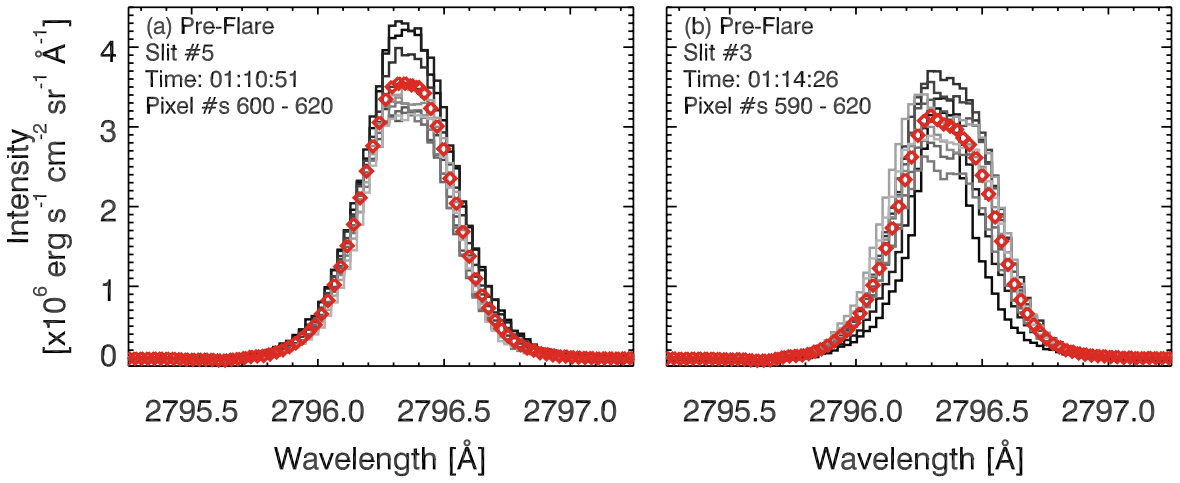

Figure 3.13: *A representative sample of pre-flare k-line profiles in greyscale and the average of the profiles in each panel overlaid as red diamonds. Panel (a) shows profiles in steps of 2 pixels (≈ 0.33″) from y-position 600 to 620 along slit position 5 at 01:10:51 UT. Panel (b) shows profiles in steps of 3 pixels (≈ 0.5″) from y-position 590 to 620 along slit position 3 at 01:14:26 UT.*

et al. (2015). They report intensities on the order of $[0.7 - 1]$ nW m^{-2} sr^{-1} Hz^{-1} for profiles in the active region they analyse, which converts to $\sim [2.7 - 3.8] \times 10^6$ erg s^{-1} cm^{-2} sr^{-1} Å^{-1}. Carlsson et al. (2015) note that their plage profiles were a mix of reversed, single peaked and flat-topped profiles with the single peaked being a subset. Additionally, it was rare for the subordinate line to be in emission.

While the pre-flare observations are of a similar intensity to the Carlsson et al. (2015) plage profiles, the majority of the pre-flare profiles appear single peaked or flat-topped. Figure 3.14 shows the value of D_c for the pre-flare region. Single peaked profiles are coloured blue. It is clear that the majority of pixels here are flagged as having a single peaked profile. The region above the pre-flare is a pore/sunspot which also usually exhibit single peaked profiles with a weaker intensity than plage (Morrill et al. 2001; Schmit et al. 2015). Recall, also, that the peak-finding algorithm is possibly over-zealous, and flags flat-topped profiles as single peaked. But Figure 3.14 illustrates the difference between the quiet Sun and pre-flare profiles so that we can conclude the pre-flare profiles are either truly single peaked or have a very small reversal in comparison to the quiet Sun.

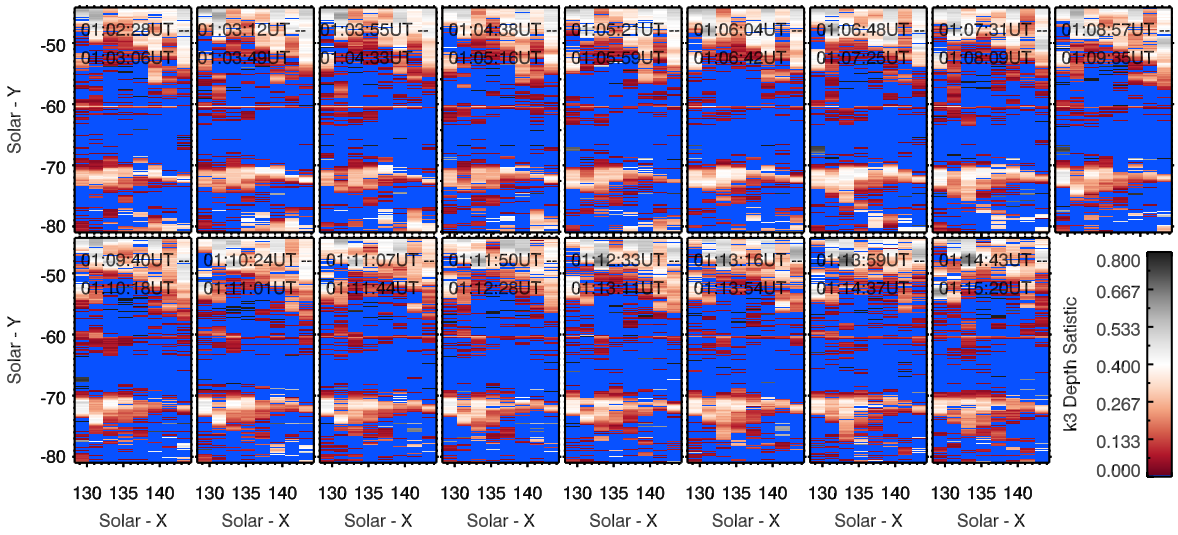

Figure 3.14: *The pre-flare k3 depth statistic as a function of time. Colour is as indicated on the colourbar, apart from $D_c = 0$ (single peaked profiles) where the pixels are shown in blue. The plage and pore profiles are mainly single peaked.*

The subordinate lines are in emission, or at least enhanced, in a number of pixels. Figure 3.15 shows an exposure from 01:07:04 UT that shows the pre-flare region.

Where the h & k lines are most intense the subordinate lines are in emission. At other locations, however, the subordinate lines are again in absorption. Pereira et al. (2015) modelled the subordinate lines pointing out that to be in emission the formation region of the subordinate lines must have a large temperature gradient of at least 1500 K at an electron density of $\sim 10^{12}$ cm^{-3}. The SJI images show that there are many small, transient brightenings in the pre-flare region so these small events could be the cause of the dominance of the single peaked and flat-topped profiles, and of the presence of subordinate lines in emission.

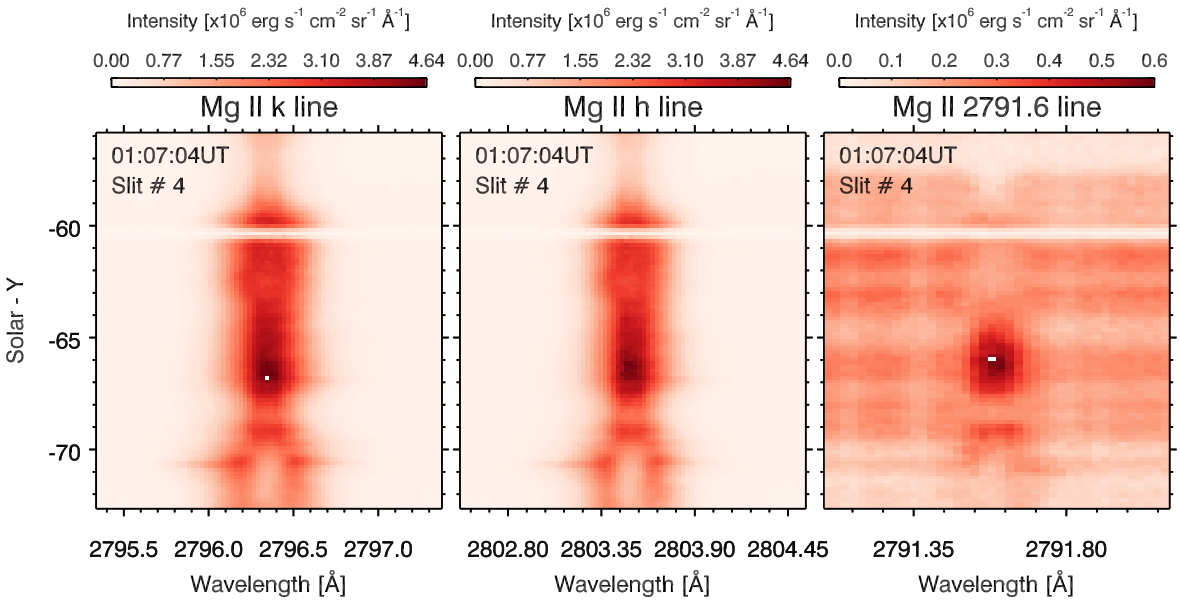

Figure 3.15: *The k-line, h-line, and 2791.6 Å subordinate line exposures, along slit position 4, at 01:07:04 UT (pre-flare). The central reversals are mostly filled in or shallow in the plage regions (middle of image). The strongest emission in each of the lines originates from a bright loop that is visible in the SJI and AIA images. The bright band near −60.5″ is the upper fiducial mark.*

The integrated intensity of the k-line in the pre-flare region is shown in Figure 3.16, where the intensity has been integrated over 2796.3509 ± 1.3Å. Each panel in this image shows a SG raster. The integrated intensity is fairly consistent in each spatial location, with some variation due to small heating events. For the most part, the intensity is approximately two to three times that of the quiet Sun, with an average of 1.475×10^6 erg s^{-1} cm^{-2} sr^{-1} (averaged across all slit positions for the

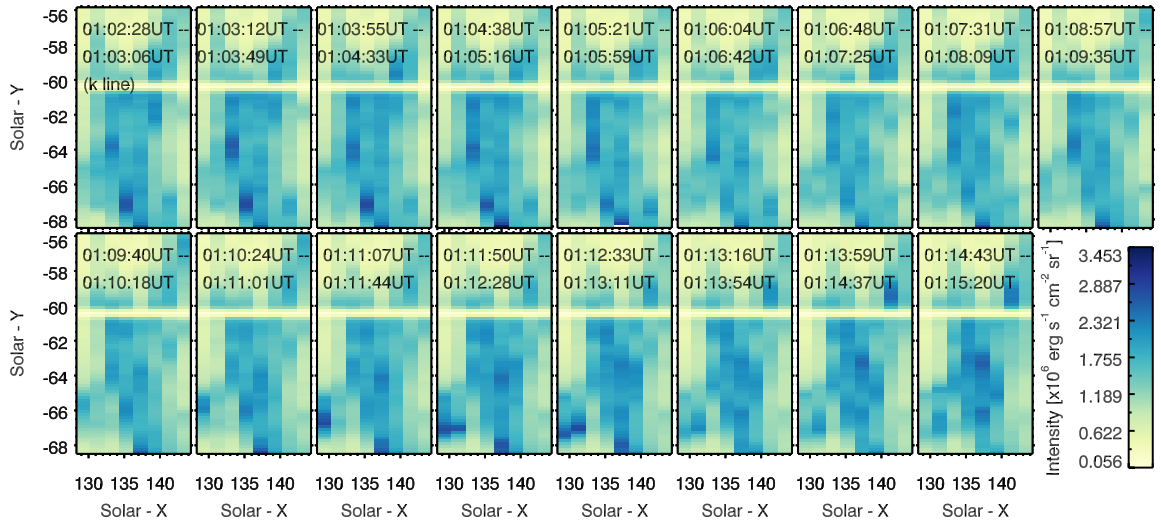

Figure 3.16: *The pre-flare k-line integrated intensity (2796.3509 ± 1.3). Each panel is a different raster. It takes approximately 5 s between exposures so that each raster is imaged over ∼ 40 s. The h-line image is similar. The low intensity row at −60.5″ is the upper fiducial mark.*

times and y-positions shown). The spread in values was quite large, though, with a standard deviation of 0.41×10^6 erg s^{-1} cm^{-2} sr^{-1}. This was mainly due to slit positions 1-3, each of which had a large standard deviation when averaging along each slit individually. Slit positions 4-8 had lower standard deviations, on the order 0.15×10^6 erg s^{-1} cm^{-2} sr^{-1}. The larger spread in values for the first few slit positions was due to a few small patches (around 1″ in size) of enhanced intensity that occur at the base of one of the hot loops visible in the EUV images. These heating events are observed throughout the chromosphere and transition region (visible in 304Å, 1600Å, and SJI images), not just in the corona. Aside from these transient events, there is not any significant variation in the intensity of the pre-flare pixels.

3.6 Mg II Flare Profiles

As discussed in § 3.3 the northern flare ribbon is observed to expand northwards and later to the west. The general behaviour of the Mg II profiles is described initially before a quantitive characterisation of the line profiles is presented.

3.6.1 General Behaviour During the Flare

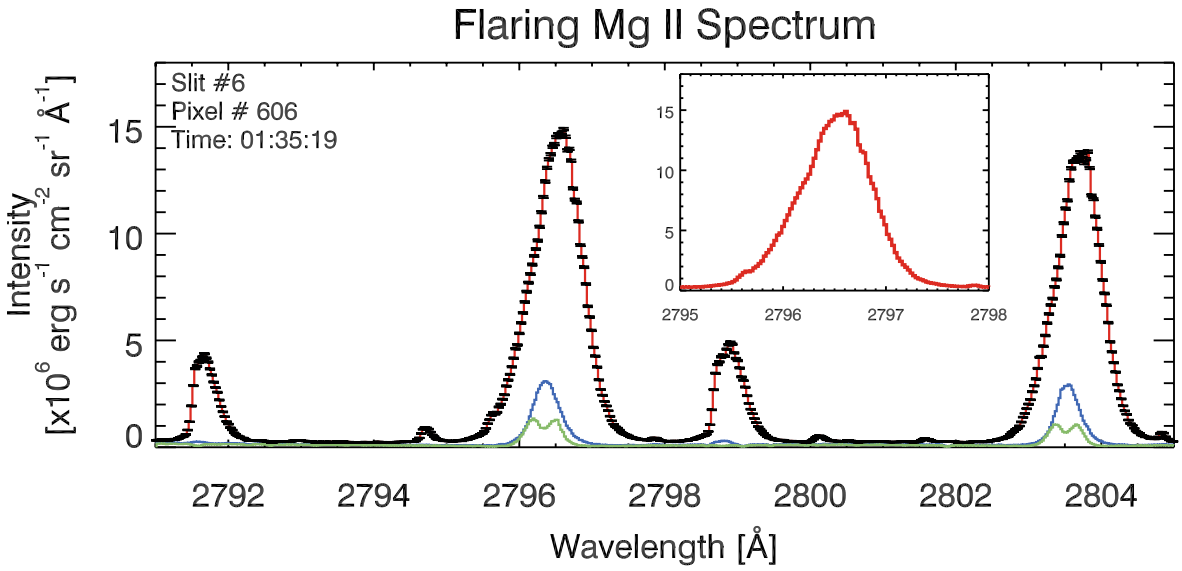

Figure 3.17: *A typical flare Mg II spectrum (red line). The spectrum in blue is the pre-flare profile for comparison, and the green is a sample quiet Sun profile. Note that in the flare profile, the central reversal is filled in, intensity increased, and line broadened over the quiet Sun profiles and pre-flare values.*

An example of a flaring Mg II spectrum is shown in Figure 3.17 where both the resonance lines and the subordinate lines are clearly enhanced by flare energy input. At this time the flare outer ribbon (the leading edge of the ribbon) as observed in the SJI images is sitting over the pixel. The blue line in this figure is a pre-flare spectrum from the same spatial location but around 30 minutes before the flare. The green line is a sample quiet Sun spectrum. As well as showing intensity enhancements, during the flare the resonance line wings are broadened, the line cores are redshifted and they show asymmetries, with a stronger blue wing. The subordinate triplet lines are also broadened and redshifted, but appear to have a red asymmetry with a strong red wing. Both the h & k lines appear single peaked.

A larger sample of k-line profiles is shown in Figure 3.18, where panels (a) & (b) show flaring k-line profiles along slit positions 6 & 4 respectively. Each greyscale profile is from a different spatial location along the slit at the time indicated, with each profile separated by ~ 0.167". While there is some variation in the line intensity,

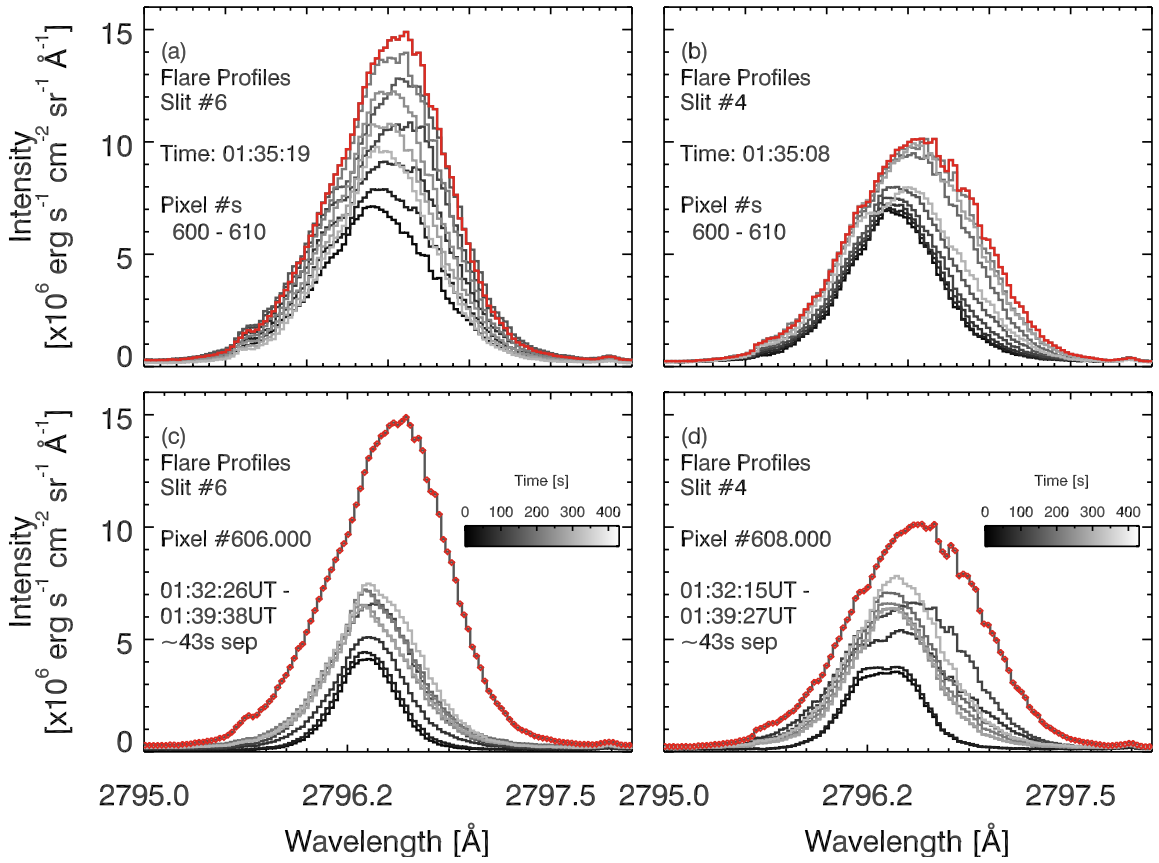

Figure 3.18: *A representative sample of flare k-line profiles in greyscale. Panel (a) shows profiles along slit position 6, in* 0.167" *steps, at t = 01:35:19 UT. Panel (b) similarly shows profiles along slit position 4 at t = 01:35:08 UT. In panel (a) and panel (b) the red profiles show the pixels with maximum intensity at that time. For these pixels, panels (c) and (d) show the time evolution over a span of ~7 minutes, where profiles are shown in 43 s steps. The colourbar indicates the time.*

and while some show stronger Doppler shifts, asymmetries, and line width, the profiles are generally similar. It is worthwhile noting that while the profiles can be described as single peaked, some are flat-topped and some show small local maxima and minima in the line core with a rather jagged structure at times. This is likely a reflection of local maxima and minima in the contribution to the emergent intensity, which is a function of the local opacity and source function in the chromosphere at different heights since the lines are optically thick. Blue asymmetries (stronger blue wing than red wing) were quite apparent in some of the profiles, and in certain profiles the blue wing appeared to have a 'shoulder' possibly indicating the presence

of a stationary (or less redshifted) component to the line.

The red profiles indicate the peak intensity along the slit at the time in each panel. Panels (c) & (d) show the time evolution of the pixels corresponding to the red profiles pixels, where the repeat cadence of the IRIS slit to each position was ~ 43 s. Time is indicated by a colourbar, with $t = 0$ noted on the right hand side of each panel. In panel (c) there was a rise in intensity for 2-3 exposures (~ 43 – 129 s) before the peak. These times corresponded to the time when the outer ribbon approached the pixel. Within the next 43 s time interval the intensity drops as the outer ribbon passes on. The intensity in each pixel decays over the next several, and the line is less redshifted than at maximum. Panel (d) shows a similar evolution but with profiles that were initially less intense and more flat-topped. During the rise phase and at the peak, the line profile is jagged, but as it cools the profile becomes more uniform. Maps of the depth statistic look very similar to Figure 3.14 and reveal that, like the pre-flare pixels, the majority of flare profiles are flagged as single peaked or flat-topped with only a minority showing a central reversal.

Surveying the flare profiles along all slit positions during the flare showed that slit positions 5, 6, & 7 contained the strongest flaring profiles (both in Mg II and in the SJI images). These slit positions were the closest to the footpoint sources observed by RHESSI. A sequence of k-line exposures from slit position 6 is shown in Figure 3.19, where wavelength is along the x-axis and spatial location along the slit is on the y-axis. Intensity is represented by colour and time of the observation is indicated on each panel. The 'missing' row of data at $y \sim -60.5$" is the upper fiducial mark of the IRIS slit. The flare occurs roughly between $y \sim -67$" and $y \sim -60$". Before the flare (top row) the line is single peaked or flat-topped (little intensity variation across the line core). Beginning at ~01:33:09 UT the intensity and line width increases. The flare peaks at ~01:35:19 UT before quickly decreasing in intensity by the next raster. The ribbon spreads further northwards and also begins to curve towards the west, causing the separation of the two more intense patches at ~01:36:02 UT (see Figure 3.5(c) for a corresponding SJI observation). In the cooling phase the line width, intensity and redshift decreases but are all still enhanced over the pre-flare. However, starting ~01:37:28 UT the filament material from the failed eruption begins to spread over the north of the field of view. This is evident in the wide, centrally reversed profiles that take on a twisted appearance as they propagate north. This obscures the flare sources and continues to do so past the time range shown here.

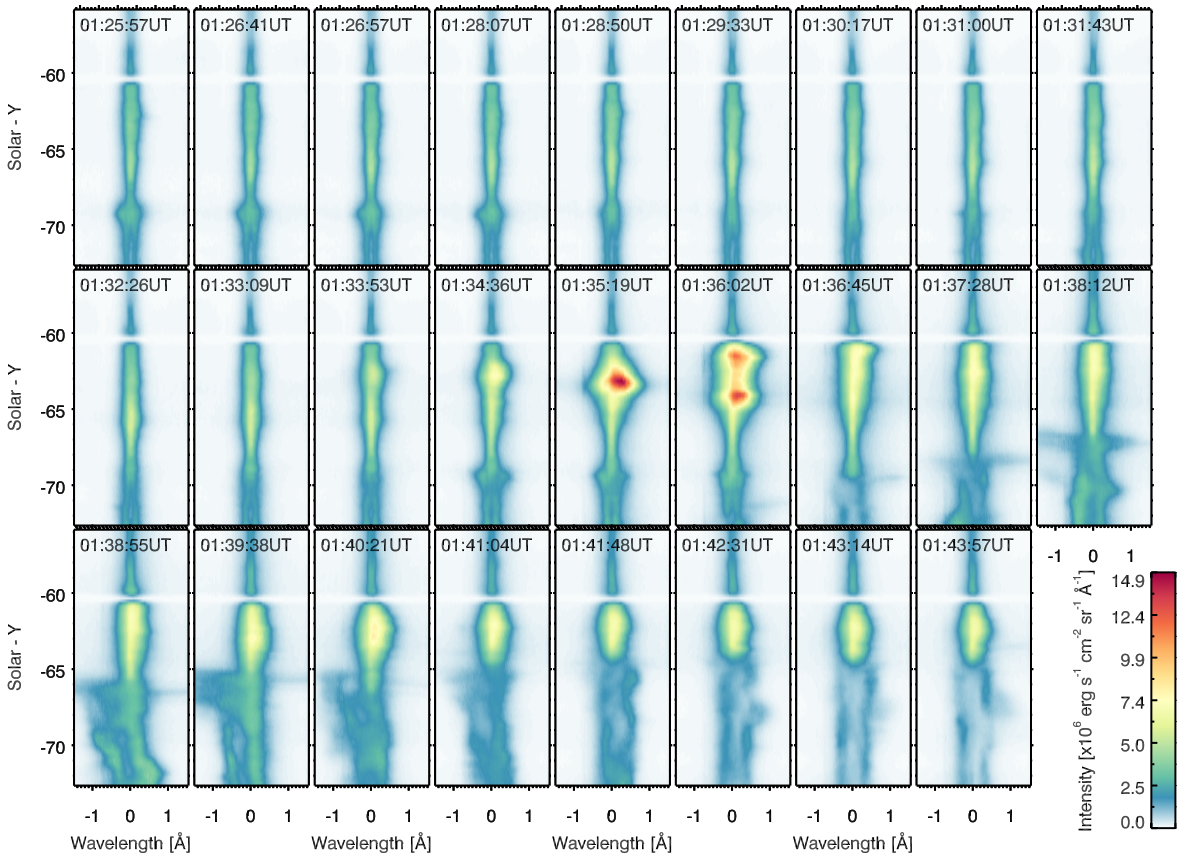

Figure 3.19: *A sequence of k-line exposures during the flare, showing wavelength on the x-axis and position along the IRIS slit the y-axis. Slit position 6 is shown. Colour represents intensity. Intensity increases with time during the flare to the peak at 01:35:19 UT. The line broadens, becomes redshifted and asymmetric. Starting around 01:36:45 UT the filament material begins falling back towards the Sun, obscuring the flare. The profiles from the filament material are Doppler shifted, broad and centrally reversed.*

Other slit positions show similar features, with the spatial location and time of flare peak varying depending on the shape of the flare ribbon near the slit. Of particular note is slit position 7, which was located near the more western edge of the ribbon. At ~01:36 UT the flare ribbon expands west and forms the 'hook'-like structure near [150, −68]" seen in Figure 3.5(d,e). Figure 3.20 shows an exposure of the k-line, h-line and 2791.6Å subordinate line along slit position 7 at 01:36:51 UT. The same features discussed previously are present, with redshifts, broad, asymmetric lines, but from this zoomed in image the variation on small spatial scales is

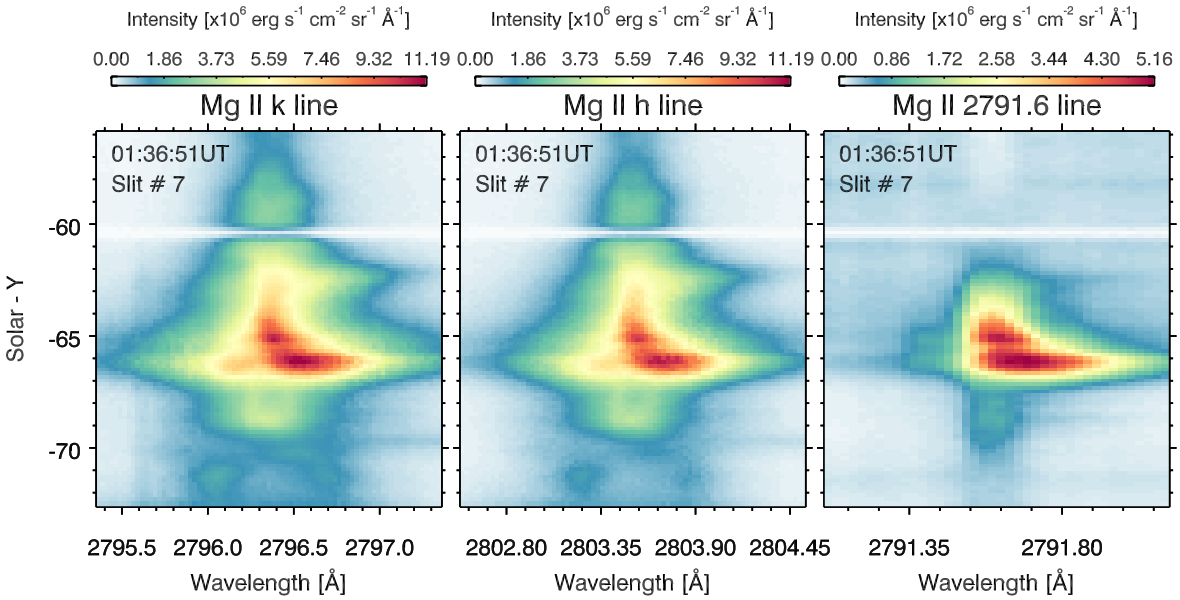

Figure 3.20: *Mg II k, h, and 2791.6Å subordinate line exposure images, at 01:37:28 UT from slit position 7. The flare peaks slightly later at this slit position. This shows the variations in Doppler shift, intensity and line width on small spatial scales.*

apparent. Both the line intensity and amount of Doppler shift of the line core vary on sub-arcsecond scales, suggesting that flare energy is deposited at small spatial scales.

Integrating the intensity across each of the resonance lines and the subordinate triplet (k-line: [2795.3509±1.3] Å, h-line: [2803.5297±1.3] Å, sub1: [2791.60±0.6] Å & sub2: [2798.82 ± 0.55] Å, where the 2798Å lines are blended and labelled together as 'sub2') the lightcurves of each line were compared. Figure 3.21 shows a flare lightcurve for each of the lines, from slit position 6 at $y = -63.25$" (lightcurves from other pixel locations are similar.). The subordinate lines are shown in the lower panel. All four lines show a similar rise time before peaking simultaneously (indicated with vertical lines) to within the cadence of the observations. Similarly they initially decay at a similar rate, falling sharply in intensity within one timeframe. After this initial decay there is a more gradual decrease over the next few minutes until ~01:45 UT at which point the resonance lines decrease more strongly and their intensity dips below the pre-flare level. The subordinate lines show no such dip and instead smoothly decay back to the pre-flare level approximately 20 minutes after the flare peak. This behaviour is due to the filament material spreading over and obscuring the field

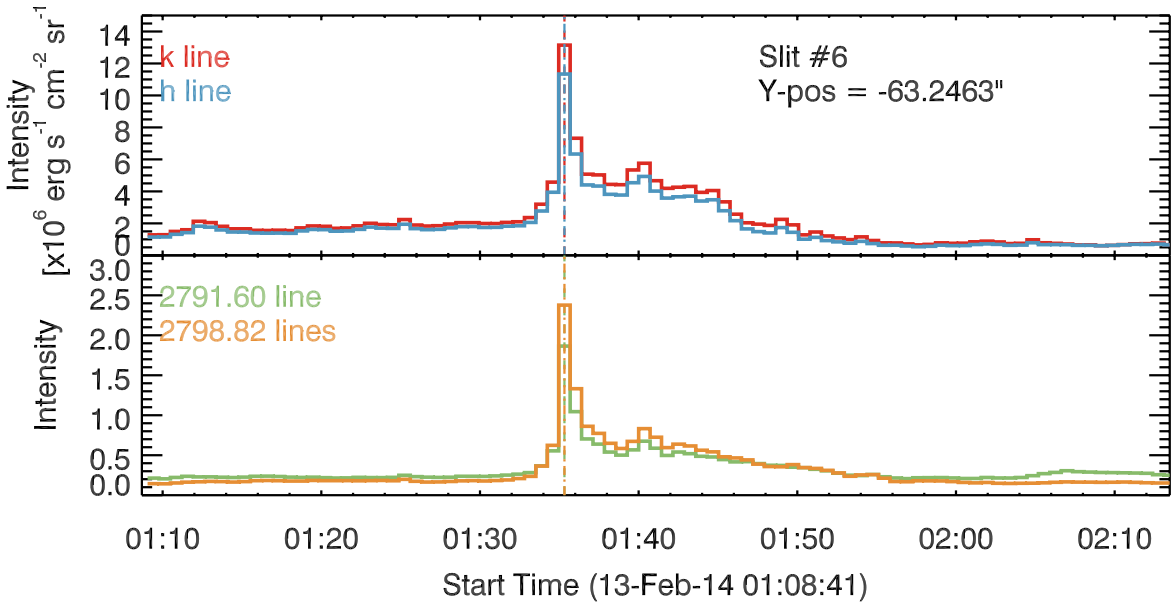

Figure 3.21: *Mg II h & k line (upper panel), and subordinate line (lower panel) integrated intensities during the flare from $y = -63.25$" along slit position 6. The vertical lines show the time of peak intensity.*

of view. Resonance line photons are absorbed since there is sufficient opacity in the filament material but there is seemingly not enough opacity at subordinate line wavelengths within the filament to absorb the flare photons. Finally, in many of the lightcurves there appears to be a second peak approximately five minutes after the main flare peak.

A cross-correlation analysis was performed on the Mg II lightcurves to determine if the resonance lines, and subordinate lines were well correlated temporally to each other. A strong correlation with a time lag of 0 would suggest that, to within the 43 s cadence of the data, features in the lightcurves are 'real' as they occur in the other lines at the same time. Additionally, it would show whether the lines cooled at similar rate. Lightcurves were broken down into four time periods: pre-flare, flare, initial decay, later decay. Two decay phases were chosen as the filament material affected only the h & k lines, so after this point a correlation would not be expected between the decay of the resonance lines and decay of the subordinate lines. Using the IDL routine `c_correlate.pro`, the cross-correlation coefficient between the lightcurves were measured as a function of time lag. The time lag ranged $\tau_L \approx [-215, 215]$ s in steps of 43 s (corresponding to ±5 time frames).

The h & k lines were, as expected, strongly correlated with a coefficient of ≈ 0.99

for the majority of the pixels and a lag of 0, so that to within the 43 s cadence of the observations there was no discernible time lag . In the pre-flare and later decay phase there were a few pixels in which the correlation coefficient dropped as low as 0.5 but during the flare and initial decay the value was very nearly 1. The k-line was not well correlated with the subordinate lines in the pre-flare or later decay. During the flare, however, the flaring profiles were well correlated with coefficients > 0.9. This continued into the initial decay phase but after the filament material obscures the resonance lines the k-line and subordinate lines are again not well correlated.

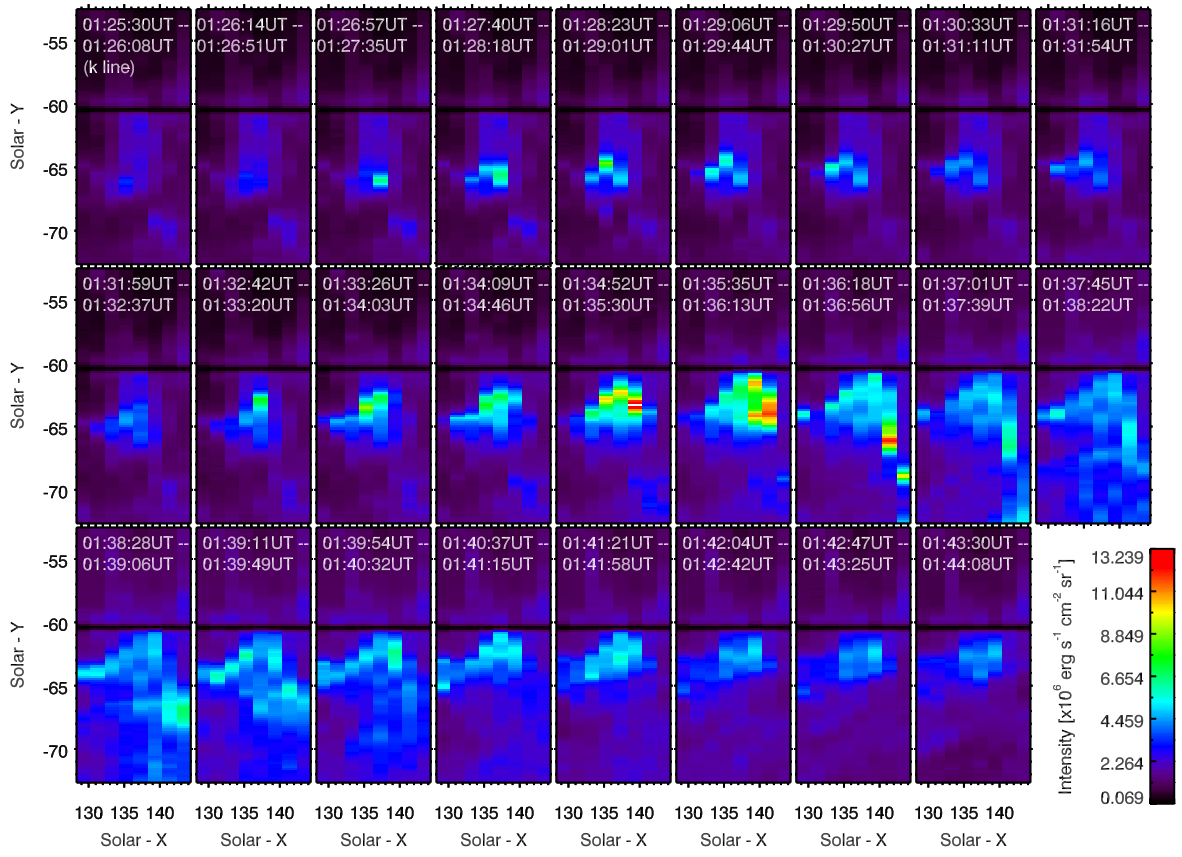

Figure 3.22: *Mg II k-line integrated intensity (2796.3509 ± 1.3Å) images during the flare. The dark solid line is the upper fiducial mark of the IRIS SG.*

The k-line integrated intensity is shown as a map for each raster in Figure 3.22 where the x-axis is slit position, and y-axis is position along the SG slit. Colour represents intensity. As before, each panel takes 43 s to produce. The more intense emission occurs near the western edge of the flare ribbon (slit positions 5-7) and

the material that enters the field of view at the end of the second row of images is the filament material (a similar map using the 2791.6Å subordinate line intensity shows no filament material). This figure illustrates the similar morphology of the flaring Mg II sources to the observations from the SJI and AIA, with the most intense emission originating from the edge of the ribbon structure. Note that the ribbon seems more compact on the x-axis in the Mg II maps than the AIA or SJI maps, as an artefact of stretching the pixels to fill the ~ 2" between each slit position.

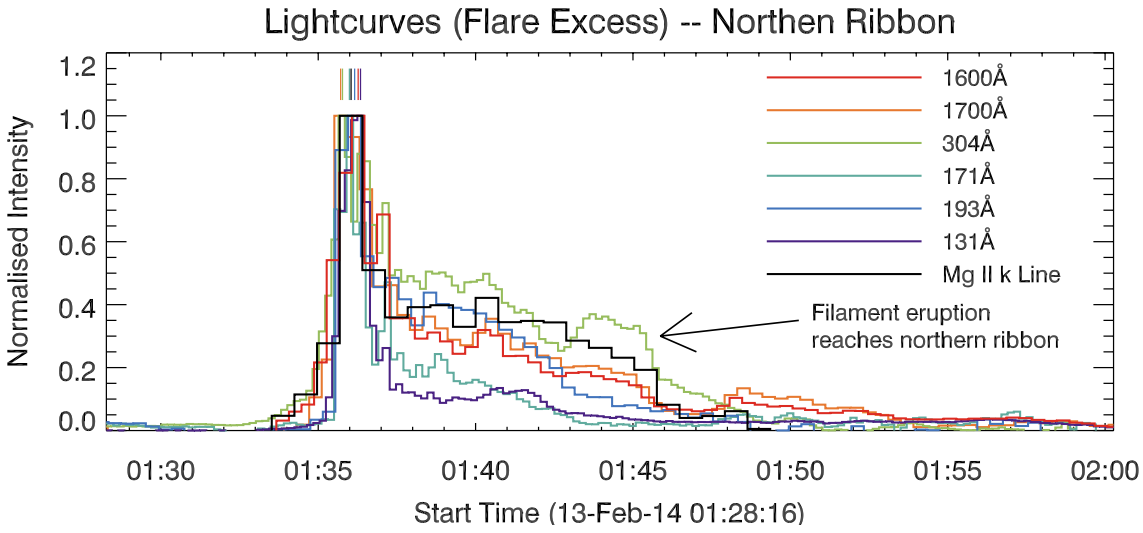

Figure 3.23: *Normalised flare excess lightcurves from several AIA filters and the Mg II k-line. These were averaged over a region of the flaring source, and vertical lines indicate the flare peak in each passband.*

As well as being co-spatial with the AIA images, the Mg II was largely co-temporal with the emission from other chromospheric passbands, and with the coronal passbands. Flare excess lightcurves from several AIA passbands sampling the chromosphere (1600Å, 1700Å, & 304Å) and the transition region/corona (171Å, 193Å, & 131Å) were averaged over several regions, and normalised. These are shown alongside the k-line flare excess lightcurve (averaged over the same location and normalised) in Figure 3.23. These lightcurves show that the NUV, UV and EUV data followed similar timescales for the rise, peak and decay during the flare. It is interesting that the chromospheric observations all exhibit a more gradual rise over a few minutes before the peak whereas the coronal observations show a quicker rise of only ~ 1 minute.

3.6.2 Mg II k:h Line Ratio

Since the lines do not have the characteristic central reversal, the question could be asked: 'are the lines optically thin during the flare?'

The optical depth of a spectral line produced in a transition from upper level j to lower level i and viewed along a path length l is $\tau_{i,j} = \int \kappa_{i,j} \mathrm{d}l$. In this expression $\kappa_{i,j}$ is the line opacity per unit mass (or mass absorption coefficient):

$$\kappa_{i,j} = n_i \frac{h\nu_{i,j}}{4\pi} B_{i,j} \varphi_{i,j} \frac{1}{\rho} = \frac{\pi e^2}{m_e c} f_{i,j} n_i \varphi_{i,j} \frac{1}{\rho}, \tag{3.4}$$

where n_i is the population of level i, h is Planck's constant, $\nu_{i,j}$ is the frequency of transition, $B_{i,j}$ is the Einstein absorption coefficient,e is the electron charge, m_e is the electron mass, c is the speed of the light, $f_{i,j}$ is the oscillator strength, ρ is the mass density and $\varphi_{i,j}$ is the absorption profile (see e.g. Mihalas 1978; Rathore et al. 2015). For the Mg II h & k lines, we can denote the ground level with $i = 0$, the h upper level with $j = h$ and k upper level with $j = k$. Since these lines are transitions from closely spaced upper levels to a common lower level the ratio of their opacities reduces to the ratio of their oscillator strengths (assuming, reasonably, that the lines have the same absorption profile):

$$\frac{\kappa_{0,k}}{\kappa_{0,h}} = \frac{f_{0,k}}{f_{0,h}} = 2. \tag{3.5}$$

Since it has twice the opacity, the k line is formed higher in the atmosphere than the h line (by a few tens of km from the simulations of Leenaarts et al. 2013a). In the optically thin case the source functions of the resonance lines are equal, and the intensity ratio is set by the opacity ratio of the two lines. Observations of the k:h intensity ratio $R_{k:h} = 2$ would therefore indicate that the lines were formed under optically thin conditions. Any other ratio would suggest that the lines are produced in optically thick conditions in which case the line ratio is an indication of the difference between the source functions of the two lines, which are formed around the height that optical depth equals unity for each line. Their source functions will be different since the k-line can track the chromospheric temperature rise to greater height than the h-line.

Generally the ratio is less than two and a little larger than unity. As Leenaarts et al. (2013a) point out, if PRD effects are neglected the source function ratio of the h & k lines can be approximated as $S_k/S_h \simeq (1/2) n_k/n_h$ where n_k and n_h are the

population densities of the upper level of each line. The factor of 1/2 arises from the ratio of statistical weights. This means that for equal source functions (and therefore $R_{k:h} = 1$) the population of the k line upper level must be double that of the h line upper level. For $R_{k:h} > 1$ the population ratio must be larger than 2. So, while not an exact relation, since PRD effects complicate the situation, the line ratio can indicate (1) whether the lines are optically thick or thin, and (2) the relative behaviour of the population density of the upper levels. Note that, as pointed out by Rathore & Carlsson (2015) when discussing the C II resonance line ratios, even if the lines are optically thick, the source function behaviour can still result in a ratio of 2, but most on-disk observations show ratios much less than 2.

For the quiet Sun pixels discussed previously the mean ratio was measured and averaging over time gives mean quiet Sun k:h ratio as $R_{k:h} = 1.18 \pm 0.01$. This is in line with previous studies of non-flaring sources (e.g Kohl & Parkinson 1976; Lemaire et al. 1981), where a range of values $R_{k:h}$ $1.14 - 1.46$ have been observed, varying with both source type and position on the solar disk. Turning to the flaring region, the ratio before and during the flare was in the range $R_{k:h} \sim [1.08 - 1.22]$ so the h & k lines were optically thick throughout. Filament material had a higher ratio ($R_{k:h} \sim [1.30 - 1.55]$, so that when the filament eruption expanded over the flaring pixels the ratio there rose. Harra et al. (2014) also found that a filament eruption affected the k:h ratio of high-lying coronal loops, increasing the ratio to greater than 2 (these observations were above the limb). Figure 3.24(a) shows the correlation between the h & k intensity, where colour represents the time during the event, starting at ~01:24 UT. The dashed lines in this figure are $y = x$ and $y = 2x$. Throughout the observations the h & k line intensities are strongly correlated (the correlation coefficient is typically > 0.95 over the duration of the event) but there is some spread that begins at $t \sim 15$ minutes. This is the result of the filament eruption.

Although there is no systematic large-scale increase or decrease of $R_{k:h}$ in response to the flare, variations in the ratio before the flare are reduced and the ratio tends to a value of around of $R_{k:h} \approx 1.15 - 1.18$ (see Figure 3.25). Figure 3.24(b) shows $R_{k:h}$ as a function of k-line intensity, where colour again represents time. The rise and peak of the flare are shown in purple and blue, where the most intense pixels cluster with a smaller spread in values. Then the filament eruption (green & yellow) begins to increase the ratio, before the post-flare has a reasonably large spread in values, dropping close to $R_{k:h} \approx 1$.

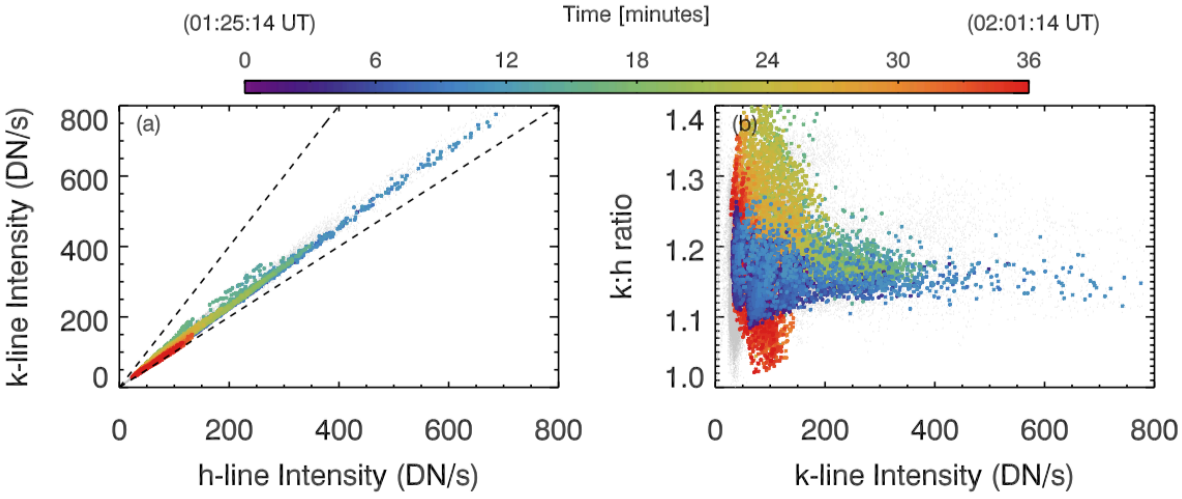

Figure 3.24: *(a) The k & h line intensities, where colour represents time during the flare. The dotted lines show $y = x$ and $y = 2x$. The intensities are typically correlated with a coefficient > 0.95. (b) The k:h ratio as a function of k-line intensity. Again, colour represents time. Note the clustering during the flare ($t \sim 5 - 15$ minutes) and the increase that results from the filament eruption ($t \sim 18 - 36$ minutes).*

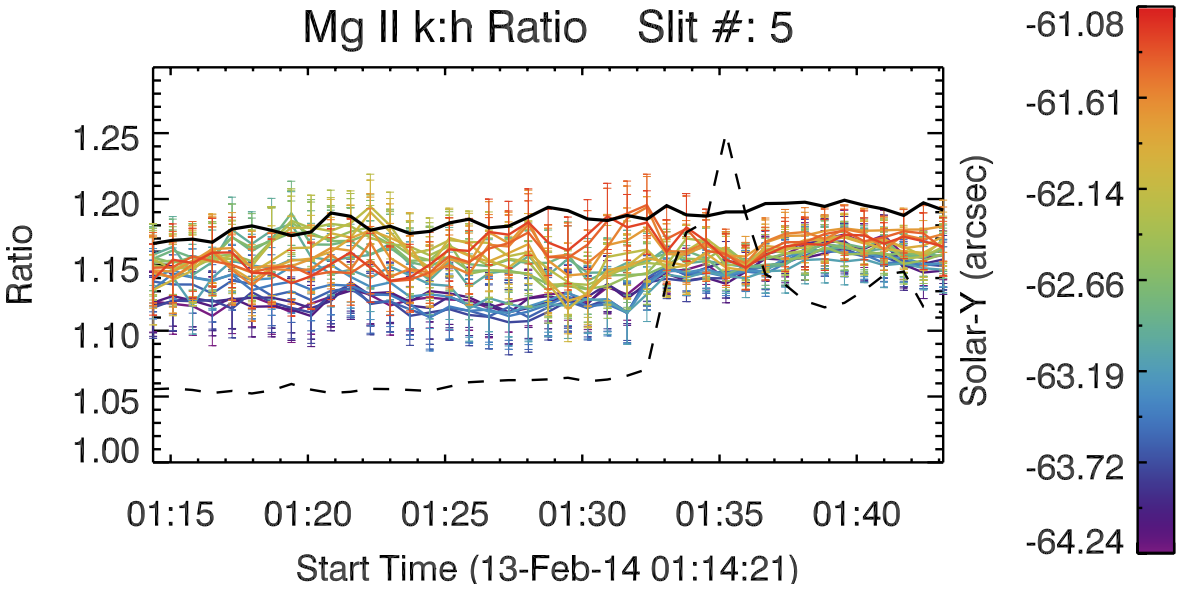

Figure 3.25: *The k:h line intensity ratios for several cuts along slit position 5 where the y-position indicated by colour. The quiet Sun average is shown in black and an example flare lightcurve is shown as a dotted line.*

In slit positions 5 & 6 in particular there is a noticeable decrease in the spread of of $R_{k:h}$ during or shortly after the flare. Values of $R_{k:h}$ for pixels within the flaring source are shown in Figure 3.25 as coloured lines, where the colour is the y-position along the slit. Errors are the combination of the k & h line intensity errors added in quadrature. The black line is the quiet Sun average as a function of time. The dotted line shows an example lightcurve (scaled to fit on the figure), to indicate the time of the flare. During the flare, the spread in values decreases with the mean standard deviation dropping from $\sigma = 0.02$ to $\sigma = 0.007$ from the pre-flare to flare.

Lemaire et al. (1984) noted a larger variation in $R_{k:h}$, between $0.9 - 1.5$ when the line was not flaring, but found that it was reasonably stable with a value of $R_{k:h} = 1.1$ during the flare itself, as did Liu et al. (2015). However, these observations had much less spatial resolution than IRIS (2.5" compared to 0.4"). Still, it is interesting that in both flares the ratio seemed to vary in time and space, but tended to a similar value during the flare itself. This could be due to differences in flare heating compared to the heating of the pre-flare atmosphere - the flare heating could be more uniform whereas small scale variations in the non-flaring chromosphere could result in the spread of $R_{k:h}$.

3.6.3 Characterising the Line Profiles

The resonance lines are optically thick throughout the flare, despite their lack of a central reversal, and are clearly non-gaussian in shape. Optically thick lines are not meaningfully fitted by Gaussians, particularly when the profiles have flat tops and extended wings as they do during the flare. Some Mg II profiles during the flare show wing asymmetries that could be interpreted as multiple components that are shifted by differing amounts (related to the atmospheric velocity at their formation height). Asymmetries might also result from how the source function varies with height. Therefore to achieve a good fit, double (or multiple) Gaussians may be required which the Gaussian components sum to produce the resultant profiles (not the case in an optically thick line). Schmit et al. (2015) did use a complex fitting algorithm using multiple Gaussian components as a means to identify the k2r, k2v and k3 components (without inferring any physical meaning from the Gaussian fit), but in our case, where any reversal is small and lost in the noise, this approach is not suitable.

Another problem is that the peak intensity of an optically thick line is not necessarily the same as the line core. The line core is the part of the line formed highest in the atmosphere, but the source function may decrease with height past a certain point, meaning that the core intensity, as defined, is somewhat lower than the peak intensity. So, for profiles that are more flat-topped, or that have wide cores, simply choosing the peak intensity as the line core is not appropriate.

Attempts were made to fit flare profiles with single or double Gaussian functions, but in all cases the reduced χ^2 statistic was significantly greater than 1. This often led to an underestimate of the line width, and misidentification of the line core position. An analytic model will not be able to be fit the emergent intensity that is a result of the complex way in which the source function varies with both wavelength across the line and height. Instead, we can characterise the lines using a non-parametric approach to identify the line centroid motion, a measure of the line width and the line asymmetry. The evolution of these metrics during the flare can reveal how the line changes responds to the input of energy during the flare, and will be simple to compare with model outputs.

Quartiles were used to produce these metrics. This is a simple statistical method that makes no assumption about the underlying distribution. Line profiles normalised cumulative distribution functions (CDFs) of intensity vs wavelength were made for each h & k line profile, and the wavelengths corresponding to the 25%, 50% and 75% percentiles were found (Q_1, Q_2, Q_3, respectively). From these the following metrics were produced:

- $\lambda_c = Q_2$, the line centroid wavelength,
- $W = Q_3 - Q_1$, a measure of the line width,
- $S = \frac{(Q_3-Q_2)-(Q_2-Q_1)}{Q_3-Q_1}$, a measure of the line asymmetry.

In addition to using the *quartiles*, it is simple to extend this method to analyse *quantiles* which are other intensity percentiles. This allows sampling further from line centroid to investigate line width or asymmetry further into line wings (and therefore deeper into the atmosphere).

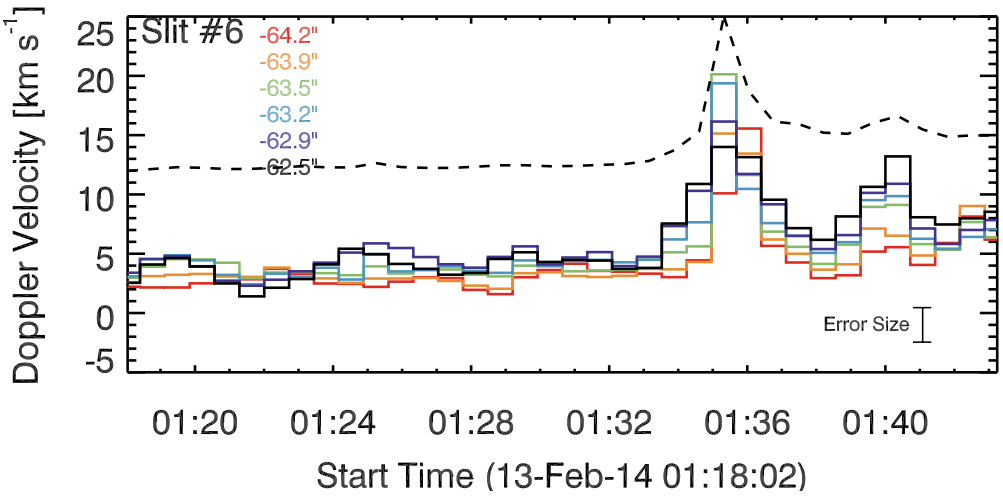

Figure 3.26: *The k-line centroid velocity from the quartiles analysis for different cuts along slit position 6. The y-position is indicated by colour and an example lightcurve is shown as a dotted line.*

3.6.3.1 Centroid Motion

Both the h & k lines show redshifts at times when the outer ribbon passes over the pixel. In the rise phase, at the peak intensity, and for a time into the decay phase of each profile, the whole line (core and wing) was generally shifted. This could indicate that the atmosphere at the line core formation height is moving downwards with an equivalent velocity. In some pixels during the decay phase the red wing remained extended for longer than the core where the shift reduced more quickly. When this happens, an interpretation could be that the atmospheric downflows have propagated past the formation height of the core, but are still affecting the line wings which are formed lower down. Using the standard Doppler shift equation, the equivalent line of sight velocity of the line centroid wavelength shifts were quantified:

$$v_{\mathrm{los}} = \frac{\lambda_{\mathrm{c}} - \lambda_0}{\lambda_0} c, \tag{3.6}$$

where λ_0 is the rest wavelength and λ_{c} the measured line centroid. It is stressed that this measures an equivalent velocity, since these are optically thick lines. Modelling is required to determine if this velocity shift does indeed map directly (or close to) the velocity of the atmosphere at the core formation height. It could be a measure of the average velocity of a range of heights over which the line forms. Averaging over

the pre-flare pixels in slit positions 3-7 (the most intense emission) gives a pre-flare velocity for the h & k lines of $v_{\mathrm{k,pf}} = 2.28$ km s^{-1} and $v_{\mathrm{h,pf}} = 1.32$ km s^{-1}. During the flare the line centroid is shifted to greater velocity in the range $v_{\mathrm{los}} \sim 10 - 25$ km s^{-1}. Figure 3.26 shows several velocity profiles where the colour denotes the y-position along the IRIS slit. The slit shown is position 6. An error bar in the lower right corner indicates the typical error size, which is a combination of the error on the rest wavelength and the error on the wavelength calibration. The rest wavelength had a standard deviation of ±0.64 km s^{-1}. De Pontieu et al. (2014) state the error on the wavelength calibration in the NUV is 1 km s^{-1}. A dotted line on the figure shows a typical k-line lightcurve for reference.

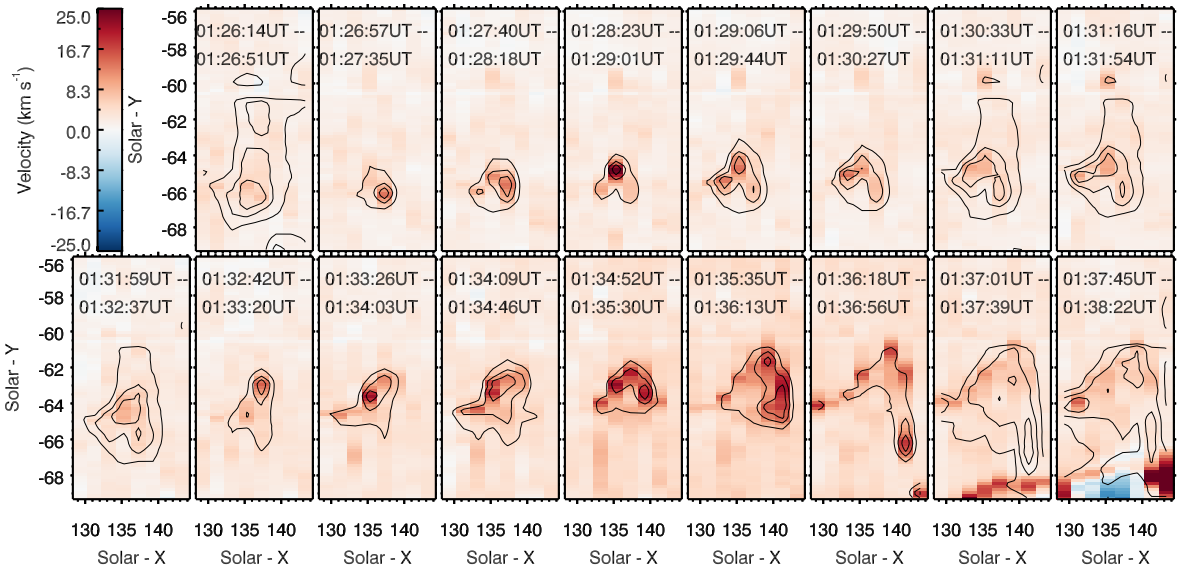

Figure 3.27: *The velocity of the k-line over time, showing the shift of the line centroid. The redshifts (interpreted as downflows) occur at locations of highest intensity enhancement, and track the outer edge of the ribbon. The* 40%, 60%, *and* 80% *intensity contours in each panel are shown for comparison.*

Like the intensity enhancements, the line centroid shifts show a gradual rise of up to a few minutes before peaking. Both the intensity and velocity enhancements decay quickly, with the peak magnitude dropping sharply over the next timeframe (43 s). However, the line centroid shifts return to the background quicker than the intensity. The velocity curves decays by half or more within 43 s, and then almost to the background within 3-4 minutes, whereas the intensity takes several more

minutes to return to background levels. If the subordinate lines are used as a proxy for the decay time (since they share the same temporal profile but are not affected by the filament material) then the time to decay to pre-flare levels is ~15-20 minutes, which is considerably longer than the lifetime of the velocity shifts. Note, also, that the second, smaller bump in the lightcurves is mimicked by the velocity profiles, which also show secondary peaks in those particular pixels.

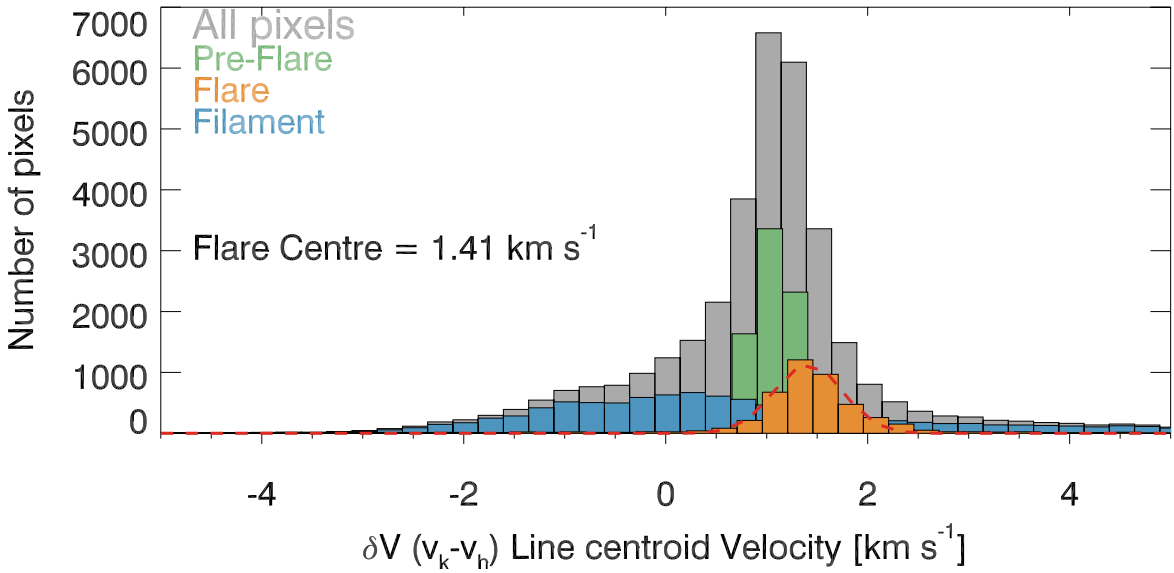

Figure 3.28: *A histogram showing the difference in h & k line velocity ($v_k - v_h$) for the whole flaring region (grey), the pre-flare (green), the filament (blue) and flare (orange). The flaring times were fitted with a Gaussian that had a centre value of $\delta v = 1.41\ km\ s^{-1}$.*

Comparing maps of the line centroid shift with the contours of 40%, 60%, and 80% of the maximum intensity at each time (Figure 3.27) reveals that in addition to being relatively short-lived, the flows are concentrated around the locations of highest intensity. They trace the outline of the ribbon structure, which suggests that the measured redshifts are co-spatial and co-temporal with the energy deposition to each pixel, and return to the background soon after the ribbon front (the outer ribbon) moves on. Note that in these maps the high velocity flows creeping in at the bottom of the final two panels are related to the filament eruption.

The h line is formed a few × 10 km deeper than the k-line in the quiet Sun though it remains to be seen if this is also true in flares. As a result Leenaarts et al. (2013b)

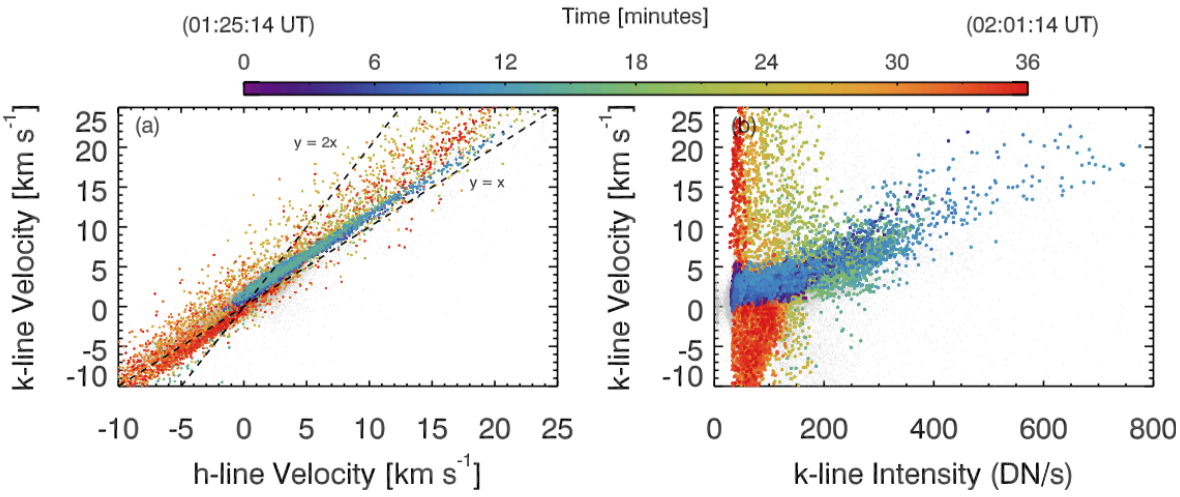

Figure 3.29: *(a) The correlation of the h & k line centroid velocities, where colour represents time in minutes from 01:25:14 UT. The spread largely results from the complex flows resulting from the failed filament eruption. Dashed lines show $y = x$ and $y = 2x$. (b) Scatter plot of k-line velocity as a function of k-line intensity, where again colour represents time. There is a large spread in the data, but at flare times (purple/blue/turquoise points), before the filament spreads over the flare ribbon, the correlation is better.*

raised the possibility of being able to measure the sign of the velocity gradient between the h & k formation heights, if not the magnitude itself. They found a reasonable correlation between line core doppler shift difference for each of the lines and the velocity difference between their formation heights (with a coefficient of ~ 0.8). Figure 3.28 shows a histogram of $\delta v = v_{\mathrm{k}} - v_{\mathrm{h}}$, for the k & h line centroid respectively (so positive δv means a larger k-line velocity). The data here covers the flaring region only. Shown in grey is the whole flaring region, where the k-line velocity is mostly larger than the h-line velocity, suggestive of a decreasing velocity gradient with depth. The pre-flare is shown in green, with a velocity difference around ~ 1 km s^{-1}. The times at which the filament material obscures the field of view are shown in blue, where there is a larger spread of $\delta v\pm \sim 5$ km s^{-1} centred around ~ 0 km s^{-1}. The flare times are shown in orange, where the distribution is shifted to slightly higher velocities. A Gaussian fit to the histogram gave the centre of the flare distribution as $\delta v = 1.41$ km s^{-1}. The histograms, and Figure 3.29(a), which shows the correlation between the h & k velocities, do suggest that the k-line does indeed have a higher line centroid velocity than the h-line, and this gradient

increases during the flare. However, this velocity difference is around the size of the uncertainty on the line centroid shifts, making it is difficult to make a firm statement here. Additionally, Figure 3.29(b) shows that during the flare the correlation between the k-line velocity and the k-line intensity increases during the flare (but still with a lot of spread), whereas there is significant scatter at other times.

3.6.3.2 Line Width

The metric $W = Q_3 - Q_1$ is a measure of the width of the spectral line, bounded by the 25th and 75th percentiles. This is analogous to the full width at half maximum (FWHM) but is not equal to it. Figure 3.30(a) shows the k-line width as a function of time. Colour refers to cuts along slit position 6 in the y-direction, and the dashed line shows a typical lightcurve for reference. As with the velocity and intensity response of the line, the width begins to increase a few frames before the peak before sharply increasing to values in the range $W \sim 0.45 - 0.55$Å, from a pre-flare plage width of $W \sim 0.25 - 0.28$Å. The maximum width for the k-line was $W \sim 0.623$Å and for the h-line $W \sim 0.561$Å. It was difficult to tell the time it took for flaring pixels to return to the pre-flare widths as the filament material obscured much of the decay phase. However, it does seem to be the case that after the initial decrease from the peak, the subsequent decay was more gradual with the lines remaining broader than the pre-flare for some time, unlike the velocity profiles which decayed within 3-4 minutes. Figure 3.30(b) shows a scatter plot of the h & k widths (this time expressed in km s^{-1}) where colour denotes time during the event. At flare times the h & k line widths are well correlated, with the k-line slightly broader. At later times, when the filament material spreads over the flare ribbon there is considerable scatter and the correlation is reduced. The k-line is still, generally, broader than the h-line. Typical flare widths are in excess of ~ 30 km s^{-1} and up to ~ 70 km s^{-1}. Maps of the width show that the broadest profiles are co-spatial with the outer edge of the ribbon, and the most intense emission.

The thermal width of a line, $v_{\rm th}$, is a function of the temperature in the formation region. For Mg II this is typically $v_{\rm th} \sim 2 - 3$ km s^{-1}. Even given the signifiant increase in temperature associated with flares, an increase to the thermal width could not account for the very broad line wings observed. Non-thermal broadening of spectral lines is often used as an indication of the presence of unresolved flows or turbulence. Since the h & k lines are optically thick, the non-thermal velocity cannot

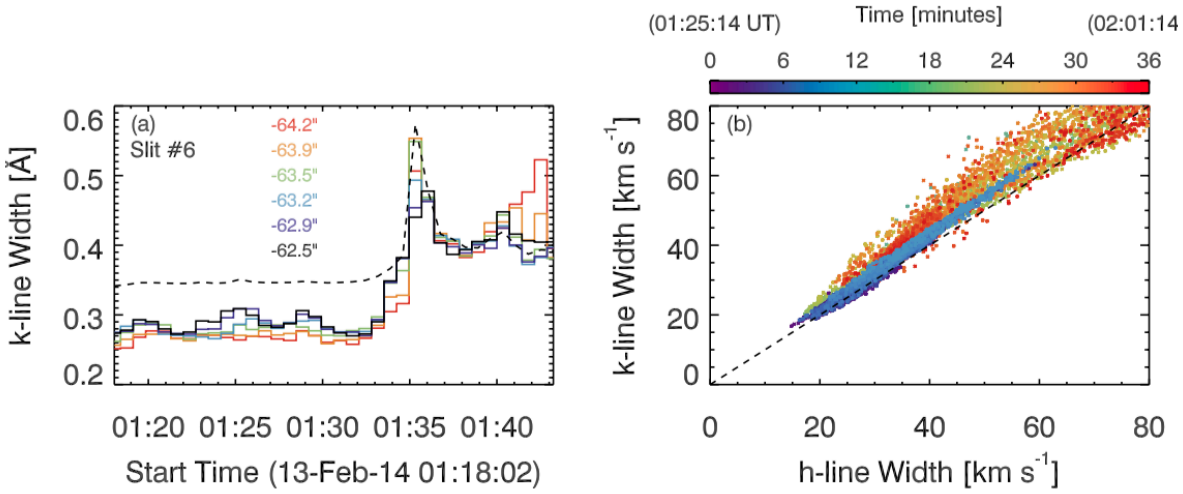

Figure 3.30: *(a) Several time profiles of k-line width from the quartiles analysis, during the flare, where colour indicates the y-position along slit number 6. The dashed line is a lightcurve for reference. Note the more gradual decay in comparison with the velocity profiles from the same pixels (Fig 3.26). (b) A scatter plot showing the tighter correlation during flare times, and that the k-line is mostly always broader than the h-line.*

be ascertained reliably. The O I 1355.6Å line, observed by the IRIS SG, however, is optically thin and formed in the chromosphere (e.g. Lin & Carlsson 2015). A *rough* estimate of the non-thermal velocities that would act to broaden the h & k lines can thus be measured, with the assumption that the same magnitude of non-thermal velocity is present at the h & k formation height.

Using the IDL routine `mpfitfun.pro` (Markwardt 2009), single Gaussian functions were fitted to the O I line and the full width at half maximum (FWHM) measured, $W_{\rm FWHM}$. This FWHM is the sum of the instrumental FWHM, $W_{\rm inst}$, the thermal velocity, $v_{\rm th}$ and the non-thermal velocity $v_{\rm nth}$:

$$W^2_{\rm FWHM} = W^2_{\rm inst} + 4\ln 2\left(\frac{\lambda}{c}\right)^2 (v^2_{\rm th} + v^2_{\rm nth}), \tag{3.7}$$

where λ is the wavelength, and c the speed of light in km s^{-1}. $W_{\rm FWHM}$ and $W_{\rm inst}$ are input in Å where $W_{\rm inst} = 0.026$Å (De Pontieu et al. 2014). $v_{\rm th}$ and $v_{\rm nth}$ are in km s^{-1}. The thermal velocity is $\sqrt{2k_BT/M}$ where M is the element mass, T is the formation temperature of the line and k_B is Boltzmann's constant. Rearranging Eq 3.7 for $v_{\rm nth}$ gives the non-thermal velocity. Along slit position 6 the average O I non-thermal

velocity was measured as $v_{\rm nth} = 9.29$ km s^{-1}.

It is clear that this non-thermal velocity is not sufficient to explain the broad wings of the h & k lines, which have widths of a few $\times 10$ km s^{-1}. Unresolved flows and/or microturbulence of $v_{nth} \sim 9-10$ km s^{-1} could be the cause of some of the Mg II h & k line broadening, particularly in the core of the line, but cannot alone explain the line width during the flare.

If we assume that the h & k lines are optically thin then we can compute their expected FWHM in the optically thin limit, $W_{\rm thin}$, as the sum of the instrumental FWHM, the thermal velocity and the non-thermal velocity using Eq. 3.7. We know that the lines are in fact not optically thin and so are broader than this limit. An opacity broadening factor (see e.g Rathore et al. 2015; Hacar et al. 2016) that describes ratio of the observed FWHM of the h & k lines, $W_{\rm obs}$, to the FWHM calculated using the optically thin assumption:

$$O_{\rm b} = \frac{W_{\rm obs}}{W_{\rm thin}} = \frac{W_{\rm obs}}{\sqrt{W_{\rm inst}^2 + 4\ln 2\left(\frac{\lambda}{\rm c}\right)^2 ({\rm v}_{\rm th}^2 + {\rm v}_{\rm nth}^2)}}, \tag{3.8}$$

where in our case the non-thermal velocity, $v_{\rm nth}$, was derived from O I observations as described above, the thermal velocity was 3 km s^{-1}, and the instrumental FWHM was 0.052Å. This ratio was calculated for several representative k-line profiles along slit positions 5 & 6 from one exposure at flare peak, yielding opacity broadening factors in the range $O_{\rm b} \sim 2.5-5.7$. It is stressed that this factor should only be interpreted as showing that flare-related opacity effects are likely to be an important reason for broadening during the flare, and that the values of $O_{\rm b}$ here were calculated assuming the non-thermal velocity derived from the O I line. Opacity broadening has been noted as the cause of excess line width for the C II multiplet (Rathore et al. 2015) as well as the width of Mg II resonance lines in plage (Carlsson et al. 2015).

Opacity broadening is not a process like stark broadening or thermal broadening where the energy of an emitted photon is changed, but is more a description of how the line's source function varies with height. The reason for opacity broadening is as follows. Optically thick lines form at various heights in the atmosphere, with the emergent intensity at each wavelength across the line originating from the height at which the wavelength dependent optical depth is unity ($\tau_\nu = 1$). The combination of the opacity of the atmosphere and the behaviour of the source function with height in the atmosphere (related to temperature and density) determines the intensity at

a particular frequency across the line. A line will appear comparatively broader if the difference between the source function of the line core and line wings is reduced. This might occur if the source function at the height of the line wing formation is increased (for example due to higher temperatures) and/or if the opacity is increased such that the $\tau_\nu = 1$ layer for the line wings forms higher than it did in the non-flaring atmosphere.

3.6.3.3 Line Asymmetry

A visual inspection of the line profiles during the flare showed that many appeared asymmetric, with a wider blue wing compared to the red wing (relative to the line centroid). Some pre-flare profiles showed asymmetries in the red wing (wider red wing). There were also profiles that showed a fairly jagged or 'bumpy' line wings. To get a sense of the overall line asymmetry the metric $S = \frac{(Q_3-Q_2)-(Q_2-Q_1)}{Q_3-Q_1}$ was used as a measure of the asymmetry relative to line centroid. Positive values of S would suggest a larger red wing, and negative values would suggest a larger blue wing. Figure 3.31 shows the k-line asymmetry at different times during the flare. Contours of 40%, 60% & 80% of the k-line intensity are overlaid.

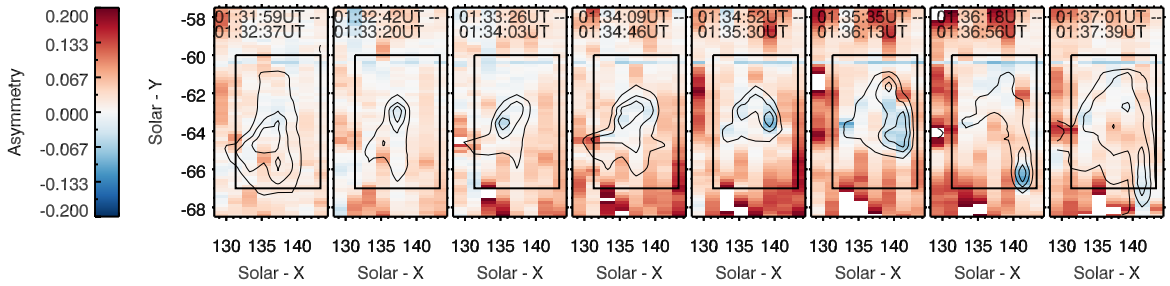

Figure 3.31: *Maps showing the asymmetry of the k-line from the quartiles analysis, were blue (negative) means a stronger blue wing, and red (positive) means a stronger red wing. A box highlights the flare ribbon, and the contours of* 40%, 60% *&* 80% *k-line intensity are overlaid. These maps use the* 25%, 50% *and* 75% *quartiles to measure asymmetry.*

The area surrounding the flare contained a red asymmetry (recall that the plage profiles in Fig 3.12 had a larger red wing compared to the quiet Sun). During the flare (mainly around t =01:35-01:37 UT) there was a clear blue asymmetry co-spatial

with the outer edge of the ribbon and high intensity emission. The blue asymmetry varies spatially and strengthens a little with time before peaking and then decaying quickly. It is interesting to note that the profiles show the strongest blue asymmetry co-spatial with the strongest downflow locations. In the final two panels patches of red asymmetry are present where some pixels are in their decay phase. Here, the line centroid shift has reduced but the red wing remains extended, which could indicate that the redshift has propagated past the formation height of the line core.

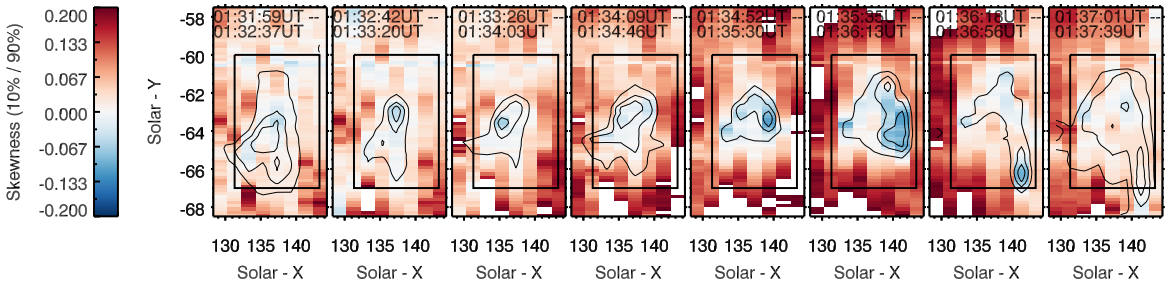

Figure 3.32: *Same as Figure 3.31 but these maps use the* 10%, 50% *and* 90% *quantiles to measure asymmetry.*

Profiles flagged as being strongly blue asymmetric are those that seemed to have the 'shoulder' feature in the blue wing. It is speculated, then, that the profiles shown as being blue asymmetric using quartiles (which are co-spatial with only the strongest intensity and strongest downflows), are profiles that have a clear secondary component to the emergent intensity. This secondary component would be formed deeper, at a height where the atmosphere has a lower velocity, and so the emission from the secondary component is not shifted as strongly as the main component. So, the line would appear with a shifted core of higher intensity (the 'main component') blended with a less intense secondary component who's blue wing appears to produce a shoulder or extended blue wing to the main component. Overall, the line would appear to have a larger blue wing than red wing, and would show a blue asymmetry. The more shifted the main component is, the more separated from the secondary component it is, and so the blue wing appears to extend further. Observations of the Mg II subordinate lines and the Fe II line during one flare have shown two distinct components (Graham et al. 2016). This could be an extreme case of what is observed here where the main component is formed in a region of atmosphere moving so fast that it is sufficiently shifted so as to appear separate from the secondary component

(note that those lines are not as broad as the h & k lines so it may be easier to observe such a separation).

In other profiles, where the downflows at the core formation height are smaller, the blue asymmetry is weaker or absent, because it is more difficult to discern this secondary component when the 'main component' is less shifted. If different quantiles are used that sample further into the line wings (and therefore deeper into the atmosphere), for example the 10th and 90th percentiles which are shown in Figure 3.32, then the blue asymmetry is indeed present in a greater number of flaring pixels, particularly near the peak of the Mg II emission (the panels showing 01:34:53 – 01:35:30 UT & 01:35:35 – 01:36:13 UT).

3.6.3.4 Comparing Velocities derived via Quartiles or Bisectors

Previous studies of optically thick lines have used different methods to identify the Doppler velocity of the line. Historically the bisector method has been used to infer chromospheric flows using H α flare observations (e.g. Zarro et al. 1988; Ding et al. 1995). Recently Graham & Cauzzi (2015) used line bisectors to analyse flare observations of the Mg II 2791.6Å subordinate line. In this section the values of line centroid velocity found via the quartiles method are compared to those found using the bisectors method.

Line bisectors are constructed by identifying the intensity at various fractions of the peak intensity. The wavelength midpoint between the two line wings at each intensity fraction is the line bisector. Figure 3.33(a,c) show two examples of a k-line near flare peak, where the 10 – 90 % line bisectors are shown as coloured boxes. Choosing a percentage level at which to define the line shift is somewhat ambiguous, since each bisector level is effectively sampling a different layer of the chromsophere. Graham & Cauzzi (2015) chose the 30% level for the 2791.6 Å line, though in their study the redshifts appeared as asymmetries in the red wing, not as a shift of the line as a whole. The 30% level, therefore, was necessary to sample the velocity shift of the wings. In the flare presented here, however, the whole line appears shifted in the rise and peak phase, and it is only in the decay phase that flows only present in the red wings. Choosing 30% might underestimate the velocity here.

Figure 3.33(b,d) show the resulting Doppler shift of each of the bisectors in each profile, where colour indicates the percentage level. It is clear in both panels that the various bisectors follow the same trends but with different magnitudes of velocity.

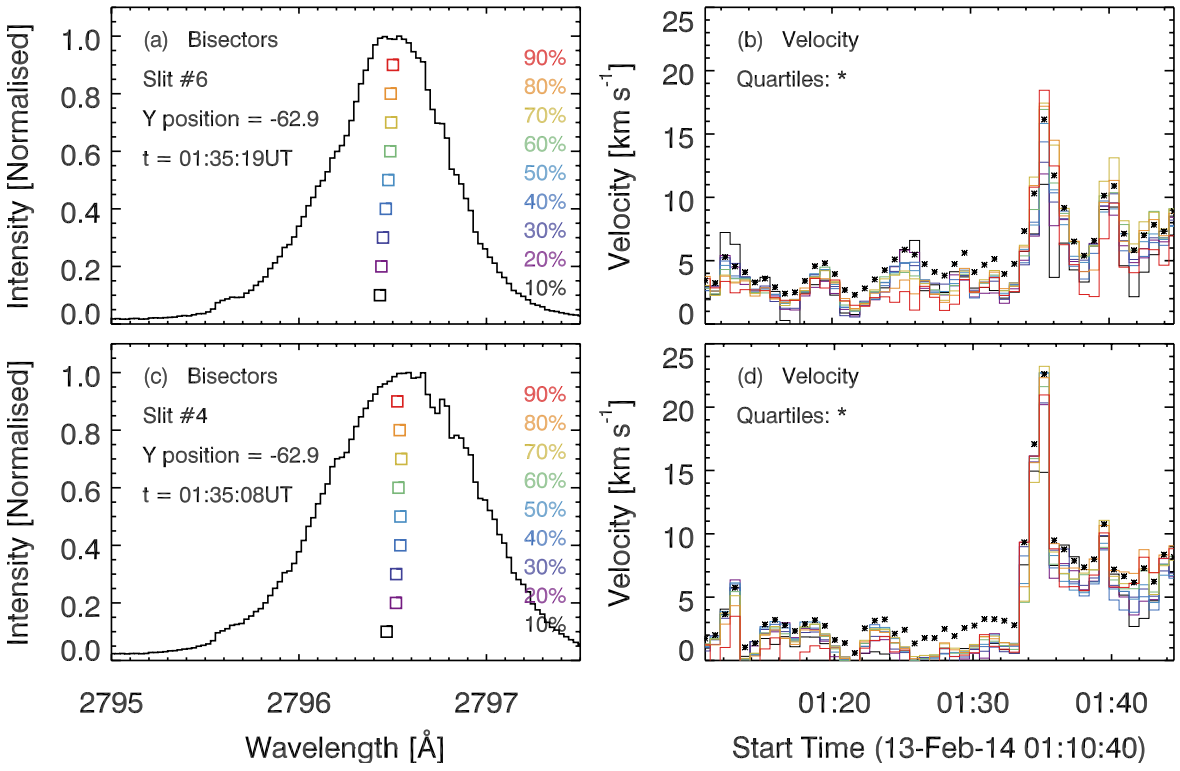

Figure 3.33: *Panels (a) & (c) show the wavelength positions for the line bisectors as coloured squares, overlaid on normalised k-line profiles, at the time, slit position and y-position labelled on each panel. Panels (b) & (d) show the velocity derived from each bisector as a function of time, where the colour indicated the percentage of each bisector. The line centroid velocities derived from quartiles are shown as black stars.*

The difference between the bisectors ranges $\sim 2-4$ km s^{-1} in the pre-flare, to as much as ~ 9 km s^{-1} at flare peak. At flare peak the $70-90\%$ bisectors show the largest shifts. Overlaying the values derived from quartiles as black stars shows that in the pre-flare phase the quartiles follow the same trends but are systematically larger by a small amount, ranging from $\sim 0-4$ km s^{-1}. At flare peak and in the decay phase, however, the quartiles reflect the mid-range of the various bisector levels. From these two pixels, as well as a larger sampling of other pixels from slit positions 6 & 7, suggests that at flare peak and decay the quartiles derived velocity is most similar to the $30-60\%$ bisector level. Given the inherent ambiguity of deriving velocity from optically thick lines the small differences between these two methods are not significant.

Comparing maps of velocity derived from each of the bisector levels to the

quartiles velocity map in Figure 3.27 confirmed that the 30 – 60% bisectors were a good match both spatially and in magnitude to the quartiles. Bisectors < 30% tended to only reveal the strongest sources, and > 60% the velocity magnitude was higher.

The shape of the bisector curve for each profile can provide an estimate of the gradient of the velocity flow since different layers are being sampled. For example, the profiles in Figure 3.33 is showing a bisector curve where the velocity is generally decreasing with depth into the atmosphere, suggesting that the magnitude of the downflow is decreasing. For some profiles in the cooling phase the bisector curve shows the opposite gradient, suggesting that the downflow has reduced in strength at the top of the atmosphere, and increases with greater depth. In such profiles, the red wing shows asymmetries while the line as a whole does not appear strongly shifted.

3.7 Summary and Conclusions

High spatial and spectral resolution IRIS observations of the NUV Mg II spectra from a moderately strong M1.8 class solar flare were analysed, with IRIS/SJI images, SDO/AIA images, and RHESSI HXR observations providing context to the Mg II data.

It has been demonstrated that the Mg II h & k lines, and the subordinate triplet lines, during flares show a clear response to the flare energy input. This response was co-spatial and co-temporal with the other UV enhancements. RHESSI observations showed that this was a largely thermal event, with 6 – 9 keV footpoint sources that were spatially associated with the flare sources. Several pre-flare X-ray peaks were observed, with associated brightening in both the EUV and UV images (spatially and temporally). Hard X-ray counts above 20 keV were relatively weak, and non-thermal sources only spatially associated with the flare ribbons for a short time (in one image).

The spatial and temporal evolution of the Mg II spectra during the flare showed intense, spatially localised energy input, with variations on scales of ~ 0.5" (note that the IRIS spatial resolution for the NUV is 0.4"). In particular it was found that the flare resulted in the following:

1. The central reversal is mostly absent in pre-flare and flare profiles. The line can appear jagged or show multiple small peaks, in some flare profiles, likely a result of variations in the behaviour of the frequency dependent source function with height.

2. Despite the lack of a central reversal the k:h ratio is lower than 2 in flare profiles, meaning that the lines are still optically thick. The k:h ratio seems to tend towards a common value of $R_{\mathrm{k:h}} \sim 1.15 - 1.18$, with a particularly noticeable decrease in the spread of values of $R_{\mathrm{k:h}}$ in two slit positions.

3. There is evidence of a slow onset of excitation lasting up to a few minutes before the flare. This is present in intensity lightcurves, line centroid velocity and line width.

4. Line centroids were redshifted, with an equivalent velocity of $\sim 15 - 25$ km s^{-1}. Doppler shifts decayed quickly, dropping significantly within one 43 s timeframe. Typically the shifts dropped to pre-flare levels with 3-4 minutes. In the decay phase the line wings were red asymmetric in some pixels, suggesting downflows persisted to deeper layers. Maps showed that the highest velocities were presents along the intense outer edge of the ribbon, with the velocity magnitude somewhat correlated to intensity.

5. The lines were significantly broader during the flare, with $W = Q_3 - Q_1$ increasing from $W \sim 0.25 - 0.28$Å in the pre-flare to $W \sim 0.45 - 0.55$Å during the flare. Enhanced widths persisted longer than the velocity shifts. It was estimated that opacity broadening (resulting from the behaviour of the opacity structure and source function as a function of height) increased the width between 2.5-5.7 times the optically thin thermally broadened limit. Increased opacity broadening leading to broad line wings indicates that flare heating was felt deep in the atmosphere, and/or the $\tau_\nu = 1$ layer (the height from which each frequency across the line is emitted) was increased so that line wings form higher than in the pre-flare atmosphere.

6. In the most intense pixels, with strongest equivalent velocities, there are clear blue asymmetries identified using the metric $S = \frac{(Q_3 - Q_2) - (Q_2 - Q_1)}{Q_3 - Q_1}$. Sampling further into the wing (using different quantile values) reveals blue asymmetries are also present in less intense profiles. It was speculated that this blue asymmetry results from a secondary component that is either unshifted or shifted to a lesser extent than the main component. In the decay phase a red asymmetry is present which could indicate that the chromospheric condensation has propagated deeper into the atmosphere (lower than the core formation height) so

that the flows only affect the line wings.

The central reversal feature is almost ubiquitous in the quiet Sun yet the profiles are mostly single peaked in the flare (and pre-flare). This behaviour has been seen in sunspot umbrae and the plage in previous observations, as well as observations of flares (Lemaire et al. 1984; Liu et al. 2015; Matthews et al. 2015).

Optically thick line formation requires NLTE radiative transfer to fully interpret the emergent profiles, but some qualitative statements can be made about the single peaked appearance of the profiles from observations alone (see Chapter 4 for a discussion of synthetic Mg II profiles from a flare simulation). In the quiet Sun the central reversal is produced because source function has a maximum in the mid-chromosphere resulting in the emission peaks, and then decreases with height to the formation layer of the line core, so that the emergent intensity is smaller. The source function is decreasing since by this point it has decoupled from the local radiation field (the Planck function) and does not reflect the chromospheric temperature rise as strongly. To produce the weakly reversed or flat-topped profiles observed in the flare, the source function cannot vary significantly between the formation height of the emission peaks and the core, so that the emergent intensity difference is reduced. To produce a single-peaked profile, the source function must be increasing with height to at least the formation height of the line core. This does not preclude local maxima below the core formation height that could result in some of the structure in the line core or wings - any local maxima or minima would affect the emergent intensity of the line.

It seems reasonable that the height range over which the usual k2 and k3 components are formed is reduced, so that the source function difference is smaller, and that the source function behaviour with height is different from in the quiet Sun. Both of these situations may be explained by the temperature and density changes associated with the flare. An increase in temperature and density will affect the ratio of Mg II/Mg II, changing the opacity structure of the atmosphere. An increase in electron density can increase the coupling to the Planck function so that the source function reflects the local temperature to a greater extent. This means that not only will the source function increase with height through the chromosphere, but it will reflect the enhanced temperature resulting from the flare.

Previous observations of flares using the Ca II H & K lines have shown that the line cores can go into emission (e.g Lemaire et al. 1984). Following the theoretical work

of Jefferies & Thomas (1960) and Athay & Skumanich (1968), McKim Malville et al. (1968) used a simplified conceptual model of a source function which is independent of frequency (complete redistribution) to show that an increase in electron density or temperature could account for these observations. They argued that the assumption of CRD is approximately valid over the core of the resonance lines, within ~ 3 Doppler widths of the line core. Writing the frequency independent part of the source function as

$$S = (1 - \epsilon')\bar{J} + \epsilon' B_\nu(T) \tag{3.9}$$

where $\bar{J}$ is the frequency-averaged mean intensity, and $B_\nu(T)$ is the Planck function. The probabilty of a collisional destruction of a photon per scattering is $\epsilon = C/A$, so that $\epsilon' = \epsilon/(1+\epsilon) = C/(A+C)$ is the photon destruction probabilty. If ϵ were to increase due to increased electron density ($C \propto n_e$) then ϵ' gets closer to unity and the source function could be more coupled to the background temperature due to the greater contribution of $B(T)$. Thus a density increase during the flare could result in a source function that increases with height as it follows the local temperature increases more strongly.

This is, of course, an oversimplification but recent modelling work does support this idea. Only one RHD flare model in which synthetic Mg II h & k were computed has been published, by Rubio da Costa et al. (2016) (though see also Chapter 4 in this thesis). These synthetic flare profiles showed central reversals unless the electron density in the Mg II formation region was artificially increased to $> 10^{14}$ cm^{-3}. When this was done the lines did become single peaked (though the resultant effects on the hydrodynamics or other synthetic radiation was not reported). Additionally, in a study where the Mg II 2791.6Å subordinate line was modelled, Pereira et al. (2015) found that these lines were in emission when the source function increased with height. This happened when there is a high temperature gradient of ≥ 1500 K between the TMR and the line formation region *and* when the line source function is more strongly coupled to the local temperature (so that if reflects this gradient). Pereira et al. (2015) note that while stronger coupling can result from many factors, they found that an enhanced electron density resulted in the tightest coupling. During the flare the subordinate lines were in emission. If it assumed that they are formed at a similar height as in the quiet Sun then this could suggest flare heating to deep layers. However, it is possible that they are formed higher in the atmosphere.

Finally, a note of caution is needed when interpreting the results of redshifts and asymmetries. The analysis would suggest a downflow at the peak of the flare that is relatively short lived. It remains to be seen from modelling if the velocity of the line centroid matches the atmospheric velocity at the formation height in flares (as it does in the quiet Sun). Asymmetries suggest that a secondary unshifted or less shifted component is present. Also, in the cooling phase while the line core redshift decreases quickly the red wing is extended suggesting that the downflow has propagated deeper. This interpretation of a chromospheric downflow is similar to the conclusions of other authors who have noted redshifts in optically thick lines. They support the theoretical predictions of a short-lived chromospheric condensation resulting from pressure increase in flares (Fisher 1989; Allred et al. 2005) when sufficient energy is deposited in the chromosphere. The fact that there is potentially a secondary component might at times result in an underestimation of the line centroid velocity, as it would in effect be measuring some averaged velocity of the two components (weighted by their relative strength).

However, modelling of downflows in optically thick lines has revealed some ambiguity in the interpretation of redshifts and asymmetries (see a review by Berlicki 2007). Gan et al. (1993) modelled H α in flares with condensations finding that both the red and blue asymmetries can result from condensations (depending on the temperature structure). Heinzel et al. (1994) found in a simulation of H α line profiles in a flare that the blue asymmetry observed at the start of the flare, before the impulsive peak, was actually a signature of *downward* propagating plasma near the transition region that preferentially absorbed red wing photons, making the blue wing appear more extended. This was short-lived and only a feature when return currents were included with the non-thermal electron beam. Similar results were found by Kuridze et al. (2015) who studied H α with the `RADYN` code. They found that velocity gradients can shift the absorption profile of the line, introducing asymmetries in the opposite sense than expected (downflows resulting in blue asymmetry).

It is worth noting that for the Mg II h & observations presented that the whole line appeared shifted at flare peak; it was not just red wing asymmetries that suggested a downflow. Additionally, the blue wing asymmetry was observed at flare peak, not at the onset as discussed in Heinzel et al. (1994). Finally, the Doppler core of H α is wider than Mg II (~ 12.8 km s^{-1} compared to ~ 2.6 km s^{-1} at $T = 10^3$ K). Therefore the absorption profile of Mg II is smaller and when shifted will probably not result

in such strong effects as seen in H α. Modelling is required to shed light on this.

Chapter 4

Mg II Flare Modelling

4.1 Introduction to Mg II Modelling

The Mg II h & k lines have been recognised as important for many decades, due to their strength and due to the fact that they carry information from multiple layers in the solar atmosphere. Opacity varies as a function of wavelength, so different wavelengths across the line profile reach optical depth unity at different geometric heights in the atmosphere (e.g Athay & Skumanich 1968). Since Mg has a large abundance (7.6 on the logarithmic abundance scale Asplund et al. 2009), and exists in the singly ionised state through the chromosphere, the h & k lines a high opacity and form over a large geometric height range. They can probe conditions from the upper chromosphere (the line core) down to the temperature minimum region (the minima and outer line wings). In order to understand observations and use these lines to test atmospheric models, numerical experiments have been performed since the early 1970s, ranging from basic formation properties, building semi-empirical atmospheres to developing detailed diagnostics of the quiet Sun. For example, Lemaire & Skumanich (1973) compared rocket borne observations to the synthetic spectra produced by model atmosphere in an effort to assess the temperature and density structure of those atmospheres.

Early modelling work was performed using basic atomic models and the simplifying assumption of complete redistribution (CRD). However, in a series of papers, beginning with Milkey & Mihalas (1973), it was shown that for lines with strong opacity that formed high in the atmosphere, CRD was not sufficient, and instead coherence between the absorbed and emitted photons must be considered. In combi-

nation with new observations of the solar chromosphere, this series of investigations included the modelling of the h & k lines (Milkey & Mihalas 1974) using partial redistribution (PRD).

As a reminder, CRD is a simplification in radiation transfer that says an absorbed photon is re-emitted at a wavelength that is not correlated to the original wavelength. The emission profile is therefore equal to the absorption profile, and the line source function is independent of frequency. Line core photons can be more easily scattered into the wings where they can escape due to the lower opacity at line wing wavelengths. This is suitable for certain lines, but for lines with high line core opacity that are formed high in the atmosphere (for example the resonance lines of single ionised magnesium and calcium), CRD is not valid. For these lines the low density in the chromosphere is not sufficient for collisions to remove the coherence of absorbed and emitted photons, since the lines can radiatively de-excite before collisions take place, meaning that fewer photons are scattered into the line wings. Coherence must be taken into account, so that partial redistribution modelling is required (see Uitenbroek 2001, and references therein for in-depth discussions). The redistribution function used in PRD modelling allows a fraction of coherence that is proportional to atmospheric conditions via the elastic collisional rate to the line's upper levels (Hubený 1982; Uitenbroek 1989). Conceptually, the formation is the same as in the CRD case, in the sense that different line components are formed at different heights according to the line opacity as a function of wavelength, but in the PRD scenario the source function *is* frequency dependent and, crucially, different wavelengths across the line decouple from local conditions at different heights. As Milkey et al. (1975) point out, not only did PRD provide a better match to the observations of the h & k lines, it provided an explanation for the centre-to-limb behaviour observed in the Ca II H & K lines (Shine et al. 1975).

Milkey & Mihalas (1974) showed that the relative wavelength positions and intensity of the k1/h1 minima were closer to observations when modelled using PRD, than when CRD was assumed, but that the modelled intensity did not match observed intensity. This was attributed to a lack of certainty in the atomic data, in particular the van der Waals broadening - increased damping by collisions reduces the coherency fraction so that the line source function thermalises in a different location and may reflect the local temperature more strongly (that is to say, the line source function will be closer to the Planck function). Of course, the model atmosphere employed

also has a large effect on the output spectra. In fact one of the most important uses of the h & k lines (often in conjunction with the somewhat weaker Ca II H & K lines) was to test model atmospheres by comparing to observations. Following advances in the computational treatment of PRD, and increased confidence in the relevant atomic data, Ayres & Linsky (1976) used a range of semi-empirical model atmospheres to produce Ca II and Mg II resonance line spectra, noting predicted minima intensities were systematically lower than expected from observations by a factor 2 or more. Radiative equilibrium model atmospheres with larger temperatures in the temperature minimum region ($T \approx 4450$ K compared to $T \approx 4150$ K), however, produced line profiles with minima intensities that more closely resembled observations.

Simultaneous observations of Ca II H & K, Mg II h & k, and H I Lyα & Lyβ from the OSO-8 satellite were used by Lemaire et al. (1981) and Lemaire & Gouttebroze (1983) to build semi-empirical model atmospheres for plage. It was found that while reasonable agreement between observed and synthesised profiles for the Ca II and H I were achieved, the plage models were unable to produce adequate Mg II profiles. Synthetic h & k spectra were largely the correct shape, but with central reversals deeper than observations and integrated intensities much lower than observed (by a factor of two). It was noted in their plage models that the chromosphere was compressed, with the result that the source function minimum shifted to greater geometrical depth and flattened. Line wings were enhanced by the temperature rise located deeper in the atmosphere and the central reversal was shallower than in quiet Sun simulations. Emission peak separation was seen to decrease. Asymmetries between the h & k line emission peaks are common in certain sources (e.g. the internetwork), with the strength varying with spatial location. Static atmospheres were unable to reproduce the red-blue asymmetry (Gouttebroze 1989), and so experiments with introducing velocity gradients or acoustic waves were performed (Gouttebroze 1977, 1989), showing that flows in the atmosphere do result in asymmetric peak intensity.

In preparation for the observations of Mg II h & k from IRIS, Leenaarts et al. (2013a,b) & Pereira et al. (2013) revisited the quiet Sun formation of these lines using state-of-the-art simulations, in an effort to not only assess model atmospheres but forward model the synthetic spectra and build diagnostics from the observables. Using a snapshot from the 3D radiation magnethydrodynamics (RMHD) numerical code, *Bifrost* (Gudiksen et al. 2011), the formation properties were studied in 1D

PRD using RH (by inputing each column as a 1D plane-parallel atmosphere), and in 3D CRD using *Multi3d* (Leenaarts & Carlsson 2009). Since the k-line has twice the opacity of the h-line it forms higher in the atmosphere (by a few ×10 km). The upper levels of both lines were populated via cascades from excited layers, followed by radiative de-excitation to the ground state as part of an ionisation/recombination loop. PRD modelling was found to be required to correctly describe the line wings and emission peaks, but the cores were well described by CRD. Additionally, since the lines are strongly scattering and dominated by radiation, their source functions are influenced by the radiation field. If the typical photon mean free path is comparable or larger than the scale length of horizontal inhomogeneities then horizontal radiation transfer effects are important and act to smooth out the line source functions. Studying these 3D effects using CRD (3D PRD calculations are still a significant computational challenge) found that the wings, minima and emission peaks were only 'marginally' affected by 3D radiation transfer, but that the line cores are'strongly' affected (Leenaarts et al. 2013a).

Several useful diagnostics were noted by Leenaarts et al. (2013b) & Pereira et al. (2013). The Doppler shift of the k3 and h3 components was tightly correlated with atmospheric velocity at their formation height (the correlation coefficient was 0.99). Since they are formed a few tens of km apart the difference in the k3 and h3 Doppler shift is an indication of the velocity gradient in the upper atmosphere. The difference in line core Doppler shift was well correlated with the difference in atmospheric velocity at the core formation heights (with a correlation coefficient of 0.8). The sign of the velocity gradient in the mid-chromosphere can be ascertained from the emission peak separation, and the intensity of the emission peaks provides a reasonable measure of the temperature at their formation height (with gas temperature ~ 500 K lower than the radiation temperature of the emission peaks). Leenaarts et al. (2013b) pointed out that their simulated spectra were too narrow (with a base width k1v-k1r $\sim 1-1.5$Å from observations compared to ~ 0.5Å from the simulations, and a smaller FWHM in the simulations) suggesting that the simulation underestimated the lower and mid-chromospheric temperature.

Observed plage profiles are more intense and broad than their quiet Sun counterparts and either single peaked, flat-topped or show a shallow reversal. Carlsson et al. (2015) noted that plage profiles in the region they studied had a $1/e$ width distribution with a mean around 30 km s^{-1} where as the quiet Sun profiles had a mean

around 20 km s^{-1}. Similarly, the radiation temperature of the k2 emission peaks in the plage was a distribution centred around 6400 K, compared to ~ 5200 K for the quiet Sun. By experimenting with a semi-empirical plage model, Carlsson et al. (2015) found that increasing the temperature of the chromospheric plateau widened the profiles, while increasing microturbulence increased the width of the core. When the chromospheric temperature rise was located deeper in the atmosphere (at larger column depth) then the profiles were wider. A hotter and denser chromosphere resulted in stronger coupling to the source function and single peaked or flat-topped profiles.

While Mg II has been investigated in quiet Sun and plage model atmospheres, the flaring scenario has been studied much less. Avrett et al. (1986) presented a study of the continua and many spectral lines including Mg II k using three semi-empirical flaring model atmospheres, including the strong flare F2 model of Machado et al. (1980). While they did not provide a detailed insight to the formation of Mg II during flares, the results were interesting in showing that a flare atmosphere with deeper transition region and steeper chromospheric temperature rise (increasing from the TMR to TR temperatures over a height of ~ 1000 km compared to ~ 1300 km) produced single peaked profiles, similar to recent plage models. Lemaire et al. (1984) also used semi-empirical model atmospheres, finding that when comparing to their Mg II flare observations the F1 model underestimated the integrated intensity. They concluded that a smaller temperature slope to the transition region would be required to be consistent with observations. More recently, Liu et al. (2015) presented some preliminary modelling results using the semi-empirical F2 model, and the grid of flare models of Ricchiazzi & Canfield (1983). These models are 1D static models of chromospheres heated by electron beams. Liu et al. (2015) found that a smaller spectral index of $\delta = 3$ (i.e. deeper heating) resulted in more intense line wings, and that the line core was affected by coronal pressure, with larger pressure (~ 100 dyne cm^{-3}) acting to fill in the central reversal. Finally, Rubio da Costa et al. (2016) used `RADYN` and `RH` to simulate flare heating of multiple atmospheric elements for a time that depended on analysis of RHESSI HXR lightcurves. They did not go into detail regarding the Mg II formation, but noted that while profiles had a similar core intensity to observations, they failed to reproduce the strong line wings. In order to reproduce the single peaked appearance of the observations, the electron density was artificially raised by about an order of magnitude to 10^{14} cm^{-3} at the Mg II line

formation region. While this was instructive in showing that enhanced electron density strengthened the coupling to the background temperature, the effects of this on the formation of other lines produced, and on the dynamics was not discussed.

It is clear that we possess a good understanding of the general behaviour of these lines in the non-flaring chromosphere, but in comparison knowledge of the flaring case is rather limited. Flares are extreme environments and having access to new diagnostics of the temperature and velocity structure of the chromosphere during a flare would be very useful. Testing models of energy transport in flares by comparing the synthetic Mg II spectra to observations is also crucial. This chapter describes the initial experiments to model Mg II in flares, focussing both on the detailed line formation, as well as what the lines can tell us about the flaring atmosphere.

4.2 RH and Flares

Since RH has not historically been used for flare studies (with the exception of the recent work by Kowalski et al. 2015; Rubio da Costa et al. 2016) it was important to ensure that the correct set up was employed before studying the Mg II formation in depth. These were to test if an atom that is large enough to include the effects of Lyβ pumping as a population pathway for the h & k upper levels was required, and to ascertain which PRD scheme could be employed (the full angle dependent or the Hybrid PRD scheme). It is also noted here that we are ignoring 3D effects both in the radiative transfer and in the atmospheric model used.

4.2.1 Lyβ Pumping of Mg II

In their studies of Mg II h & k and subordinate lines in the quiet Sun Leenaarts et al. (2013a,b); Pereira et al. (2013, 2015) used a 10 level plus continuum Mg II model atom. This atom was shown to be large enough to capture the ionisation-recombination loop that populates the h & k upper levels.

This model atom does not include the $5p^2\ P_{(\frac{1}{2},\frac{3}{2})}$ levels, which allow a possible route to populating the h & k upper levels via Lyβ pumping. This mechanism was suggested by Lemaire et al. (1981) as a potential explanation for the mismatch between the Mg II h & k line observations and their computed spectra (see also Bruhweiler et al. 1982, for the stellar case). Their simulations sought to create an

atmospheric model for plage by iterating the solution to match observations of Ca II H & K, H I Lyα & Lyβ and Mg II h & k from the OSO-8/LPSP spectrometer. The plage model successfully reproduced observations of Ca II and H I but failed to capture the correct intensity of the Mg II h & k lines. A possible reason for this, suggested by the authors, was that cascades through excited energy levels above the h & k upper levels could offer additional pathways to to populating those levels. One of these excited levels, $5p^2\ P_{\frac{1}{2}}$, has a transition wavelength to the ground state of 1025.97 Å (in air). This is only ~0.24Å redward of the Lyβ line core wavelength, and so absorption of Lyβ wing photons could lead to excitations from the Mg II ground state to the $5p^2\ P_{\frac{1}{2}}$ level. Though not discussed by Lemaire et al. (1981), the $5p^2\ P_{\frac{3}{2}}$ level, which has a wavelength of 1026.11Å for transitions between the ground state (~ 0.38 Å into the red wing of Lyβ), could also be populated in this way. Electrons populating the $5p^2\ P$ levels would then cascade down to the h & k upper levels. However, later investigations using a larger model atom that accounted for Lyβ fluorescence found that in actuality this mechanism is not significant for populating the Mg II resonance line upper levels (Lemaire & Gouttebroze 1983). While noting that the emergent profiles were unaffected in plage, and speculating that even the larger flux of Lyβ in flares would likely not have a significant effect, it is a worthwhile experiment to check the conclusion of Lemaire & Gouttebroze (1983) in the flare scenario. Note that Leenaarts et al. (2013a) confirm the result that Lyβ pumping has a negligible effect on quiet-Sun populations and profiles.

For the flare case a series of snapshots from a RADYN atmosphere were used as input atmospheres to RH. This particular simulation was provided by Dr J. Allred (*private communication*, 2015), and is discussed in more detail later in this chapter (the 'reference flare simulation'). For now it is simply noted that this model was of a strong flare (energy flux injected was $F = 1 \times 10^{11}$ erg s^{-1} cm^{-2} for 20s) so that any effects of Lyβ pumping would be pronounced. Snapshots were made at $t = [10, 20, 22, 25, 40]$ s into the simulation. Synthetic spectra were produced using two 21 level plus continuum Mg II atoms: one with Lyβ fluorescence to the $5p^2\ P$ levels switched on, and one where this transition was not included. This 21 level plus continuum atom was provided by Dr Jorrit Leenaarts, and was created using the HAO-Diper[1] package of Dr Phil Judge. This model atom contains 53 transitions when including the Lyβ pumping pathway, and 51 when omitting this pathway. The

[1] http://www.hao.ucar.edu/modeling/haos-diper/

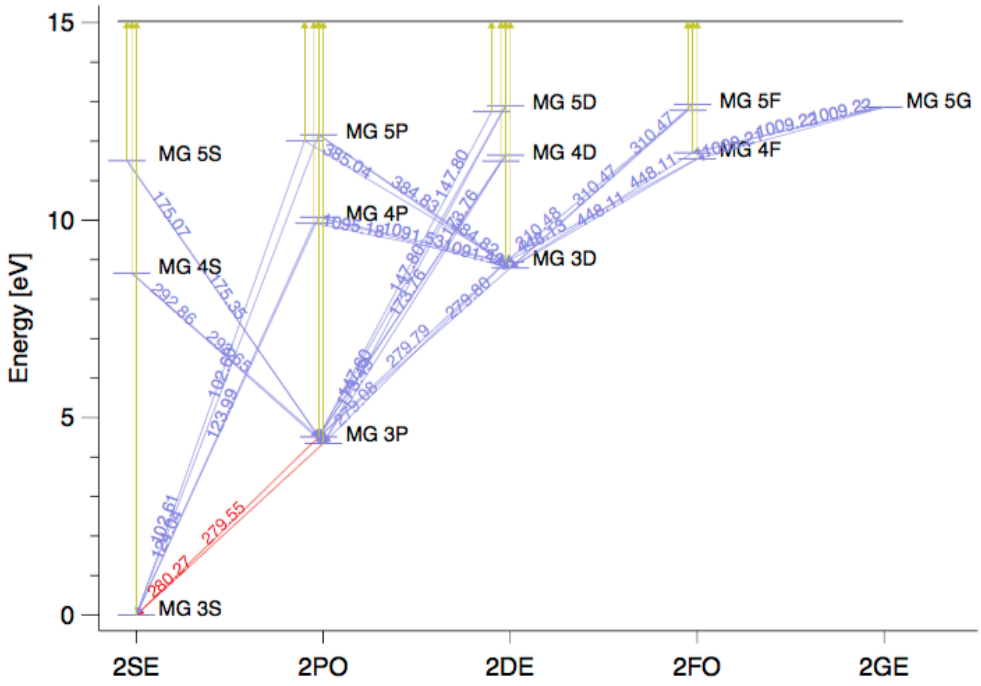

Figure 4.1: *Mg* II *model term diagram, with the resonance lines highlighted in red. The Ly* β *pumping transitions are the* $3s - 5p$ *transitions.*

term diagram is shown in Figure 4.1, where the h & k lines are highlighted in red.

Figure 4.2 shows the results of including Lyβ pumping during flares. In the first column is the percentage increase in the populations of $5p^2\ P_{\frac{1}{2}}$ (black line) & $5p^2\ P_{\frac{3}{2}}$ (green line) when Lyβ pumping is allowed. In the other two columns show the emergent h & k line profiles are shown, where the black line is the profile computed with the effect of Lyβ and the orange line is the profile omitting Lyβ pumping. The rows are different times in the simulation, as indicated. During the flare, when the Lyβ flux is enhanced, there is indeed a greater population of the $5p^5P$ levels above a height of 0.92 Mm, but a decrease below. This has a negligible affect on the emergent intensity of the h & k lines, however. Intensity is slightly greater in both the core and k2 peaks to a varying degree over the line profile and over time, when Lyβ pumping is included. Typically this difference is small in the line wings (> 0.5Å from line core), and in the range $\sim 0 - 3\%$ closer to line core. During the heating phase of the flare, the difference is greatest around the k2 emission peaks. In the cooling phase the

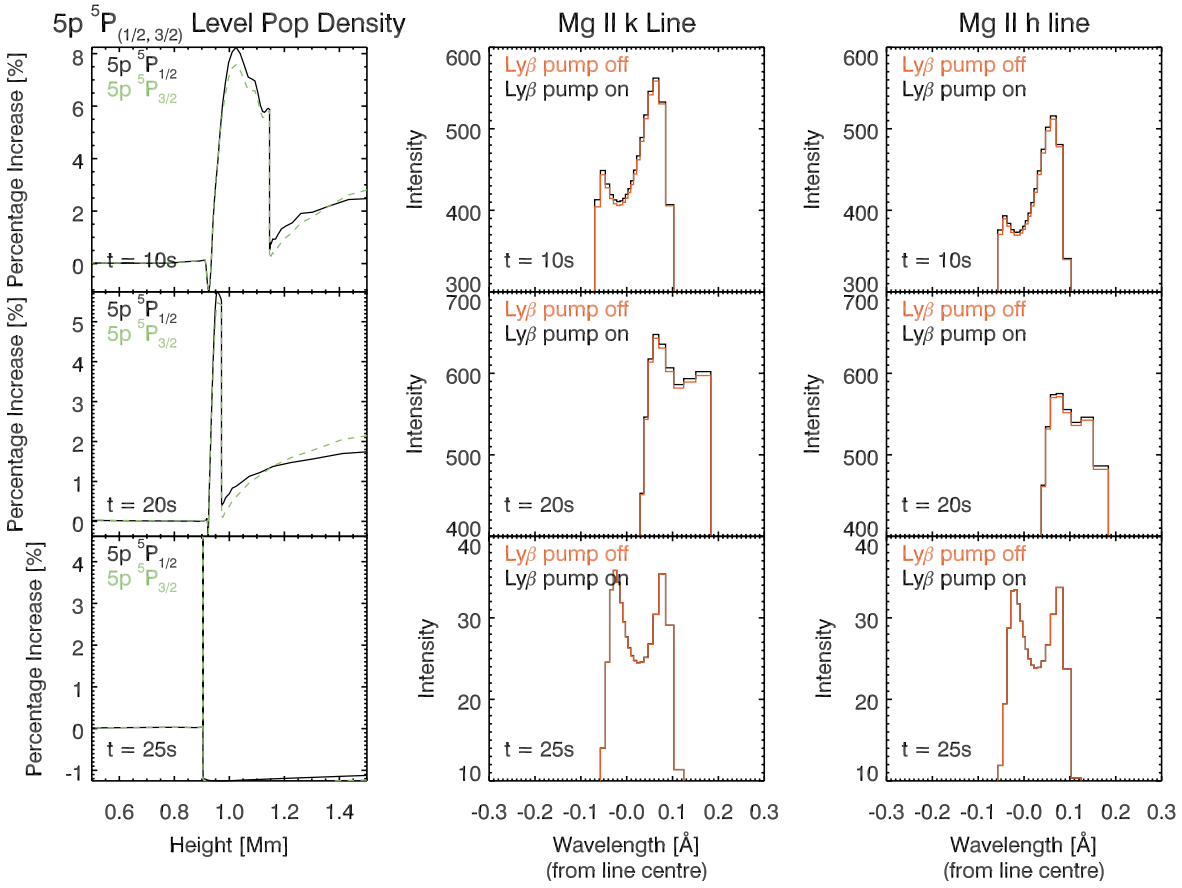

Figure 4.2: *The effect of including Lyβ pumping from the ground state to $5p^5P$ levels at $t = 10,\ 20$ & 25 s into a flare simulation, indicated in the bottom right corner of each panel. In the first column the percentage increase in populations for each of the levels in the case of including Lyβ pumping($5p^5P_{1/2}$ in black, and $5p^5P_{3/2}$ in green). The other two columns show the h & k line profiles, where black lines are when pumping is included and orange is when it is omitted.*

difference is much reduced and less than $\sim 1\%$ in line core. The effect of including Lyβ pumping is negligible for the purposes of the study here since other assumptions (namely the absence of 3D radiation transfer) are likely to be more important.

Leenaarts et al. (2013a) show the emergent intensity from the FALC semi-emprical atmosphere (Fontenla et al. 1993) using the 10 level plus continuum Mg II, where the k2 peak intensity is $I_{k2} = 2.3 \times 10^{-9}$ J s^{-1} m^{-2} sr^{-1} Hz^{-1}. This experiment was reproduced here, and compared to the effect of including a larger number of levels in the Mg II model atom. The result of this comparison is shown in Figure 4.3(a,b) for the FALC atmosphere & F2 atmosphere respectively. Recall that the FALC atmosphere is

a semi-empirical quiet chromosphere, and F2 is a semi-empirical flare atmosphere. These synthetic spectra are symmetrical about the line core due to the absence of flows in these model atmospheres.

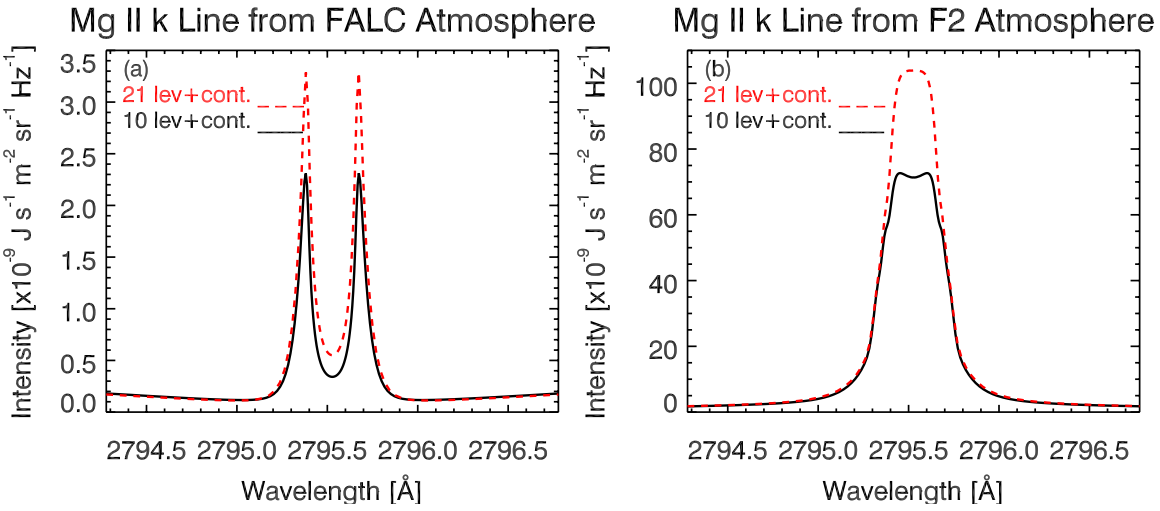

Figure 4.3: *The differences in k-line emergent intensity between using the 10 level plus continuum (black line) and the 21 level plus continuum (red, dotted line) Mg II model atom. Panel (a) shows the effect when using the FALC semi-empirical atmosphere, and panel (b) the F2 semi-empirical atmosphere.*

The larger model atom produced more intense k2 peaks than the 11 level plus continuum model atom ($I_{k2} = 3.2 \times 10^{-9}$ J s^{-1} m^{-2} sr^{-1} Hz^{-1}). Additionally, in the F2 flare atmosphere the core intensity was larger when using the 21 level plus continuum model atom. So, while Lyβ pumping was not very important, the larger atom was used anyway. The computation time when using the large atom with the Lyβ transitions is not terribly greater than omitting them (approximately 2 minutes), and is small compared with the effect of including additional active elements. Therefore for the numerical experiments discussed from this point forward, the 21 level plus continuum model atom, including the $3s - 5p$ transition, was used.

4.2.2 Complete or Partial Redistribution?

As mentioned previously, PRD was found to be an important consideration for the study of Mg II line profiles in the quiet Sun due to the low density of the chromosphere. During flares the density and temperature structure of the atmosphere can

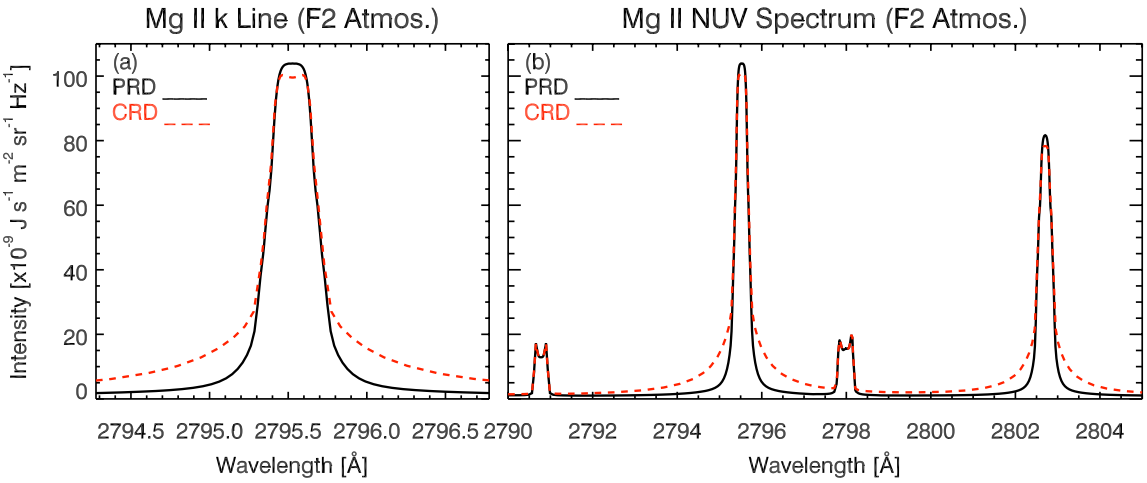

Figure 4.4: *Illustrating the requirement for PRD when computing synthetic Mg* II *spectra. This example uses the F2 semi-empirical flare atmosphere. In panel (a) the k line is shown, and in panel (b) a wider view of the Mg* II *NUV spectra. In both the black line is when PRD is assumed, and the red dotted line is when CRD is assumed.*

change significantly, and collisional rates could increase enough such that complete redistribution is no longer so bad an assumption. Using the same RADYN snapshots from the previous section, the RH experiments were re-run with Mg II h & k computed assuming CRD. This was also done for the F2 semi-empirical flare atmosphere. Figure 4.4 shows the spectrum computed from the F2 model atmosphere with the assumption of either CRD or PRD. It is clear that in this particular atmosphere the number of collisions is still not large enough to allow the assumption of CRD. The line core is not affected as strongly as the inner wings, which show a substantial difference. This is similar to quiet Sun simulations of both Mg II h & k and Ca II H & K, where the line cores showed modest differences compared to the k1 components and inner wings (Milkey & Mihalas 1974; Leenaarts et al. 2013a; Uitenbroek 2002, e.g.).

The more realistic RADYN flare atmospheres show that CRD is still not adequate for the inner wings even with the enhanced density and temperature compared to the F2 atmosphere. Figure 4.5 shows Mg II spectra from three snapshots of a RADYN simulation processed through RH. Again red dotted lines show profiles assuming CRD and black solid lines the profiles when PRD is used. While it appears that the core is in better agreement, this is a product of the high intensity line core, but zooming in on the line wings shows a discrepancy in the inner wings, which are

still a few $\times 10^{-9}$ J s^{-1} cm^{-2} sr^{-1} Hz^{-1} more intense when using CRD. Because CRD cannot adequately describe the line wings, PRD was used for the research presented here.

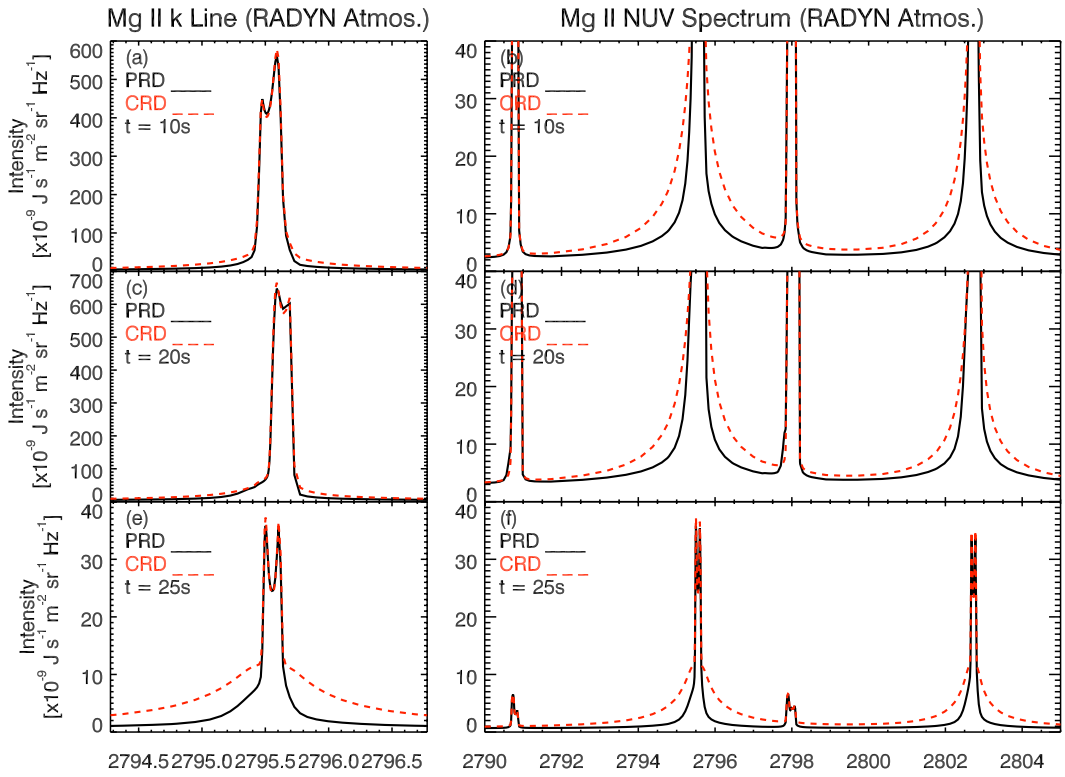

Figure 4.5: *Illustrating the requirement for PRD when computing synthetic Mg* II *spectra. This example uses the RADYN snapshots. In panels (a),(c),(e) the k line is shown, and in panel (b),(d),(f) a wider view of the Mg* II *NUV spectra. In both the black line is when PRD is assumed, and the red dotted line is when CRD is assumed. Snapshot times are indicated on each panel.*

4.2.3 PRD Angle Dependence in Flare Simulations

In the development of PRD in RH, Uitenbroek (2001) allowed simplifications to remove the angular dependence, reducing the computational cost (a common feature of PRD numerical codes). For atmospheres in which there are no macroscopic flows, the absorption profile is no longer a function of angle, and if it is also assumed that the radiation field is isotropic then the expression for the ratio ρ can be much

simpler to evaluate. This is the angle-averaged PRD scheme. It approximates the full angle-dependent case well when used appropriately (i.e. a static atmosphere), as shown by, e.g. Milkey et al. (1975) and Uitenbroek (2002). Typically this means that velocities should be smaller than the thermal speed due to the way in which Doppler shifts are treated in the angle-averaged scheme. Uitenbroek (2002) demonstrated that for the Ca II H & K lines there was almost no difference in line formation when using RH with either angle-averaged or full angle-dependent PRD in the static FALC atmosphere. The small differences present on the order of a few percent, were found to be due to the increase in probability of scattering a photon vertically where it is easier to escape, as opposed to shallower angles, resulting from removing the assumption of isotropic radiation.

As mentioned by Uitenbroek (2002) and Leenaarts et al. (2012), when macroscopic velocities exceed the Doppler velocity the full angle-dependent PRD scheme must be employed, since the assumption of an isotropic radiation field is no longer valid. Additionally, the absorption profile can no longer be considered independent of angle. Using the full angle-dependent PRD for multiple active atoms in a flare simulation is substantially more time intensive (recall that 'active atoms' are those for which RH solves the detailed RT). Fortunately, Leenaarts et al. (2012) developed a fast approximation to full angle-dependent PRD for atmospheres containing macroscopic velocity flows. This is known as the Hybrid PRD scheme. It was shown to save significantly on computational time, and to output solutions that are close to full angle-dependent PRD (and certainly better than the angle-averaged PRD). This scheme works by recognising that the main difference between profiles computed using angle-averaged PRD compared to full angle-dependent PRD is due to the absorption profile of a moving element receiving incoming Doppler-shifted rays from different directions (and that the radiation anisotropy is a minor contribution). Therefore, the simpler angle-averaged treatment of the redistribution can be maintained, with the addition of transforming the radiation field from the rest frame from the observer to that of the moving element. This in effect means that the radiation can again be considered isotropic. Then the ratio ρ_r computed from the moving element's rest frame can be transformed back into the observer's rest frame to recover the emission profile. Leenaarts et al. (2012) found good agreement between the full angle-dependent and Hybrid PRD schemes, noting a saving of time of two orders of magnitude when using the Hybrid PRD scheme.

Obviously, it would be advantageous to use the quick, yet accurate, Hybrid PRD scheme for investigating Mg II formation from RADYN snapshots, particularly if including a number of active elements. Leenaarts et al. (2012) demonstrated the close agreement for velocities of magnitude a few km s^{-1}, but since a flare atmosphere can contain upflows of hundreds of km s^{-1} and downflows of several tens of km s^{-1}, it was necessary to confirm that the Hybrid PRD scheme was suitable for use in flares. Again using the set of RAYDN snapshots from previously, the emergent profiles of Mg II h & k computed using full angle-dependent PRD and the Hybrid PRD approach were compared and shown in Figure 4.6.

The comparison of emergent intensity profiles indicate only small departures from the full angle dependent PRD solution (shown for near vertical rays here, but similar for other viewing angles). Small differences will arise due to not fully accounting for radiation anisotropy but these differences are tolerable given the computation time saved. Additionally, while the source functions show some differences above the $\tau = 1$ height, most of the line contribution comes from around the $\tau_\nu = 1$ surface since they are optically thick lines. The $\tau_\nu = 1$ height of the wavelengths shown in the right hand column of Figure 4.6 are close in each PRD scheme.

For these experiments (where only H and Mg II were included in the active set) computation times for the full angle-dependent PRD computations were around, $t \approx 12500$ s per snapshot, whereas the computation time for the Hybrid PRD scheme was a much lower at $t \approx 200$ s. If more species are included in the active set then run times increase substantially (it is desirable to have more atoms in the active set so that formation properties of other spectral lines can be investigated at a later date without having to rerun simulations, and to better account for background opacity). Given the small difference in emergent profiles, and significant saving in computation time the Hybrid PRD scheme was utilised for the investigation of Mg II in flare atmospheres. A cautionary note, however, is that if studying a future simulation that contains a much higher velocity in the formation region of Mg II, then this test should be performed again.

4.2.4 Statistical Equilibrium Assumption

As discussed in § 2.1.2.3, using statistical equilibrium and ignoring the history of the atmosphere can lead to discrepancies in the population densities of atomic states.

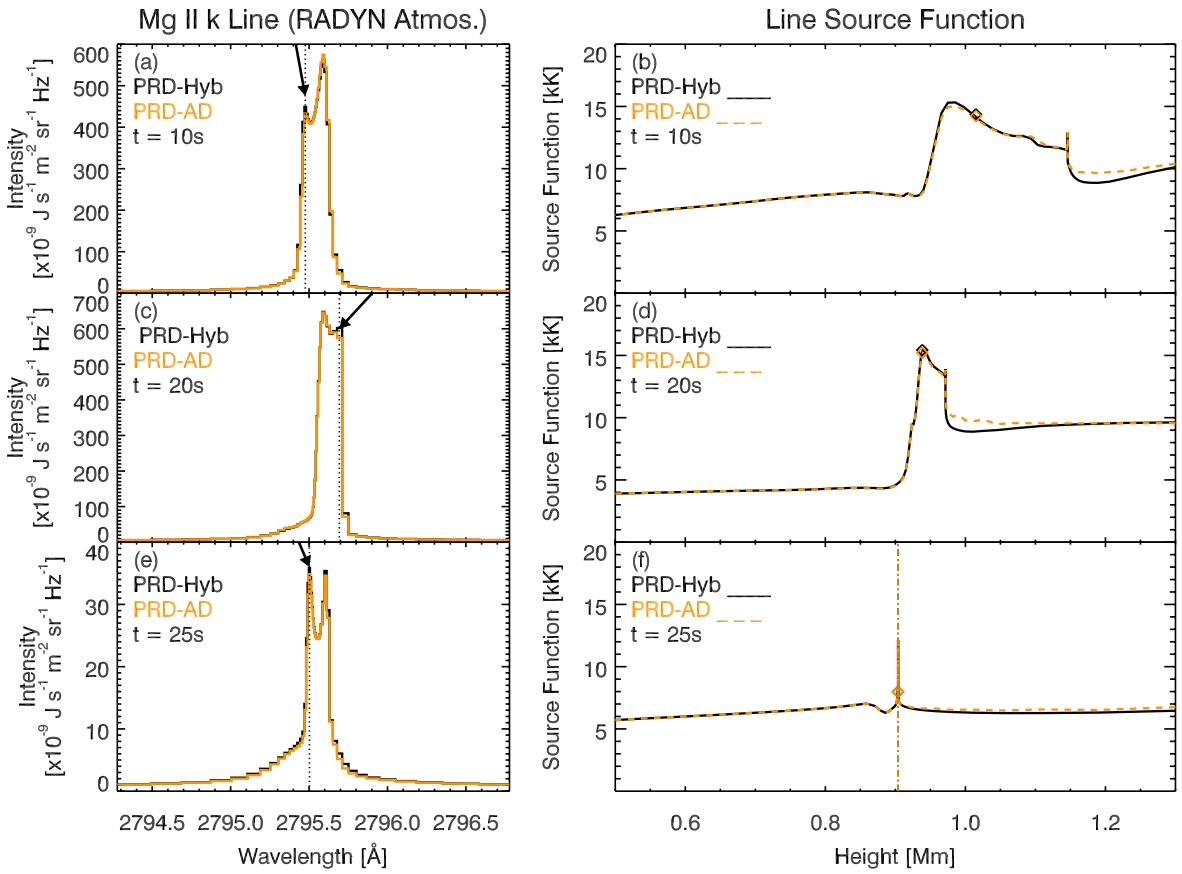

Figure 4.6: *Demonstrating the suitability of using the Hybrid PRD scheme in a RADYN flare atmosphere. In panels (a),(c),(e) the k line is shown, and in panel (b),(d),(f) the source functions of the wavelengths indicated by an arrow in the left hand columns. In both the orange line is when full angle-dependent PRD is used, and the black line is when the Hybrid PRD scheme is used. Diamonds show the $\tau = 1$ height for the wavelength plotted. The source functions are in units of radiation temperature. Snapshot times are indicated on each panel.*

The effects of this assumption on hydrogen, and the effects on the output Mg II k line profiles were investigated by comparing two simulations: one where hydrogen was assumed to be in statistical equilibrium, and one in which the RADYN hydrogen populations where used RH.

A RADYN flare simulation was processed through RH in which hydrogen was included in the active set, and the population levels computed by RH using statistical equilibrium (this flare simulation is the 'reference flare simulation' discussed later in this chapter). Comparing the ionisation fraction computed by RADYN to the ionisation

fraction computed by RH showed that, indeed, ignoring the history of the atmosphere led to some discrepancies where there were differences during the flare of $\sim 1.5 - 5\times$ the ionisation fraction. These were larger during the decay phase of the flare where differences could be larger than an order of magnitude. Comparing Hα line profiles from each simulation showed that while there was around a $10 - 15\%$ difference in the intensity of the line core, the profile shape and evolution was the same in both simulations. This result is consistent with Kowalski et al. (2015) who state that they found "satisfactory agreement" when comparing Balmer lines and continua that overlap in the RADYN and RH results.

The flare simulation was re-processed through RH, but with hydrogen set to be a passive element. With this setup the hydrogen populations output from the RADYN atmosphere were used in RH. Comparing the Mg II k-line profiles from each of the RH simulations showed little difference. Some intensity differences were present across the line profile but these were typically small and less than 5%, and there was no difference in the overall line shape.

So, while the hydrogen ionisation fraction from assuming statistical equilibrium differs from the non-equilibrium ionisation result, RH is still useful in studying the hydrogen lines if PRD is required, for example the Lyα line. Including hydrogen as an active element does not significantly affect the Mg II lines.

Leenaarts et al. (2013a) believe that statistical equilibrium is appropriate for magnesium, in the quiet Sun, noting that when the temperature is large enough to produce a significant fraction of Mg III the relaxation time is short. During flares the electron density is increased, which would further reduce the relaxation time. This is evidenced by the fact that the discrepancy in the hydrogen ionisation fraction between statistical equilibrium and non-equilibrium ionisation was smaller in the flare simulation than in the simulations reported by Carlsson & Stein (2002) where differences could be larger than two orders of magnitude. In fact, in the shocks present in the simulations of Carlsson & Stein (2002) the statistical equilibrium solution approached the non-equilibrium ionisation solution. However, since flare dynamic effects occur on short timescales, particularly following initial energy deposition, there is still the possibility that in the early stages of the flare statistical equilibrium is not appropriate.

4.3 Mg II Formation Properties in a Solar Flare

Before studying a specific simulated flare (which can be compared to observations), the formation properties of Mg II were studied in a 'reference flare simulation'. The RADYN simulation used here was provided by Dr. J. Allred (this simulation was also used by Kuridze et al. 2015) but the analysis of this simulation, the production of synthetic spectra using RH and the analysis of those spectra were performed by me. Snapshots of this flare atmosphere were produced for each second of simulation time, and RH used to compute the resulting Mg II spectra.

4.3.1 RADYN Simulation Description

The initial atmosphere was the QS.SL.HT radiative equilibrium atmosphere (described in Chapter 2 and in Allred et al. 2015). This atmosphere has a loop length of 10 Mm, a coronal temperature of 3 MK, and the coronal electron density was 6×10^9 cm^{-3}. As usual, non-radiative heating was applied to grid cells with column mass less that 1×10^{-6} g cm^{-2} and greater than 7.6 g cm^{-2}, to maintain energy balance in the corona and photosphere respectively. A reflecting boundary in the corona (loop top) models incoming waves from the other half of the loop. The boundary in the sub-photosphere is transmitting.

This simulation used the Fokker-Planck treatment of non-thermal electron beam energy transport (Allred et al. 2015), with heating applied for 20 s followed by relaxation for 40 s. The beam energy flux was 1×10^{11} erg s^{-1} cm^{-2} (usually referred to as F11 in the RADYN literature), with a spectral index $\delta = 4.2$ and low energy cutoff $E_c = 25$ keV. The temperature, electron density, velocity and column mass structure of the atmosphere is shown as a function of time during the heating phase in Figure 4.7 and during the cooling phase in Figure 4.8. Note that upflows are negative velocities, that in both figures colour represents time, and that in both figures the dashed lines show the $t = 0$ s state.

In this simulation the energy deposition peaks around 1 Mm initially before slowly moving higher in the atmosphere to roughly 1.2 Mm by $t = 10$ s. Although the peak of the energy deposition is over a narrow layer in the mid-chromosphere, a tail extends into the corona and down into the lower atmosphere. Temperature increases occur quickly at locations where radiation losses are unable to balance energy depo-

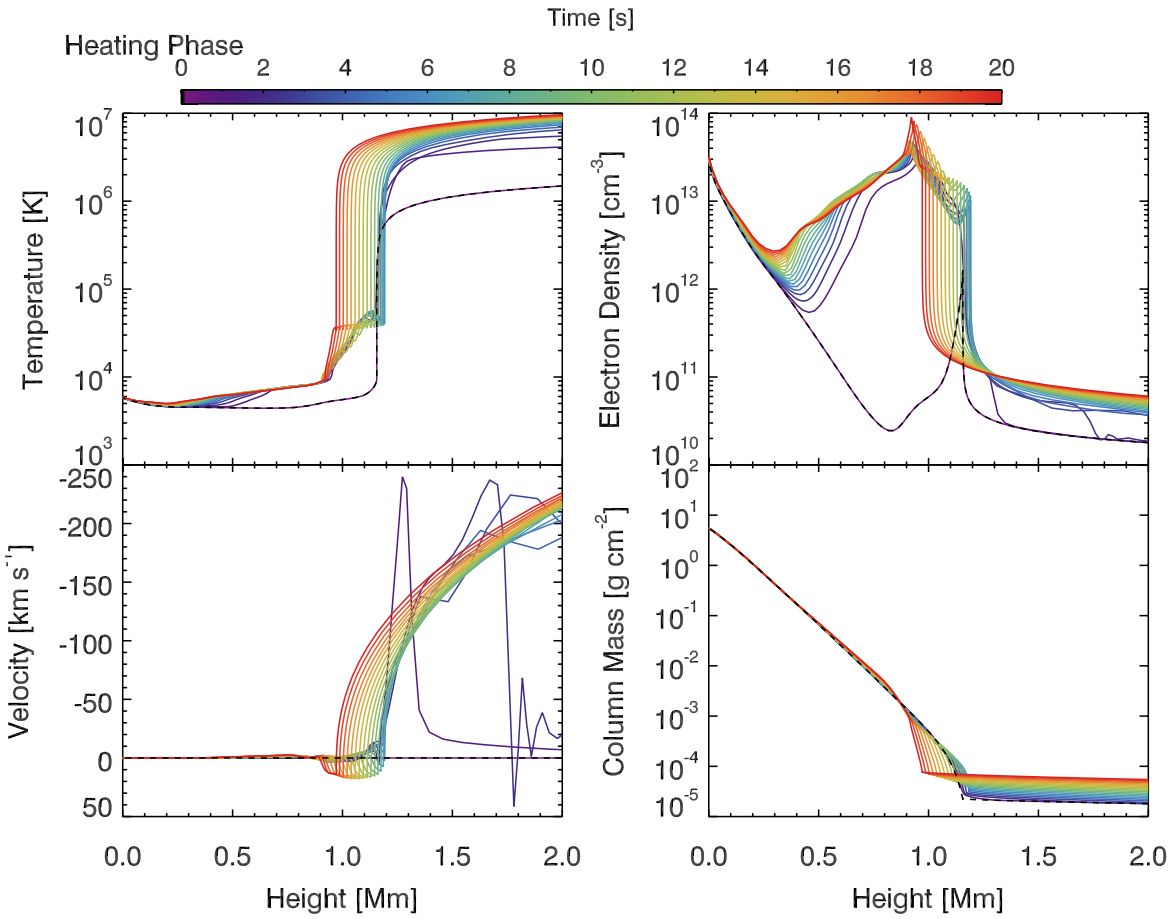

Figure 4.7: *The atmospheric evolution of the RADYN reference flare simulation described in § 4.3. Colour represents time and the dotted line is the equilibrium starting solution ($t = 0$ s). Top left panel shows the temperature, top right shows the electron density, the bottom left shows velocity (upflow is negative) and the bottom right shows column mass.*

sition, with the corona showing a several MK increase. In the mid-chromosphere a temperature plateau exists between $\approx 0.5 - 1$ Mm, where temperatures increase by $3000 - 4000$ K. Between $\approx 1 - 1.2$ Mm temperatures increase over a small distance from $T \sim 7500$ K to $T > 50,000$ K, and a small bubble forms, above which is a local temperature minimum, before temperatures climb through the transition region to over $T > 100,000$ K. Radiative losses at this local temperature minimum increase such that it becomes deeper and the transition region moves somewhat higher in the atmosphere (by a few tens of km) at $t = 7$ s. At locations of temperature enhancement, ionisation results in increased electron density (as does non-thermal

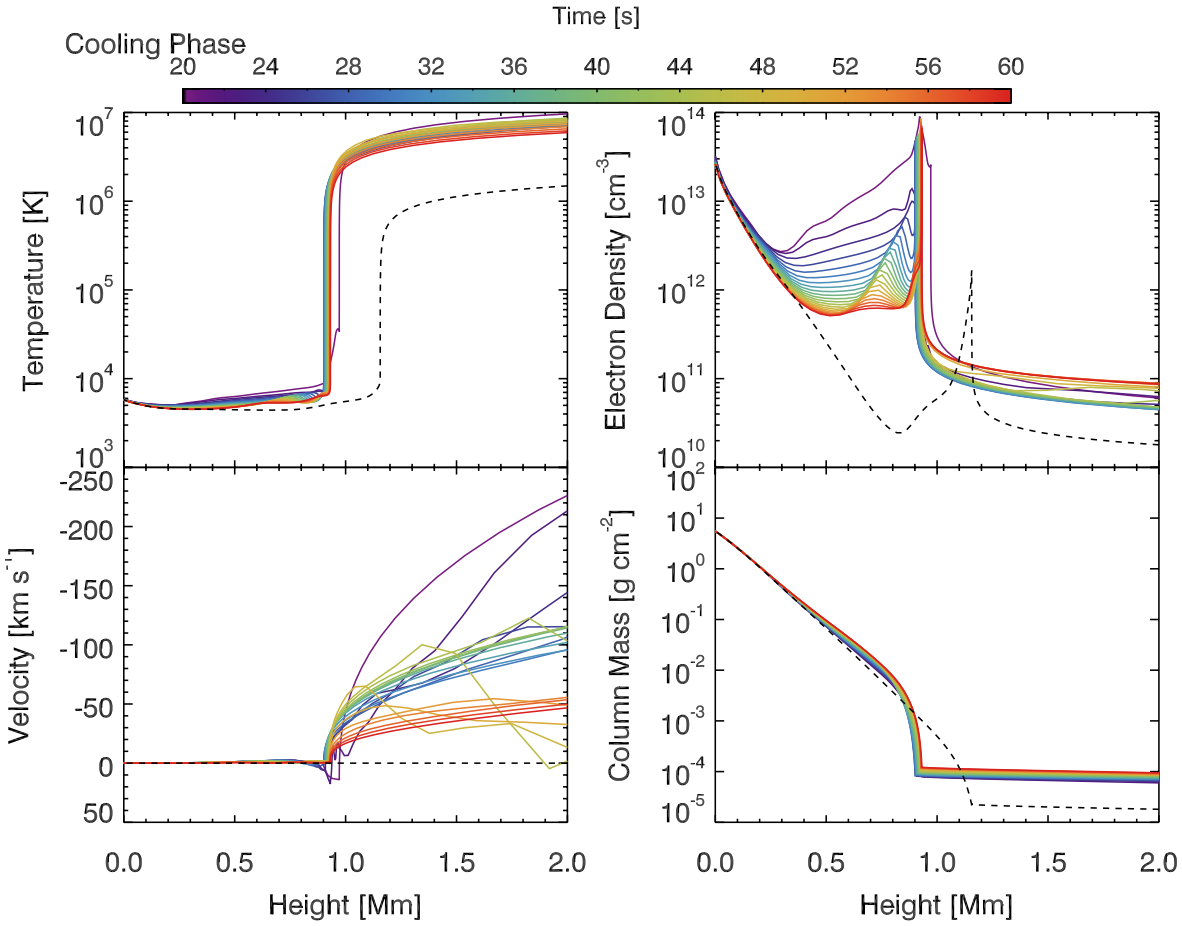

Figure 4.8: *Same as in Figure 4.7, but showing the cooling phase of the simulation ($t = [20 - 60]$ s). The dotted line is the equilibrium starting solution ($t = 0$ s).*

collisional ionisation from the beam). Between 0.5 – 1.2 Mm the electron density has increased by orders of magnitude from $\sim 2 \times 10^{10}$ cm^{-3} to $> \times 10^{13}$ cm^{-3} in some locations. At $t = 7$ s there is a peak of $\sim 3 \times 10^{13}$ cm^{-3} at 0.9 Mm. The pressure difference associated with temperature enhancements drives flows, including at the local temperature minimum, where material is driven away, decreasing the density. Fast upflows in excess of 225 km s^{-1} are present and a downflow of dense material travelling at a few $\times 10$ km s^{-1} originates from the small temperature bubble.

Mass motions changes the density structure of the atmosphere so that the beam energy deposition profile changes also. Between $t = 7 - 20$ s the chromosphere becomes compressed as the transition region moves deeper in the atmosphere. The temperature gradient joining the plateau in the lower chromosphere to the transition region steepens. The peak electron density is $\sim 9 \times 10^{13}$ cm^{-3} at a height of $\sim$

0.9 Mm. The column mass structure in the bottom right panel of Figure 4.7 shows the compression of the chromosphere towards the end of the heating phase. Below 0.9 Mm the column mass is slightly enhanced down to ~ 0.5 Mm.

Once flare energy deposition ceases, the plateau in the chromosphere slowly cools. A local temperature minimum forms at 0.9 Mm where radiative cooling is more effective. Recombination takes place and the electron density begins to drop quickly towards pre-flare levels. Strong upflows are still present, and towards the end of the simulation the upper atmosphere contains downflows due to the reflecting upper boundary condition. Though the chromosphere continues to cool, a temperature 'bump' is present that smooths as it propagates deeper. As a consequence the electron density structure also contains a local maximum as it returns to pre-flare levels. By the end of the simulation (t = 60 s) the atmosphere has not yet returned fully to the pre-flare state. Chromospheric temperatures are still enhanced by 1-2 thousand kelvin, and the corona has temperatures in excess of 5 MK. Additionally, the transition region is still in its new location deep in the atmosphere (< 1 Mm) so that the chromosphere is compressed. The column mass is thus greater at lower heights that in the pre-flare atmosphere. Since temperatures are greater in the chromosphere the electron density is still orders of magnitude greater than the pre-flare state in the locations of enhanced temperature, though much reduced from the flare peak values (now a few $\times 10^{11}$ cm^{-3}).

4.3.2 Mg II h & k Profiles

The Mg II h & k line profiles during the heating phase are shown in Figure 4.9 and Figure 4.10 shows profiles from the cooling phase. In both figures the h lines are shown in red and the k lines shown in black, with times indicated in the top left corner. The line intensity increases by over an order of magnitude from the quiet Sun values, with a typical value on the order of $I_\nu = 4.5 - 6 \times 10^{-7}$ J s^{-1} m^{-2} sr^{-1} Hz^{-1} in the line core (the k3 and k2 components plus near line wings). The profiles initially show a clear central reversal that is shallower than the quiet Sun several, with emission peaks that are largely symmetric about the line core. Over the course of the simulation the k2r peak becomes dominant, making the profiles asymmetric and the reversal becomes even more shallow until t = 9 s at which point the lines start become more symmetric. The intensity of the k2r component drops somewhat and

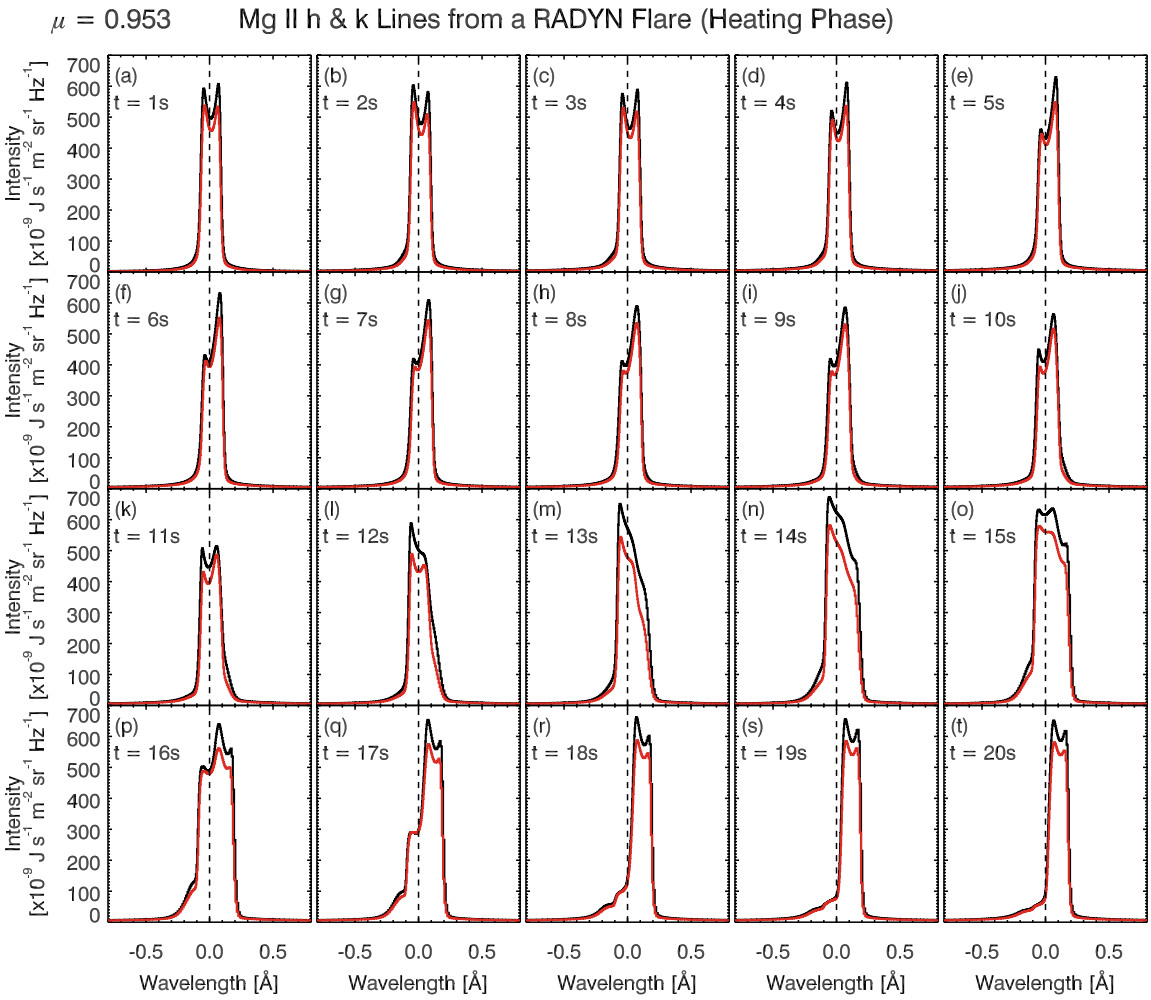

Figure 4.9: *The Mg II h & k line profiles (k line in black, h line in red), from the the reference flare simulation. These profiles are near vertical ($\mu = 0.953$) rays, and the vertical dashed lines show line centre. The wavelength scale is distance from line centre in angstroms ($\lambda_{\mathrm{k,rest}} = 2795.5276$ Å and $\lambda_{\mathrm{h,rest}} = 2802.7046$ Å). Simulation time is indicated in the top lefthand corner of each panel.*

the initially slightly redshifted core moves back to the rest position. From $t = 10$ s the line wings start showing some clear asymmetries and the line broadens further from a FWHM of ~ 0.17 Å to ~ 0.27Å (this is when the transition begins to move deeper into the atmosphere and stronger downflows are present). Though the core broadens, the wings are still narrow in comparison to flare observations.

At $t = 12$ s the k2v peak is now becoming dominant and the central reversal is not clearly visible over the subsequent seconds. The profiles begin to show a complex and at times multi-peaked core, with stronger asymmetries and shoulders

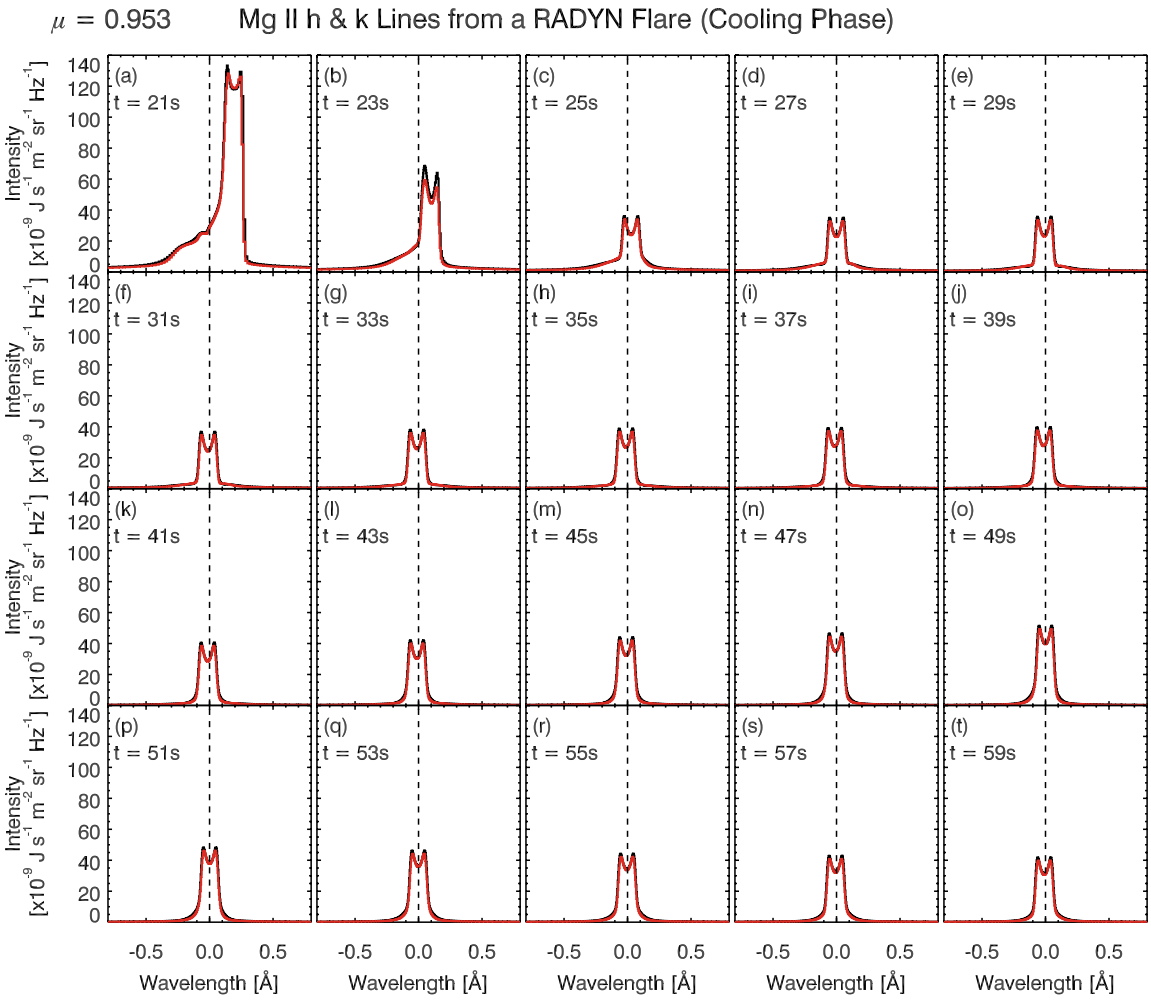

Figure 4.10: *Same as in Figure 4.9 but for the cooling phase of the simulation (no applied flare heating).*

in the line wings. Beginning at $t = 17$ s the blue wing falls sharply in intensity from $\sim 500 \times 10^9$ J s^{-1} m^{-2} sr^{-1} Hz^{-1} to $\sim 300 \times 10^9$ J s^{-1} m^{-2} sr^{-1} Hz^{-1}, creating a shoulder and a strongly redshifted line with a shallow central reversal. The blue wing continues to decrease in strength and the line narrows. By the end of the heating phase the asymmetry extends further into the blue wing and is of low intensity. The maximum specific intensity for the k-line occurs at $t = 14$ s with a value $I_{\nu,\mathrm{k}} = 6.72 \times 10^{-7}$ J s^{-1} m^{-2} sr^{-1} Hz^{-1}. However, for the h-line this occurs later at $t = 18$ s with a value $I_{\nu,\mathrm{h}} = 5.87 \times 10^{-7}$ J s^{-1} m^{-2} sr^{-1} Hz^{-1}. For the most part the h & k lines are similar in behaviour, with the k line more intense (as expected). There are a few times, however, when the profiles *do* show differences, mainly in the line wings - for example the red wings at $t = 14$ s.

In the cooling phase the intensity drops substantially, first to around $I_\nu \sim 1.2 \times 10^{-7}$ J s^{-1} m^{-2} sr^{-1} Hz^{-1}, before declining further to $I_\nu \sim 0.3 \times 10^{-7}$ J s^{-1} m^{-2} sr^{-1} Hz^{-1} where it remains for the rest of the simulation, with only small fluctuations. In the cooling phase the asymmetries disappear after a few seconds and the profiles appear largely symmetric about a centrally reversed core.

Lightcurves are shown in Figure 4.11, where solid curves are the k-line and dashed curves are the h-line. Integrating over $\lambda_{\rm rest} \pm 0.5$ Å in panel (b) shows that in addition to the initial large increase of the line intensity there is a second enhancement that begins at $t = 11$ s, peaking at $t = 15$ s. This is due to the increase in line width, not any substantial change to the line core intensity. The line width begins to decrease after this peak (with the line becoming quite asymmetric in the blue wing). An inset shows that the k line is always more intense than the h line, though the magnitude of the difference does vary.

Taking the theoretical line core to be the wavelength corresponding to the maximum height of the $\tau_\nu = 1$ curve, the lightcurves of the blue and red wings were computed, integrating the blue wing between $[\lambda_{\rm core} - 0.35$ Å , $\lambda_{\rm core}]$ and the red wing between $[\lambda_{\rm core}, \lambda_{\rm core} + 0.35$ Å$]$. These are shown in panel (b) where the red curves are the red wing, and blue curves are the blue wing. Initially the blue wing is more intense before being overtaken by the red wing at $t = 3$ s. This lasts until $t = 11$ s after which the blue wing is much stronger and dominates until flare heating ceases. Even in the cooling phase the stronger blue wing persists for several seconds (the profiles do show asymmetries even into the cooling phase, though weaker than at flare peak). Though the cooling phase does show some structure in the lightcurves, there are no notable asymmetries after $t \sim 30$ s.

Integrating $\lambda_{\rm core} \pm 0.1$ Å around the core gives the lightcurves shown in panel (c), where several interesting features are present. First, the intensity over the line core drops following the initial energy deposition (after 1 s). Second, the lightcurve includes a sharp decrease at $t = 11$ s for the k line and $t = 12$ s for the h line. Intensity then climbs to a peak that coincides with the end of flare energy deposition and decreases in the cooling phase. Third, the h & k lines have the usual pattern of stronger k line intensity, but they are out of step at times. This suggests that the core of the k line shifts to a region of lower intensity before the h line. The causes of this will be explored in the next section.

It is important to note that the intensity of the line cores is up to one order of

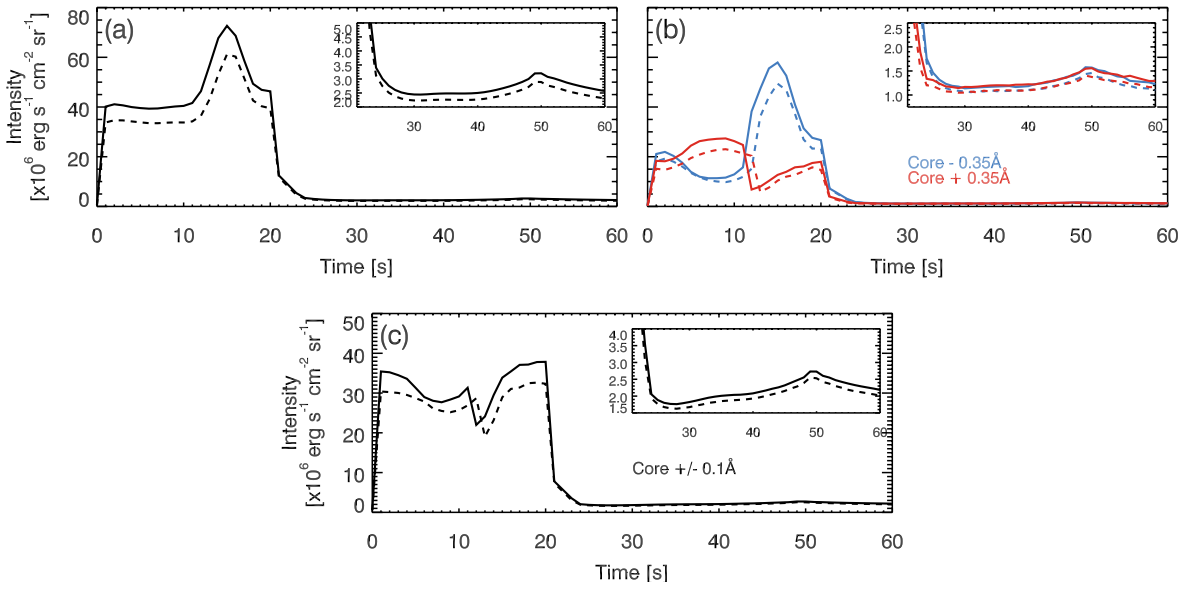

Figure 4.11: *Integrated intensity of the Mg II k line (solid) and h line (dashed). In panel (a) intensity is integrated over the whole line, $\lambda_{\text{rest}} \pm 0.5$ Å. In panel (b) the blue curves show the intensity integrated over $[\lambda_{\text{core}} - 0.35$ Å, $\lambda_{\text{core}}]$, and the red curves the intensity integrated over $[\lambda_{\text{core}}$, $\lambda_{\text{core}} + 0.35$ Å$]$. Panel (c) shows the intensity integrated over $\lambda_{\text{core}} \pm 0.1$ Å.*

magnitude larger than typical flare profiles observed by IRIS. This is true if using the 11 level model atom also. The typical simulated flare intensities are on the order $\sim 2 \times 10^8$ erg s^{-1} cm^{-2} sr^{-1} Å^{-1}, whereas the typical intensities observed in an X-class flare are on the order $\sim 5 \times 10^7$ erg s^{-1} cm^{-2} sr^{-1} Å^{-1} (e.g. Liu et al. 2015). This discrepancy will be investigated in future work. For now we can focus on the formation properties of the lines form in the simulated flare.

4.3.3 Mg II h & k Formation

The Mg II line profiles showed a complex response to the changing atmospheric conditions during the flare simulation. A very useful means to understand why the emergent profiles appear as they do is to use Eq 2.8 to study the contribution to the emergent intensity as a function of height in the atmosphere. Not only can we use the full integrand to determine where the intensity originates, we can decompose this equation to the constituent variables to understand the source function, and effect of opacity on the line formation.

To illustrate the following discussion several images will be shown using the four-panel representation of Eq 2.8 similar to that implemented by Carlsson & Stein (1994). In these figures, each panel contains a background image representing a constituent part of Eq 2.8, as indicated in the top left corner. The top left panel shows χ_ν/τ_ν. The top right shows the frequency dependent source function S_ν. The bottom left shows the attenuation by optical depth $\tau_\nu e^{-\tau_\nu/\nu}$ and the bottom right shows the contribution function, C_I. Within each panel the atmospheric velocity is plotted as a blue line, where upflows are negative (blueshifts) and downflows are positive (redshifts), and the $\tau_\nu = 1$ surface is plotted as a dashed red line. In the source function panel the green dot-dashed line is the source function of the theoretical line core, and the orange dot-dashed line is the Planck function. Both are in units of radiation temperature. Finally, in the contribution function panel, the emergent intensity is shown, in units of radiation temperature. Images are inverse scale (bright is weak, dark is strong), and the C_I images are normalised in each wavelength bin so that contributions to the wings are visible and not washed out by intense the line core.

4.3.3.1 k-Line Formation

Mg II is depopulated in regions of high temperature $T >\sim 30,000$ K due to ionisation to Mg III, and populations increase over quiet Sun levels in the mid-lower chromosphere in response to increased density and more modest temperature enhancements of a few thousand kelvin. Since the k-line upper and lower levels are depopulated, optical depth unity is not reached until greater depths.

t=1-2 s: The line core is formed just below 1.05 Mm (about 0.2 Mm lower than in the pre-flare). A clear central reversal is present because the source function increases from the continuum level until $\sim$ 1 Mm, after which it decreases with height. The emission peaks, and the line core intensities are much greater than in the quiet Sun. Enhanced temperatures means that the Planck function is larger and as a result the line source function is also increased. Even though the source function of the line core has decoupled from the Planck function, the enhanced electron density means that S_ν tracks the Planck function to a greater extent than in the quiet Sun, which can be seen in the top right panel Figure 4.12a. In that panel the line core source function (green line) follows the Planck function (orange line) to a height of

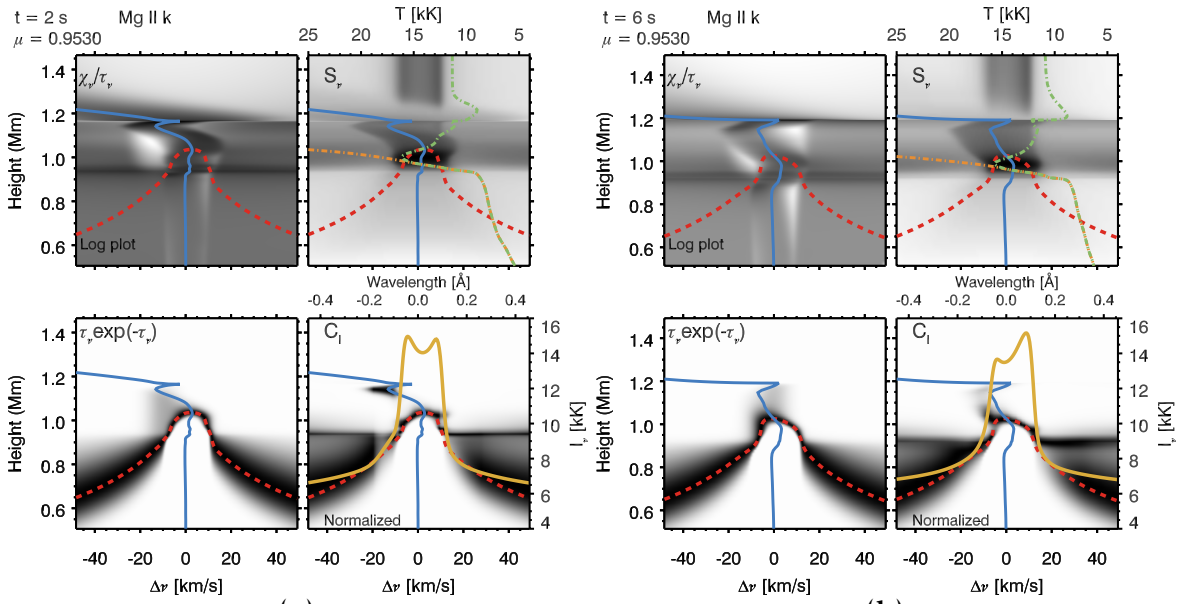

Figure 4.12: *Mg II line formation in the reference flare simulation at (a) $t = 2$ s and (b) $t = 6$ s. Each panel shows the image of the quantity labelled in the corner of the image. Images are inverse scale. The atmospheric velocity (blue, dashed), $\tau_\nu = 1$ curve (red, dashed), line source function (green, dot-dashed), Planck function (orange, dot-dashed), and emergent intensity (yellow, solid) are also plotted. Positive velocity is redshift/downflow. In the bottom right panels the contribution function has been normalised at each wavelength.*

about 1 Mm, which is only a few tens of km below the formation height. The k2 emission peaks form between 0.95 – 1 Mm, near source function maximum. Most of the emission originates from around the $\tau_\nu = 1$ surface meaning that the line can still be considered optically thick. However, some optically thin emission is present at ~ 0.1Å blueward of the line core, formed at a height of 1.1 Mm. This is the result of a velocity gradient in the upper atmosphere of a few tens of km s^{-1} which affects the opacity structure at that height. Photons produced by emitters within this gradient are are shifted blueward of line centre, and so are not attenuated due to the low optical depth of bluer photons at that height.

Stronger upflows result in this optically thin emission becoming stronger over time, dominating over the optically thick emission between 0.1-0.2Å blueward of line core. This is the source of a small asymmetry in the blue wing visible in the emergent profiles. A small downflow shifts of only a few km s^{-1} the line core slightly,

and as can be seen in Figure 4.12a the contribution function at the k2r peak, and immediately redward of it, has two peaks at 0.95 Mm, and 1.05 Mm. This figure also shows the slight shift of the core of the $\tau_\nu = 1$ curve, which results in the emission peaks being formed at (slightly) different heights.

t = 3-6 s: Over the next several seconds the redshift of the line core reduces and the line core starts to become blueshifted by < 5 km s^{-1} as the velocity structure changes. There is now an upflow at the line core formation height (≈ 1.025 Mm) which shifts the line core to the blue. A velocity gradient (an upflow) is present beginning near the core formation height, which increases in magnitude with height. This upflow suddenly decreases at 1.15 Mm, reducing before a fast upflow of > 100 km s^{-1} carries chromospheric material into the transition region at 1.2 Mm. Since the $\tau_\nu = 1$ surface near the line core now forms in the velocity gradient, the optically thin blueshifted emission contributes closer in height of $\tau_\nu = 1$. It extends from line core into the blue wing by 0.1Å. A local maximum in the source function immediately beneath the transition region results in a small amount of optically thin emission to the line core.

Although a central reversal is still present since the source function still decreases with height, the k2 peaks are asymmetric, with the k2r peak being formed at greater depth due to the shifted $\tau_\nu = 1$ curve. It is formed in a region that has a higher source function than the region where the k2v peak (which is more decoupled from the local temperature). Note that the height differences here are small (only a few tens of km), but occur near the peak in the source function so that even being formed a few 10s of km lower in the atmosphere can result in a stronger source function and therefore stronger emergent intensity, particularly since doppler shifts to the line core also result in doppler shifts to the absorption profile, meaning that here blue photons are absorbed more readily than red photons. Figure 4.12b shows the formation at $t = 6$ s.

t=6-10 s: The velocity structure creates an asymmetric $\tau_\nu = 1$ curve that peaks blueward of line core. Greater extinction of blue photons compared to red photons due to the shifted absorption profile means that the $\tau_\nu = 1$ curve immediately blueward of the k2v peak is sharp, before smoothing back out to the wing $\tau_\nu = 1$ height (which has remained steady at $\sim 0.65 - 0.9$ Mm in the wavelength range shown). The reduction in gradient of the upflow draws the optically thin blue shifted

emission back towards the line core (the height difference between the k2v peak and the line core is only a few km by $t = 10$ s, and it could be that without this optically thin contribution, the central reversal would be more difficult to observe). By this time the small temperature bubble just below the transition has formed, causing the condensation to begin propagating down into the deeper chromosphere. A narrow region a few tens of km thick of dense material in the condensation results in a local source function maximum (since there is an increase to the Mg II populations) at a height of ~ 1.15 Mm. There is also a maximum in the opacity at low optical depth, with emitters producing redshifted emission. The source function maximum and opacity maximum result in optically thin emission that is redshifted 0.1-0.2Å from line core, into the red wing resulting in a bimodal contribution function at these wavelengths with optically thick emission from $\sim 0.8 - 0.95$ Mm (extending along the $\tau_\nu = 1$ curve), and optically thin emission from the condensation.

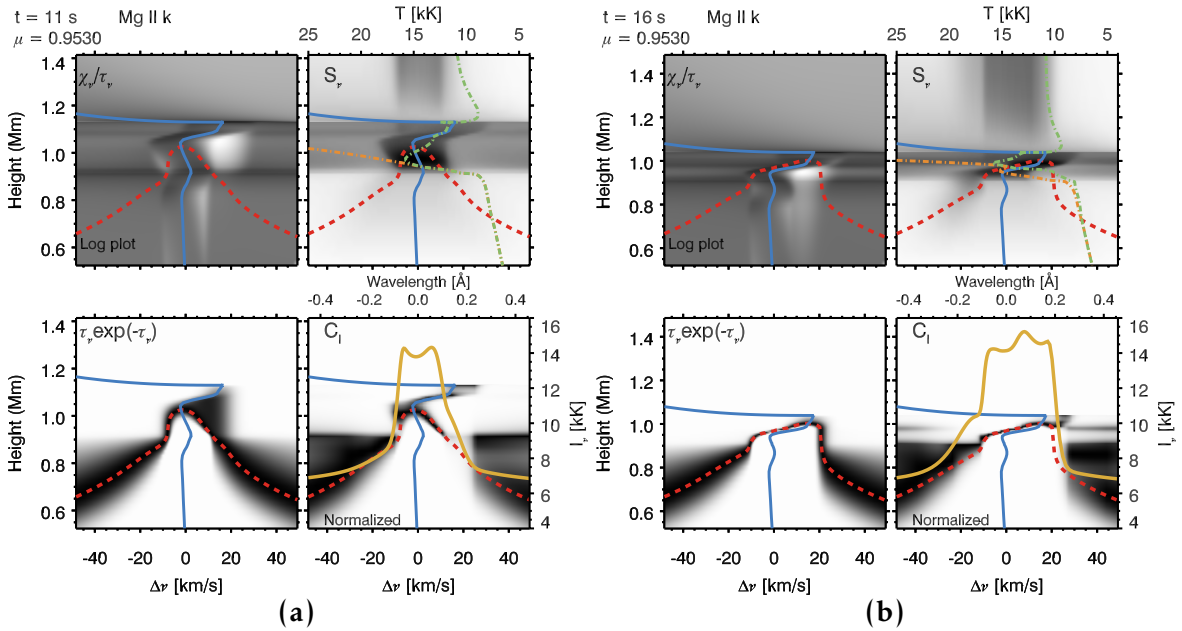

Figure 4.13: *Mg II line formation in the reference RADYN simulation at (a) $t = 11$ s and (b) $t = 16$ s. Panels are as described in Figure 4.12.*

t = 11-16 s: Figure 4.13a shows the formation at $t = 11$ s. The atmosphere is being compressed with the downflow approaching the formation height of the k line core. The k2v and k2r components become largely symmetric around the line core, since the source function maximum region spans a greater geometrical extent, so

that the difference in intensity is much smaller. The optically thin emission from the downflow extends further into the red wing causing an asymmetry compared to the blue wing. Additionally, there is a strong optically thin contribution to the core intensity from the leading edge of the downflow resulting from a local maximum of the source function. This contribution is of similar intensity to the optically thick emission so that the contribution function here is bimodal. There is a significant change in line formation at $t = 12$ s, when the source function maximum at the downflow height increases further. The $\tau_\nu = 1$ curve now lies along the downflow so that the redshifted line core (recall that we define the line core as the wavelength of the maximum height of the τ_ν curve) is located higher in the atmosphere, changing from 1 Mm to 1.05 Mm. A redshifted absorption profile means that photons on that side of the line core are preferentially absorbed, reducing the intensity there compared to the blue wing. Over the next few seconds the line core widens (increasing in FWHM from ~ 0.17Å to ~ 0.27Å), and the blue side of the core remains more intense since the source function is stronger at that formation height (a little lower than the line core and near red wing).

t = 16-20 s: Figure 4.13b shows the line at $t = 16$ s where the complex source function behaviour, and the shape of the $\tau_\nu = 1$ curve due to the downflow, is illustrated. The line core is actually located in the small trough at $v \sim 15$ km s^{-1}, and not in the centre peak as might be expected if presented with just the observations of emergent intensity. This results from a source function that contains several local maxima because of the temperature and density structure of the atmosphere, producing several components to the emergent profile. Indeed, it seems as though the wide core of the $\tau_\nu = 1$ surface is a combination of two optically thick components - one that is stationary or slightly blueshifted, and one that is redshifted. Note the structure within S_ν, which is shown in Figure 4.14 at several wavelengths across the line. As time progresses the strength of the source function blueward of line core decrease until the line core is reduced in width and and resembles a narrower, redshifted profile with strong blue asymmetry in the line wing.

During the flare the line wings have a $\tau_\nu = 1$ layer that lies from $0.65 - 0.9$ Mm across a wavelength range of $0.1 - 0.5$ Å from line centre. Contributions to the emergent intensity come from largely around the $\tau_\nu = 1$ surface, but the range of heights contributing to wing emission spans several 100 km at times. Notably, there

is some intense contribution from a height of ~ 0.9 Mm.

t= 21-60 s: By the end of the heating phase the line core is formed at a depth of 0.95 Mm due to the compression of the atmosphere. Once heating ceases the atmosphere cools and the line intensity drops as a result. At the end of the simulation, and in the whole cooling phase, the column mass is increased and transition region located deeper than in the initial equilibrium atmosphere. The line core and emission peaks are formed in a narrow layer immediately below the transition region. This is consistent with the results of Carlsson et al. (2015) who found that a transition region with higher column masses produced profiles where the k2 and k3 components were formed at the base of the transition region, and close in height to each other.

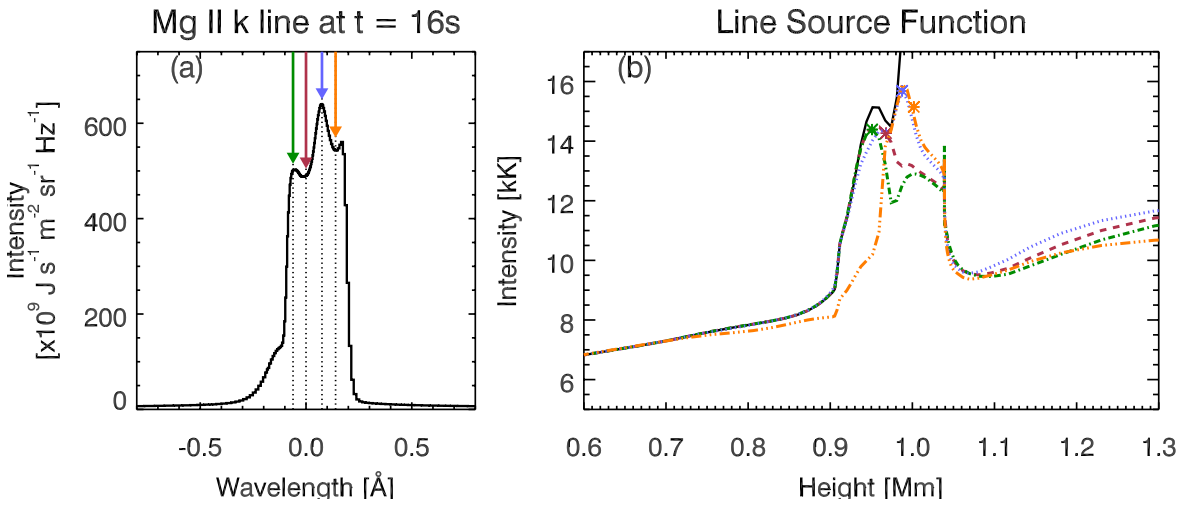

Figure 4.14: *Panel (a) shows the k line at $t = 16$ s, with arrows indicating wavelengths for which the source functions are shown in panel (b). Also shown in panel (b) is the Planck function (black, solid). On each source function a star indicates the $\tau_\nu = 1$ height. The orange line (triple-dot dashed) represents the theoretical line core source function.*

It is instructive to look at the source function behaviour in more detail, as shown in Figure 4.14. The orange, triple-dot dashed line is the source function of the line core. Its source function reaches $\tau_\nu = 1$ at ~ 1.01 Mm when S_ν is decreasing from a maximum value just below this location. While the source function initially

decouples from the Planck function (black solid line) at much greater depth near 0.75 Mm, a locally increased electron density and Mg II k line upper level population density means that it is once again coupled higher in the atmosphere. The blue dotted line source function shows the peak blueward of the core, which reaches $\tau_\nu = 1$ at ~ 0.99 Mm where the source function is a maximum, resulting in a peak intensity. Continuing blueward, a trough is reached at ~ 0.96 Mm because the Planck function is again decreasing from a peak (red, dashed line), and going to the final wavelength indicated (green dot dashed line), there is once again an intensity peak due to a strong source function at that location. Note that from red to blue in wavelength (from the core to the final peak) the line is formed at progressively lower height. That is, from the core, the k2v is formed lower in the atmosphere. This is one of the profiles formed during the strong condensation (profiles from $t = 12 - 17$) that show a wider core. It appears that these profiles could be 'stationary components' plus a 'redshifted component', resulting in the complex core observed, particularly at $t = 15 - 17$ s. The shifted k3 component forms highest in the atmosphere, followed by the k2 emission peaks (k2v, k3, and k2r parts of this component are indicated by purple, orange and blue arrows). Since the source functions are not strongly decoupled then they are close in intensity and the reversal is fairly shallow. Below the formation region of this redshifted profile, there is a stationary profile, with k3 component indicated by the burgundy line and the green line the k2v component (the k2r component blends with the wing of the the redshifted component). This behaviour continues until the end of the heating phase, but the atmosphere is compressed so much that the 'stationary component' is formed in a region where the source function is substantially reduced in comparison with the source function from within the condensation. Though we discuss 'the line core', with our theoretical definition we are in essence focussing on the most shifted, most intense, component. There are effectively two cores here, however.

4.3.3.2 Comparing h & k Line Formation

For the most part the h line formation properties follow the k line, with intensity differences of $\sim 20 - 30\%$ due to difference in the source functions between the two lines which themselves result from differences in the population densities between the h & k upper levels. Observations of the h & k lines have shown the k line is more intense than the h line, and that typically their intensity ratio is > 1 but < 2

(recall from Chapter 3 that in an optically thin regime the ratio would be equal to 2). Modelling of quiet Sun profiles (e.g. Leenaarts et al. 2013a) confirm that this is a result of the k line forming higher in the atmosphere due to higher opacity of that line. The ratio of the oscillator strengths of the k to h line is 2, and so the k line reaches optical depth unity somewhat higher in altitude than the h line. The lines do not usually have a ratio of unity, instead having a range of values centred roughly around $R_{k/h} \sim 1.2$ depending on the source (plage, quiet Sun, etc.,). This is because the the source functions at their respective $\tau = 1$ heights are not equal (a function of temperature and of populations of the respective upper levels). See Linsky & Avrett (1970) for a more in depth qualitative discussion of source function behaviour in the qualitatively similar Ca II H & K lines.

Leenaarts et al. (2013a) discuss the quiet Sun Mg II h & k source functions, stating that the source function ratio depends roughly on the ratio of the statistical weights and the ratio of the upper level population densities (which are a function of temperature, among other factors, in the atmosphere), $S_k/S_h \approx (1/2)n_k/n_h$. Therefore, for the source functions to be equal, the k line would have an upper population roughly twice that of the h line ('roughly' since PRD effects complicate this), and for a ratio > 1 the k line must have an upper level population greater than twice that of the h line upper level. Changes to the population ratio of the k upper level relative to the h upper level will have an impact on the source function ratios.

Lightcurves and line profiles show that, as in observations, the h line is weaker than the k line, but at $t = 12$ s in the flare simulation the h & k lines first show notable differences in their formation over and above the expected intensity difference. At $t = 12$ s the k line's $\tau_\nu = 1$ surface forms along the leading edge of the condensation with a strong opacity and source function (resulting from an increased density of emitters in the condensation), effectively producing a redshifted line core component. Increased density raises the height of the k-line $\tau_\nu = 1$ layer. Only at $t = 13$ s do h-line formation conditions mimic those of the k line. The two lines continue to show some differences over the next few seconds of simulation time, but these are more subtle and a result of smaller difference between their source functions.

If we again identity the line core as the wavelength corresponding to the maximal value of the $\tau_\nu = 1$ surface, then we can identify the line core formation height. The line core formation heights are shown in Figure 4.15 where the red stars show the

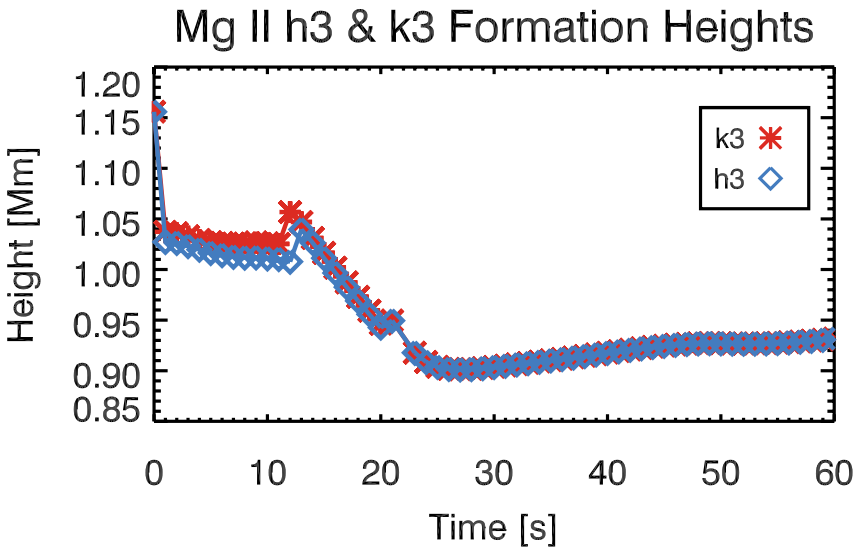

Figure 4.15: *The k3 (red stars) and h3 (blue diamond) formation heights as a function of time during the flare, defined by the height at which $\tau_\nu = 1$ is maximum for each line.*

maximum height at which $\tau_\nu = 1$ for the k-line and the blue diamonds show he maximum height at which $\tau_\nu = 1$ for the the h-line. This identification of line core picks out the redshifted components that emerge at $t = 12$ s (k line), and $t = 13$ s (h-line), formed somewhat higher than the previous profiles. Over the first few seconds of the flare, before the condensation affects the dynamics, both profiles form steadily deeper in the atmosphere as temperature increases and population levels decrease, though the separation in formation height increases even before jump at $t = 12$ s. The k-line decreases from ~ 1.16 Mm to ~ 1.04 Mm after initial energy input, then decreases slowly to ~ 1.025 Mm by $t = 11$ s. The h-line decreases initially to ~ 1.03 Mm after initial energy input, then decreases to ~ 1 Mm by $t = 12$ s. After the h line catches up to the k-line they are formed close in height, and form progressively lower down to ~ 0.95 Mm during the energy input phase, and ~ 0.9 Mm during the decay phase. At these times the atmosphere is compressing and so the profiles become more alike, evident in the k/h intensity ratio, $R_{k/h}$ also (see Figure 4.16). Initially the ratio decreases before slowly rising until $t = 12$ s, peaking at $t = 13$ s and decreasing thereafter. After the time of peak intensity in the lightcurves, the $R_{k/h}$ is smaller, meaning that the source functions are almost equal in size. The lines are formed in a narrow layer, unlike at the peak where they are formed over a larger

height difference.

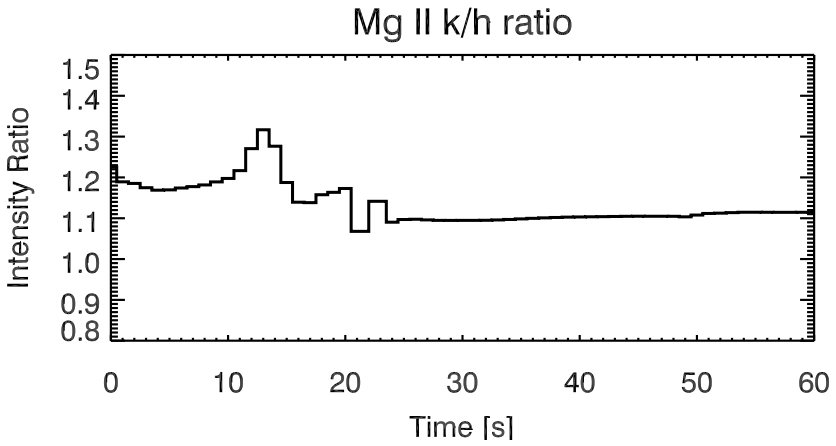

Figure 4.16: *The k/h line intensity ratio as a function of time during the flare.*

So, why do the h & k lines show this behaviour? That is, why is there is an increasing separation in the formation heights, and why is does the k-line respond to the downflow before the h-line? The answer could lie in the relative populations of the h & k lines. The relative population of k to h line upper levels is shown in Figure 4.17, where colour represents simulation time. In the core formation region ($\sim 0.95 - 1.05$ Mm) the ratio of k upper level population to h upper level population increases over the first few seconds during the flare from $\sim 2.2 - 2.6$ at a height of 1 Mm, beginning to decrease again after $t = 13$ s. The k-line upper level has a relatively stronger source function in comparison to the h-line, due to this increased population, and so $R_{k/h}$ begins to slowly rise before peaking strongly at the same point in time as the population ratio peaks.

To understand the origin of this changing relative population the rates out the h & k lines were investigated. The net rate of each level, i, per Mg atom is $P_{\mathrm{net,i}}$:

$$P_{\mathrm{net,i}} = \frac{1}{n_{\mathrm{Mg}}} \sum_j (n_i P_{ij} - n_j P_{ji}) \tag{4.1}$$

where $i = 3p\ ^2P_{\frac{1}{2},\frac{3}{2}}$ (h & k upper level respectively), n is the population density, and P_{ij} & P_{ji} are the collisional plus radiative rates for transitions $i \rightarrow j$ and $j \rightarrow i$ respectively. Net rates out of both the h & k levels were computed by including an additional sum over i in Eq 4.1. This was to understand whether the h & k levels are

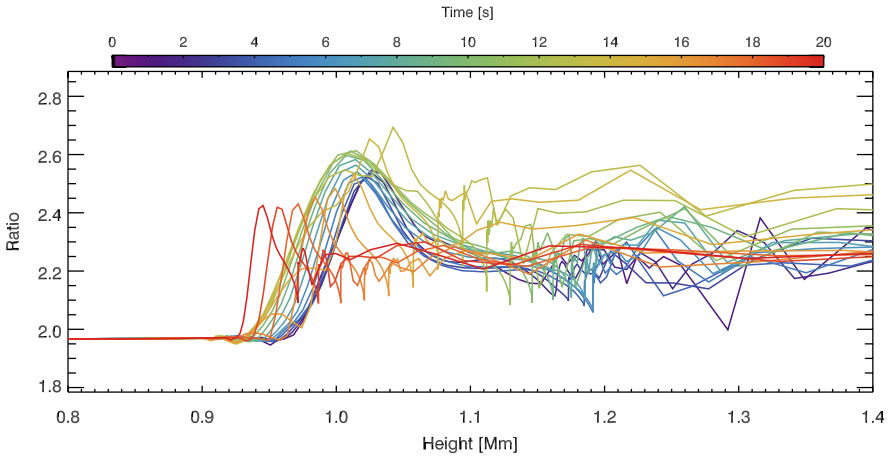

Figure 4.17: *The k/h upper level population density ratio as a function of time during the flare.*

populated mainly via cascades down from excited levels, in flaring conditions like in non-flaring conditions (Leenaarts et al. 2013a). This is indeed the case.

The majority of the cascades from excited states to populate both the h & k line upper levels come via the $3d$ levels - the subordinate line upper levels. The h & k upper levels are populated and then radiatively de-excite to the ground state. As with the h & k lines, the subordinate lines increase significantly in intensity over the course of the flare, and are in emission. Increased subordinate line emission means more de-excitations to the h & k upper levels, populating them. Since two of the three subordinate lines de-excite to the k-line upper level, and only one to the h-line, the k-line has an additional pathway to being excited. Over the flare the net rates into the k-line from the excited states grows faster than the net rates into the h-line. Thus, the k-line to h-line upper level population density ratio increases, and the formation height difference steadily increases. When the downflowing material reaches an altitude at which it strongly affects the h & k upper levels, it affects the k-line first due to the already greater population. The h-line 'catches up' when the population density is large enough, which happens in part due to increased collisional coupling between the k & h lines. Thereafter, the line profiles become more similar, with $R_{k/h}$ and population ratio both falling.

Collisions between the two resonance line upper levels mean that the k line populates the h line (at the formation height), reducing the ratio between the two. While radiative de-excitation still dominates, it is worthwhile noting this increase in

coupling between the h & k line during the flare. Leenaarts et al. (2013a) note that coupling is not very important for the quiet Sun where radiative effects were orders of magnitude larger, but it seems that the increased electron density and temperature increases the importance of coupling during flares.

4.4 Modelling Mg II Emission from the 2014-Feb-13 Flare

Observations of the 2014-Feb-13 M class solar flare were presented in Chatper 3. Using the RHESSI derived electron beam parameters provided by Dr P. Simões (reported in Kerr et al. 2015, and in Chapter 3), this flare was simulated using RADYN. This is a demanding simulation for RADYN, with a soft spectrum and high energy flux, meaning that only $t = 3$ s of solar time was completed. Snapshots every $t = 0.1$ s were processed using RH to obtain the Mg II synthetic spectra. The preliminary results of this simulation are presented here to allow comparison to observations.

4.4.1 RADYN Simulation of the 2014-Feb-13 Flare

The initial atmosphere was the QS.SL.LT radiative equilibrium atmosphere described in Allred et al. (2015). This atmosphere has a loop length of 10 Mm and a coronal temperature of 1 MK. As usual, non-radiative heating was applied to grid cells with column mass less that 1×10^{-6} g cm^{-2} and greater than 7.6 g cm^{-2}, to maintain energy balance in the corona and photosphere respectively. A reflecting boundary in the corona (loop top) models incoming waves from the other half of the loop. The boundary in the sub-photosphere is transmitting.

This simulation used the treatment of non-thermal electron beam energy transport discussed in Abbett & Hawley (1999), and often referred to as the 'Emslie beam' treatment (c.f Chapter 2). RHESSI derived beam parameters were computed at four time intervals. The third interval (01:36:15UT + 40s) was the only time at which a strong non-thermal footpoint source was co-spatial with the flaring ribbons, and so beam parameters from this time were used for this simulation. The spectral index and low energy cutoff derived from observations were $\delta = 9.752$ and $E_c = 20.557$ keV respectively. To obtain the energy flux the observed power in non-thermal electrons should be divided by the source area. Dennis & Pernak (2009) studied HXR source sizes, performing a comparison of the standard imaging

techniques. From their sample they noted that most HXR footpoint sources observed by RHESSI were unresolved (RHESSI has a spatial resolution limit down to $\sim 2''$ FWHM), which was also noted by Krucker et al. (2011) in a comparison between HXR and optical sources in a flare. Measuring the source area with RHESSI therefore might overestimate the area. Recently, Milligan et al. (2014) and Kowalski et al. (2016) used the optical or UV source area as a proxy to determine the energy flux. This assumes that the HXR footpoints and UV/optical ribbons are co-spatial, which may not always be the case - as discussed in Chapter 1 flare ribbons tend to be more extended structures. Here we use the IRIS SJI images to determine an estimate for the source area, recognising that this may result in an overestimate of the energy flux (the smaller source area would result in a larger energy flux). From the 1330Å filter of the IRIS SJI, the area of flaring sources greater than 30-60% of maximum intensity was measured. Using this range of source size, and a measured power in the non-thermal electrons of $P = 3.77 \times 10^{27}$ ergs s^{-1}, the range of beam energy flux was is $F \sim [7.23 \times 10^{10} - 2.56 \times 10^{11}]$ erg s^{-1} cm^{-2}. A value of 1×10^{11} ergs s^{-1} was used. Figure 4.18 shows the evolution of atmospheric temperature, electron density, velocity (upflow is negative), and column mass where as usual colour represents time.

The dynamics of this flare simulation occur on faster timescales than in the simulation presented in § 4.3.1. Coronal temperatures immediately above the transition region quickly increase to several million kelvin, and a large high temperature bubble forms in the mid-upper chromosphere as a result of helium ionisation to He III. Radiative losses from He II reduce following ionisation, so energy input is no longer balanced and temperatures can increase dramatically to $T > 1$ MK. A similar process is described in more detail in Chapter 5.

This high temperature bubble expands creating dense flows that propagate upwards at 100 s of km s^{-1} and downwards, through the denser chromosphere, at several 10 s of km s^{-1}. The bubble itself is under-dense as material is evacuated by these high velocity flows, so that the density difference between the middle of the bubble and the leading edges is > 2 orders of magnitude by $t = 3$ s. The bubble's temperature approaches 10 MK over narrow geometric heights of only a few 10s of km. Note that the electron density approaches a value of $\approx 10^{14}$ cm^{-3} in the downward propagating shock. Additional electron density enhancement at greater depth results from a heated lower chromosphere where the temperature has increased by

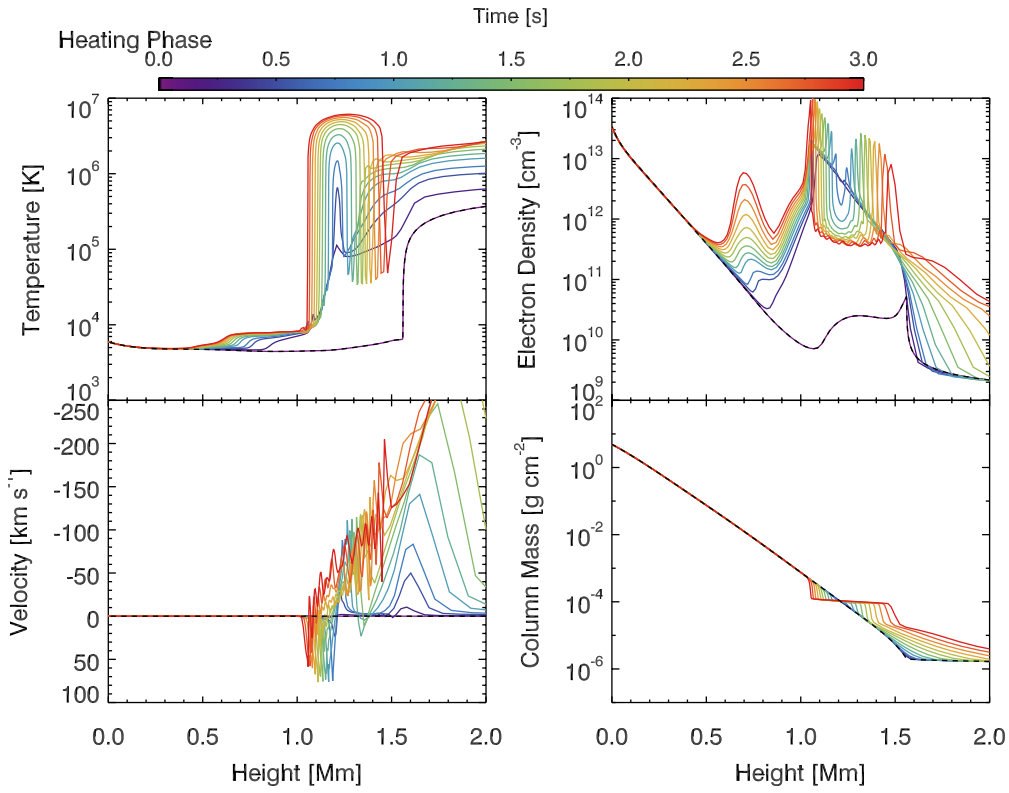

Figure 4.18: *RADYN simulation of the first 3 s of the 2014-Feb-13 solar flare, where colour represents time during the simulation. Top left panel shows the temperature, top right the electron density, bottom left the velocity where upflows are negative, and the bottom right the column mass.*

2-3 thousand kelvin. Over the remainder of the simulation, the chromosphere is compressed by the expanding bubble - the column mass decreases at lower altitudes as the bubble changes the density structure of the chromosphere. In the shock the velocity structure is jagged but smoother above and below.

4.4.2 Mg II Profiles from the Simulation of the 2014-Feb-13 Flare

Processing snapshots at a cadence of 0.1 s through RH yields the Mg II h & k synthetic spectra from this flaring atmosphere. These are shown in Figure 4.19 where as before the h line is shown in red and the k line in black. Profiles are shown every 0.2 s, with simulation time indicated in the upper left corner of each panel. It is clear that these profiles show some similarities to the previous simulation discussed, but also differences, with a few very complex profiles that occur when chromospheric

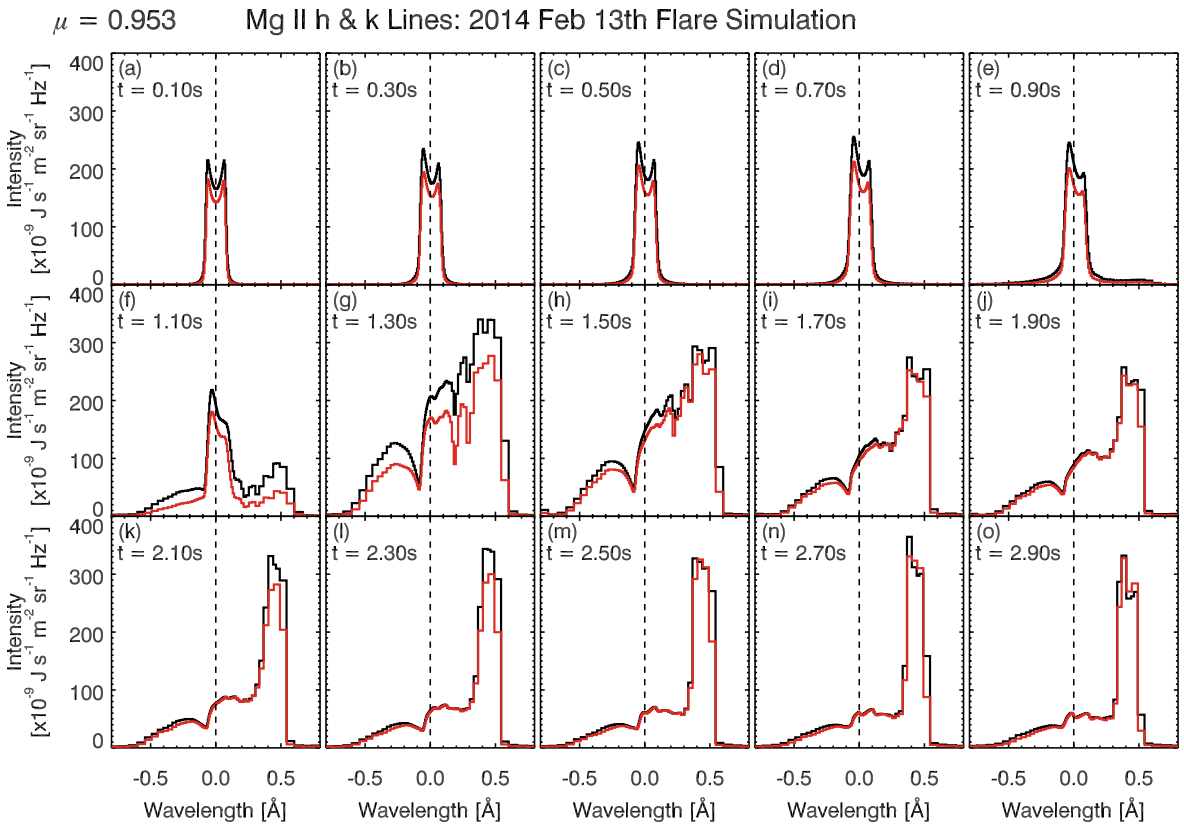

Figure 4.19: *Mg II h & k line profiles produced using snapshots from the RADYN simulation of the first 3 s of the 2014-Feb-13 solar flare. The k line is shown in black, and the h line shown in red. Simulation time is indicated in the top left of each panel.*

condensations develop. The profiles within the first second (first row in Figure 4.19) resemble the previous simulation, but are somewhat weaker, with an intensity on the order $1.5 - 2.5 \times 10^{-7}$ J s^{-1} m^{-2} sr^{-1} Hz^{-1} in the core. Small asymmetries between the k2v and k2r peaks are present and core becomes slightly redshifted by < 5 km s−1. Over time the central reversal becomes less prominent and closer in intensity to the k2r peak. Beginning around $t = 1.1$ s, the line core is difficult to distinguish from k2r, and both line wings show asymmetric enhancements. As time progresses there is a stronger redshift of the line, with a Doppler velocity $> 50 - 60$ km s^{-1}. The blue wing emission is more extended than the red wing, with emission present over 1Å from line core. This could be a secondary component (itself somewhat redshifted). This is a more extreme version of behaviour seen in the previous simulation (where velocities were lower). By $t = 2.1$ s the profiles appear single peaked or at least with

a shallow central reversal. The emission blueward of this redshifted profile have a decreasing intensity with time, falling from $\sim 200 \times 10^{-9}$ J s^{-1} m^{-2} sr^{-1} Hz^{-1} to $\sim 40 \times 10^{-9}$ J s^{-1} m^{-2} sr^{-1} Hz^{-1}.

So, as before we see profiles with enhanced intensity over the pre-flare, with asymmetries and a redshifted component that is temporally associated with a fast downflow in the atmosphere. Over time emission blueward of this component decreases in intensity so that it appears as an extended blue wing. Differences here are the jagged profiles (e.g. at $t = 1.3$ and $t = 1.5$ s), and that the profiles appear single peaked towards the end of the simulation.

4.4.3 Mg II Formation in the Simulation of the 2014-Feb-13 Flare

In the first second the formation properties of the line are fairly simple. The profiles are centrally reversed due to a difference in formation heights between the core and emission peaks, with the core being formed at a height where the line source function is decreasing away from the Planck function. At the formation height of the emission peaks the source function is more strongly coupled to the Planck function and is at a maximum. Core formation height has dropped from the pre-flare of ~ 1.5 Mm (just below the transition region height in the starting atmosphere), to ~ 1.15 Mm, and the emission peaks are formed ~ 1.10 Mm. Compared to the previous simulation, this is geometrically higher, but overall the line profiles form deeper relative to the pre-flare formation height. Temperatures are greater in the mid-upper chromosphere than in the previous simulation due to the temperature bubble, which drives down the $\tau_\nu = 1$ surface.

Flows develop by $t = 0.5$ s, and the line core becomes slightly redshifted by a few km s^{-1} due to a downflow at the core formation height. This downflow is at the bottom of a velocity gradient that extends to a fast downflow of ~ 20 km $^{-1}$ at a height of 1.2 Mm. At this height there is an increase in opacity at low optical depth, causing redshifted optically thin emission to contribute strongly to the red wing. Similarly, an upflow of similar magnitude at a height of ~ 1.23 Mm causes blueshifted optically thin emission contributing to the blue wing. The k2v peak begins to become more intense relative to the k2r peak due to a difference in formation height. The redshifted $\tau_\nu = 1$ surface means that the k2r peak is formed closer in height to the line core, where the source function is less coupled to the Planck function. By

$t = 1$ s the flows propegating downwards from the hot bubble in the mid-upper chromosphere are greater (the condensation has a speed in excess of 60 km s^{-1}). The peak of this downflow is still located somewhat above the core formation height, but the core does track the velocity gradient. The line core and k2r component, which are formed so close in height that their intensities are almost equal, are redshifted by ~ 15 km s^{-1} which is the local speed of the downflow just below a height of 1.15 Mm. The k2v peak is formed a few tens of km lower in a region of source function maximum, and so has a greater intensity, and is not Doppler shifted. Since the condensation front has a high density there is a local maximum to the source function in the condensation's leading edge. This results in redshifted optically thin emission that extends to ~ 0.8Å from the rest wavelength in the red wing. This is why the extended red wing is more intense than the blue wing in Figure 4.19 (e,f).

When the condensation reaches a denser layer (where the h & k line cores are formed), there is a sufficient amount opacity for the $\tau_\nu = 1$ layer of the h & k lines to form at the leading edge of the downflow. There is a redshifted opacity profile due to the downflow, so the the emergent intensity is also redshifted.

Profiles appear complex due to the velocity structure here. All three components (k2v, k3 and k2r) are redshifted and formed over a layer only a few km thick, just below the sharp temperature gradient in the bubble where temperatures increase from a few thousand kelvin to $T > 1$ MK over a few tens of km. The local maximum in source function means that it approaches the Planck function, but it is sufficiently decoupled that the radiation temperature is not equal to the gas temperature.

Local density and temperature variations ahead of the condensation affect the upper and lower level population density resulting in some structure to the $\tau_\nu = 1$ surface at wavelengths blueward of the redshifted line core. The result is the emergent profiles at $t = 1.3$ & 1.5 s in Figure 4.19. The 'jagged' appearance of the profiles results because some of the emergent intensity originates from lower in the atmosphere, sufficiently far from the narrow source function maximum region, and is therefore less intense.

Over time the formation heights of the k2 and k3 components is so close that the profiles appear single peaked. Also, since the source function becomes more coupled to the Planck function, the peak intensity increases. Towards the end of the simulation the profiles narrow as the intensity blueward of the peak drops, a result of the condensation is travelling deeper into the atmosphere where the source

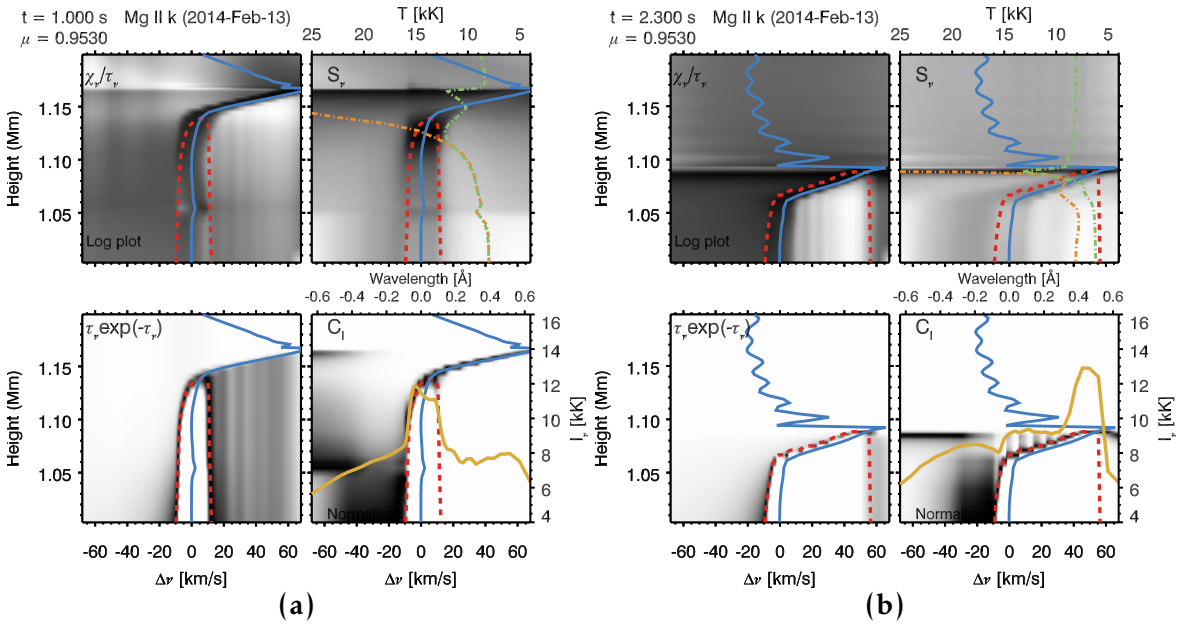

Figure 4.20: *Mg* II *line formation in the RADYN simulation of the 2014-Feb-13 flare at (a) $t = 1$ s and (b) $t = 2.3$ s. Panels are as described in Figure 4.12 .Note the reduced height scale in comparison to previous similar figures.*

function drops quickly along the condensation front.

Figure 4.20 shows the formation properties at two snapshots from the simulation. The first shows $t = 1$ s, where the peak in the opacity at low optical depth results in strong optically thin emission in the red wing produced within the dense condensation. The second snapshot shows $t = 2.3$ s where the single peaked profile formation is illustrated. There the maximum of the $\tau_\nu = 1$ curve is located at a redshift of $\sim 45-50$ km s^{-1}, where the intensity also peaks. The usual k2 emission peaks are not visible, as they are formed where the source function (therefore intensity) is lower. The source function panel (top right) shows that the line core source function (green dot-dashed line) tracks the Planck function (orange dot-dashed line) strongly at that height.

4.5 Atmospheric Properties at the Core Formation Height

The Mg II h & k lines are complicated but offer the potential for diagnostics of the 'low temperature' part of the flaring atmosphere - the heated low-mid chromosphere. Building detailed correlations as in Leenaarts et al. (2013a,b) will require a survey of

a large number of flare simulations, but some initial comments can be made, based on the two simulations presented here. It is clear that the lines are formed in the low-mid chromosphere during flares, where enhanced temperatures are sufficient to increase the line intensity, but not too hot to ionise to Mg III. Optical depth unity (where the bulk of the emission originates) is reached lower in the atmosphere due to depopulation of Mg II in the upper chromosphere. Thus we are able to probe conditions just below or at the jump to transition region temperatures. This jump can either be an expanding bubble, a transition region that moves deeper, or even a shallower gradient to temperatures of a few$\times 100,000$ K before the main transition region (as will be seen in the next chapter). Perhaps the most useful atmospheric properties to consider initially are velocity, temperature and electron density. Questions we must ask include:

• Does the doppler shift of the line core match the atmospheric velocity at the core formation height? Can line asymmetries be used to learn about gradients above the main formation height?

• The lines are more intense in the flare since their source functions are greater. This occurs in part due to enhanced temperatures. How strongly does the line intensity follow the atmospheric temperature rise?

• The source functions can be more or less coupled to the Planck function during the flare affecting the size of the central reversal, and at some instances showed a single peak – is there a threshold electron density required for single peaked profiles?

In the following sections the atmospheric properties at the height of $\tau_{\nu_0} = 1$ are investigates, where ν_0 is the line core frequency.

4.5.1 Line Core Velocity

It is clear that in the presence of a strong and dense condensation the profiles were redshifted along the leading edge of the condensation. The Doppler width of the lines is fairly low ($\sim 2-3$ km s^{-1} in the quiet Sun, increasing slightly in response to flare temperatures) meaning that the line core is sensitive to mass motions. As

discussed previously, Leenaarts et al. (2013b) found an excellent correlation between the Doppler shift of the line core and the atmospheric velocity at the formation height.

The correlations between Doppler shift and atmospheric velocity in the flaring simulations are shown in Figure 4.21(a,b) for the reference simulation and the 2014-Feb-13 flare simulation respectively. These figures show the line core Doppler shift of the k line (stars) and h line (diamonds) as a function of atmospheric velocity at their formation height, were colour represents time during the simulation. The dashed line is $y = x$.

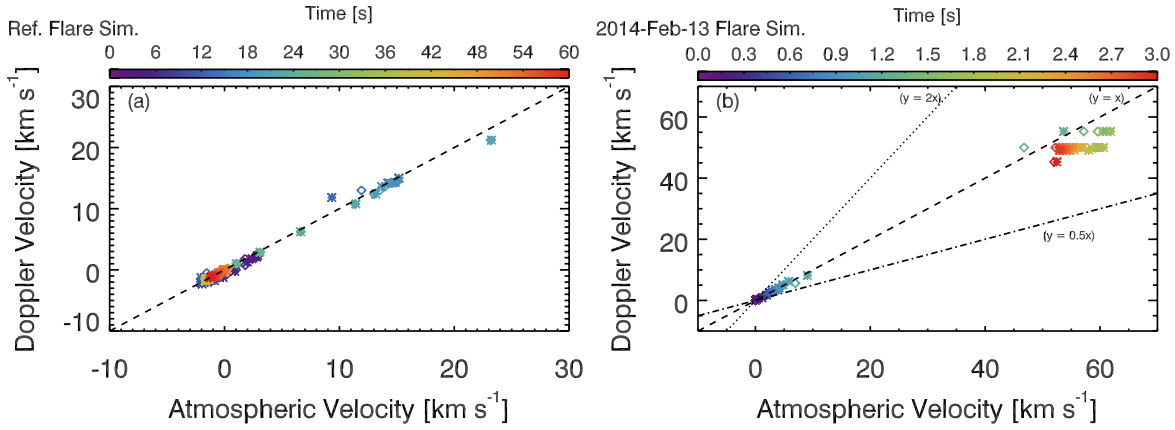

Figure 4.21: *The correlation between Doppler shift and atmospheric velocity for the h line (diamonds) and k line (stars), where colour represents simulation time. Panel (a) shows the reference flare simulation and Panel (b) shows the 2014-Feb-13 flare simulation. The dashed line shows $y = x$, dotted line $y = 2x$ and dot-dashed line $y = 0.5x$.*

In the reference flare simulation there is an excellent correlation throughout, with both h & k core Doppler shifts matching the atmospheric velocity well. This is true also for lower velocities in the 2014-Feb-13 flare simulation, but for large velocities that occur in the latter stages of the simulation the correlation is not as tight. Doppler shifts of the line core from around $t = 1.3$ s (when the strong condensation reaches the core formation height) are lower than the actual velocity in the condensation, with a difference of up to ~ 10 km s^{-1}. There is a systematic improvement in the correlation when the atmospheric velocity decreases, as the condensation travels deeper into the chromosphere, while the Doppler shift remains fairly constant around 50 km s^{-1}.

Temperatures rise significantly through the condensation up to $T > 1$ MK which increases the thermal width of the resonance lines, which possibly decreasing the sensitivity to atmospheric velocity.

The difference in the h & k Doppler shift ($v_{k3} - v_{h3}$) is well correlated with the difference in the velocity of the atmosphere at their respective formation heights, though in the 2014-Feb-13 flare the same scatter is present. From this velocity difference the sign of the velocity gradient can be recovered with confidence. Since the formation height difference during the flare is, for the most part, smaller than in the quiet Sun, this difference is small.

A larger number of simulations are required to determine if this tight correlation always has a larger spread at high velocities, or if this only happens when the temperature is higher than a certain threshold (or, indeed, if these two situations always arise together). Even with this difference, the atmospheric velocity is only between $5 - 10$ km s^{-1} larger than the Doppler shift would suggest. We can be confident then that the Doppler shift captures the direction of the mass motions and gives a good approximation to the true velocity magnitude.

4.5.2 Temperature and Electron Density

Line intensity is related to the temperature and electron density of the plasma in the formation region. Profiles with reversals are those in which optical depth unity in the line core is reached as the source function is decreasing in height and is weaker than the source function of the two emission peaks. A deeper reversal is likely to be the case when the line core is formed high in the atmosphere, where the source function is completely decoupled from the local temperature. A shallower reversal would suggest a smaller difference in formation height between the core and peaks so that the core optical depth unity is reached where the the source function is more coupled the local temperature to a greater extent (the source function has decreased less). No central reversal could suggest either that the core source function is increasing with height, and/or that the k2 and k3 components are formed over a small region in which there is little difference in their source functions. In a single-peaked profile, higher intensity would imply a higher temperature since the source functions follows the Planck function.

Enhanced electron density can act to increase the coupling between the source

function and the background radiation field, so that the line source function tracks the Planck function to greater altitude before decoupling. Such behaviour has been seen by Rubio da Costa et al. (2016) who experimented with increasing the electron density in the formation region of Mg II h & k lines. They obtained single-peaked profiles as a result, due to stronger coupling to the Planck function. Additionally, Pereira et al. (2015) noted in their study of the Mg II subordinate lines that while several factors can result in greater coupling to the local temperature, in their simulations this occurred in regions of high electron density.

So, during flares the increased electron density could increase the coupling of the Mg II h & k (and subordinate line) source functions to the Planck function. The Planck function itself has increased due to temperature enhancements. Higher line core intensity would then imply hotter plasma, and the size, or lack of, the central reversal could carry information about the electron density. While more simulations will be necessary to identify any quantitative diagnostics of temperature or electron density we can show preliminary correlations from these initial numerical experiments. Figure 4.22(a,b) shows the intensity of the line cores, expressed as a radiation temperature, compared to the atmospheric temperature at their formation height. Also shown on these figures are the electron density at the formation height.

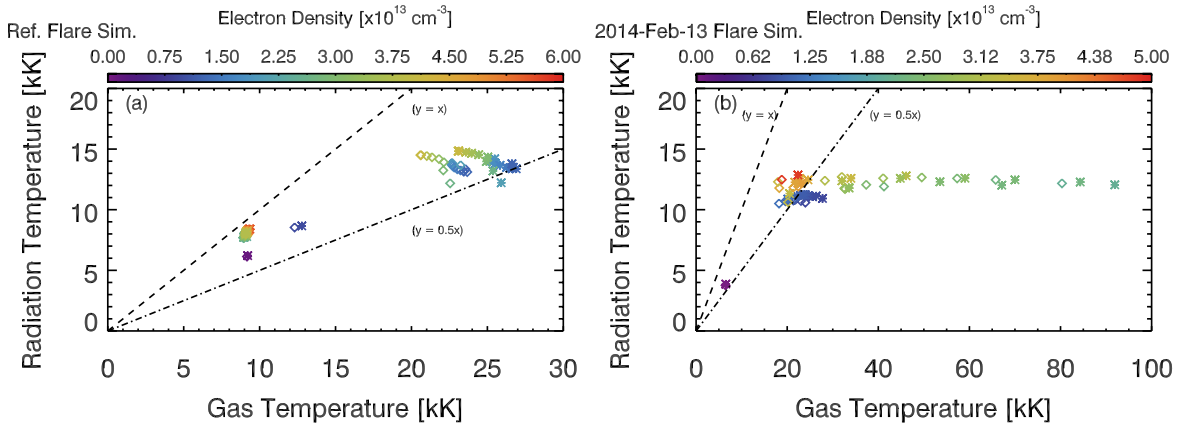

Figure 4.22: *The k (stars) & h (diamonds) line core intensity, expressed as a radiation temperature versus the atmospheric temperature. Colour represents the electron density at the formation height of the line core in each case. The dashed line is $y = x$ and the dot-dashed line is $y = 0.5x$. Panel (a) shows the reference flare simulation, and panel (b) the 2014-Feb-13 flare simulation.*

Initially, in both simulations, the radiation temperature is around half the gas temperature. In the reference flare simulation the effect of higher electron density on high intensity (high radiation temperature) profiles is to make the radiation temperature slowly approach the atmospheric temperature. These high intensity profiles are from the heating phase, and it is clear that while the core intensity is enhanced due to flare heating, the source functions are decoupled from local temperatures. Higher density strengthens the coupling. The lower intensity profiles are from the cooling phase, and while these profiles do exhibit a central reversal, the high electron density means that the radiation temperature is approximately equal to the atmospheric temperature.

The 2014-Feb-13 flare simulation is more complicated. Here the radiation temperatures are somewhat lower, never really getting above half of the gas temperature. Instead, at several times the radiation temperature completely decouples from the atmospheric temperature. These are the same points for which the velocity correlation deviates. A narrow over-dense region a few 10s of km thick allows a local enhancement to the h & k level populations, which subsequently produce a local source function maximum. This maximum is decoupled from the Planck function, however, so it does not feel the background temperature rise. So the line cores formed within the condensation are even more decoupled from the local temperature and show no correlation whatsoever. The clustering around the $y = 0.5x$ line are from early times before the condensation becomes important.

These two conflicting pictures do not present a clear conclusion for flaring profiles. The differences result from the steepness of the temperature gradient in the chromosphere, which in turn affects the magnitude of the condensation (a steeper gradient results in larger velocity condensation). So, it may result from studying more flare simulations that two regimes exist - smaller condensation preserves some correlations since the h & k lines will be formed in lower temperature plasma, and larger velocity condensations will result in a more complex relationship between atmospheric properties and line intensity.

While the core is usually decoupled from the Planck function, the k2 peaks seemed to be formed in a region of source function maximum, and so could be a better gauge of atmospheric temperature (in the quiet Sun a good correlation between k2r and k2v radiation temperature and the atmospheric temperature at their formation height was found by Leenaarts et al. 2013b; Pereira et al. 2013).

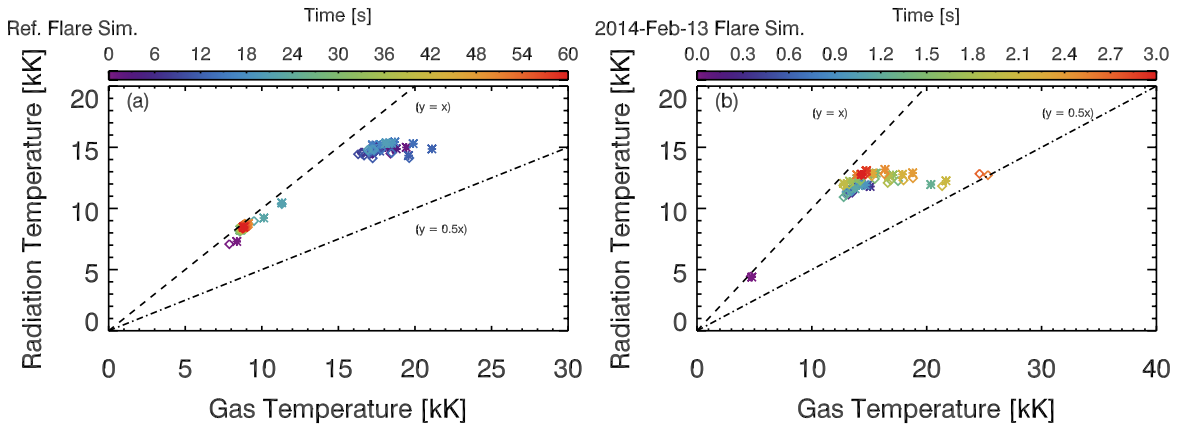

Figure 4.23: *The k (stars) & h (diamonds) line peak intensity, expressed as a radiation temperature versus the atmospheric temperature. Colour represents the time in the simulation. The dashed line is $y = x$ and the dot-dashed line is $y = 0.5x$. Panel (a) shows the reference flare simulation, and panel (b) the 2014-Feb-13 flare simulation.*

During the flare the k2r and k2v components can become difficult to identify, and so the maximum intensity was used instead. The maximum intensity seemed to normally originate from somewhat lower compared to the line core, where the source function was maximum and more coupled to the Planck function. Figure 4.23 shows the maximum intensities, converted to radiation temperature, plotted as a function of the atmospheric temperature at their formation height. Colour represents simulation time.

Both simulations exhibit a tighter correlation when the maximum intensity is used, with radiation temperatures lying closer to the $y = x$ line suggesting that they are indeed more coupled than the line core. A drift away from $y = x$ at higher temperatures shows that the coupling is not exact when the maximum intensity is formed at greater heights. Still, the radiation temperatures lie near the gas temperature and, are not more than half of the gas temperature at later times during the flare. If we are confident in the conversion of IRIS data from DN s^{-1} to physical units then we should have an estimate of the range of atmospheric temperature given the maximum intensity.

4.6 Comparing to Observations

Qualitatively, the simulations mostly reproduce what has been seen in IRIS observations of Mg II h & k in flares that were presented in Chapter 3 (see also Kerr et al. 2015; Liu et al. 2015; Matthews et al. 2015). Generally during flares the line cores appear single peaked, though Matthews et al. (2015) report that in the 2014-March-29 X class flare, not *all* profiles were single peaked, and note the sometimes jagged appearance of the profiles. A similar appearance was seen in a few profiles from the 2014-Feb-13th flare, as discussed in Chapter 3. Synthetic profiles showed complex line cores, sometimes appearing with a clear reversal, other times showing single or multiple peaks. Subordinate lines in both simulations and observations go into emission during flares.

4.6.1 Line Width and Microturbulence

A notable discrepancy between simulated profiles and the observations is the widths of the resonance lines. Simulated flaring profiles have an increased width over the quiet Sun simulations, but are narrow in comparison to flare observations. Simulations show a FWHM of $\sim 20-30$ km s^{-1} compared to observations which show widths up to 70 km s^{-1}. For the simulations presented so far a constant microturbulent velocity of $v_{\rm turb} = 2$ km s^{-1} was applied, but it is likely that flares will produce a higher $v_{\rm turb}$. To obtain an estimate of the microturbulent velocity during the flare, observations of the O I 1355.6Å line were fitted with a single Gaussian and the average value of $v_{\rm turb}$ during the flare was derived from the fit results (see Chapter 3). Lin & Carlsson (2015) demonstrated that this line is formed in the mid-upper chromosphere, and is optically thin, allowing the non-thermal velocity to be determined. Since the O I 1355.6Å line forms in a roughly similar region of the atmosphere to the emission peaks and line core of the h & k lines, the value of $v_{\rm turb}$ derived from O I 1355.6Å was assumed to be similar to the value at the formation height of h & k. This value of $v_{\rm turb} = 9.2$ km s^{-1} was adopted as the microturbulence at all heights in a re-run of the 2014-Feb-13 flare simulation. This is perhaps rather crude as the microturbulence is likely to vary over the formation region of Mg II, but as an initial experiment is satisfactory, particularly since $v_{\rm turb}(z)$ is not well known in the chromosphere.

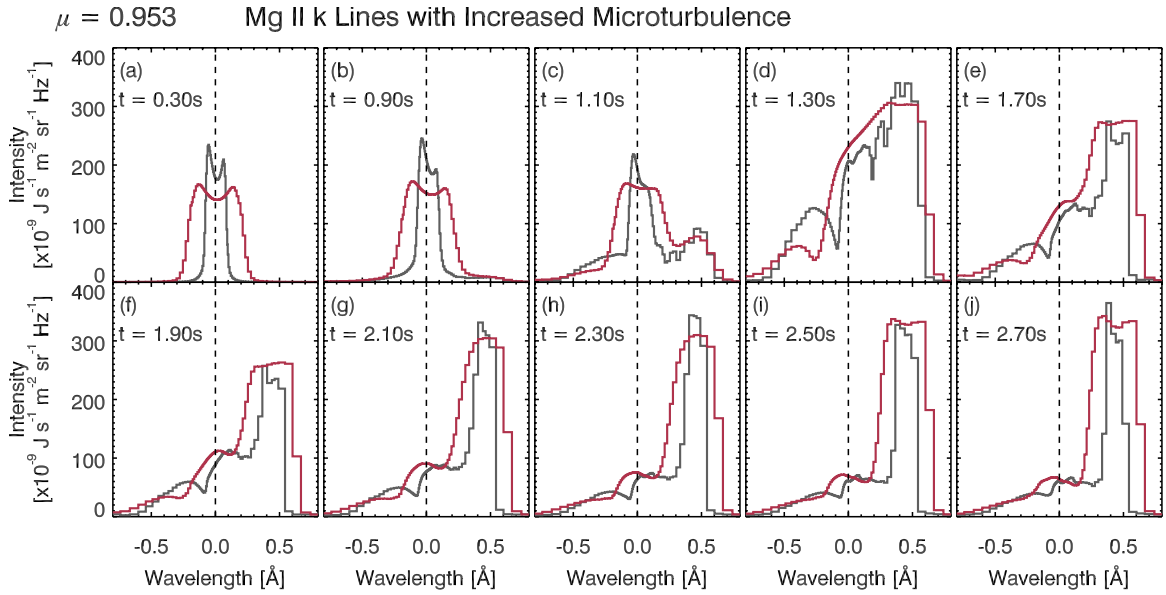

Figure 4.24: *Mg* II *k line profiles from the 2014-Feb-13 flare. Grey lines are the profiles shown previously in Figure 4.19. The orange lines are the profiles computed with increased microturbulence of 9.2 km* s^{-1}.

Increasing the microturbulence did, indeed, broaden the profiles but only in the core and inner wings, not in the far wings (see Figure 4.24). Additionally, the profiles are smoother. Rubio da Costa et al. (2016) simulated profiles with a much larger value of microturbulence of 27 km s^{-1} and obtained similar results, though with a more obvious single peak.

While the profiles were widened, the far wings are still not as broad as observations. To get wider wings the wing source function must be enhanced. Microturbulence does not seem to be the cause.

4.6.2 What Would IRIS see?

Understanding the formation properties of the Mg II lines during flares is useful as we wish to use observations of these profiles to aid in the interpretation of what is happening to the flaring chromosphere. In order to take advantage of the forward modelling of spectral lines it is useful to convert the synthetic data to the resolution of the instrument. The RH spectra are unevenly binned in wavelength, with a coarser grid in the line wings and finer in the line core, so they were first re-binned to a constant grid of resolution 5 mÅ. Synthetic spectra were then convolved with the

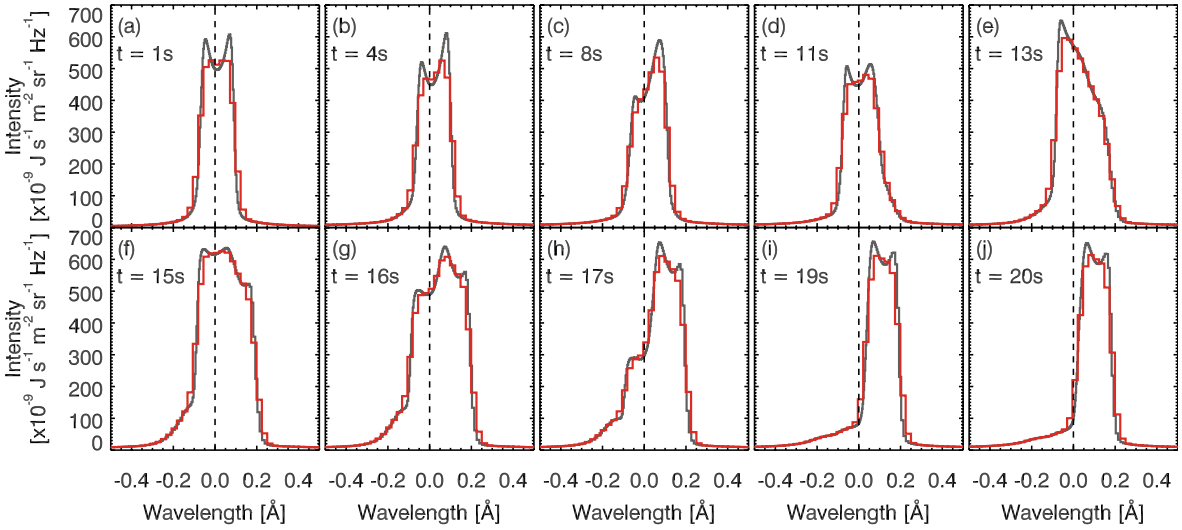

Figure 4.25: *Mg* II *k line profiles from the reference flare simulation. Grey lines are the profiles from RH. The red lines are the those profiles at IRIS resolution.*

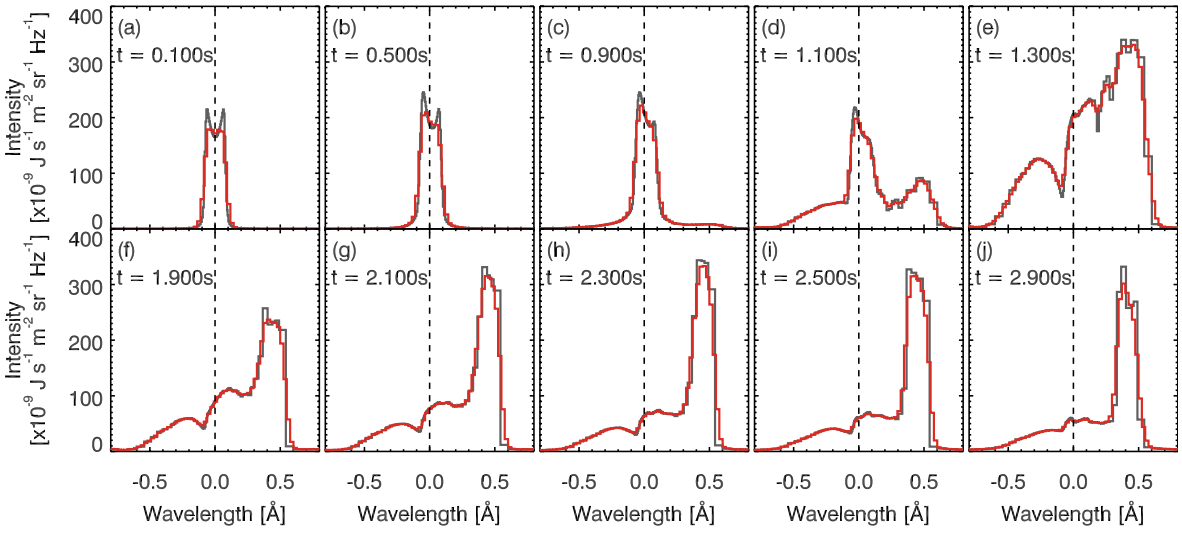

Figure 4.26: *Mg* II *k line profiles from the 2014-Feb-13 flare simulation. Grey lines are the profiles from RH. The red lines are the those profiles at IRIS resolution.*

instrumental spectral point-spread function, which was assumed to be a Gaussian profile with full width at half maximum (FWHM) of 52 mÅ (De Pontieu et al. 2014; Heinzel et al. 2015), before they were re-binned to a wavelength grid with a pixel scale of 25.46 mÅ (the highest resolution of IRIS SG for the NUV - onboard summing can reduce the pixel scale to 50.92 mÅ). Effects of the signal-to-noise ratio (SNR) were ignored since flares have a high count rate (so a high SNR).

The results of this convolution are presented in Figure 4.25 & 4.26 for the reference simulation and the 2014-Feb-13 flare simulation respectively. At times, the k3 and one of the k2 peaks have a similar intensity so that the presence of the reversal can be in doubt (and indeed at times some profiles appear single peaked). At the resolution of IRIS the profiles can lose distinguishing features present in the original profiles. The central reversal disappears or becomes so small that it would likely not be categorised as a reversal. Generally, the asymmetric cores appear similar at IRIS resolution but with different peak intensity. The profiles formed in the downflow, that consist of a stationary component and redshifted component, lose some of the structure in the line core, so that observationally identifying these separate components would likely be more difficult. For example, the small peak redward of line core (~ 0.5) in Figure 4.26(f) is smeared out by the IRIS instrumental profile. The central reversals present in numerical simulations would be challenging to observe.

4.6.3 Finding the Line Centroid Observationally

Previously the theoretical line core has been discussed, defined as the part of the spectral line formed highest in the atmosphere. It was confirmed that the Doppler shift of the line core was well correlated with the velocity of the atmosphere during the flare. Observational identification of the wavelength at which the maximum height of the $\tau_\nu = 1$ surface is reached is not possible, and so a suitable technique to locate the line core must be identified, if we wish to have a diagnostic of atmospheric velocity. To ascertain if locating the line centroid via the quartiles or bisectors methods described in Chapter 3 approximates the theoretical line core well, the synthetic spectra were processed using those techniques. The Doppler shift of the line core was then compared to the line centroid identified by each technique.

Figure 4.27(a,b) shows the comparison of the actual core doppler shift (grey line) compared to the observational methods applied to the reference flare simulation and the 2014-Feb-13 flare simulation, respectively. The quartiles derived velocity is the black line, and the bisector results are shown in colour (70% in blue, 50% in green, & 30% in red). Generally the observational methods do a good job at identifying the trends and direction of flows, but underestimate the magnitude of the velocity. In particular, the observational methods miss the initial rise in velocity present in the simulation. In the reference flare simulation the observational methods are

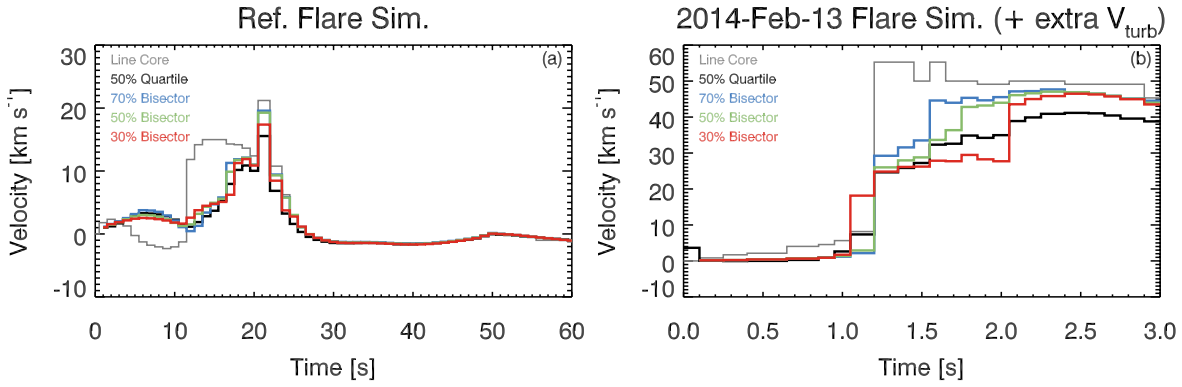

Figure 4.27: *The actual line core doppler shift is shown in grey, alongside the observational derived values. The quartiles method gives the black line. The bisectors are shown in colour, where* 70% *is in blue,* 50% *is in green, &* 30% *is in red Panel (a) shows the reference flare simulation, and panel (b) the 2014-Feb-13 flare simulation.*

influenced by the stronger red peak between $t = 5 - 10$ s so mis-characterise the velocity as a redshift. At larger Doppler shifts, however, the direction of flows is correct. Both simulations show that at times the observational methods do approach the actual line core doppler shift. This happens when the asymmetry is reduced. Stronger asymmetries will adversely affect techniques which use intensity weighting. Since neither technique produced an exact match it will be necessary to further investigate methods to find an observational equivalent of the theoretical line core, or aternatively, a property of the line that gives a good proxy for plasma velocity. Perhaps pre-selecting different line components, if it appears that a stationary and redshifted components are both present, will reduce the impact of asymmetries.

4.6.4 Observed Peak Intensity and Temperature

It was shown in Section 4.5.2 using data at the RH native resolution that the radiation temperature of the line peak can provide a reasonable estimate of the gas temperature. This was repeated using the simulated output at IRIS resolution, with the result that the correlation is not as good. There is a large amount of scatter between $y = x$ and $y = 0.5x$, meaning that the radiation temperature lies between the actual temperature and half the actual temperature (see Figure 4.28). However, as we saw in Figure 4.25 the IRIS instrumental profile can smear out some structure in the line cores so that small peaks are no longer present. When that happens, the line core is identified as

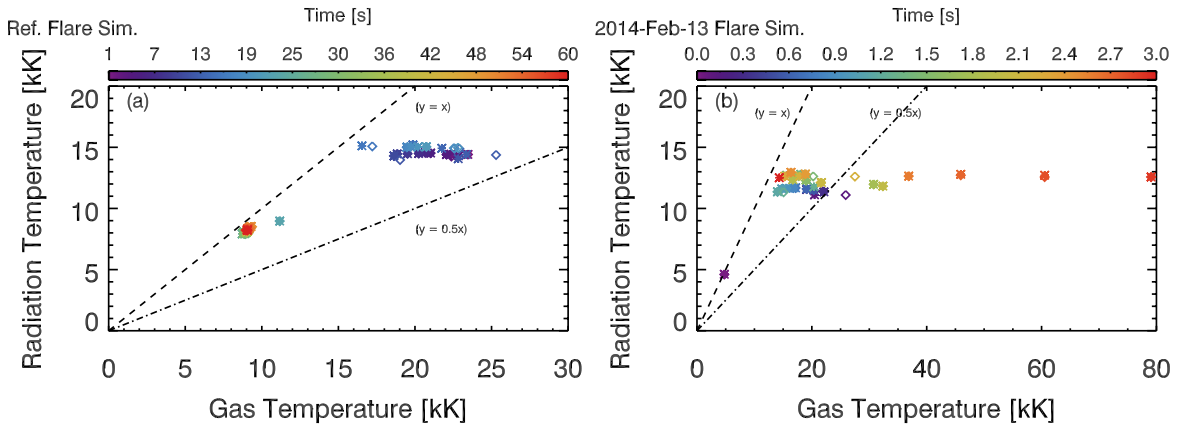

Figure 4.28: *The k (stars) & h (diamonds) line peak intensity, expressed as a radiation temperature versus the atmospheric temperature. Colour represents the time in the simulation. The dashed line is $y = x$ and the dot-dashed line is $y = 0.5x$. Panel (a) shows the reference flare simulation, and panel (b) the 2014-Feb-13 flare simulation, both at IRIS resolution.*

the peak intensity, and the line core radiation temperature had a weaker correlation to the gas temperature.

4.7 Summary and Conclusions

The formation of the Mg II h & k lines during solar flares has been explored using two numerical codes - one, RADYN, simulates the flaring atmosphere and the second, RH, uses snapshots of those atmospheres to produce synthetic spectra. By necessity only 1D effects were considered, but 3D effects can be important when the mean free path of photons exceeds the spatial scales of inhomogeneities since photons can then be absorbed in a distant location. Leenaarts et al. (2013a) investigated this in the quiet Sun, and found that the line core is the most affected by 3D effects, where the line core was brighter when 3D effects were included.

Before investigating the formation, it was first confirmed that Ly β pumping is not an important pathway to populating the Mg II h & k upper levels, that the assumption of CRD is not valid for the line wings, but is sufficient for the line core, and that the Hybrid PRD scheme in RH is suitable for flare studies.

Two flare simulations were used to produce Mg II spectra, and their formation properties were studied in detail. Additionally, the microturbulence was increased

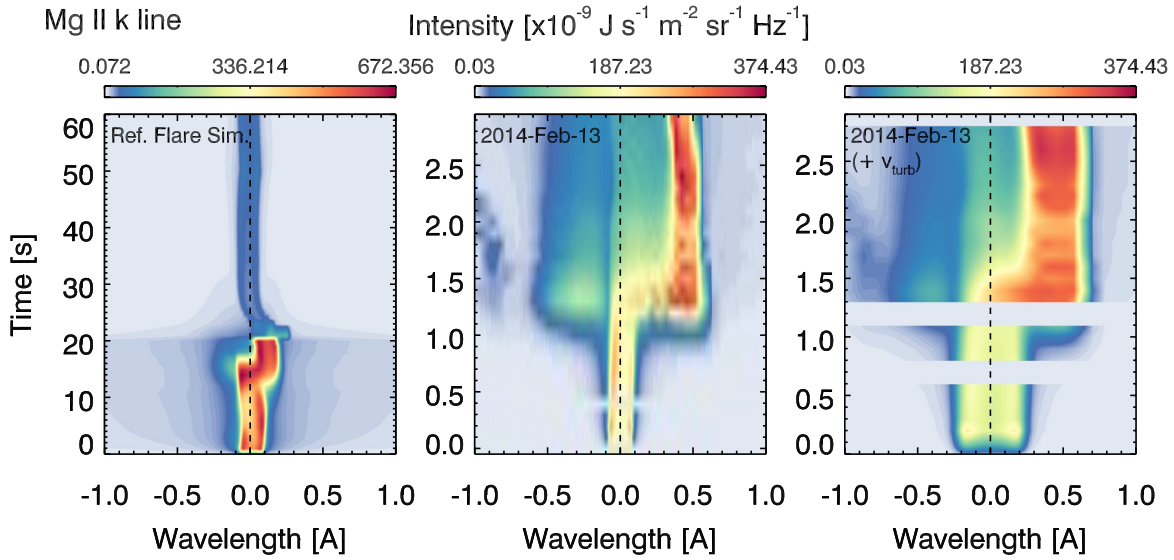

Figure 4.29: *Mg II k line profiles from the three simulations, plotted with wavelength along the x-axis and time. along the y-axis. Missing data is when the simulation did not converge. Colour represents intensity.*

in one of those simulations. Generally, the lines were enhanced by 1-2 orders of magnitude in the line core compared to a non-flaring atmosphere and enhanced to a lesser extent in the line wings. Doppler shifts were seen in the line core, with redshifts of a few tens of km s^{-1} present once the condensation developed in the atmosphere. Asymmetries both of the k2 peaks, and in the line wings were present. At times, two components to the line were present, one Doppler shifted and formed slightly higher in the atmosphere by a few tens to 100 km, and one stationary (or less shifted). The most Doppler shifted component was the more intense. Cores were usually centrally reversed, though shallow and at times difficult to discern from the k2 peaks. Indeed, a few profiles appeared single peaked. The subordinate lines were in emission. Taking the ratio of k to h line intensity shows that, like observations, the lines are optically thick throughout. Changes to this ratio over time reflect the varying source functions of the line which are related to the population ratio of the upper lines. Two important discrepancies between the models and the observations are the line width, and line intensity.

Figure 4.29 shows a 'summary' of the k-line intensity as a function of wavelength and time for each of the simulations, with colour representing intensity. From this the width of the lines, intensity, Doppler shifts and asymmetries can be seen. Comparing

to observed profiles (c.f. Chapter 3) the synthetic h & k lines have much narrower wings than the observations show, and while increasing microturbulence (third panel) widens the doppler core of the line, the wings are still too narrow. From this figure it is clear that while the general behaviour between the simulations is the same, there are differences (intensity, width, enhancements far into the wings, depth of reversal) depending on the flare heating.

Studying the line contribution functions established the formation properties. In summary, the common features of the line formation were:

- During the flare, the higher temperatures in what was the pre-flare upper chromosphere means that Mg II was ionised to Mg III at those heights, but more modest temperature enhancements in the lower-mid chromosphere of a few thousand kelvin increased the population of the k & h line upper levels there. This had the result that the $\tau_\nu = 1$ surface was driven deeper into the atmosphere to around 1 – 1.1 Mm. The formation 'structure' was largely preserved. That is, the line core was formed highest, followed by the emission peaks (if present) and then the line wings at decreasing height. The core region was formed just below the temperature rise from a few $\times 10,000$ K to $> 100,000$ K, and emission peaks formed only a few 10s-100 km deeper. Line wings were formed higher than in the quiet Sun (at a height of 650 km), but did not vary much during the flare.

- The source function of the line core was stronger than the line wings, increasing in response to the steep temperature gradients in the chromosphere. While the wings were enhanced and tracked the Planck function's increase in the lower atmosphere, the temperature increase was not as strong as in the mid-upper atmosphere resulting in narrow profiles.

- Shallow, or absent, central reversals resulted from stronger coupling to the Planck function (and therefore the local temperature) due to the enhanced electron density. Flows at the formation height of the line core shifted the opacity structure of the atmosphere. The absorption profiles were also Doppler shifted. The result of the changing opacity structure was that the $\tau_\nu = 1$ theoretical line core was shifted from the rest wavelength and was asymmetric, so that the emergent intensity was also Doppler shifted. For large Doppler shifts, the core was formed close in height to one of the k2 emission peaks

(depending on direction of the flow), so that they were close in intensity. At the same time, the other emission peak would be formed somewhat lower (due to the asymmetric $\tau_\nu = 1$ surface) in a region of stronger source function so that it was more intense, with the end result being an asymmetric line. An upflow would result in a stronger k2r peak, and a downflow would result in a stronger k2v peak. When the profiles appeared single peaked this was a result of the close formation height of the line core components so that intensity differences were small.

- The contribution to the emergent intensity of the line originated from along or near to the $\tau_\nu = 1$ curve, meaning that the line was optically thick during the flare. At wavelengths further into the line wings the contribution to the emergent intensity was greatest near the $\tau_\nu = 1$ curve, but often a much larger region contributed to wing intensity than in the quiet Sun (spanning several hundred km).

- Optically thin contributions were produced from mass motions within the plasma above the main formation height of the line, resulting in some additional asymmetry in the line wings. Flows meant that the emission from lower density regions was Doppler shifted to wavelengths at which the optical depth was low at that height (peaks in χ_ν/τ_ν). Such asymmetries can be exploited to infer the strength or direction of flows above the core formation height (e.g the patch near −1Å in panels 2 & 3 of Figure 4.29).

- Strong, dense, condensations shifted the whole line core of the line to the red, where the enhanced density was sufficient to raise the height of the $\tau_\nu = 1$ curve to track the leading edge of the condensation. Doppler shifts reduced as the condensation propagated deeper, past the main formation height of the line. At these times the line core appeared to have more than one component, with a lower intensity, less shifted component alongside the more intense component. Compression of the chromosphere pushed the formation height of this second component even lower, so that it was formed in a region of smaller temperature (and therefore source function), so the intensity of this component reduced. These could appear as multiple peaked profiles, or asymmetric profiles.

Degrading the profiles to IRIS resolution can reduce or mask the central reversal.

Observations would likely show a more single peaked profiles. Rubio da Costa et al. (2016) also showed that artificially increasing the electron density in the h & k formation region could increase the coupling to the local temperature even more, so that the profiles are definitely single peaked. The challenge then, is to have flare simulations that self-consistently reproduce the high electron densities required, and to identify under what conditions flare observations do show reversals. For example, Liu et al. (2015) noted that flare profiles that were co-spatial with an HXR source had reversals and became single peaked following the HXR peak. Since the profiles viewed at IRIS resolution smear out some important details that might be present in the real spectra it is recommended that for flares *no on-board summing* takes place and that full IRIS resolution is used.

Carlsson et al. (2015) modelled Mg II profiles in a plage atmosphere, finding that they too were formed at the base of the transition region and that profiles were not wide enough, even with microturbulent velocities similar to those used here. They did note that a chromospheric temperature rise located deeper in the atmosphere (at densities large enough for the line wing formation) resulted in wider profiles. So, like in flares, while microturbulent broadening can play a role, it cannot explain the wide wings. Opacity broadening in flares must play a role also. Opacity broadening is the name given to additional broadening caused by the behaviour of the source function with height in the chromosphere (see, e.g., Rathore & Carlsson 2015; Rathore et al. 2015). Narrow profiles occur when the source function increases steeply in the upper atmosphere. This would result from a large temperature gradient in the mid-upper chromosphere, with a relatively much cooler lower chromosphere. The emergent profile has more intense k2 an k3 components due to the stronger source function, compared to the k1 and line wings, which are formed deeper with smaller source functions. If, on the other hand, the temperature rise began deeper or was less steep, the difference in the strength of the source functions between the k2/k3 and k1 components would be smaller and the lines wider. In the flare simulations presented here this is indeed the case, with temperature at the core formation height much larger than the plateau in the chromosphere. The source function of the line wings is therefore much less than the core source function (albeit, still enhanced over the quiet Sun), and the emergent intensity smaller. If the large temperature rise occurred deeper, just above the continuum formation height, and had a gentler increase to the transition region, then the source function of the wings would be greater and the

profiles wider. To explain the wide profiles from an increased opacity broadening factor, would require a hotter lower chromosphere than is produced by current simulations.

While concrete diagnostics have yet to be developed, these lines are still important for illustrating flaring processes. We have learned that asymmetries in the line wings can be the result of optically thin contributions from high lying velocity gradients, that the shift of the line core can be used to approximately infer the atmospheric velocity, that shallower central reversals can tell us that electron density is greater, and that the radiation temperature can be used to give reasonable estimate of the range of temperatures in the atmosphere. Since opacity broadening is important in the line wings, then the width tells us about the temperature structure between the wing formation height and the core formation height (narrow profiles are a large temperature difference and vice versa).

Chapter 5

Alfvén Wave Heating in Solar Flares

The research presented in this chapter was published in Kerr et al. (2016)

5.1 Alfvén Wave Heating in the Chromosphere

As discussed in Chapter 1, the standard model (or electron beam model) and collisional thick target model (CTTM), describes energy transport by beams of non-thermal electrons that stream along field lines, depositing their energy collisionally in the chromosphere. The standard model has been successful in explaining many of the observed properties of solar flares, and RHESSI observations of solar X-rays are often used to compute the non-thermal electron flux spectrum (e.g. Holman et al. 2003). These electron spectra can be used as input to numerical codes for simulating solar flares, as in the preceding chapters. Stellar flares are also often simulated, and interpreted observationally, in the framework of the solar flare standard model and CTTM (e.g. Allred et al. 2006; Kowalski et al. 2012, 2015). While the electron beam model of energy transport is attractive because it can neatly explain many of observed properties of flares, there are some as-yet unexplained observations that are difficult to reconcile with a scenario that includes *only* energy transport by electron beams, for example evidence of heating at the TMR and below (c.f Chapter 1)

It has been suggested that additional or alternative transport and heating mechanisms could be at play that acts either in tandem with electron beam energy transport or instead of (e.g Emslie & Sturrock 1982; Metcalf et al. 1990; Fletcher & Hudson 2008). Any such mechanism must be able to heat the chromosphere (leading to

the enhanced radiation observed), reproduce the observed high velocity upflows (chromospheric evaporation) and explain the presence of accelerated electrons (localised HXR bremsstrahlung footpoint sources indicate unambiguously the presence of accelerated electrons in the flaring chromosphere).

Alfvén waves are transverse incompressible MHD waves that propagate along the magnetic field, and which have been shown to be near ubiquitous in the quiet corona (McIntosh et al. 2011). Collisional damping of Alfvén waves in the chromosphere was studied by De Pontieu et al. (2001) as a potential quiet Sun heating mechanism. This and further work found that upward propagating high frequency ($f > 0.6$ Hz) waves from the photosphere were efficiently damped by collisional dissipation in the chromosphere, mainly via ion-neutral collisions (Leake et al. 2005; Khodachenko et al. 2004). Since a solar flare is, fundamentally, a large scale restructuring of the solar magnetic field it is very reasonable to expect that downward-propagating Alfvén waves would be produced by such perturbations. Studying their role as a potential flare heating mechanism is logical.

Downward-propagating Alfvén waves were studied in the flare context by Emslie & Sturrock (1982) in an effort to explain TMR heating during solar flares. For waves with frequencies $f = 1 - 10$ Hz and $k_x \approx 1 \times 10^{-5}$ cm^{-1} they demonstrated that dissipation of Alfvén waves in the TMR could deliver enough energy to heat the region by a few hundred Kelvin. This matches the observations of TMR heating reported by Machado et al. (1978). In this scenario, Alfvén waves are produced by perturbations in the coronal magnetic field, and are damped by the chromospheric plasma via resistive dissipation, resulting in heating. The discussion of Alfvén wave flare heating was renewed by Fletcher & Hudson (2008) who explored the viability of Alfvén waves as an energy transport mechanism. They argued that a 5-10% perturbation of the coronal magnetic field could supply enough energy to heat the whole chromosphere, not just the TMR, without the need for electron beams. Additionally, they proposed mechanisms to accelerate electrons *in situ* that could explain the observed chromospheric HXR sources, drawing comparisons to magnetospheric physics and the acceleration of auroral electrons. McClements & Fletcher (2009), Haerendel (2012), and Melrose & Wheatland (2013, 2014) also discussed the ability of Alfvén waves to accelerate electrons. The details of any such process have yet to be worked out fully.

Russell & Fletcher (2013) showed that while the extreme temperature and density

gradients through the TR result in reflections of Alfvén waves travelling downwards from the corona, a significant fraction of the Alfvén wave energy flux can be transmitted through to the chromosphere, given appropriate wave parameters. These transmitted waves were subsequently damped by ion-neutral collisions and an enhanced electron resistivity. Short period (P< 1 s) waves were damped effectively with whereas long period ($P > 10$ s) waves were only damped by $\sim 7\%$. The bulk of the damping occurred in the TMR, but heating was also observed in the upper chromosphere.

Using the 1D hydrodynamics flare code HYDRAD (Bradshaw & Mason 2003) to investigate Alfvén wave heating of the upper chromosphere, Reep & Russell (2016) followed the approach of Emslie & Sturrock (1982), but using ambipolar resistivity rather than classical resistivity employed by Emslie & Sturrock (1982). Ambipolar resistivity accounts for the ion-neutral collisions that have proved to be important for Alfvén wave damping (De Pontieu et al. 2001). In the pre-flare atmosphere this can result in a resistivity that is more than two orders of magnitude larger than the classical result in parts of the chromosphere where ion-neutral collisions are important. During the flare the relative difference will be variable according to the evolution of the atmosphere since the collisional frequencies are functions of the atmospheric structure. It was found that for certain Alfvén waves parameters, the waves were damped in the mid-upper chromosphere resulting in strong heating that compared well to a standard electron beam heated simulation. Other parameters produced results that were consistent with the findings of Emslie & Sturrock (1982), with strong TMR heating, but negligible heating to the upper chromosphere. Alfvén wave flare simulations using HYDRAD also produced explosive chromospheric evaporation for wave numbers $k_x > 1 \times 10^{-4}$ cm^{-1}, a key result that Alfvén wave energy transport must achieve.

It must be noted that while low frequency (high period) Alfvén waves have been observed in the solar atmosphere (e.g McIntosh et al. 2011), there have been no observations of the high frequency ($f = 1 - 100$ Hz) Alfvén waves that are considered suitable for flare energy transport by Emslie & Sturrock (1982), Russell & Fletcher (2013) & Reep & Russell (2016). McIntosh et al. (2011) report wave periods of $\sim 100 - 600$ s, but using observations at a higher spatial resolution than those of McIntosh et al. (2011), Kuridze et al. (2012) was able to observe periods down to

~ 70 s. Current space-based telescopes lack the temporal and spatial resolution to observe high frequency Alfvén waves, and the ground-based study of Kuridze et al. (2012) was limited to a cadence of 7 s. So, the lack of observations of high frequency waves may be due to instrument resolution.

Additionally, there have been arguments against Alfvén wave energy transport as an explanation for the observed heating at the temperature minimum regin based on time delays. Emslie & Sturrock (1982) quoted a travel time from energy release site to the TMR of $t \sim 30$ s. However, Metcalf et al. (1990) noted that the result of Emslie & Sturrock (1982) was dependent on the magnetic field geometry, and that the delay may increase to ~ 60 s based on their estimates of the magnetic field at the height of their observations. Metcalf et al. (1990) reported a time delay between the onset of HXR and the heating of the TMR (as inferred from inversions of the Mg I line) of ~ 2 minutes. They rejected Alfvén wave heating as the cause of their observed TMR heating because the wave travel time was too short to explain this delay. As Russell & Fletcher (2013) notes, though, the travel time and associated time delays during the flare would depend on the local Alfvén speed which is a function of the density and magnetic field strength structure, which is not well constrained.

Ultimately, the ability to discriminate between models of energy transport is required, which necessitates the study of chromospheric radiation. Coronal observations, while useful, will tend to be ambiguous since strong mass flows and the optically thin nature of the radiation will smear and superpose. This might obscure subtle signatures of energy transport. The chromosphere, however, produces some radiation that is optically thick, allowing us to probe the atmosphere at different locations. Since this radiation carries information about multiple locations there is the opportunity to identify observational differences resulting from different energy transport mechanisms. High spatial, spectral and temporal resolution data of chromospheric and TR radiation are now available from the IRIS spacecraft. Additionally, with the upcoming ground-based Daniel K. Inouye Solar Telescope (DKIST) we will have new high resolution observations in the optical and infrared (IR). These resources provide the opportunity to test simulations of energy transport in flares by comparing the synthetic spectra output by advanced models to observations.

This chapter presents the incorporation of an approximated form of Alfvén

wave heating into the RADYN code, describes some initial results of varying wave parameters, and finally compares in detail an Alfvén wave simulation of a flare with a standard electron beam simulation. In these initial experiments each energy transport mechanism acts alone, but in future experiments the scenario in which Alfvén wave energy transport is complementary to non-thermal electron beam energy transport will be explored.

5.2 Implementing Alfvén Wave Heating in RADYN

The mathematical framework using the WKB approximation for downward propagating Alfvén waves (AW) to treat heating in the flaring chromosphere was developed by Emslie & Sturrock (1982), and updated by Reep & Russell (2016). These authors constructed and solved the wave equation for Alfvén waves that travel along a 1D flux tube with finite resistivity, finding an expression for the amplitude of the wave as a function of distance along the tube. From this, the decrease in the Poynting flux could be calculated as a function of height, and this decrease in wave energy flux is assumed to heat the surrounding plasma. Their approach is implemented here to include a heating rate due to the dissipation of Alfvén Waves, Q_{AW}, into RADYN. This heating rate is then added as an additional term in the equation of internal energy conservation.

The WKB approximation is an assumption that the parallel wavelength is less than or equal to the scale lengths of the Alfvén speed so that reflections are considered negligible. This is valid in the chromosphere for $f \geq 1$ Hz. Russell & Fletcher (2013) found negligible reflections of AWs once in the chromosphere, for periods equal to or shorter than 1 s. This approximation allows the analytic solution found by Emslie & Sturrock (1982) for the period-averaged Poynting flux as a function of height, which is used to compute the instantaneous heating rate. This simple approach is appropriate for initial investigations. A full model wave of MHD wave propagation is significantly more challenging, particularly if we also wish to have the spatial and temporal resolution required to simulate flares. However, wave reflections are not accounted for, and the waves are modelled as travelling instantaneously though the flare loop.

5.2.1 Supporting Variables

To compute the heating rate (discussed below in § 5.2.2) several additional variables must be calculated by RADYN. The variables presented in this section were added as modules to be included by RADYN when heating via Alfvén wave dissipation is being modelled. It is necessary to compute: the collisional frequencies that contribute to the resistivity, the resistivity itself, the magnetic field strength, the Alfvén speed, and the perpendicular wave number.

The Poynting flux is damped via collisional dissipation, and so first the collisional frequencies for electron-neutral collisions, $\nu_{e,n}$, electron-ion collisions, $\nu_{e,i}$, and neutral-ion collisions, $\nu_{n,i}$, were computed. In the following expressions the subscripts i, n, t, and e refer to ions, neutrals, total, and electrons respectively. Geiss & Bürgi (1986) quote an expression for the electron-neutral collisional frequency,

$$\nu_{e,n} = 6.97 \times 10^{-14}\ T^{0.1} n_H, \tag{5.1}$$

where T is temperature in Kelvin, and n_H is the number density of neutral hydrogen in m^{-3}. There are other formulae for $\nu_{e,n}$ quoted in the literature, for example $\nu_{e,n} = 4.5 \times 10^{-15}\ T^{1/2}\ (1 - 1.35 \times 10^{-4} T)\ n_H$ (Schunk & Nagy 2009), and $\nu_{e,n} = 1.95 \times 10^{-16}\ T^{1/2}\ n_H$ (Priest 1982). These three expressions are shown as a function of height in Figure 5.1(a), at $t = 0$ in a RADYN atmosphere. As can be seen, the Priest (1982) expression is around one order of magnitude lower than the other two values in the lower atmosphere. The expression from Schunk & Nagy (2009) produces values that are around 1.5 times less than the Geiss & Bürgi (1986) derived values. The Geiss & Bürgi (1986) expression was chosen since it is close to the Schunk & Nagy (2009) value, and avoids the need to deal with the negative frequencies that result at high temperatures from the Schunk & Nagy (2009) expression. At high temperatures $\nu_{e,n}$ is not the dominant collisional frequency and is, anyway, small due to the lack of neutrals. Setting negative values of $\nu_{e,n}$ to zero in the code would not greatly affect the final result of Q_{AW}, but using Eq 5.1 allows us to avoid this eventuality.

The electron-ion collisional time, τ_e, is quoted by Holman (2012) as

$$\tau_{e,i} = \frac{3}{4}\left(\frac{m_e}{2\pi}\right)^{1/2}\left(\frac{k_b\ T}{n_e\ \lambda\ e^4}\right)^{3/2}, \tag{5.2}$$

where m_e is the electron mass, k_b is Boltzmann's constant, n_e is electron number density, e is electron charge and and λ is the Coulomb logarithm:

$$\lambda = \begin{cases} 8.96 - \ln(\overline{Z} n^{1/2} T^{-3/2}) & , T < 1.16 \times 10^5 \overline{Z^2} \\ 14.6 + \ln(n^{-1/2} T) & , T > 1.16 \times 10^5 \overline{Z^2}. \end{cases}$$

Holman (2012) notes that the mean atomic number weighted by the relative ion abundance is $\overline{Z} \approx 1.1$, and the weighted mean square atomic number us $\overline{Z^2} \approx 1.4$ is the approximate weighed mean. The electron-ion collisional frequency, $\nu_{e,i}$, is then,

$$\nu_{e,i} = 1/\tau_{e,i}. \tag{5.3}$$

Finally, the neutral-ion collisional frequency, $\nu_{n,i}$, is discussed by Russell & Fletcher (2013), correcting their typo in the first term involving T which should be $T^{1/2}$, and in Schunk & Nagy (2009),

$$\begin{aligned} \nu_{n,i} = 2.65 \times 10^{-16}\ T^{1/2}\ (1 - 0.083\ \log_{10}\ T)^2\ n_p \\ + 2.11 \times 10^{-15}\ (n_e - n_p), \end{aligned} \tag{5.4}$$

where n_e and n_p, the proton number density, are in units of m^{-3}. Note that we have taken the number of ions to be $n_e - n_p$. Due to momentum conservation we can relate the ion-neutral collisional frequency, $\nu_{i,n}$, to the neutral-ion collisional frequency:

$$\rho_n \nu_{n,i} = \rho_i \nu_{i,n}. \tag{5.5}$$

Here ρ_i is the mass density of ions, ρ_n is the mass density of neutrals and $\nu_{i,n}$ is the ion-neutral collisional frequency. We will utilise Eq 5.5 when discussing the Cowling resistivity below. The three frequencies $\nu_{n,i}$ $\nu_{e,n}$ and $\nu_{e,i}$ are plotted as a function of height in Figure 5.1(b) which shows that $\nu_{e,n} > \nu_{e,i}$ in the lower atmosphere, while in the mid-to-upper chromosphere (and into the TR) the electron-ion collisions dominate. This is true for whichever expression we choose to use for $\nu_{e,n}$, and so while recognising the uncertainty in the choice of expression for $\nu_{e,n}$, all three choices at least follow the same pattern relative to the other collisional frequencies. The collisional frequencies that are shown in Figure 5.1(b) are the $t = 0$ values for the QS:SL:LT radiative equilibrium starting atmosphere. If a different starting atmosphere is used then these frequencies will have a different height

dependence. For example, using the VALC or FALC atmospheres, or the semi-empirical atmosphere of Avrett & Loeser (2008) will not produce the small peak in $\nu_{e,i}$ near 1.6 Mm, which is due to the increased electron density at that height in the radiative equilibrium atmosphere (the electron density stratification is shown in Figure 2.1). For comparison to the starting atmsphere used here the collisional frequencies as a function of height in the Avrett & Loeser (2008) atmosphere can be seen in Figure 1(b) in Tu & Song (2013), and the neutral-ion collisional frequency in the VALC atmosphere is shown in Figure 2 in De Pontieu et al. (2001).

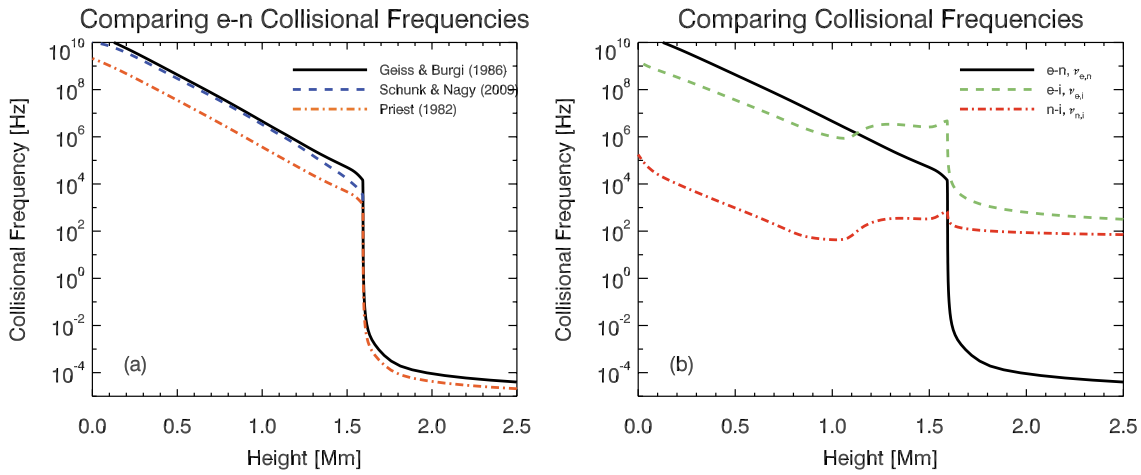

Figure 5.1: *(a) The electron-neutral collisional frequency, using the three expressions found in the literature: Geiss & Bürgi 1986 (black solid), Schunk & Nagy 2009 (blue, dashed), Priest 1982 (orange, dot-dashed). (b) The electron-ion (green, dashed), electron-neutral (black, solid) and neutral-ion (red, dot-dashed) collisional frequencies.*

Damping via collisions is expressed as a non-zero resistivity of the plasma through which Alfvén waves propagate. Ohm's law was written as $\eta \mathbf{j} = \mathbf{E} + \frac{1}{c}\mathbf{v} \times \mathbf{B}$, where η resistivity. Emslie & Sturrock (1982) used a classical resistivity in their derivation of the wave equation However, it has been shown that ion-neutral collisions are important for wave dissipation in the chromosphere (e.g. De Pontieu et al. 2001; Khodachenko et al. 2004; Leake et al. 2005), and so to better account for these interactions Reep & Russell (2016) used an ambipolar resistivity, rather than the classical resistivity. Their approach is employed here.

If the effect of neutrals is included then we can write $\mathbf{E} + \frac{1}{c}\mathbf{v} \times \mathbf{B} = \eta_{\perp} j_{\perp} + \eta_{\parallel} j_{\parallel}$,

where $\eta_\perp$ is the perpendicular resistivity and $\eta_\parallel$ is the parallel resistivity. In this case the resistivity perpendicular to the magnetic field in wave equation contains an additional contribution due to ion-neutral collisions (A. Russell *private communication*, 2016). This is the so-called Cowling resistivity, η_C (Cowling 1956). Reep & Russell (2016) obtained the frequency-dependent expression for the Cowling resistivity. The parallel resistivity is written as:

$$\eta_\parallel = \frac{m_e(\nu_{e,i} + \nu_{e,n})}{n_e\, e^2}. \tag{5.6}$$

The perpendicular resistivity is:

$$\begin{aligned} \eta_\perp &= \eta_\parallel + \eta_C \\ \eta_\perp &= \eta_\parallel + \frac{B^2\rho_n}{c^2\nu_{n,i}\rho_t^2}\frac{1}{(1+\xi^2\vartheta^2)}. \end{aligned} \tag{5.7}$$

In Eq 5.7 the Cowling resistivity is the second part of the addition, where ρ_t is the total mass density, c is the speed of light, B is the magnetic field strength, and the multiplicative factor $1/(1+\xi^2\vartheta^2)$ is the frequency-dependence. Here, ξ is the hydrogen ionisation fraction, $\vartheta = \omega/\nu_{ni}$, and $\omega = 2\pi f$, for wave frequency f. In the low frequency limit ($\vartheta << 1$) the Cowling term reduces to the wave-frequency independent expression,

$$\eta_C \approx \frac{B^2\rho_n}{c^2\nu_{n,i}\rho_t^2},\ \vartheta << 1 \tag{5.8}$$

For the majority of situations, $\omega < \nu_{n,i}$, but we retain the full wave-frequency dependent form of η_C to be complete. Note that ion-neutral collisions add resistivity perpendicular to the field, but Eq 5.7 is in terms of $\nu_{n,i}$ as Eq 5.5 is used to substitute $\nu_{n,i}$ for $\nu_{i,n}$.

RADYN is a 1D radiation hydrodynamics code, and so does not model magnetic fields, but we wish to model the heating rate from the perturbation of a magnetic field. As will be shown, Q_{AW} does not require the perturbation itself to be simulated, it models the heating rate from an injected energy flux. This energy flux is dissipated via resistivity, the terms for which include the magnetic field strength. A magnetic field strength is imposed at $t = 0$, which evolves with height as a function of pressure, $P(z)$ (Zweibel & Haber 1983). If we express the photospheric magnetic field strength

as B_{ph}, and the photospheric pressure as P_{ph}, then the magnetic field strength is computed as:

$$B(z) = B_{ph}\left(\frac{P(z)}{P_{ph}}\right)^{\alpha}, \tag{5.9}$$

where the exponent α must be less than 0.5 (see § 5.3). RADYN employs an adaptive grid so $B(z)|_{t=0}$ is interpolated to the new grid at the start of each timestep. The magnetic field does not influence the dynamics or radiation transfer calculations directly, only via the value of Q_{AW}.

The geometry of a flux tube can be captured even in a 1D treatment. Magnetic flux is constant within a flux tube (by definition), and so the tube area decreases as magnetic field increases. The perpendicular wavelength of an Alfvén wave would decrease with decreasing area. The magnetic field imposed at $t = 0$ increases with depth into the atmosphere, so area must decrease. Using the scaling of the magnetic field, the effect of decreasing area can be applied to the perpendicular wavenumber in our 1D model. The perpendicular wave number is allowed to vary either linearly with $B(z)$ or as the square root of $B(z)$:

$$k_x(z) = k_{x,0}\left(\frac{B(z)}{B_0}\right), \tag{5.10a}$$

$$k_x(z) = k_{x,0}\sqrt{\frac{B(z)}{B_0}}, \tag{5.10b}$$

where $k_{x,0}$ is the perpendicular wave number at the loop apex and B_0 is the magnetic field at the loop apex. These represent different loop geometries. A linear variation models expansion of the loop in one direction and variation with the square root of $B(z)$ models a flux tube that expands radially with height. Figure 5.2 shows an example of $B(z)$ and $k_x(z)$ in a RADYN atmosphere, where $B_{ph} = 1000$ G, $\alpha = 0.139$ and $k_{x,0} = 4\times10^{-4}$ cm^{-1}. A linear variation model gives a higher gradient of k_x in the chromosphere.

Finally, we compute the Alfvén speed, v_A. Reep & Russell (2016) derived an expression for the Alfvén speed that includes the effects of neutrals,

$$v_A(z) = \frac{B}{\sqrt{4\pi\rho_t}}\left(\frac{1+\xi\vartheta^2}{1+\xi^2\vartheta^2}\right)^{1/2} \tag{5.11}$$

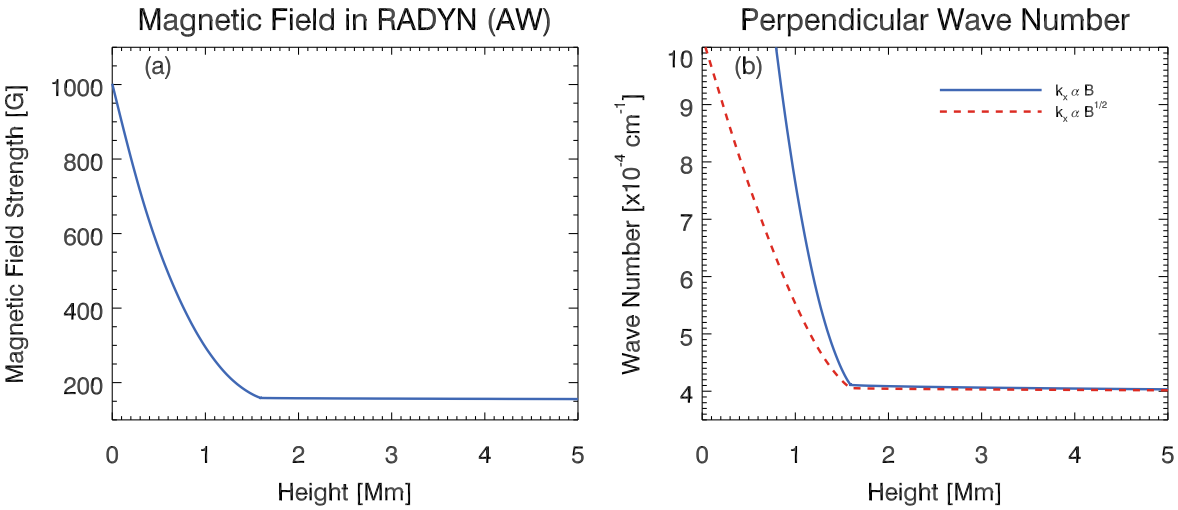

Figure 5.2: *(a) The magnetic field as a function of height, where* $B_{ph} = 1000$ *G &* $\alpha = 0.139$*. (b) The perpendicular wave number as a function of height, where* $k_{x,0} = 4 \times 10^{-4}$ cm^{-1}*. The blue solid line shows the case where* k_x *is linear with* $B(z)$ *(Eq. 5.10a), and the red dashed line shows the case where* k_x *varies as the square root of* $B(z)$ *(Eq. 5.10b).*

In the low frequency limit ($\vartheta << 1$, when $\omega << \nu_{n,i}$) this reduces to $v_A = \frac{B}{\sqrt{4\pi\rho_t}}$, and in the high frequency ($\vartheta >> 1$, when $\omega >> \nu_{n,i}$), or in the fully ionised case, we obtain the standard result $v_A = \frac{B}{\sqrt{4\pi\rho_i}}$.

5.2.2 Alfvén Wave Heating Rate

The period-averaged Poynting Flux is $S(z) = \frac{1}{8\pi} v_A(z) A(z)^2$, where A(z) is the amplitude of the perturbation. Emslie & Sturrock (1982) derived an expression for the wave amplitude that satisfies the wave equation in the case of a non-zero resistivity and an Alfvén speed that varies with height:

$$A(z) = A_0 \left(\frac{v_A(z)}{v_{A,0}} \right)^{-1/2} \exp\left\{ -\frac{1}{2} \int_0^z \frac{\mathrm{d}z'}{L_D(z')} \right\}, \tag{5.12}$$

where A_0 and $v_{A,0}$ are the amplitude and Alfvén speed at a distance $z = 0$ along the flux tube (i.e. at the apex of the loop), and $L_D(z)$ is the effective damping length as a function of height along the loop. The period-averaged Poynting flux can then be written as a function of height,

$$S(z) = \frac{1}{8\pi} v_A(z) A_0^2 \left(\frac{v_A(z)}{v_{A,0}}\right)^{-1} \exp\left(-\int_0^z \frac{\mathrm{d}z'}{L_D(z')}\right). \tag{5.13}$$

Gathering the terms that represent the top of the loop, and defining S_0 as the initial time-averaged Poynting flux, then $S_0 = (1/8\pi)\, v_{A,0}\, A_0^2$ and Eq 5.13 simplifies to

$$S(z) = S_0 \exp\left(-\int_0^z \frac{\mathrm{d}z'}{L_D(z')}\right). \tag{5.14}$$

The damping comprises parallel and transverse damping, such that the effective damping length is

$$\frac{1}{L_D(z)} = \frac{1}{L_\perp(z)} + \frac{1}{L_\parallel(z)}. \tag{5.15}$$

where the transverse and parallel damping lengths are defined as

$$L_\perp(z) = \frac{4\pi v_A}{c^2\, \eta_\parallel k_x^2}, \tag{5.16a}$$

$$L_\parallel(z) = \frac{4\pi v_A^3}{c^2\, \eta_\perp \omega^2}. \tag{5.16b}$$

Substituting these into Eq 5.15 gives us the effective damping length

$$L_D(z) = \frac{4\pi v_A^3}{c^2\, (\eta_\parallel k_x^2 v_A^2 + \eta_\perp \omega^2)}. \tag{5.17}$$

As the Alfvén wave propagates along the field, the Poynting flux is damped according to Eq 5.14. The decrease in Poynting flux is assumed to heat the plasma so that the volumetric heating rate, measured in units of ergs s^{-1} cm^{-3}, is defined as

$$Q_{AW}(z) = \frac{\mathrm{d}S}{\mathrm{d}z} \tag{5.18}$$

Often the heating rate per unit mass, $Q_{AW}(z)/\rho(z)$, is discussed, with units of erg s^{-1} g^{-1}. Figures 5.3a,b, & c show the damping length, the normalised Poynting flux and the resulting normalised volumetric heating rate respectively, at $t = 0$ in a simulation where $f = 10$ Hz, $k_{x,0} = 1 \times 10^{-4}$ cm^{-1}, $S_0 = 1 \times 10^8$ erg s^{-1} cm^{-2}, $B_{ph} = 1000$ G, and $\alpha = 0.139$. An Alfvén wave with these properties would be undamped in the corona due to the large damping length (in excess of 1000 Mm), but in the upper chromosphere (just below the TR) the damping length reduces considerably and the Poynting flux decreases sharply over a relatively small region.

With these properties the wave deposits energy in the mid-upper chromosphere. The time evolution of these properties, and the atmospheric response to Q_{AW} is discussed in § 5.4.

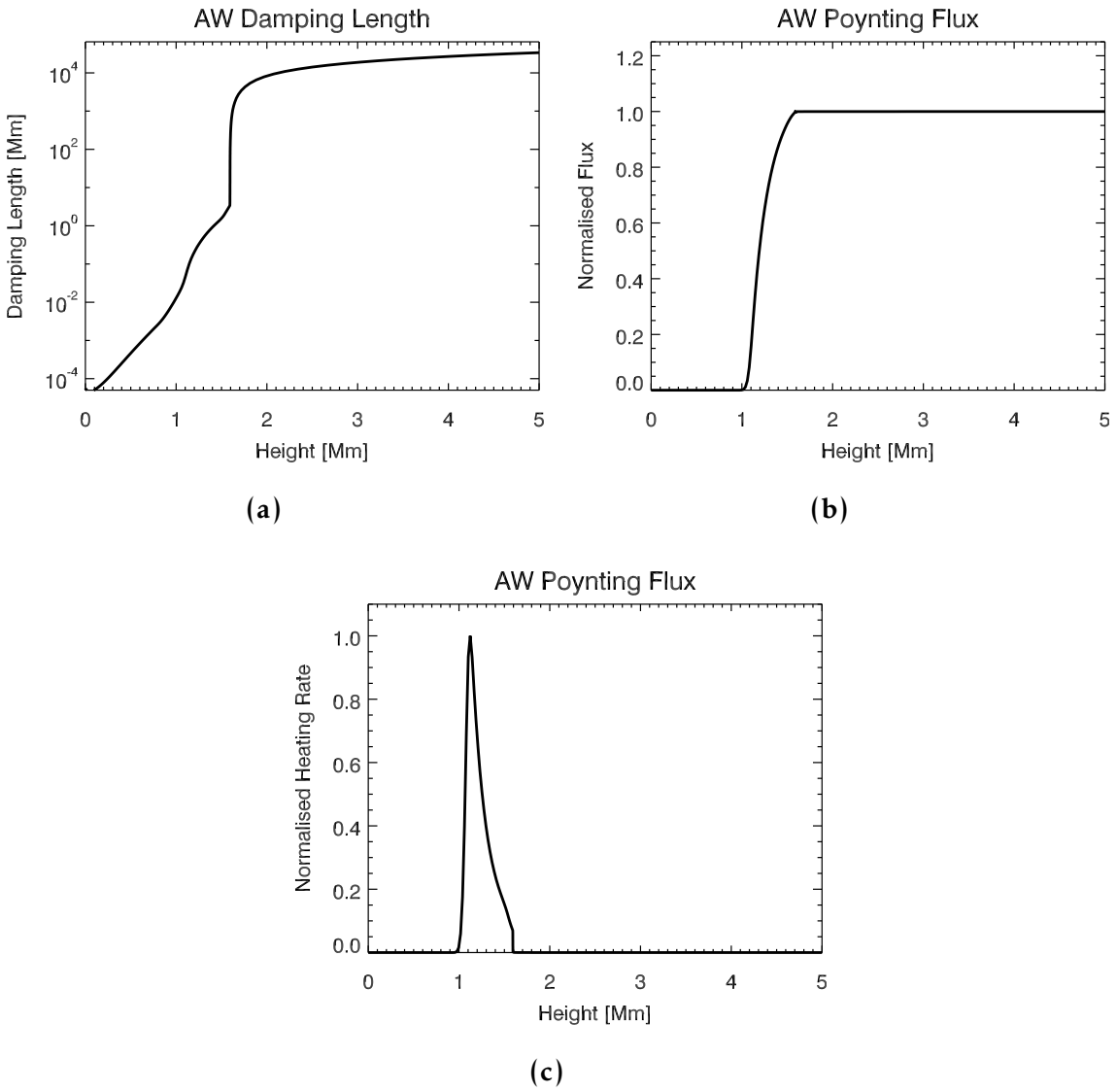

Figure 5.3: *Example of AW damping at $t = 0$ in a RADYN atmosphere. Initial conditions were $k_{x,0} = 1 \times 10^{-4}$ cm^{-1}, $B_{ph} = 1000$ G, $\alpha = 0.139$, $S_0 = 1 \times 10^8$ $erg\ s^{-1}\ cm^{-2}$ and $f = 10$ Hz. (a) Shows the effective damping length, (b) shows the decrease in Poynting flux, and (c) shows the resulting heating rate. Panel (b) and (c) are plotted on a normalised scale.*

With this implementation it is now possible to use RADYN to simulate a solar flare with energy transport due to (i) a beam of non-thermal electrons alone, (ii) resistive dissipation of a monochromatic Alfvén wave alone or (iii) an electron beam and monochromatic Alfvén wave in tandem. It is stressed that, presently, Alfvén waves are modelled as a monochromatic wave. That is, a single frequency and wavelength. It is likely that a spectrum of waves would be produced by perturbations associated with the restructuring of the magnetic field during flares, and future research will involve incorporating a spectrum of Alfvén waves.

The following parameters are set on input and kept fixed in time during the simulation: photospheric magnetic field strength, B_{ph}, the perpendicular wave number at the apex of the loop, $k_{x,0}$ and the wave frequency, f. The parameter α that describes the variation of B with height is currently set internally within the code. The scaling of k_x (either Eq 5.10a or 5.10b) can also be specified as an input. The Poynting flux at the top of the loop, S_0, is an input parameter, but is allowed to vary with time. This set up was used for ease of initial coding, but it would not be difficult to adapt this to allow all input parameters to vary with time, or to allow α to be set as an input parameter.

5.3 Parameter Space

There is a large parameter space to explore with these simulations, but we can set some limits and estimates on the allowed values of variables.

Magnetic field strength: The photospheric magnetic field strength is input, and from this the magnetic field strength as a function of height is computed according to Eq 5.9. The value of the exponent, α, that appears in this expression is uncertain but can be constrained using the condition that the plasma beta, β (the ratio of plasma pressure to magnetic pressure), increases with depth in the atmosphere. With the model of the magnetic field strength employed the plasma beta is:

$$\beta = \frac{8\pi P(z)}{B(z)^2} = \left(\frac{8\pi P_{ph}^{2\alpha}}{B_{ph}^2}\right)\frac{P(z)}{P(z)^{2\alpha}} = \left(\frac{8\pi P_{ph}^{2\alpha}}{B_{ph}^2}\right)P(z)^{1-2\alpha}. \tag{5.19}$$

To have β increasing with depth then $\alpha < 1/2$. The pressure at the top and bottom of the atmosphere is already specified in the pre-flare ($t = 0$) RADYN atmosphere, and

so we can approach the choice of α in two ways (both of which require specifying the photospheric magnetic field). We can, for a suitable choice of B_{ph}, decide on the desired coronal magnetic field, B_c, and solve for α:

$$\alpha = \frac{\log(B_{ph}/B_c)}{\log(P_{ph}/P_c)}. \tag{5.20}$$

Alternatively, we can set a value for α to obtain $B(z)$ for the chosen B_{ph}. Since the chromospheric and coronal magnetic field strengths are not well established observationally, both methods seem somewhat arbitrary, and so we simply follow the approach of Russell & Fletcher (2013) and Reep & Russell (2016) by initially setting $\alpha = 0.139$. Russell & Fletcher (2013) arrived at this value by deciding upon a coronal magnetic field strength and a photospheric strength. The choice of α will change $B(z)$, and therefore the Q_{AW}, so should be experimented with as a free parameter. This will be done in future work, but for the time being $\alpha = 0.139$ is fixed for all simulations discussed here.

The photospheric magnetic field strength in active regions is easier to measure, and is on the order several hundred Gauss to a few kG (e.g. Solanki 2003). For this work we choose $B_{ph} = 1000$ G for all simulations but, future experiments will vary B_{ph}. With $B_{ph} = 1000$ G, and $\alpha = 0.139$, the coronal magnetic field is ~ 155 G.

Wave number: In order for the MHD regime to be valid the wavelength should correspond to scales greater than (i) the proton gyroradius and (ii) the proton skin depth. Otherwise the assumption that the magnetic field advects with the centre of mass of the plasma, and not just the electrons, is not correct and the Hall term cannot be ignored when deriving the solution for the wave amplitude. If the coronal density is on the order $n \sim 10^9$ cm^{-3} then the ion skin depth, $\delta_i = 2.28\times10^7\ (1/n)^{1/2} \approx 721$ cm. This means that wave numbers less than $\approx 1\times10^{-3}$ cm^{-1} (corresponding to scale of ~ 6280 cm) are acceptable. These wavenumbers are orders of magnitude greater than the inverse of the proton gyroradius ($r = \frac{102}{B}T^{1/2}$ cm). Initial efforts will use a parameter space in the range $k_{x,0} \in [1\times10^{-6}, 1\times10^{-3}]$ cm^{-1}.

Wave frequency: As noted in the previous section, the WKB approximation requires the gradient length scale of the Alfvén speed to be greater than or equal to the wavelength of the Alfvén wave. A lower bound on wave frequency, in the chromosphere, would be on the order $f = 1$ Hz. Simulations of flare heating by Alfvén

waves by Russell & Fletcher (2013) demonstrated that waves with periods 10 s or longer experienced damping of only 7 % or less, whereas periods 1 s or less were substantially damped. Additionally, De Pontieu et al. (2001) report that in the quiet Sun waves of short period are effectively damped because damping is proportional to $\omega/\nu_{n,i}$, and simulations of chromospheric heating by Hasan et al. (2000) confirm that high frequency, short period (a few seconds) waves could explain observations. For downward propagating waves in a flare, it is reasonable to expect that the processes involved are much faster than in the quiet Sun. Observations of flares show a large range of timescales from a few minutes & a tens of seconds, to scales as short as on the order 100 ms to a few tens of ms (e.g HXR and radio observations by Aschwanden et al. 1995; Kiplinger et al. 1983). Observations of MHD waves of these periods have yet to be observed in the chromosphere, however the frequency range in the initial set of experiments is taken to be the same as that used in Reep & Russell (2016): $f \in [1, 100]$ Hz.

Initial Poynting Flux: Typically the energy flux required is on the order $F \sim 10^{9-11}$ erg s^{-1} cm
This is measured by calculating the instantaneous power in non-thermal electrons from HXR emissions (e.g. Holman et al. 2003) and dividing by the source area. This requires a knowledge of the source area, and it is now generally accepted that HXR sources overestimate this area due to the comparatively poor spatial resolution and methods of image reconstruction. If the source area is instead inferred from higher resolution optical or UV emissions then the energy flux could be significantly greater. Krucker et al. (2011) reported an energy of $> 5 \times 10^{12}$ ergs s^{-1} cm^{-2}, using optical footpoint area. Such fluxes derived under the assumption of CTTM are in line with the radiative output of flares. For example, Milligan et al. (2014) found an output of a few $\times 10^{11}$ ergs s^{-1} cm^{-2}.

We would expect that if Alfvén waves are a viable mechanism to transport either all or a significant amount of the flare energy to the chromosphere then they must also have energy fluxes in the range $S \sim 10^{9-11}$ erg s^{-1} cm^{-1}.

Following Emslie & Sturrock (1982) the energy flux carried by a (period-averaged) Alfvén wave is:

$$< S >= \frac{1}{8\pi} v_A \delta B^2, \tag{5.21}$$

where δB is the perturbation to the magnetic field. This expression can be re-written

as

$$< S >= \frac{1}{2\,(4\pi)^{3/2}\,\rho^{1/2}} B_{bg}\delta B^2 = \frac{B_{bg}^3}{2\,(4\pi)^{3/2}\,\rho^{1/2}}\left(\frac{\delta B}{B_{bg}}\right)^2, \tag{5.22}$$

where B_{bg} is the background magnetic field. In the RADYN starting atmosphere the mass density in the corona is $\rho = 1.31 \times 10^{-15}$ g cm^{-3}. If we use the same value for $\alpha = 0.139$ and photospheric magnetic field $B_{\rm ph} = 1000$ G as in Reep & Russell (2016) and Russell & Fletcher (2013) then the coronal background magnetic field is $B_{bg} =\sim 155$ G, and:

$$< S > = 1.155 \times 10^{12}\left(\frac{\delta B}{B_{bg}}\right)^2 \text{ ergs s}^{-1}\text{ cm}^{-2}. \tag{5.23}$$

This means that:

- $< S > = 1 \times 10^{9}$ ergs s^{-1} cm^{-2} would require a perturbation of $\sim 2.9\%$,
- $< S > = 1 \times 10^{10}$ ergs s^{-1} cm^{-2} would require a perturbation of $\sim 9.3\%$,
- $< S > = 1 \times 10^{11}$ ergs s^{-1} cm^{-2} would require a perturbation of $\sim 29.4\%$.

Considering the large scale restructuring of the magnetic field that occurs during a solar flare such perturbations seem reasonable for our initial numerical experiments (in their analysis of Alfvén wave energy transport Fletcher & Hudson 2008 and McClements & Fletcher 2009 use a value of 10 % based on observations of photospheric magnetic field strength changes). Though no direct measurements of the coronal magnetic field perturbation have been reported in the literature, there are numerous observations of changes to the photospheric magnetic field during flares (e.g Sudol & Harvey 2005; Wang et al. 2012). Future experiments will vary the value of the coronal magnetic field. Increasing the magnetic field would reduce the magnitude of perturbation required (coronal magnetic field strength above actitve regions has been deduced from microwave and radio observations in a few cases to be in excess of 1 kG, e.g. Brosius et al. 2002 and Brosius & White 2006).

5.4 Preliminary Numerical Experiments

For these simulations, and for the detailed description of the simulations in the next section, the pre-flare atmosphere used was the QS.SL.LT model atmosphere

discussed in Allred et al. (2015) and in § 2. Non-radiative heating was applied to maintain the photospheric and coronal energy balance in grid cells with column mass greater than 7.6 g cm^{-2} (photosphere) and less than 1×10^{-6} g cm^{-2} (corona). A fixed boundary condition is used in the sub-photosphere and a reflecting boundary condition at the top of the loop, to mimic the effect of disturbances from the other half of the flux tube.

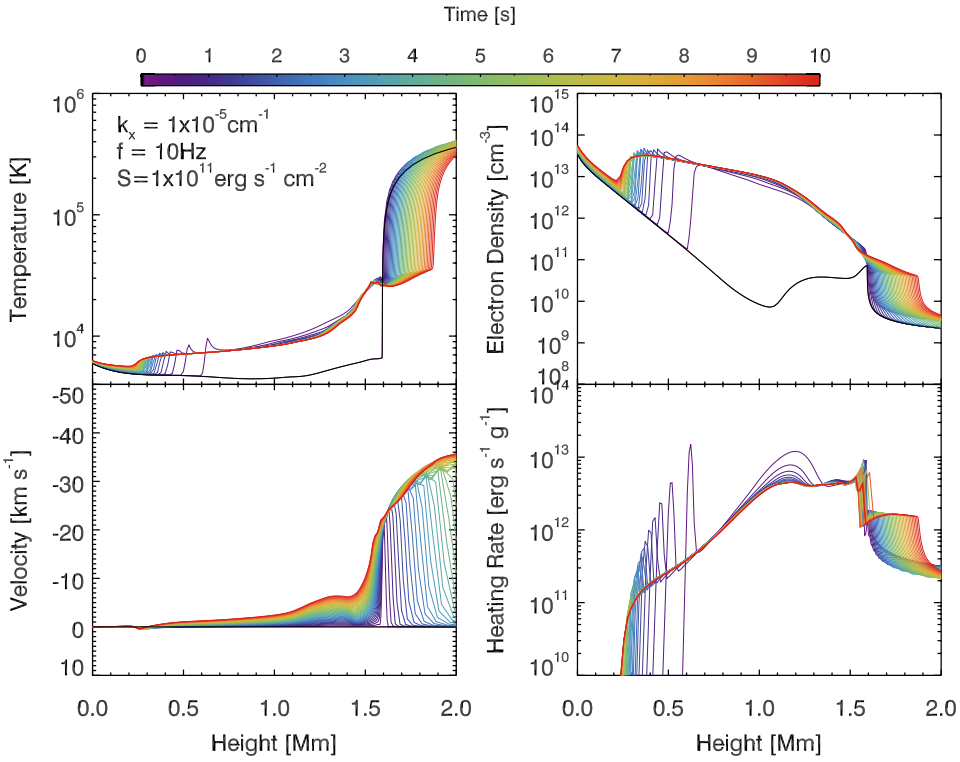

Figure 5.4: *A flare simulation with AW heating. Parameters were:* $S_0 = 1 \times 10^{11}$ *erg* s^{-1} *cm*$^{-2}$, $k_{x,0} = 1 \times 10^{-5}$ *cm*$^{-1}$, $f = 1$ *Hz. The top left panel shows temperature, top right shows electron density, bottom left the atmospheric velocity (upflows are negative), and the bottom right the heating rate per gram. Colour represents time.*

A detailed comparison between an AW flare simulation and a standard electron beam simulation is presented in § 5.5, but four initial numerical experiments are briefly presented in this section. There is a large parameter space to survey, which takes a lot of computation time, and so representative cases are shown. The parameters of the four simulations presented here shown in Table 5.1, and the results

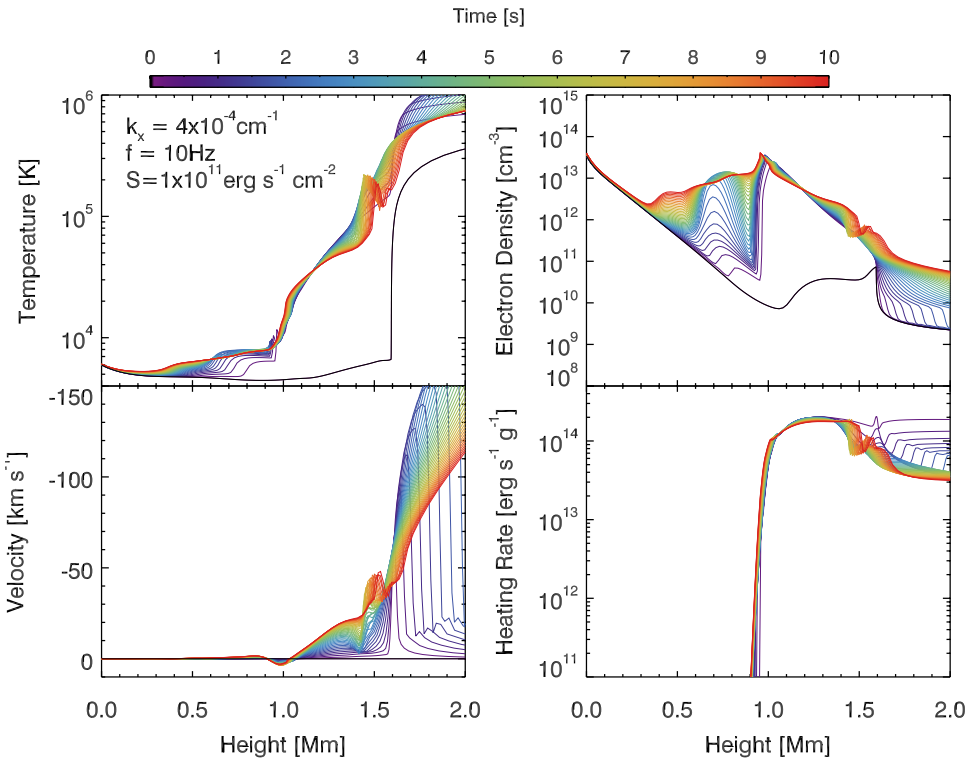

Figure 5.5: *A flare simulation with AW heating. Parameters were:* $S_0 = 1 \times 10^{11}$ *erg* s^{-1} *cm*$^{-2}$, $k_{x,0} = 4 \times 10^{-4}$ *cm*$^{-1}$, $f = 10$ *Hz. Panels as described in Figure 5.4.*

of each simulation are illustrated by Figures 5.4 (AW_Sim1), 5.5 (AW_Sim2), 5.6 (AW_Sim3) & 5.7 (AW_Sim4). These figures show the temperature, electron density, atmospheric velocity and heating rate as a function of time. In each simulation, the duration of energy input was 10 s, with constant wave parameters.

	S_0 [erg s^{-1} cm^{-2}]	f [Hz]	$k_{x,0}$ cm^{-1}	B_{ph} [Gauss]	α
AW_Sim1	1×10^{11}	10	1×10^{-5}	1000	0.139
AW_Sim2	1×10^{11}	10	4×10^{-4}	1000	0.139
AW_Sim3	1×10^{10}	1	1×10^{-4}	1000	0.139
AW_Sim4	1×10^{10}	100	1×10^{-4}	1000	0.139

Table 5.1: *AW flare simulation parameters*

Comparing AW_Sim1 & AW_Sim2 we can see the effect of varying the wave

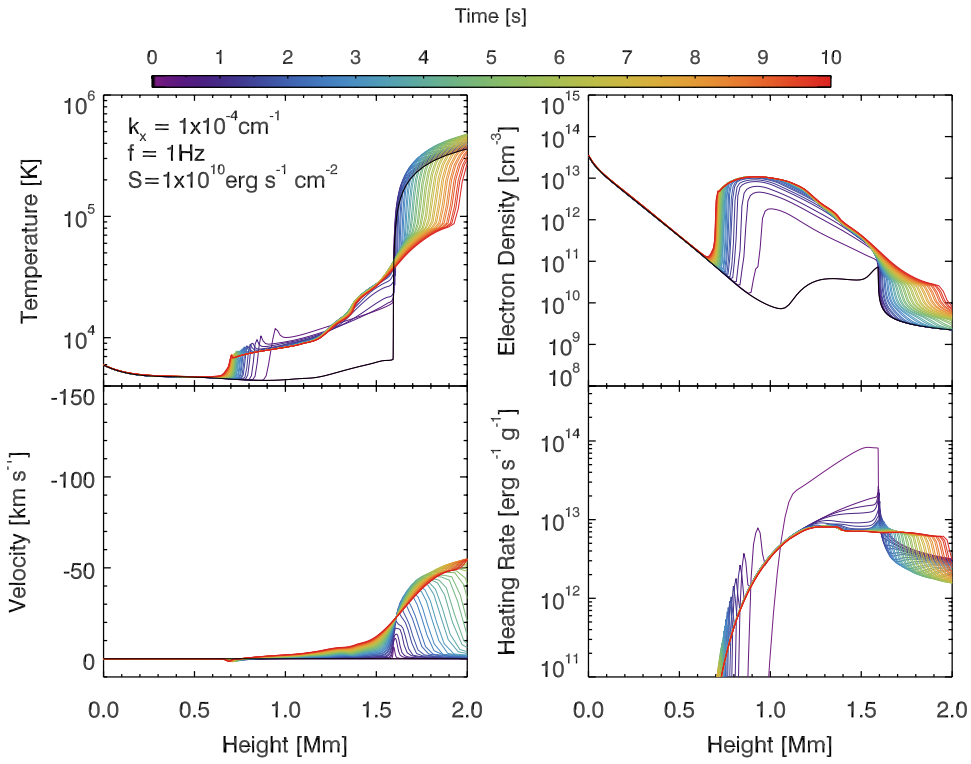

Figure 5.6: *A flare simulation with AW heating. Parameters were:* $S_0 = 1 \times 10^{10}$ *erg* s^{-1} *cm*$^{-2}$, $k_{x,0} = 1 \times 10^{-4}$ *cm*$^{-1}$, $f = 1$ *Hz. Panels as described in Figure 5.4.*

number of the injected AW. Both simulations heat the chromosphere to varying degrees, a consequence of the dependence of the damping length on wave number. A lower value of k_x reduces the contribution from the parallel resistivity relative to the perpendicular resistivity (for the same frequency) and results in a longer damping length, $L_D(z)$. The Poynting flux is damped over a broader region of the atmosphere, penetrating deeper and heating the TMR directly. The temperature in the lower atmosphere is greater in AW_Sim1 than in AW_Sim2 due to the reduced k_x. This higher temperature in the lower atmosphere means that the electron density is also greater at these altitudes. However, the mid-upper atmosphere is barely heated in comparison to the other simulations (both electron beam and AW) since the magnitude of the heating rate is reduced over the whole atmosphere. Consequently, pressure differences are smaller and the upflows are weaker. That said, the AW heating rate does still raise the temperatures to some degree in the upper atmosphere. In the case of larger k_x (AW_Sim2) the damping length is greatly reduced with the Poynting flux unable to penetrate as deeply into the atmosphere. The energy deposition per

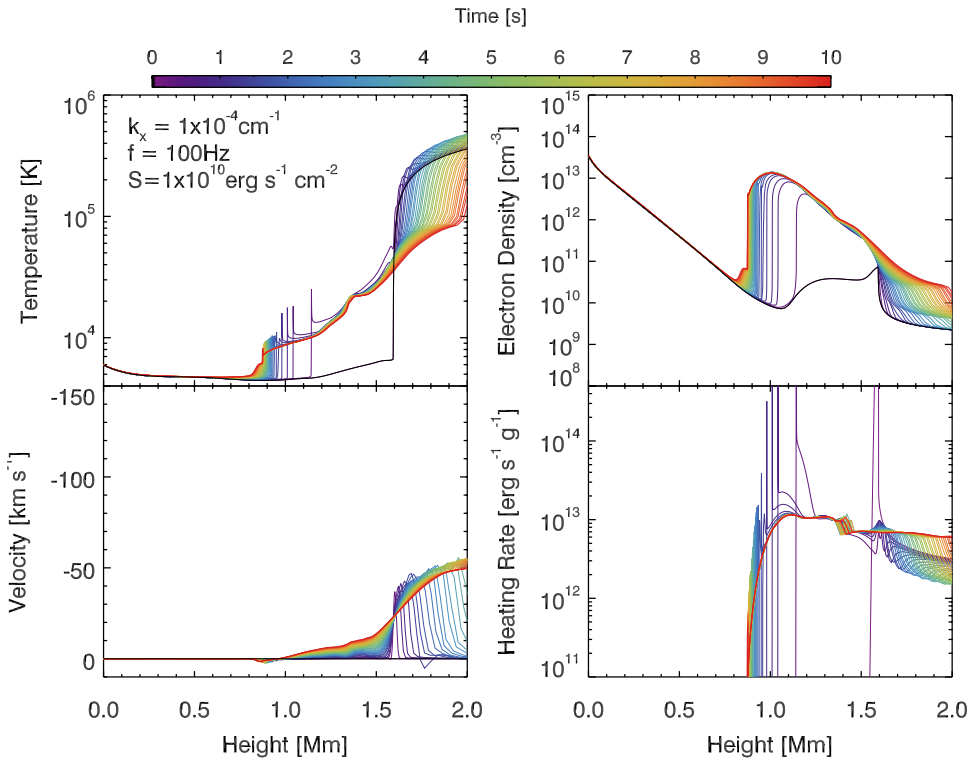

Figure 5.7: *A flare simulation with AW heating. Parameters were:* $S_0 = 1 \times 10^{10}$ *erg* s^{-1} *cm*$^{-2}$, $k_{x,0} = 1 \times 10^{-4}$ *cm*$^{-1}$, $f = 100$ *Hz. Panels as described in Figure 5.4.*

mass is higher in the mid-upper chromosphere resulting in temperature increases of hundreds of thousands of kelvin. The corona shows temperature enhancements also due to a non-negligible heating rate at high altitude. Strong heating of the whole chromosphere and associated high pressures produce high velocity upflows. Heating deep in the chromosphere is reduced in comparison to the case of smaller k_x (AW_Sim1), but there is still some temperature enhancement as a result of radiative backwarming. AW_Sim2 is discussed in detail in § 5.5.

Keeping the value of k_x constant at an intermediate value of 1×10^{-4} and varying the frequency shows similar (but not as drastic) differences. The lower frequency in the (AW_Sim3) simulation, where $f = 1$ Hz, has the effect of reducing the contribution of the perpendicular resistivity (ion-neutral damping), increasing the damping length. Poynting flux is damped less at high altitude due to the longer $L_D(z)$ so that there is less heating in the upper atmosphere compared to the mid-lower (for this choice of k_x). The opposite case of higher frequency (AW_Sim4) where $f = 100$ Hz

increases the effect of ion-neutral damping which decreases the damping length compared to lower frequencies. The wave does not penetrate as far as in AW_Sim3.

The effectiveness of collisions and, consequently, the resistivity of the plasma, varies as functions of both the density of the particles and the temperature of the plasma, but the atmosphere evolves following energy input. This evolution has a feedback to the heating rate, making the evolution non-linear. Changing the temperature will increase the collisional frequencies, but the associated flows and ionisation will change the density structure which would act to vary the rates. Changes in atmospheric structure act to shorten or lengthen the effective damping length. A smaller damping length results in more energy deposition per unit volume, and vice versa. Therefore the volumetric heating rate varies in strength and location as a function of time. The density of the material at the location of energy deposition dictates the temperature rise, which again changes the collisional rates. Of course, this energy input may be offset by radiative losses, as discussed in the next section.

Effective damping lengths for for AW_Sim3 & AW_Sim4 are shown in Figures 5.8a & 5.8b respectively. In these figures the damping length is computed at all heights, but the wave itself might be completely damped before reaching certain depths and so the lowest value of damping length does not equate to the deposition height. Instead it is the trend to shorter damping lengths with increasing distance into the loop (from the corona) that is important. In Figure 5.8a we can see that following energy input the damping length increases in the mid-chromosphere by 1-2 orders of magnitude in response to the changing atmosphere so that the damping length varies from $L \sim 100$ km at ~ 0.95 Mm to $L > 1000$ km at ~ 1.5 Mm (later in the simulation the value of the upper value approaches $L \sim 10,000$ km). Between ~ 0.95 Mm and ~ 0.90 Mm there is a sharp there is a sharp step, over which the damping length decreases from $L \sim 100$ km to $L \sim 1$ km. The location of this step progressively moves deeper into the atmosphere during the simulation. The gradient of this step also increases with time. Correspondingly, the heating rate shows penetration to greater depths, with a significant amount of energy dissipated over the gradient of the step so that spikes appear in the heating rate.

Figure 5.8b shows the damping length for the higher-frequency simulation. During the flare the damping length increases to similar values in the upper-chromosphere as that in the low frequency case. In the mid-lower atmosphere, however, the step in damping length occurs higher in the atmosphere, initially between ~ 1.2 Mm and

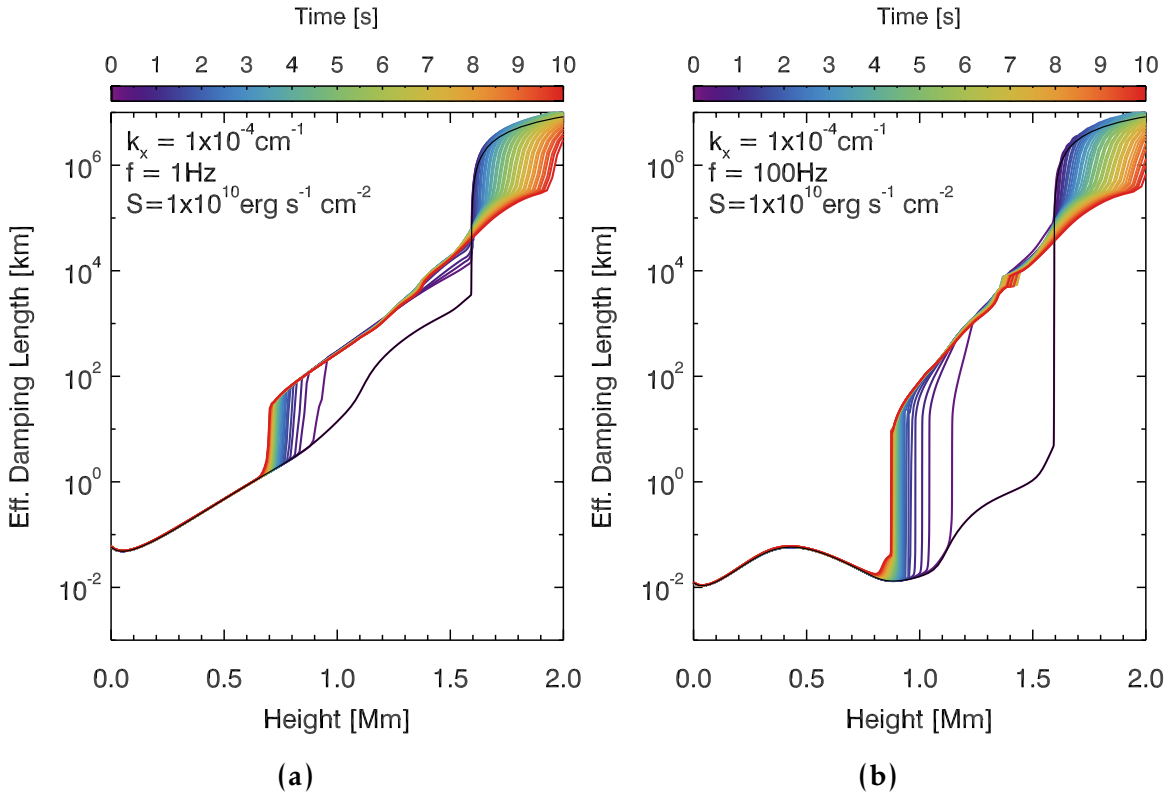

Figure 5.8: *Damping length for AW_Sim3 & AW_Sim4. Parameters were* $S_0 = 1 \times 10^{11}$ *erg* s^{-1} cm^{-2}, $k_{x,0} = 1 \times 10^{-4}$ cm^{-1}, *and in panel (a)* $f = 1$ *Hz, and in panel (b)* $f = 100$ *Hz. Colour represents time.*

~ 1.1 Mm. The size of this step is also larger than in the low-frequency case, with the damping length decreasing from $L \sim 1000$ km to $L \sim 0.1$ km. This is due to the increased contribution from the resistivity associated with ion-neutral collisions makes damping more efficient. Efficient damping results in a sudden decrease in the damping length (the 'step' feature in these figures). This large decrease in damping length over a narrow height range results in the narrow spikes in the heating rate. As the simulation progresses the location of the step moves deeper in the atmosphere, and the spatial gradient over which it decreases steepens. Decreasing the wave number will increase the damping length so that it is not small enough to dissipate wave energy effectively until lower in the atmosphere.

This initial survey demonstrates that the damping of AWs can heat different locations of the atmosphere depending on the wave properties. This is crucial if AWs are to be considered a viable flare heating mechanism. A future goal of this research

is to not only identify which wave parameters can adequately heat specific locations in the atmosphere, but to extend this effort to model a spectrum of waves so that the heating of the TMR *and* strong heating of the mid-upper chromosphere can be achieved in a single simulation.

5.5 Detailed Comparison Between an EB and AW Simulation

Beam-driven and wave-driven models of energy input will have different heating profiles, and different time evolution, which will form the basis of discriminating between models. High spatial, spectral and temporal resolution data of chromospheric and transition region (TR) radiation in the near-UV (NUV) and far-UV (FUV) are now available from IRIS. For example, Kerr et al. (2015); Liu et al. (2015) and Graham & Cauzzi (2015) discuss the complex chromospheric Mg II spectra observed during flares. The Daniel K. Inouye Solar Telescope (DKIST) will also provide high resolution chromospheric observations in the optical and infrared (IR). These resources provide the opportunity to probe models of energy transport in flares by comparing the synthetic spectra output by advanced models to observations. The atmospheric and radiative response to energy transport via AW is here compared with the response from an EB simulation.

Two simulations are compared here, one in which the flare energy transport mechanism is a non-thermal EB (referred to as F11) and one in which the energy transport is via AW dissipation (also referred to as S11). Both have the same injected energy flux of 10^{11} ergs cm^{-2} s^{-1}, which is constant for $t = 10$ s. This deposition time models the length of time the beam or wave delivers energy to a particular location in the chromosphere, which is consistent with the 'dwell time' implied by rapid footpoint motion.

EB simulation parameters were: $\delta = 5$ and $E_c = 25$ keV.

AW simulation parameters were: $f = 10$ Hz, $k_{x,a} = 4 \times 10^{-4}$ cm^{-1} and $B_0 = 1000$ G.

5.5.1 Atmospheric Response to Energy Input

The atmospheric response to either AW or EB energy input is shown in Figures 5.9 & 5.10, where the top panel of each figure represents the EB simulation and the bottom panel the AW simulation. The colour of the lines refers to the time in the simulation, where, where times are plotted in the range $t = [0, 10]$ s in 0.5 s intervals. The temperature, electron density, velocity, H ion fraction, He II ion fraction and flare heating rate (Q_{EB} & Q_{AW}) are shown. Additionally, Figures 5.11 & 5.12 show net heating rate in the atmosphere, where positive quantities heat the atmosphere and negative quantities cool the atmosphere. The sum of heating and cooling terms is shown as a black solid line. If locally positive, this total contributes towards raising the temperature, ionisation and excitation at that location. If locally negative it contributes towards cooling, de-excitation and recombination.

5.5.1.1 Electron Beam Simulation (F11)

Within the first second of energy deposition the temperature in the mid-upper chromosphere increases significantly over the background. Temperature rises to $T \approx [40,000 - 85,000]$ K in the chromosphere between 1.15 – 1.5 Mm and lower down, between 0.6 – 1 Mm, temperature increases to $T \approx [6000 - 7000]$ K. A steep temperature gradient joins these two regions. The heating results in a increased electron density (by more than three orders of magnitude at 1 Mm) between 0.5 – 1.6 Mm, following ionisation. In the lower atmosphere, flare energy largely goes into ionisation of hydrogen, which is ionised at heights > 1 Mm, and partially ionised between 0.5 – 1 Mm. Helium ionisation takes place also, with He II quickly formed between $\sim$ 1.05 – 1.6 Mm. In the upper atmosphere, just below the original TR position, T increases to $\approx [85,000 - 90,000]$ K, enough to form a modest amount of He III at $\sim$ 1.5 Mm. A pressure wave at the TR (1.6 Mm) begins due to the sudden temperature increase to approximately a hundred thousand kelvin, producing a strong upward mass motion with at greater than 50 km s^{-1}. Figure 5.11(a) & (b) show that the temperature, and ionisation, increase is rapid, with beam energy input mostly balanced by radiative losses by $t = 1$ s.

Between $t = 1 - 4$ s, energy input into the lower chromosphere at 0.6 – 1 Mm largely results in increased hydrogen ionisation causing the temperature plateau to only slowly increase in temperature. The plateau extends to deeper layers (< 0.5 Mm),

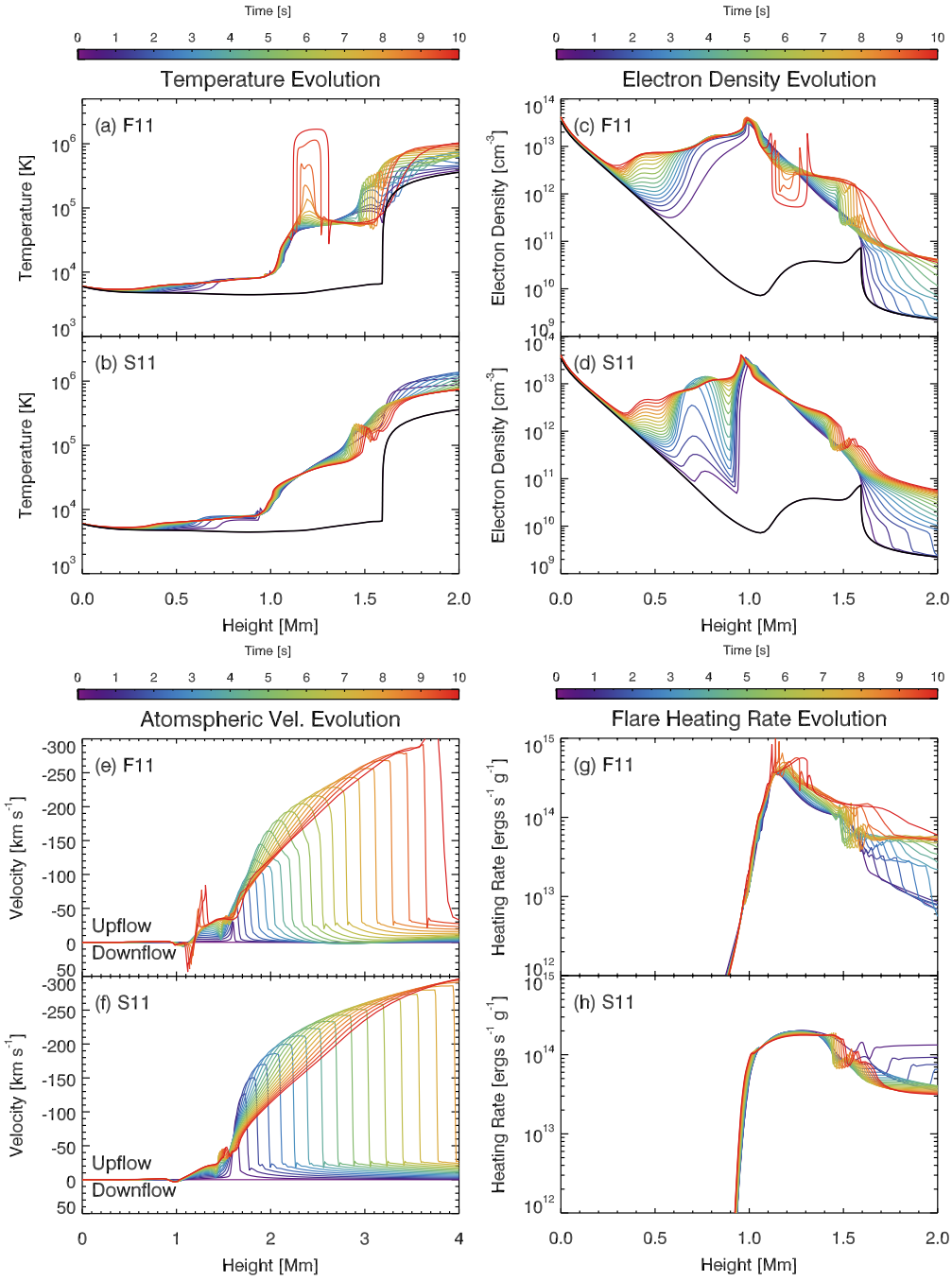

Figure 5.9: *The evolution of the atmosphere for F11 & S11 simulations, where (a) & (b) show temperature, (c) & (d) show electron density, (e) & (f) show velocity with upflow negative, (g) & (h) show flare heating rate per mass. Colour represents time with output plotted at 0.5 s intervals.*

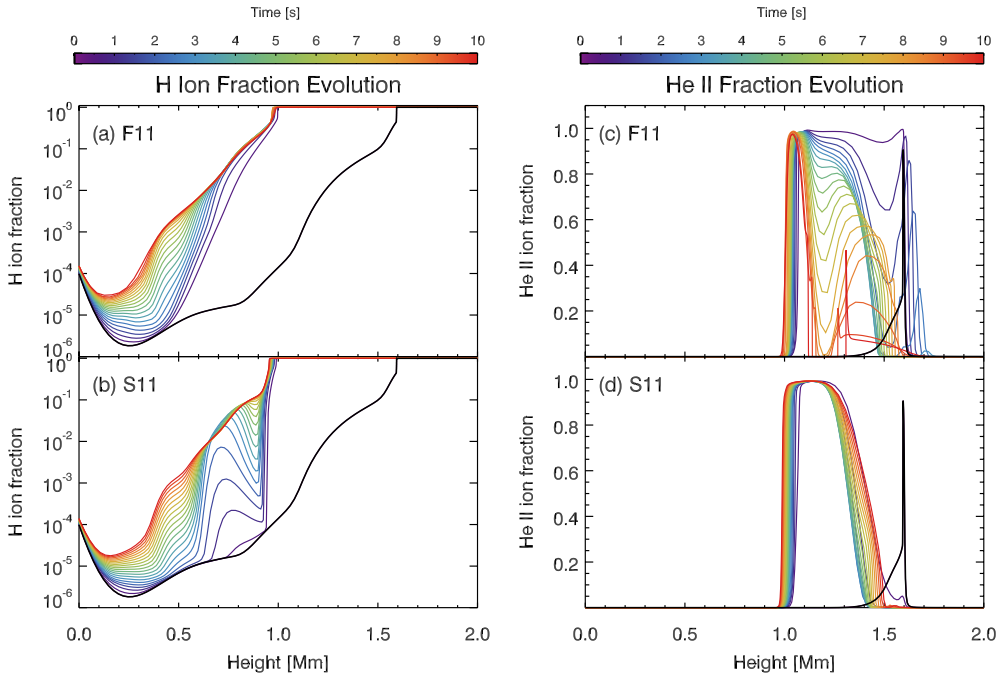

Figure 5.10: *The evolution of the atmosphere for F11 & S11 simulations, where (a) & (b) show H ionisation fraction and (c) & (d) shows the fraction of He* II. *Colour represents time with output plotted at 0.5 s intervals.*

and electron density increases there following further ionisation. The transition from $T \approx 7000$ K to $T \approx 40,000$ K, at $1 - 1.15$ Mm, steadily grows steeper with increasing temperature towards 1.15 Mm. At 1.15 Mm the temperature increases by a few tens of thousands kelvin to $T \approx 60,000$ K, but radiative losses largely balance (and occasionally exceed) energy input between $1.15 - 1.4$ Mm meaning that the temperature changes little over this time period, and actually decreases by several thousand kelvin at ~1.4 Mm. Radiative losses decrease with time above this height and are no longer able to balance energy input, resulting in a temperature bubble in excess of $T = 200,000$ K. Figure 5.11(c) illustrates the energetics at this time. Within this bubble He is almost completely ionised to He III. Above 1.6 Mm the temperature continues to increase but not smoothly. Loop density is enhanced there by strong upflows (which have increased to $v \sim 150$ km s^{-1}), so the beam deposits more energy at greater height. A strong conductive flux helps to increase temperature at heights > 2 Mm.

Between $t = 4 - 7.5$ s there is not much change at heights < 1.15 Mm, where

the atmosphere continues to evolve in a similar manner to previously. The peak of the electron beam heating rate moves slightly higher, to 1.18 Mm. Losses are just unbalanced at this point allowing the temperature to rise to $T = 85,000$ K. Losses are able to balance, and at times exceed, energy input between $\sim 1.2 - 1.35$ Mm resulting in a drop in temperature. There is a corresponding drop in electron density as recombination to He II take place. Note also at this time the amount of He III in the mid-chromosphere around 1.18 Mm increases due to high temperatures so that a narrow region of almost fully ionised He begins to form. Initially, the hot bubble at heights > 1.4 Mm was smoothed out as it was heated to > 400,000 K, due to a conductive flux into the cooler material ahead of the bubble, which increases the temperature in those regions. However, increased temperature at ~ 1.5 Mm leads to an increased pressure which drives material away, making a narrow, under-dense region that is a few 10s of km thick. Radiative losses decrease as a result of decreased density allowing the temperature to increase further. Immediately ahead of this under-dense region is a locally over-dense region which due to increased radiative losses forms a local temperature minimum.

Between $t = 7.5 - 10$ s a large temperature bubble, ~ 200 km thick with $T > 1$ MK, forms in the mid-upper chromosphere near 1.2 Mm. High chromospheric temperatures ionise a large proportion of the He II to He III at $\sim$ 1.2Mm, causing decreasing radiative losses from He II that can no longer balance the beam energy deposition. This leads to an increasing temperature at that location (in excess of 1.5 MK by the end of the simulation), and further ionisation. The high temperature difference within the bubble compared to the surrounding plasma, of a few hundred thousand kelvin, results in a large pressure difference, creating flows that drive material away. The dense downflow (chromospheric condensation) reaches a speed of $v \sim 45$ km s^{-1}, and results in strong radiative losses. Upflows increase the density higher in the loop, increasing the heating rate at high altitudes, causing the temperature of the corona to rise and the TR to move to a higher location. Figure 5.11(d,e) shows the decrease in radiative losses allowing temperature to quickly rise followed by the emergence of the hot bubble.

5.5.1.2 Alfvén Wave Simulation (S11)

The obvious difference between the atmospheric evolution in the AW simulation (the lower panels in Figure 5.9) is the lack of the high temperature bubble in the

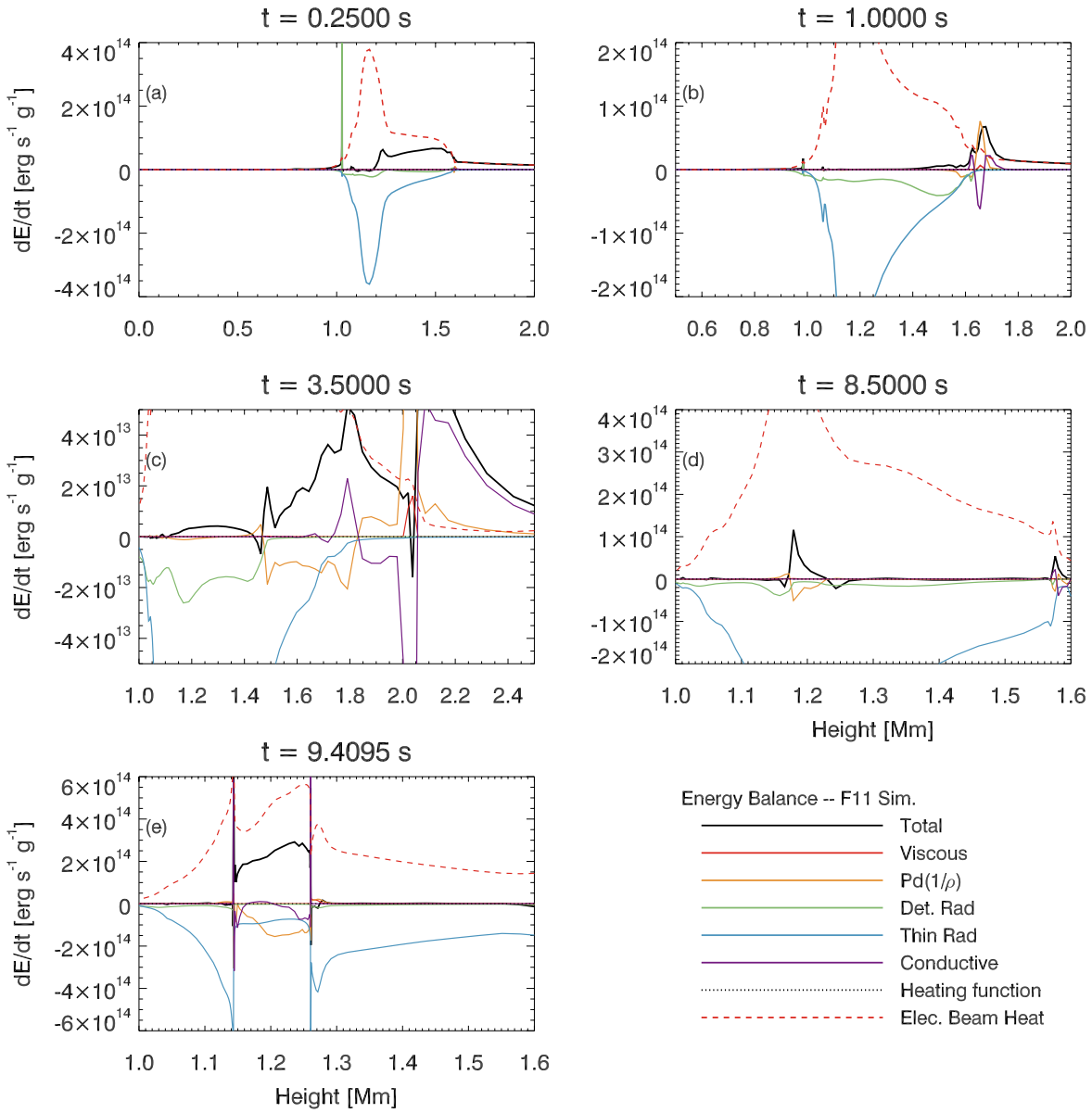

Figure 5.11: *Contributions to the energy balance in the EB simulation are shown: total (black), viscous heating (red), work done by pressure (yellow), optically thick radiation computed in detail (green), optically thin radiation (blue), conductive flux (purple), the background heating function (black, dotted) and the flare heating rate (red, dashed). Positive represents heating, and negative cooling. Each panel represents a time as indicated in the text.*

mid-chromosphere. However, Figure 5.9 shows that aside from this major difference, the AW energy deposition also produces a flare atmosphere, with strong temperature

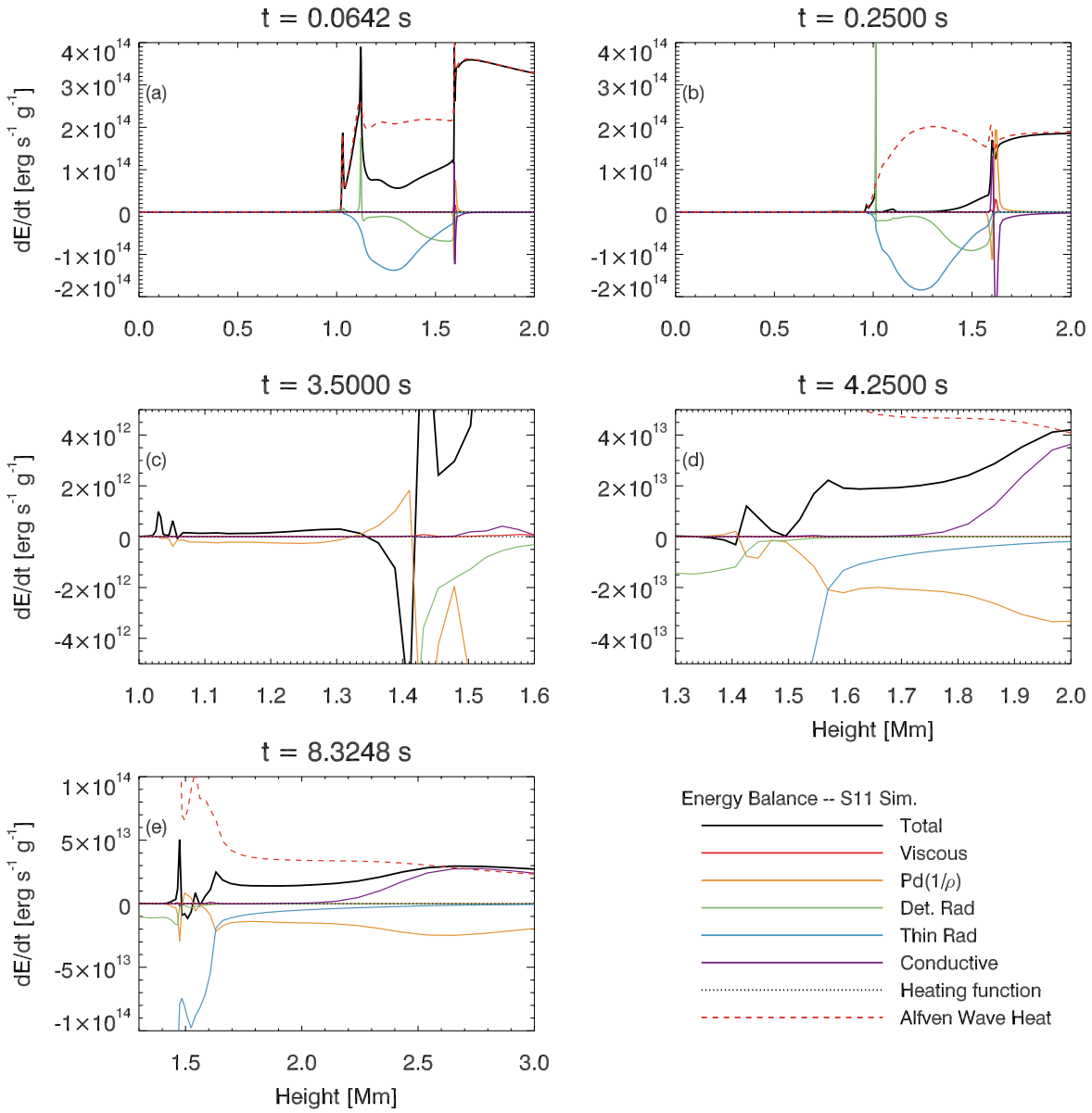

Figure 5.12: *Energy balance in the AW simulation. Lines are as described in Figure 5.11.*

and density enhancements, and a strong upflow in the upper atmosphere.

As with the EB simulation, within the first second of energy deposition, the atmosphere in the AW simulation immediately responds to the strong energy input, resulting in a temperature increase across the entire chromosphere. The peak of the AW heating rate is at a similar height to the peak of the electron beam heating rate (within ~ 0.1 Mm), but is broader. The temperature in the lower atmosphere, between

0.7 – 0.95 Mm, quickly rises to $T \approx [6000 - 7500]$ K. In the mid-upper chromosphere temperatures climb through a shallow spatial gradient from $T \sim 7500$ K at 0.95 Mm to $T \sim 200,000$ K at 1.55 Mm.

Radiative losses almost completely balance energy input up to a height of $\sim$ 1.3 Mm by $t = 0.25$ s. Figure 5.12(a,b) illustrates the energy balance at these times showing that following the rapid ionisation the radiative losses increase sufficiently to mostly balance flare energy input. Hydrogen is fully ionised a heights above 1 Mm, and ionisation continues gradually to greater depth. The large temperature in the mid-chromosphere of $T \sim 10,000 - 40,000$ K results in ionisation of heavier elements, with most of the He ionised to He II between 1.05 – 1.3 Mm. The majority of He is fully ionised to He III at heights > 1.4 Mm where the temperature is $T \sim 90,000$ K. This raises the electron density between 0.9 – 1.6 Mm, with a peak at the hydrogen ionisation boundary (between 0.9 – 1 Mm) of $n_e \sim 4 \times 10^{13}$ cm^{-1}. By $t = 0.25 - 0.5$ s a strong pressure wave at 1.65 Mm pushes chromospheric material into the corona with velocities in excess of $v \sim 130$ km s^{-1}.

Over the next few seconds ($t = 1 - 5$ s) radiative losses are effective in balancing the energy input between 0.6 – 0.9 Mm, and so temperature increases only modestly to $T \sim 8000$ K. Hydrogen ionisation is increased, creating a small region of high electron density $n_e = 1 - 1.5 \times 10^{13}$ cm^{-3}. Above $\sim$ 1.15 Mm the temperature decreases with time. Between 0.95 – 1.15 Mm, there is a steep gradient in temperature, $T \approx [8000 - 35,000]$ K. This gradient gets steeper as the atmosphere evolves. Ionisation to He II occurs following the temperature enhancements, producing a small electron density enhancement at 1 – 1.05 Mm. The pressure changes associated result in small upflows of a few $\times 10$ km s^{-1}. The initial high velocity upflow has reached > 2.5 Mm with velocity of $v \sim 200$ km s^{-1}.

Over this time period, this temperature range between 1.15 – 1.45 Mm decreases from to $T \approx [35,000 - 90,000]$ K to $T \approx [30,000 - 70,000]$ K. This is the result of two effects. Hot plasma is pushed upwards at a few $\times 10$ km s^{-1} due to an increase in pressure above 1.15 Mm, leaving cooler material in its place. Added to this is that radiative losses at height > 1.25 Mm begin to exceed the energy input, slowly decreasing the temperature (see Figure5.12(c)). A narrow high temperature ($T \sim 100,000$ K) bubble begins to form at $\sim 1.4 - 1.5$ Mm, above which the temperature also increases. The TR is heated both as a result of energy deposition and via a conductive flux propagating upwards. Figure 5.12(d) shows the decrease in radiative

losses that allow the formation of the high temperature at 1.4 Mm, and the upwards propagating pressure wave.

For the remainder of the simulation ($t = 5 - 10$ s) there is not a great deal of change, with the atmosphere evolving as it has previously, with the exception of the temperature bubble which cools by a few$\times 10,000$ K as it drifts upwards. The cooling of material between $1.25 - 1.4$ Mm created a pressure difference that in turn produced flows of material, leading to the under-dense region that became the bubble (similar to the process that resulted in the high-altitude temperature bubble in the electron beam simulation). Since it is under-dense, the heating rate is reduced. Despite this, the bubble is strongly heated, as the radiative losses are also reduced due to the lack of emitting material here. A local temperature minimum forms above the bubble due to the locally increased density resulting in enhanced radiative losses which decrease temperature. Figure 5.12(e) illustrates the energetics at this time.

Comparing the AW and EB simulations showed that the AW simulation has a larger temperature between $z \sim [0.97 - 1.1]$ Mm, initially by $\Delta T \sim 7500$ K. Over time this region moves deeper, so that by the end of the simulation $z \sim [0.93 - 1.07]$ Mm is $\Delta T = 10,000$ K hotter in the AW model. Initially the AW simulation was warmer in the upper atmosphere also, but by the end of the simulation both were similar. As previously noted, the > 1 MK bubble dominates the mid-chromosphere in the EB simulation, but is not present in the AW simulation.

Both simulations show flows. The low density evaporation in the upper atmosphere is initially faster in the AW simulation (by a few $\times 10$ km s^{-1}) as the upper atmosphere is more heated at the beginning of the simulations. Towards the end of the simulations the flows have a similar speed. Both simulations exhibit a second, slower, upflow that originates from lower in the atmosphere. These are both high density flows resulting from pressure differences in temperature bubbles, but the AW simulation the bubble forms higher in the chromosphere and is significantly cooler. The resulting flows are a few $\times$ 10 km s^{-1} up to 50 km s^{-1}. The > 1 MK bubble that forms in the EB simulation in the mid-chromosphere is significantly hotter than the same location in the AW simulation ($\sim$MK in the EB simulation compared to a few$\times 10^4$K in the AW simulation), leading to a larger pressure difference and faster flows up to $\sim$80 km s^{-1}. A small downflow of up to $\sim$ 10 km s^{-1} is present in each simulation around 1 Mm, but the EB simulation produces a second downflow (from

the > 1 MK bubble) of up to ~ 40 km s^{-1}.

In the EB simulation, the tail of the energy deposition extends deeper, increasing the temperature there more than in the AW simulation (by a few ×10K). This, together with the non-thermal collisions from the beam, is enough to populate the excited states of hydrogen and to ionise H I to H II, at greater depths than in the AW simulation. Both the hydrogen ionisation fraction and electron density are lower in the AW simulation at heights $z < 0.95$ Mm, and it takes a number of seconds for the AW simulation to reach the same state as the EB simulation. Radiative backwarming heats the lower atmosphere, which brings the population of hydrogen excited levels and H II up to similar densities in comparison to the EB simulation by $t \sim 2.25$ s, in the region $z \sim [0.65 - 0.80]$ Mm. Over the next few seconds the level of H ionisation in the AW simulation becomes similar to that in the EB simulation.

5.5.2 Ca II 8542Å line comparison

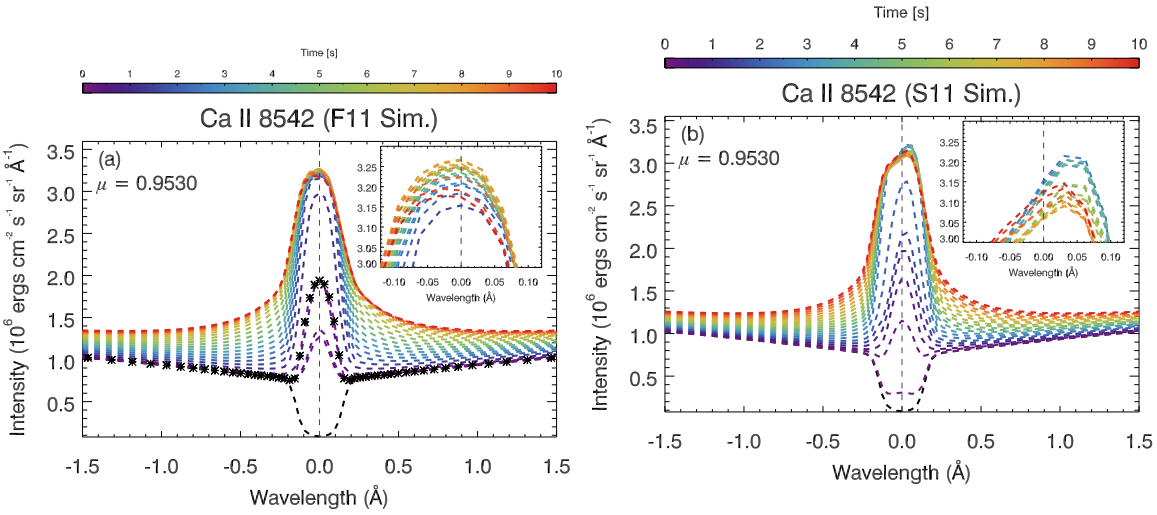

Figure 5.13: *The Ca II 8542 Å line, computed in (a) the EB simulation and (b) the AW simulation. Colour represents time. In panel (a) symbols are overlayed on the profile at $t = 0.072$ s to help it stand out against profiles from $t < 1$ s.*

The Ca II 8542 Å line is part of the Ca II subordinate infrared (IR) triplet. The Ca II triplet has been found to be excellent tracers of solar activity since it is sensitive to the chromospheric temperature and magnetic structures (e.g. Shine & Linsky

1972; Linsky et al. 1979). In the quiet Sun they formed in the deepest layers of the chromosphere (e.g Uitenbroek 1989). Shine & Linsky (1972) and Linsky et al. (1979) note that the 8542 Å line is the most opaque of the triplet, and is wider, but that it shows a greater response to activity than the 8498 Å or 8662 Å. Since this line is formed deep in the atmosphere, and can be well-observed from the ground, it is a good candidate for investigating potential differences in line formation between the AW and EB simulations.

The profiles from the EB simulation are shown in Figure 5.13a, where colour represents time ($t = [0,\ 0.072,\ 0.25,\ 0.302,\ 0.5]$ s and then every 0.5 s thereafter, with symbols plotted on the $t = 0.072$ s profile for clarity, showing the initial high intensity). In the EB simulation, the Ca II 8542 Å line was in emission by $t = 0.072$ s, having previously being in absorption in the pre-flare atmosphere. The line core intensity was increased to $\sim 1.9 \times 10^6$ ergs cm^{-2} s^{-1} sr^{-1} Å^{-1} but decreased to $\sim 1.3 \times 10^6$ ergs cm^{-2} s^{-1} sr^{-1} Å^{-1} at $t = 0.25$ s, though the wing intensity continued to rise. As the simulation progressed the core intensity rose steadily, exceeding its early high value and increasing further to a peak of $\sim 3.27 \times 10^6$ ergs cm^{-2} s^{-1} sr^{-1} Å^{-1} at $t = 7.6$ s. Over time a small blueshift developed and the profile widened. The core intensity showed only small changes in the latter half of the simulation, but the wings showed a consistent intensity increase.

The AW simulation produced spectra that were similar, but which had a stronger asymmetry. Additionally, the line did not show the initial high intensity that the EB simulation did, and overall took longer to reach a similar level of core intensity compared to the EB profiles. The peak intensity of the profile is located redward of the line centroid and peaks at $t \sim 3.5$ with a value of $\sim 3.22 \times 10^6$ ergs cm^{-2} s^{-1} sr^{-1} Å^{-1}.The final intensity in the far wings is also lower than the EB simulation. The line appears redshifted initially, but this decreases with time, ending with a small red asymmetry. Figure 5.13b shows these profiles, where again colour represents time ($t = 0, 0.064, 0.25, 0.5$ s and then every 0.5 s thereafter).

We investigate the formation properties of the lines in the AW and EB simulations to shed light on the stronger asymmetry in the AW simulation and why the AW simulation took a few seconds longer for the profiles to reach their peak. To do this we make use of the line contribution function as described in Chapter 4. Since spectra were computed by RADYN recall that the assumption of CRD is used and the

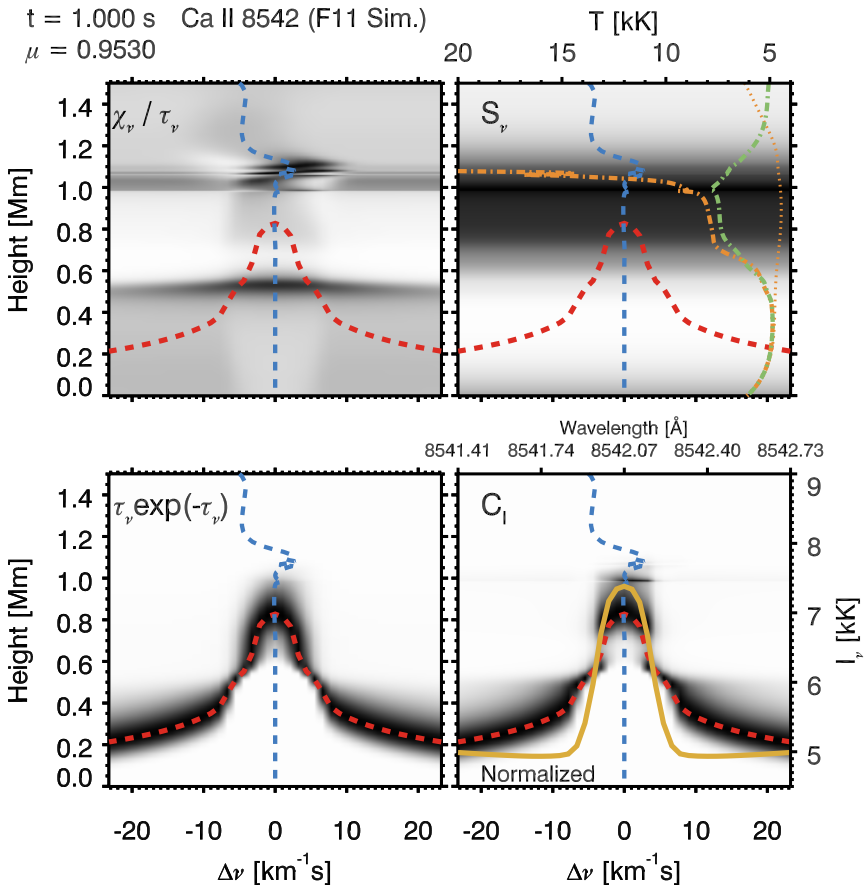

Figure 5.14: *Ca II 8542Å line formation in the EB (F11) simulation at $t = 1$ s. Each panel shows the image of the quantity labelled in the corner of the image. Images are inverse scale. The atmospheric velocity (blue, dashed), $\tau_\nu = 1$ curve (red, dashed), line source function (green, dot-dashed), Planck function (orange, dot-dashed), Planck function at $t = 0$ s (orange, dotted), and emergent intensity (yellow, solid) are also plotted. Positive velocity is redshift/downflow. In the bottom right panels we have normalised the contribution function at each wavelength.*

source function is not dependent on frequency over the line.

We show made the usual four-panel diagrams of Carlsson & Stein (1997). As a reminder, the top left panels show the term χ_ν/τ_ν (indicating where there is a high density of emitters at low optical depth), the top right panels show the source function, S_ν (the ratio of emissivity to opacity), the bottom left panels show $\tau_\nu e^{-\tau_\nu/\mu}$, and the bottom right panels show the product of the other panels, the line contribution function to the emergent intensity, C_I. Dark corresponds to high values, and C_I is normalised at each frequency. In these diagrams positive velocity is downflow.

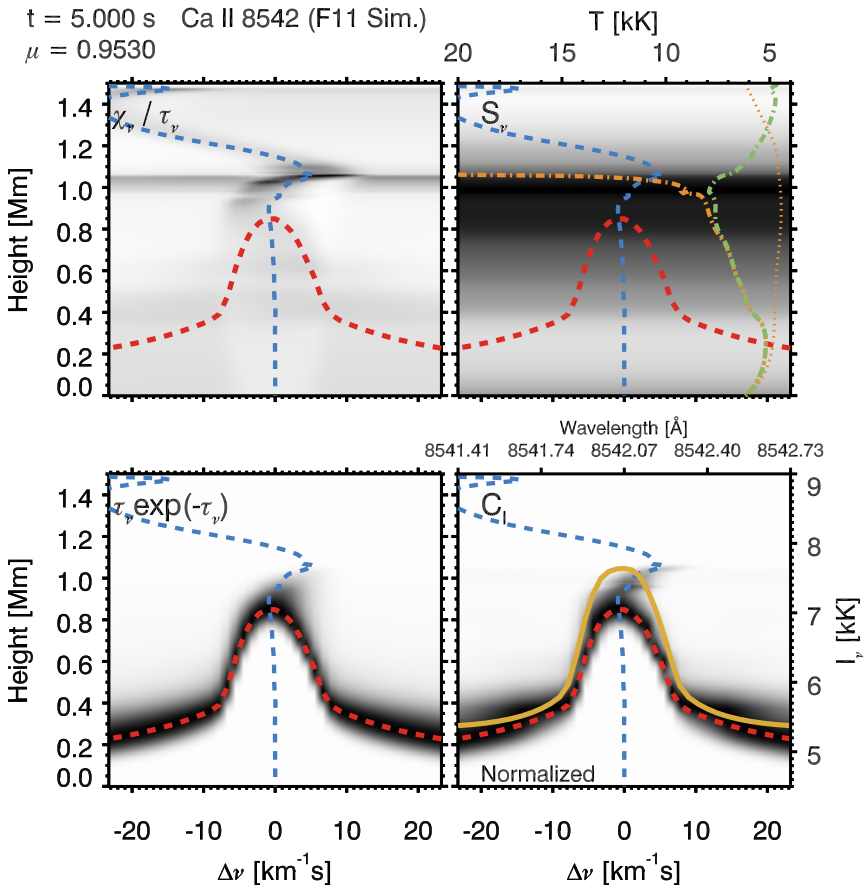

Figure 5.15: *Ca II 8542Å line formation in the EB (F11) simulation at $t = 5$ s. Lines are as described in Figure 5.14.*

Several other properties are shown: atmospheric velocity (blue, dashed line), the $\tau_\nu = 1$ curve (red, dashed line), the line source function (green, dot-dashed line), the Planck function (orange, dot-dashed line) & Planck function at $t = 0$ s (orange, dotted line) and the emergent intensity (yellow, solid line).

Ca II 8542Å formation (Electron Beam Model):

Figure 5.14 shows the formation at $t = 1$ s and Figure 5.15 the formation at $t = 5$ s.

Following flare energy input there is a reduction in the population of the Ca II 8542Å upper levels by two orders of magnitude above 1 Mm due to the temperature enhancement following energy deposition, and an increase of one of magnitude around ~ 0.9 Mm. The contribution function peaks here with an additional smaller (optically thin) contribution to the line core from between 0.9 – 1.1 Mm. The majority of the line contribution comes from around the $\tau_\nu = 1$ curve and so the line is still

optically thick. Increased temperature results in a stronger source function that increases with height to the $\tau_{nu} = 1$ curve (the line source function is strongly coupled to the Planck function, see top right panel in Figure 5.14), and so the line core is in emission. Line wings are formed lower in the atmosphere than the core, with far wings formed at only 0.2 Mm above the photosphere. Temperature increases deeper in the atmosphere down to ~ 0.8 Mm depopulates the upper levels, driving down the formation height of the line core to ~ 0.75 Mm at $t = 0.25$ s. The line source function at this altitude is still strongly coupled to the Planck function, which is smaller at this lower height so the emergent intensity decreases. The line core still has an extended optically thin contribution from $0.75 - 1.1$ Mm.

Over the next second ($t = 0.25 - 1.25$ s; see Figure 5.14), the upper level begins to repopulate around a height of $\sim 0.8 - 1$ Mm. As a result the $\tau = 1$ height moves upward to ~ 0.85 Mm where it remains for the rest of the simulation. The line core is formed in a region where the source function is enhanced significantly, and the line appears narrow as a result since the wings have not changed much.

Between $t = 1.25 - 6$ s, the upper level is repopulated across a wider range of heights, which widens the $\tau = 1$ curve in the near wings, so that emission from the near wings originates from higher layers, and intensity increases. This has the effect of increasing the line width. A downflow of $\sim 5 - 7$ km s^{-1}, located initially around ~ 1.1 Mm but which propegates deeper, redshifts the radiation from the emitters that contributes the optically thin component above the main formation layer (see the increase of the χ_ν/τ_ν term redward of the line core in Figure 5.15). The contribution of optically thin emission to the emergent profile is 'pushed' into the near red wing so that it is a little wider than the near blue wing. A small upflow $\sim 1 - 2$ km s^{-1} at the line core formation height slightly shifts the core to the blue. As time progresses the red wing contribution increases since the downflow travels deeper into the atmosphere. A second downflow develops at the end of the simulation when the hot, under-dense bubble forms in the mid-chromosphere. This has a velocity ~ 50 km s^{-1}. There are not enough emitters at the height of the condensation (1.2 Mm) to have much effect on the Ca II 8542Å line. However if the simulation were to be run for longer the condensation could have reach deep enough to influence the line formation.

Ca II 8542Å formation (Alfvén Wave Model):

Figures 5.16 & 5.17 illustrate the formation of the line at $t = 3.5$ s & $t = 8.5$ s.

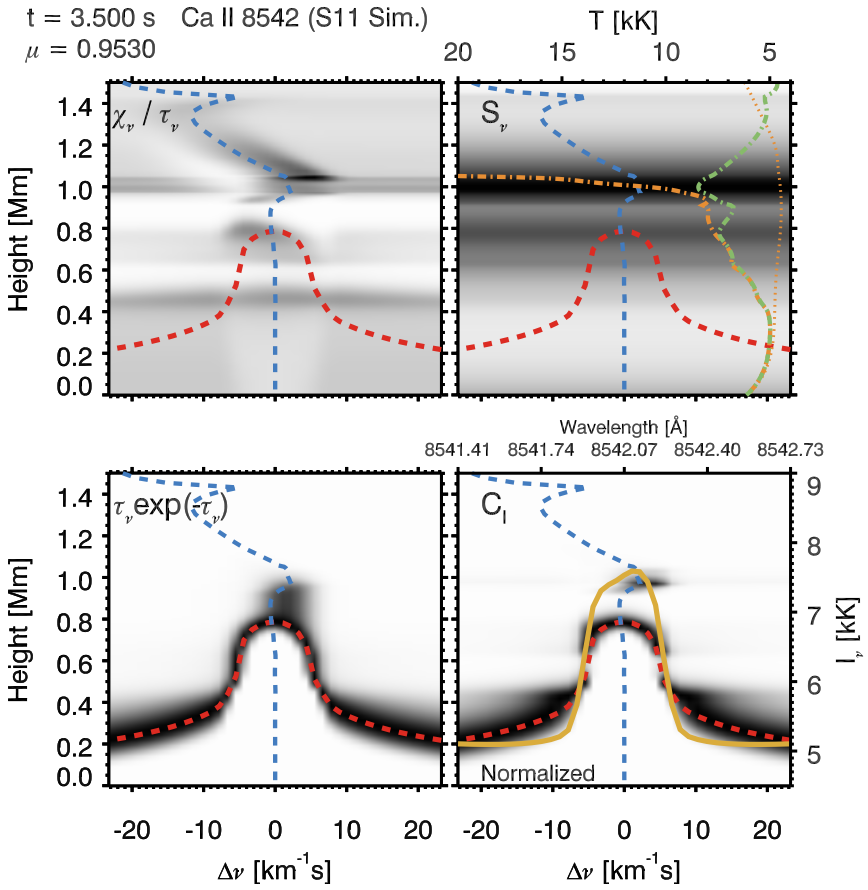

Figure 5.16: *Ca II 8542Å line formation in the AW (S11) simulation at $t = 3.5$ s. Lines are as described in Figure 5.14.*

Unlike the EB simulation, in the AW model the source function is not strongly coupled to the Planck function until somewhat later, so the profile is in absorption initially before going into emission by $t = 0.25$ s. Also unlike the EB simulation, there is not a sufficient amount of Ca II to produce the optically thin emission above the core formation height, apart from a narrow layer around 1.0 Mm that is a few km thick. The formation height of the line core is lower than in the EB simulation, around 0.65 Mm, due to the depopulation of emitters above this height. Consequently the line intensity is lower compared to the profiles formed in the EB simulation due to the smaller source function at this height.

Between $t = 0.25 - 1.25$ s, the absorption profile is shifted to the blue at heights > 1.1 Mm, by an upflow, so that more blue-wing photons are absorbed than red-wing

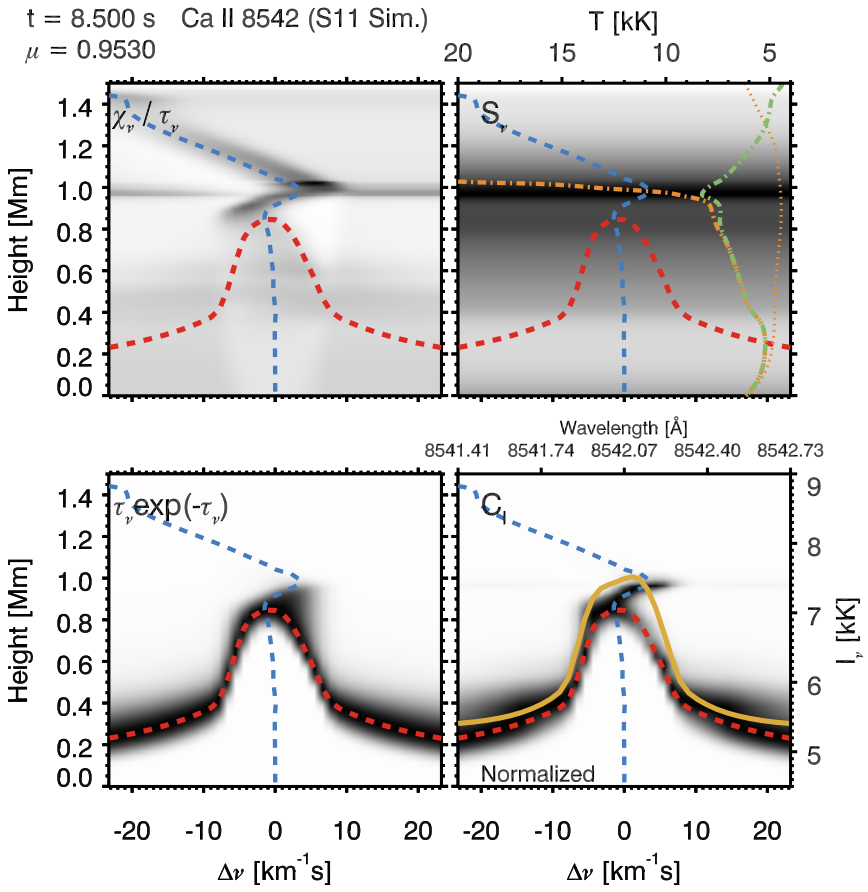

Figure 5.17: *Ca II 8542Å line formation in the AW (S11) simulation at $t = 8.5$ s. Lines are as described in Figure 5.14.*

photons. This creates a small but growing asymmetry, particularly when combined with the fact that a small downflow ($1-2$ km s^{-1} in size) begins to develop that results in the red wing being enhanced by an optically thin contribution. The emergent profile appears redshifted due to this, though the actual downflow is located above the line core formation height. Although originating from a narrower region than in the EB simulation (a few 10s of km compared to ~ 100 km), the optically thin component is reasonably strong since it it is formed in a region that is ≈ 2000 K hotter than in the EB simulation.

Beginning around $t = 2$ s the fraction of Ca II increases, increasing the number of emitters at greater heights and raising the formation height of the line core (see Figure 5.16 showing formation at $t = 3.5$ s). By $t = 6.5$ s the line is now formed around 0.81 Mm. This formation height does not vary greatly over the remainder of the simulation. The optically-thin redshifted component arising from the downflow

means that the red wing is broadened. Line intensity peaks redward of the line core, making the line appear asymmetric. Towards the end of the simulation the downflow (~ 5 km s^{-1}) travels deeper into the atmosphere. As this happens, the optically thin contribution is also redshifted, and contributes more and more to the near wing, rather than immediately adjacent to the line core. Due to this, the peak intensity decreases and the red wing is broadened. Also the optically thin contribution is no longer distinct from the optically thick contribution - it now appears as an 'extension' from the main contribution, similar to the EB simulation (see Figure 5.17 showing formation at $t = 8.5$ s).

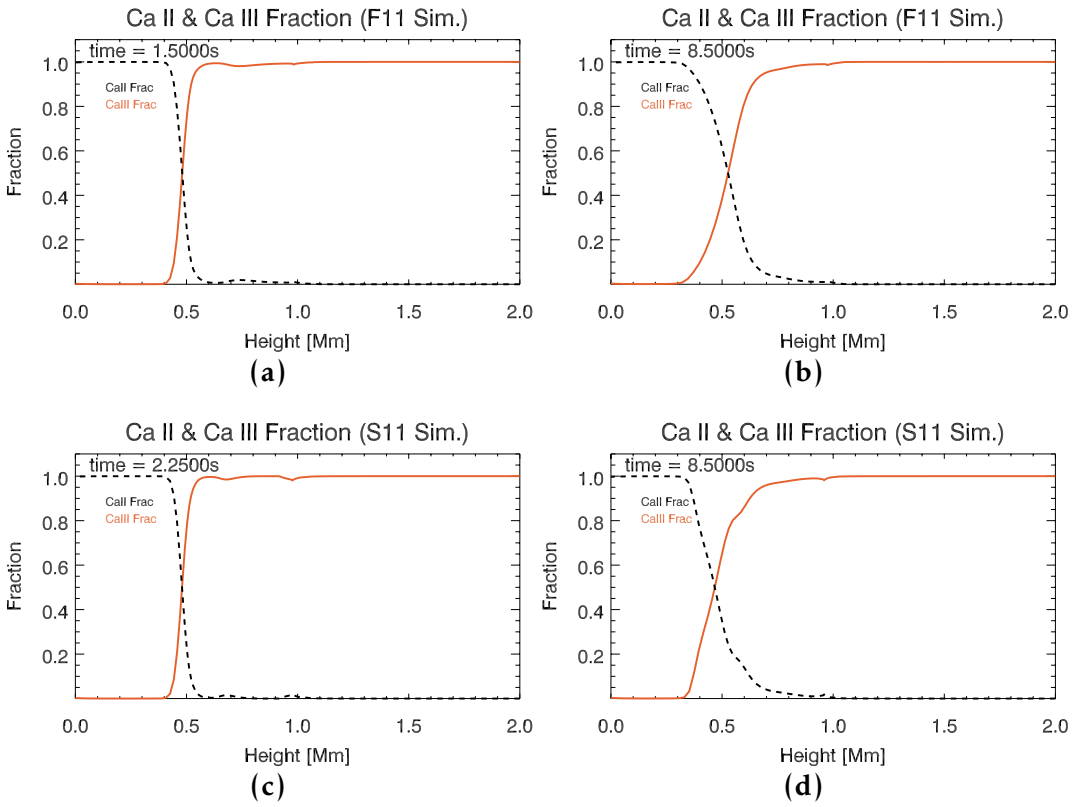

Figure 5.18: *Fraction of Ca* II *(black, dotted) and Ca* III *(orange, solid) at different times as indicated. Panels (a) & (b) show the EB simulation, and panels (c) & (d) show the AW simulation.*

In summary, the differences between the EB and AW synthetic Ca II spectra are the line core intensity (larger in the EB simulation), the red asymmetry (larger in the AW simulation) and the length of time to reach the peak intensity (shorter in the EB

simulation). These are all, mostly, due to the formation height difference between the two simulation - forming lower down means lower intensity, so the longer the line was formed at greater depth in the AW simulation, the longer it remained weaker in comparison to the EB simulation. Ca II 8542Å in the AW simulation formed lower down for a longer period of time because the Ca II upper and lower levels were not repopulated as quickly as in the EB simulation.

In both simulations the fraction of Ca III initially increases significantly in the chromosphere. In the pre-flare atmosphere less than 10 % of Ca was in the Ca III ionisation state, but Ca II was ionised to Ca III down to the lower atmosphere, so that the fraction was 50 % at 0.5 Mm. Figure 5.18 shows the fractions of Ca II and Ca III in each simulation at an early time, and then towards the end of the simulation to illustrate the differences. The ratio is $n_{\text{Ca II}}/n_{\text{Ca III}} \sim 50\%$ between 0.5-0.6 Mm. In the EB simulation, recombinations to Ca II begin around $t = 1$ s in the region $z \sim [0.7 - 0.9]$ Mm. The upper level of the 8542Å line is re-populated as a result. This proceeds until populations are large enough to increase the formation height of the line core (and therefore line intensity). In the AW simulation, it takes longer for recombinations to Ca II to occur as the electron density is lower in this region of the atmosphere (recall that the amount of ionised hydrogen is reduced compared to the EB simulation). The hydrogen ionisation does not catch up to the EB simulation until $t \sim 2.25$ s, which in turn liberates electrons that can recombine to Ca II. This process starts at $t = 2.25$ s but takes a few seconds to produce a sufficient fraction of Ca II to raise the formation height of the 8542Å to a similar location as that in the EB simulation. Similarly, the the optically thin component that produces the red peak/wing enhancements originates from a narrow region around the small downflow in the AW simulation, since there were not enough emitters between that location and the core, with the result that it only contributes towards the red peak and wing. In the EB simulation, however, the Ca II 8542Å upper level is populated sufficiently between the condensation and core formation height to produce an additional contribution to the line intensity around the whole core, not just redward of the core.

5.5.3 Mg II k line comparison

Observations of Mg II lines during flares from the IRIS spacecraft may help to discriminate between models of heating in flares, and so the formation of the k-line in each of the simulations was investigated. Following the approach from Chapter 4, RADYN snapshots at intervals of $t = 0.25$ s were used as input to RH. Figure 5.19 shows the k-line profiles as computed using the EB simulation and the AW simulation atmospheres with

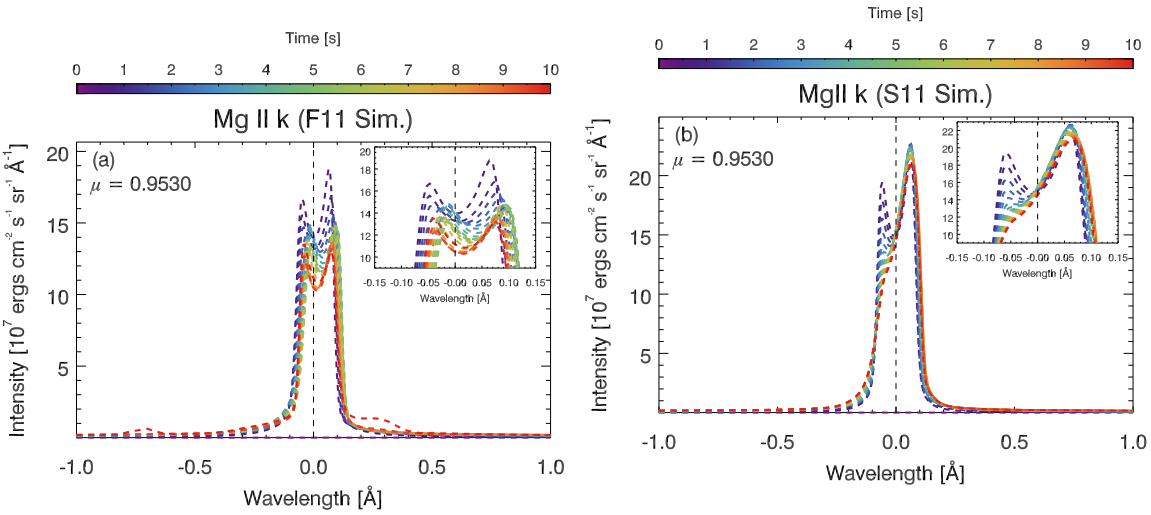

Figure 5.19: *The Mg II k line, computed in (a) the EB simulation and (b) the AW simulation. Colour represents time.*

The central reversal quickly became shallower in the EB simulation, but was a clear feature of the line throughout the simulation. Intensity increased as did the line width. Between $t = 0.25 - 0.5$ s k2r is stronger than the k2v, but over the next few seconds they become gradually more symmetric around the line core. The core itself appears slightly redshifted. The near blue wing (blueward of the k2v peak) developed an intensity enhancement. This additional 'bump' moves further blueward with time. From $t \sim 4 - 7$ s the redshift decreases while the k2r component varies in strength relative to the k2v peak before returning to be almost the same intensity as k2v. At the latter stages of the simulation two features appear in the wings of the line. From 0.15 and 0.5 Å from line center in the red wing a intensity enhancement appears. A similar, but weaker, enhancement to the blue wing is

present 0.75Å.

Unlike Ca II 8542Å , the Mg II k-line showed strong differences between the AW & EB simulations. The AW simulation profiles were more intense than those from the EB simulation, but initially showed a central reversal. The k2r peak became strong relative to the k2v peak by $t = 1.25$ s, while the line core appears slightly shifted towards the k2v peak. In the latter half of the simulation the k2r component was so dominant, and the reversal feature so shallow and shifted that it became difficult to identify it as a clear component. Instead, the profile appeared to have a single dominant peak (the k2r component) with an extended blue wing or shoulder.

To better understand the reasons for the different line profiles, the detailed line formation was studied in the same manner as the Ca II profiles. The difference here is that since RH uses PRD, the source function is frequency dependent, and varies across the line. Figures 5.20 5.21 5.22 & 5.23 illustrate the discussion of line formation, where the images and lines are as described in Figure 5.16.

Mg II k line formation (Electron Beam Model):

Figures 5.20 & 5.21 shows the line formation at $t = 2.75$ s and $t = 10$ s.

Strong heating in the chromosphere depopulates the k-line upper level high in the atmosphere, driving down the formation height so that the line core (k3) formed around ~ 1.1 Mm. The k2r and k2v emission peaks formed somewhat lower, at $\sim 1 - 1.05$ Mm where there is a local source function maximum. The central reversal is shallower than in the pre-flare, but still present since the source function of this component has decoupled from the the Planck function at the core formation height. Therefore, the source function decreases with height, forming the reversal. Conversely, at the formation height of the k2 emission peaks, the source function is more strongly coupled. The line wings form over a wide range of heights, from $\sim 0.7 - 1$ Mm in the wavelength range shown. Within the first second of heating a small downflow (< 5 km s^{-1}) develops immediately above the core formation height, which over the next 1-2 seconds moves deeper in the atmosphere, slightly redshifting the line core.

Between $t \sim 1-3$ s, the peak of the opacity is also shifted redward by the downflow that increases in magnitude to ~ 5 km s^{-1}. The extinction profile of the red wing is steepened as a result since red wing photons are preferentially absorbed relative

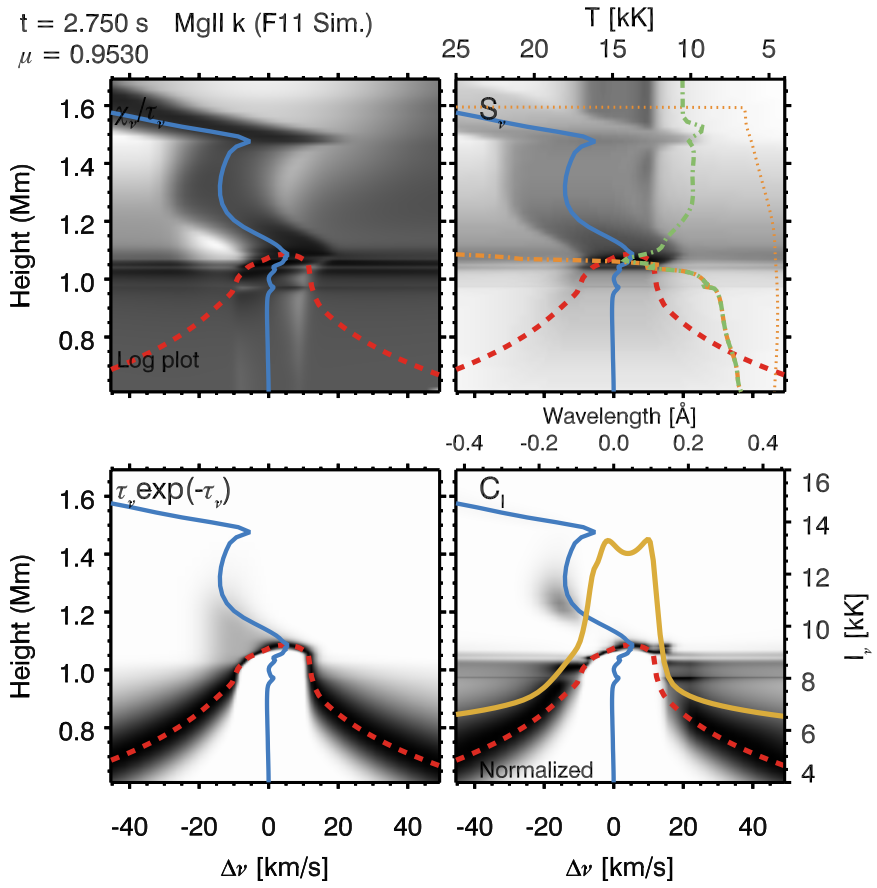

Figure 5.20: *Mg II k line formation in the EB (F11) simulation at $t = 2.75$ s. Lines are as described in Figure 5.14.*

to the blue wing. Higher in the atmosphere (between $\sim 1.1 - 1.2$ Mm) an upflow means that emitters produces some optically thin emission that is shifted to bluer wavelengths (approximately 0.10 - 0.15 Å bluewards of the rest wavelength). The line core source function is shown as the green line in top right panel, from which it can be seen that the shallowness of the reversal is due to the fact that the k3 component is more strongly coupled to the background radiation field than it is during quiet Sun conditions. It remains coupled to the height of source function maximum and has only decoupled a few 10s of km before reaching the formation height of the core itself. The intensity difference between the k2 emission peaks and the core is therefore smaller than in the quiet Sun where the formation height difference can be a few hundred km.

The downflow travels deeper into the atmosphere, reducing in magnitude as it enters denser material, so that between $t = 3 - 7$ s the redshift of the line is reduced.

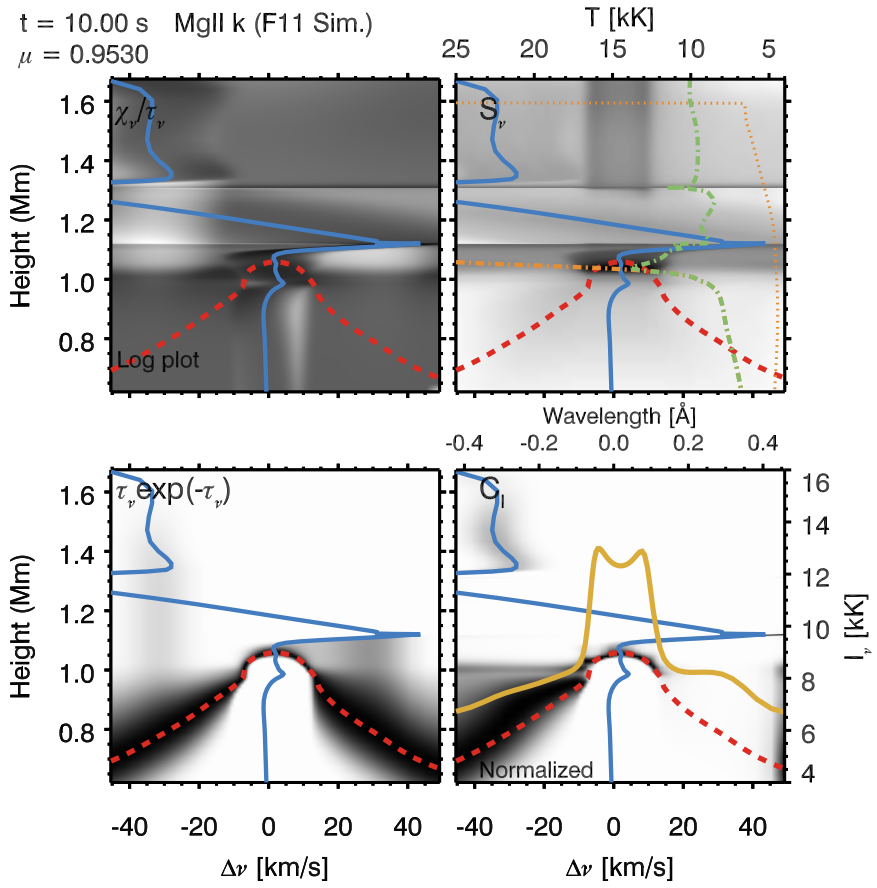

Figure 5.21: *Mg II k line formation in the EB (F11) simulation at $t = 10$ s. Lines are as described in Figure 5.14.*

The formation heights of the k2 emission peaks vary relative to each other, but only slightly and so while one or the other may be more intense for short periods they are largely similar. As the upflow speed increases the contribution of optically thin blue-wing emission is pushed further out, to around 0.15 - 0.20 Å from the core. It originates from a height of $\sim 1.3 - 1.4$ Mm

As before, the hot temperature bubble dominates the atmospheric dynamics at the end of the simulation. The strong condensation produced by the shock does not reach the core formation height, so has little effect on the wavelength of the k3 or k2 components. The k2r component is reduced in intensity relative to the k2v, as the absorption profile above the formation height is shifted redward. The k2r component forms lower than k2v, in a cooler region so is less intense. Additionally the population of the Mg II k upper level increases at the condensation height, resulting in a strong red-shifted source function in a narrow region only a few km thick.

The lower left panel of Figure 5.21 shows the increased attenuation of red wing photons. The combination of enhanced, strongly redshifted source function, means that the red wing contribution between 0.15 - 0.45 Å from the rest wavelength is almost exclusively from the condensation. This is optically thin contribution, formed away form the $\tau_\nu = 1$ surface. Similarly, the upflow results in emission between $\sim 0.60 - 0.80$ Å blueward of the rest wavelength.

Mg II k line formation (Alfvén Wave Model):

Figures 5.22 & 5.23 show the formation at $t = 1.5$ s and $t = 10$ s in the AW simulation.

In the AW simulation, the line core is formed around 1.1 – 1.15 Mm, and like in the EB simulation, shows a central reversal, at least initially. The k2r and k2v peaks are formed around 1.05 – 1.1 Mm, and are of roughly equal intensity since there are no notable velocity gradients at their formation height. A shallow velocity gradient is present between the mid-chromosphere (around 1.15 – 1.2 Mm) and the TR, but is initially small. Despite forming at the same height as their counterparts in the EB simulation, the k2 peaks are more intense since the AW simulation is warmer at this height. The source function of the k2 components is not fully de-coupled from the background temperature, so that the source function is larger when the atmosphere is hotter. This means that the central revresal is actually somewhat deeper than in the EB simulation since there is a larger difference in intensity between the k2 emission peaks and the k3 component.

Within the first two seconds the velocity gradient becomes steeper, blueshifting the line core by ~ 2 km s^{-1}. The shifted $\tau_\nu = 1$ surface means that the k2r peak is formed slightly deeper in the atmosphere (though only by a few km), where the source function is stronger, since it is more strongly coupled to the radiation field. This results in a more intense k2r vs k2v peak. Additionally, a shallow downflow of ~ 2 km s^{-1} is present below 1.05 Mm, causing some redshifted emission from this height, which widens the k2r peak. Note also that the central reversal has become shallower since the formation height difference between the core k2v component has reduced.

Over the duration of the simulation the upflow increases in strength to $\sim 5 - 7$ km s^{-1} at the core formation height, shifting the line core further. Since the velocity at the formation height of the k2 components is smaller than the core, these do not show a significant doppler shift. Some blueshifted optically thin emission is present

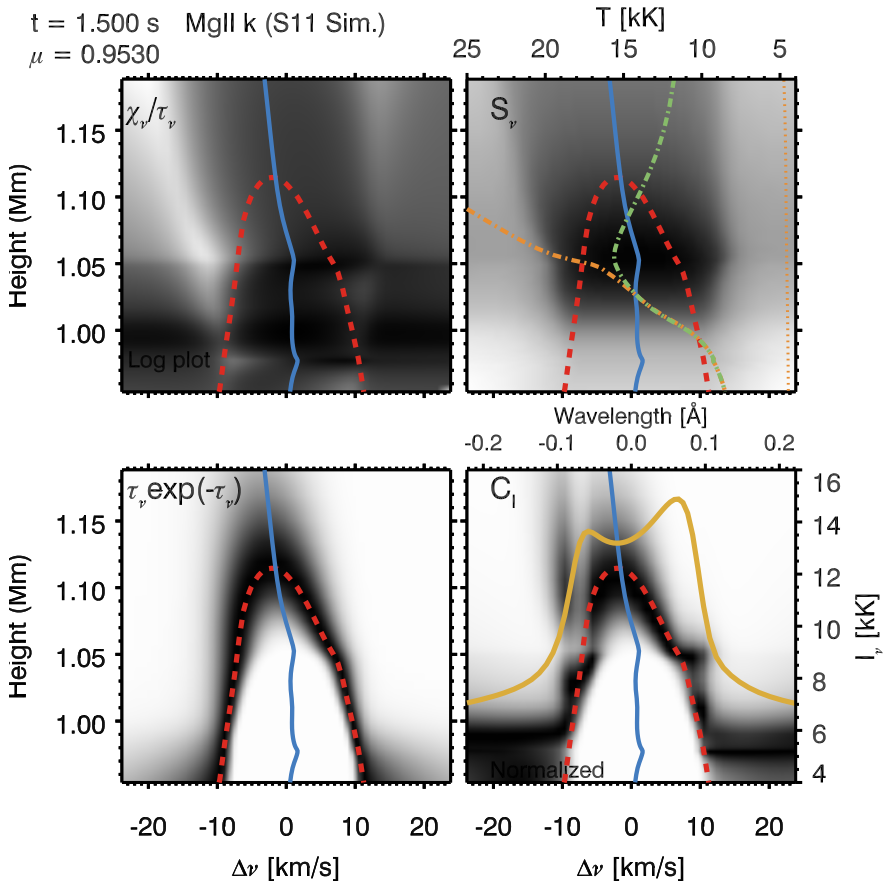

Figure 5.22: *Mg II k line formation in the AW (S11) simulation at $t = 1.5$ s. Lines are as described in Figure 5.14.*

in the blue wing. The contribution to the emergent intensity between ~ 0.10 - 0.15 Å blueward of the rest wavelength originates not from the $\tau = 1$ surface but from a greater height of $\sim 1 - 1.2$ Mm. The k2r peak, consequently, is significantly more intense than the blue, since it is formed in a region of source function maximum. The line core became hard to distinguish by $t = 5$ s, since it formed at very nearly the same height at the k2v component (on the $\tau = 1$ curve, that is, where the line core is defined as the maximum of the $\tau = 1$ surface).

In the latter half of the simulation, there are no drastic changes, but the $\tau = 1$ surface (and the theoretical line core) becomes more blueshifted as the velocity gradient increases, which also results in a larger contribution of optically thin emission. This now extends further into the blue wing and originates from heights $z \sim [1.1 - 1.3]$ Mm. The blue wing is therefore wider than might have been expected if the emission there was fully optically thick, since the $\tau = 1$ surface shows a steep extinction profile.

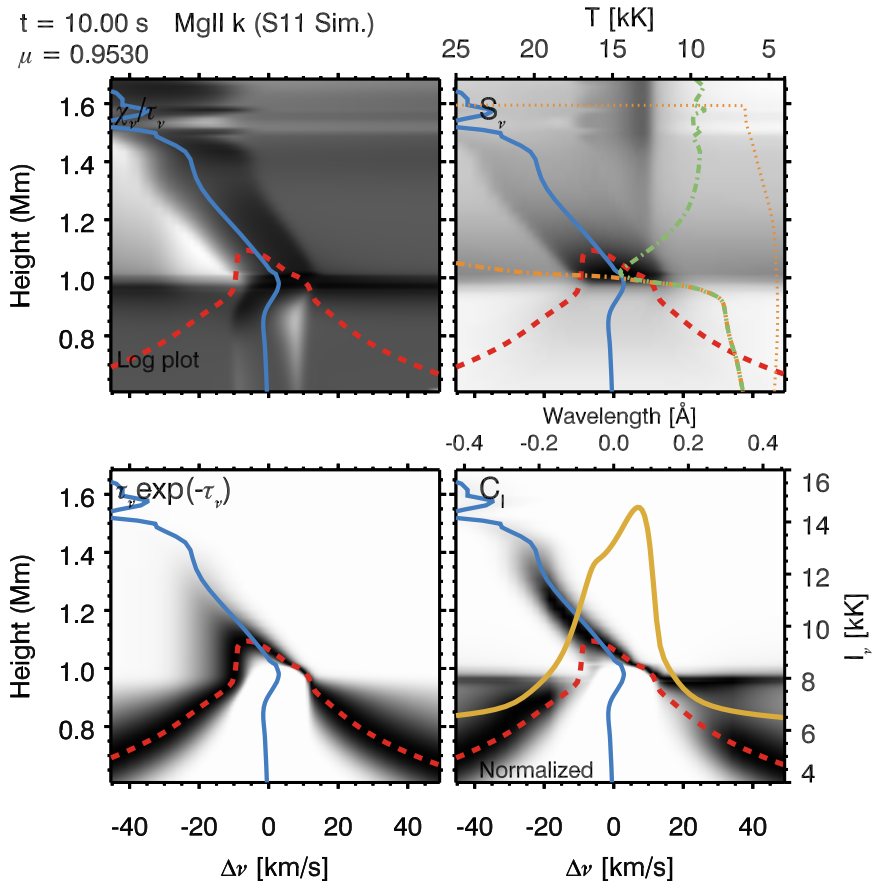

Figure 5.23: *Mg II k line formation in the AW (S11) simulation at $t = 10$ s. Lines are as described in Figure 5.14.*

Observationally, k2r might be confused with the line core since the central reversal has all but vanished. A small condensation near the k2r formation height broadens this feature (see Figure 5.23).

5.6 Summary and Conclusions

The research presented in this chapter describes initial efforts to model solar flares using radiation hydrodynamics in which the energy transport mechanism is via an approximated form of Alfvén wave dissipation. This mechanism could act either in concert with electron beams, or as an alternative mechanism that is able to heat the flaring chromosphere alone.

The preliminary experiments show that, as in Emslie & Sturrock (1982) and Reep & Russell (2016), Alfvén wave dissipation is able to heat different parts of the

chromosphere to varying degrees depending on the choice of wave parameters (with the caveat that these models are of monochromatic waves). Ion-neutral collisions are effective in dissipating the wave energy that subsequently heats the chromosphere in both the lower atmosphere (as reported by Emslie & Sturrock (1982)) *and* the upper atmosphere depending on wave parameters. A high frequency wave will decrease the damping length due to an increased contribution from ion-neutral damping even in the upper atmosphere where there are fewer neutrals. Damping via electron-ion and electron-neutral collisions becomes important for larger wave numbers (the damping length is decreased due to an increased contribution from parallel resistivity). These results, using a simulation with important radiative losses included in detail, help to support the previous work of Russell & Fletcher (2013) & Reep & Russell (2016). Being able to strongly heat the mid-upper atmosphere is an important requirement for Alfvén waves to be considered an alternative heating mechanism to electron beams.

One simulation was selected for a detailed comparison to identify if any discriminating features between electron beams and Alfvén waves would present themselves observationally. The simulations had the same energy flux injected for a period of 10 s, and the Alfvén wave parameters chosen so that the energy would be deposited in roughly the same region of the chromosphere. The atmospheric evolution showed some interesting similarities in that both showed strong heating over the whole chromosphere, but dominating in different locations. The significant difference was the presence of the under-dense high temperature bubble that produced strong shocks in the electron beam simulation. The explanation for the absence of this feature in the Alfvén wave simulation was that energy deposition was not as concentrated in the mid chromosphere so that significant ionisation of He to He III did not take place. While the AW heated model did not reach such high temperatures in the mid-chromosphere, the upper chromosphere was hotter, and at around 1 Mm the atmosphere was $\sim 5,000 - 10,000$ K warmer.

The effect of the different energy deposition profiles on the density, velocity and ionisation structure of the atmosphere resulted in differences to the radiation output. The Ca II 8542Å lines were similar at the end of the simulations, but in the AW simulation the spectra took longer to increase to the level of the profiles produced by the electron beam simulation, due to the additional ionisation of hydrogen in the lower atmosphere that increased the electron density there subsequently allowing

recombination to Ca II. This timing difference could be observable, but recall that the WKB assumption means that the travel time of the Alfvén wave through the atmosphere was not considered here. Simulations by Russell & Fletcher (2013) and discussions by Fletcher & Hudson (2008) suggest that the travel time can be on the order of several seconds. Therefore, longer timescales may be more important. It is encouraging to note that the final states of the spectra are similar, however, as it suggests that Alfvén waves are able to heat the atmosphere in a similar manner to electron beams and produce radiation signatures similar to those observed (e.g. the observations by Kuridze et al. 2015; Rubio da Costa et al. 2016).

In the case of Mg II k, in both simulations the lines peak early and are more intense than the quiet Sun profiles, due to their formation height being pushed deeper in the atmosphere where stronger coupling to the Planck function results in a much shallower central reversal. The line source functions are also more intense since this part of the atmosphere shows a large temperature enhancement. Differences between the simulations, largely due to the velocity structure of the atmosphere, present themselves quickly. Over time the central reversal becomes difficult to distinguish from the k2v component in the Alfvén wave simulation. The profile becomes asymmetric with a strong red peak and weaker blue peak and line core. The electron beam simulation contains a central reversal for the duration of the simulation and is largely symmetric around the line core. As the high velocity flows associated with the temperature shocks propagate through the atmosphere the far wings become enhanced by red- and blueshifted emission.

Neither simulation provides a good match to observations of Mg II k lines, particularly the electron beam simulation which had a prominent central reversal. The profiles from the Alfvén waves could be interpreted observationally, however, as single peaked, redshifted profiles with an extended blue wing or shoulder, not dissimilar to observations of Mg II in flares. The 'theoretical core' (peak of the $\tau = 1$ surface) is in fact formed in upflowing plasma, but more blue wing photons are absorbed than red wing photons, leading to the net red asymmetry (see also Heinzel et al. 1994; Kuridze et al. 2015). This highlights the difficulty in interpreting observations of these optically thick lines, and, is an exciting avenue for further research, looking at other IRIS lines such as C II and Fe II in similar simulations.

The WKB approximation means that reflections are not considered. In the intial

stages of the flare the WKB approximation is a reasonable approximation in the chromosphere as the wavelength is larger the Alfvén speed scale lengths. This was confirmed to be the case for the simulation presented in detail here (AW_Sim2), and is more generally is true for frequencies 1 Hz or greater. Russell & Fletcher (2013) showed that Alfvén waves would require such frequencies to pass into the chromosphere. The density and temperature contrast between the corona and chromosphere is large, meaning that the Alfvén speed decreases sharply through the TR into the chromosphere. Reflection of waves propagating down from the corona would occur, while some wave energy would be transmitted through to the chromosphere. This model might be underestimating heating of the corona by reflected waves.

When the flare atmosphere is heated the density and temperature structure of the chromosphere change, which affects the Aflvén speed and therefore wavelength. It was found for the simulation presented in detail (AW_Sim2) that the WKB approximation is valid everywhere in the chromosphere initially, but that at later times in the simulation ($t >\sim 5$ s) the condition that the wavelength is less than the scale length of the Alfvén speed was not always held in the uppermost part of the chromosphere (near 1.5 Mm). This would result in some reflection back to the corona. Also, at ~ 1 Mm while the the WKB approximation was valid, the wavelength approached the scale length. This height should also be monitored carefully in future experiments as reflections might occur there. Further work is necessary to consider how to more accurately model Alfvén energy transport after the initial stages of energy deposition.

The second restriction that the wave travel time does not enter in the computation of the heating rate, so that the atmosphere is assumed to not change during propagation. The heating rate is then applied and the atmosphere evolves to the next timestep. Then the heating rate at the next timestep is recomputed given the new state of the atmosphere.

Still, as preliminary research, assessing the validity of the physics behind Alfvén wave heating during flares, this approach has shown to be useful and interesting. Future efforts will study these simulations further, but with the aim of identifying the key physics involved so that better, more realistic models can be developed.

The parameter space is large, and the simulations complex. Further work will focus on filling in the parameter space and studying these simulations in greater detail in an effort. This will include changing the magnetic field, and energy flux

in addition to the frequency and wave number. Changing conditions during the flare (the density and temperature structure) in response to flare heating has a corresponding effect on the heating rate which varies in strength as a function of both height and time. Since the effectiveness of collisions varies strongly due to both temperature and density, future experiments should also consider the pre-flare atmosphere used (Dr J. Allred (NASA/GSFC) has a suite of initial atmospheres with a variety of coronal temperatures, loop lengths, and densities which he has agreed to share).

As discussed previously, accelerated electrons are definitely present in the flaring chromosphere. Two scenarios present themselves: Alfvén waves act alone to transport and dissipate flare energy, and secondary effects accelerate electrons locally, or Alfvén waves act as an additional mechanism in concert with electron beams (an attractive scenario as waves could directly heat the lower atmosphere, and beams could heat the upper atmosphere and produce the observed strong downflows). The first case has been tested so far (though note that no effort is made here to explain the presence of accelerated electrons), but the second case warrants attention also. This is possible with the code in its present form, and initial experiments are underway. These open new questions, however, as the distribution of energy to each mechanism is not well constrained. Tying to observations will be key. Identifying flares that either do not have a strong HXR signature or in which the energy deposited by an electron beam (as derived from RHESSI observations) is not sufficient to account for observed radiative losses (e.g. Fletcher et al. 2013), will be useful in helping to ascertain if Alfvén waves can account for the radiation observed (either alone or in tandem with beams).

Finally, waves have so far been simulated as monochromatic AWs, which are able to heat different parts of the atmosphere effectively depending on their parameters. It is more likely that a spectrum of waves would be produced by strong flare perturbations of the magnetic field, and so research into simulating multiple waves is an exciting avenue of research.

Chapter 6

Continuum Enhancements in Solar Flares

The research concerning the 2011-Feb-15th white light flare presented in this chapter was published in Kerr & Fletcher (2014).

6.1 Introduction to White Light Flares

Solar flares that exhibit enhancements to the white light (WL) continuum are known as white-light flares (WLF; Švestka 1966; Neidig 1989). Enhancements to the visible continuum have been known about since the first flare was observed by Carrington (1859), but the difficulty in observing these small enhancements against the bright photospheric background, and the lack of systematic optical broadband spectroscopy, means that there is still debate as to the mechanism(s) that results in WLF emission Neidig (1989). Indeed, the typical contrasts in flares are usually just a few percent up to a few ×10% (Matthews et al. 2003; Chen & Ding 2005), which are also short-lived. The difficulty in observing these events led to the notion of 'Big Flare Syndrome' where WLFs were considered to be rare events, associated only with the most energetic of flares.

Though still relatively difficult to observe, it is thought now that WLFs are not as rare as previously thought, and have been observed in flares of GOES C-class (e.g Matthews et al. 2003; Hudson et al. 2006). Indeed, Jess et al. (2008) observed a GOES C2.0 WLF, with a source source that had a 300% contrast. This very high contrast may be explained by the high cadence of observations (so that they caught

the exact peak of the event), and the small size of the source. Nevertheless, strong WL emission was observed in what would normally be considered a weak event. Finally, Kretzschmar (2011)'s superposed epoch analysis suggests that most flares from GOES classes C to X present WL continuum enhancements.

Since WL enhancements appear to be present in a large subset of flares of varying size, WLFs pose an interesting challenge to our understanding of flare energy transport, not least because they seem to carry a significant fraction of the radiated energy during flares (e.g Woods et al. 2006; Kretzschmar 2011). One of the most important questions regarding WLF emission is what is/are the emission mechanism(s) responsible? The answer to this question will shed light on the location in the atmosphere from which WLF emission originates. Consequently, models of flare energy transport must be able to deposit sufficient energy in these locations.

WLFs have enhancements in the continuum at wavelengths $\lambda > 3600$Å, so that they cover wavelengths in the optical part of the Balmer continuum ($\lambda = [912, 3646]$ Å), and the Paschen continuum ($\lambda = [3647, 8206]$Å). Švestka (1966) reported that the majority of WLF emission appeared as localised sources with a "bluish white" or white colour. Neidig (1989) reviewed WLF characteristics, noting that contrast was greater for wavelengths $\lambda < 4000$Å. This could be due to either the presence of a Balmer jump, indicating a hydrogen free-bound spectrum (observed in some WLFs, but not all, e.g Fang & Ding 1995), the smaller background intensity at bluer wavelengths, or a hotter flare temperature than in the quiet Sun.

In some WLFs the Balmer jump at 3646Å has been observed. For example, Neidig (1983),Neidig & Wiborg (1984), Donati-Falchi et al. (1984), and Hiei (1982) all discuss flares in which a Balmer jump was observed. The Balmer jump was observed to be smeared out and located redward of its usual location in Neidig (1983). Those flares, and similar events, showed a relatively flat contrast with wavelength at $\lambda > 4000$ Å, whereas there was a jump in contrast observed around $\lambda < 4000$ Å. Other observations, however, do not contain Balmer jumps and instead show a smoother decrease in contrast with increasing wavelength, (e.g Machado & Rust 1974; Boyer et al. 1985). The lack of complete WLF spectra has meant that is has been difficult to determine how many flares do and not have a Balmer jump (Fang & Ding 1995, reported that, by 1995, only 10-15 flares with good spectral coverage exist in the literature).

A classification based in part on the presence or lack of a Balmer jump has

developed, so that WLFs can be classed as Type 1 or Type 2 (Machado et al. 1986). Fang & Ding (1995) studied three WLFs, two of which were considered Type 1, and one that was considered Type 2, summarising both the differences between those events, and the differences between Type 1 and Type 2 WLFs in general. Typically, Type 1 WLFs have a good temporal correlation with the peaks of hard X-rays (HXRs), whereas Type 2 WLFs do not, with the WL enhancement either preceding or lagging the HXR and microwave emission. Type 1 WLFs have a strong Balmer jump, and in one observation a weak Paschen jump (Neidig & Wiborg 1984), whereas Type 2 do not. Finally, Type 1 WLFs have strong and broad Balmer lines, with clear central reversals. Type 2 WLFs generally have weak emission in the Balmer lines only up to H11, with no higher order lines affected by the flare.

As well as the temporal correlation with HXRs several studies have found a good spatial correlation also (e.g Matthews et al. 2003; Fletcher et al. 2007; Watanabe et al. 2010; Krucker et al. 2011). While WLF and HXR sources are generally co-spatial Fletcher et al. (2007) note that there are small separations (though the spacecraft roll angle introduced an unknown error to this co-alignment). Not all WLFs have a spatial correlation with HXRs, with some events showing no overall one-to-one correspondence (Sylwester & Sylwester 2000). Sylwester & Sylwester (2000) and Matthews et al. (2003) both note that some flares had WLF sources that were better correlated with soft X-ray (SXR) emission, with the speculation that those flares could be Type 2. Nevertheless, the good temporal and spatial association between WLFs and HXRs has led to the assumption that the flare energy deposition responsible for HXR footpoint emission is also responsible for WLF emission for Type 1 events.

Different models of WLF emission have placed the origin in the chromosphere, TMR or photosphere, with no consensus as to the emission mechanism responsible. Two leading theories have emerged: (1) chromospheric recombination (free-bound) radiation, and (2) an enhanced photospheric (or upper photospheric) H^- continuum. Of course, a combination of these mechanisms is also possible, with the dominance of each mechanism varying from flare to flare.

Over-ionisation of hydrogen occurs during flares, either due to non-thermal collisions with accelerated electrons or the increased temperature during the flares, allowing electrons to recombine to levels 2 or 3, creating an enhanced Balmer and Paschen recombination spectrum (e.g Hudson 1972). Since recombination timescales in the chromosphere are short (<1 s, e.g Metcalf et al. 2003), this can explain the tight

correlation between WLF and HXR emission. This mechanism would also explain the observed Balmer jumps, and the one weak Paschen jump observed (Neidig & Wiborg 1984).

H^- ions are produced when atomic hydrogen captures an electron. This extra electron is only weakly bound, with an ionisation potential of only 0.754 eV. Increased absorption and re-radiation by H^- will locally raise the temperature. This results in an enhanced H^- contribution to the the WL continuum, which will appear blackbody-like. If this mechanism dominates the whole WL spectrum, then Balmer and Paschen jump will not be observed.

The presence of Balmer jumps in some WLF spectra is convincing evidence that hydrogen free-bound radiation is responsible for the emission for WL emission. Neidig & Wiborg (1984) observed three flares with Balmer jumps, and one with a weak Paschen jump, leading them to conclude that recombination must be the dominant mechanism producing WL. This was in agreement with Machado & Rust (1974), who although not observing a discontinuity at bluer wavelengths did observe a frequency dependence to the WL contrast, as opposed to the flatter relation one might expect from H^-.

A number of authors instead attributed only the Balmer continuum wavelengths ($\lambda < 3646$Å) to recombination radiation and determined that enhanced H^- was the explanation for enhancements at Paschen continuum wavelengths. Analysis by Boyer et al. (1985) ruled out both an optically thin free-bound and an optically thin H^- origin for the WL enhancements to Paschen continuum wavelengths due to the requirement for an unfeasibly large emitting region and excessive energy input requirements, respectively. An optically thick H^- origin was concluded the most probable explanation, with a temperature enhancement to the upper photosphere, decreasing with depth into the lower photosphere. Hiei (1982) suggested a similar situation. In that flare a Balmer jump was observed, but the strength of the spectrum at wavelengths redward of the jump suggested that the observed enhancements could not solely be due to recombination radiation. Instead Hiei (1982) proposed that the Balmer recombination spectrum was responsible for continuum enhancements $\lambda \leq 3646$ Å, but that enhanced H^- was required to explain enhancements longer than λ3646Å. This was based on the ratio of intensities at wavelengths redward and blueward of the Balmer jump. Neidig (1983) agreed with this assessment from a similar analysis.

More recent studies such as Kretzschmar (2011), and Watanabe et al. (2010, 2013), suggest that longward of the Balmer jump the enhancements are photospheric in origin resulting from increased temperatures during flares. Watanabe et al. (2013) used optical continuum filtergrams from *Hinode*/SOT to study the temperature and height distribution in a limb flare. They found that the centroids of the sources were displaced from each other by a few hundred km in sequence from Ca II H, red continuum, green continuum to blue continuum. From an assumption of the height of emission of the Ca II H images they noted that the continuum images must originate from the photosphere. Additionally, they find a temperature enhancement of $\sim 100 - 200$ K during the flare from assuming a blackbody spectrum, and that, curiously, at later times the blue continuum was somewhat hotter than the the red, by ~ 60 K that they suggest may indicate heating from below.

A problem in interpreting the WL emission as being from the deepest layers of the flaring atmosphere (at least, the enhancements longward of the Balmer jump) is how to get energy to the required depths. Direct heating by non-thermal electron beams is insufficient, with the bulk of the beam energy deposited in the mid-upper chromosphere. Metcalf et al. (1990) states that electrons with an energy of 350 keV are required to reach the TMR, and Neidig (1989) notes that to heat the upper photosphere electrons with energy in excess of 900 keV would be required. Based on observations of TMR heating and ionisation via inversions of the Mg I 4751Å & 5173Å lines, Metcalf et al. (1990) found that there is not enough total power carried by these electrons to explain the required heating rates in the TMR. From a survey of nine WLFs observed by both TRACE and RHESSI, Fletcher et al. (2007) demonstrated that to account for the WL radiative losses, the low energy cut-off must be lower than 20 keV, suggesting that the bulk of the energy required lies in low energy electrons that are unable to penetrate deeply into the atmosphere.

Radiative backwarming (e.g Aboudarham & Henoux 1986; Machado et al. 1989; Metcalf et al. 1990) could resolve this issue. In this model, energy deposition in the chromosphere results in an enhanced Balmer and Paschen continuum via recombination radiation. As well as propagating outwards from the solar atmosphere where it is observed, this radiation can propagate down into the lower atmosphere, where it is absorbed by H^- and locally heats the atmosphere by a modest amount. Thus, only one energy source is required rather than two *in-situ* sources. The extent to which the the H^- spectrum dominates over the Paschen recombination spectrum

is likely to vary from flare to flare, but as mentioned above most authors suggest that the H^- dominates in the majority of cases. This model requires a strong Balmer continuum to produce the WL emission across the spectrum, and so Type 2 WLFs may need another explanation (though Machado et al. 1989, speculate that SXR & UV backwarming in the post-impulsive phase may account for this). Recently, Kleint et al. (2016) analysed a flare where both the optical and NUV continua were observed. The NUV continuum was observed at ~ 2830 Å by IRIS, and the the optical continuum at 6173 Å by SDO/HMI and in the infrared (IR) at 10840 Å by the Facility Infrared Spectrometer (FIRS). They found that the optical/IR data was consistent with an enhanced H^- emission (with temperatures increasing to ~ 6300 K), but that the NUV intensity exceeded the blackbody prediction. It was suggested that the optical/IR emission during the flare originated in the photosphere, but that the NUV emission must result from an enhanced Balmer continuum (recombination radiation). Further, by comparing the energetics of the optical and NUV emission they propose that Balmer continuum backwarming could explain the enhancements to the H^- continuum.

This chapter will describe the WL emission from the 2011-Feb-15th X2.2 class solar flare, observed using the *Hinode* Solar Optical Telescope (SOT) at three passbands in the Paschen continuum. As well as describing how WLF sources from *Hinode*/SOT were identified and calibrated, an analysis is presented to characterise the emission under one of two idealised models: either of solely optically thick H^- origin from the photosphere so that the emission appears like a blackbody, or solely of optically thin chromospheric origin, so that the emission appears as hydrogen recombination radiation. Obviously these are limiting cases, and so some comment on the core-halo appearance of WL sources (which assumes a combination of emission mechanisms) is made, and the initial results of an analysis of a WLF observed jointly by IRIS and *Hinode*/SOT are presented. This X class flare from 2015-March-11th sampled both the NUV Balmer (IRIS) and optical Paschen (SOT) continua.

6.2 Observations of the 2011-Feb-15th Solar Flare

The Solar Optical Telescope's Broadband Filter Imager (BFI), on board the *Hinode* spacecraft (Tsuneta et al. 2008; Shimizu et al. 2008; Suematsu et al. 2008), observed an X2.2 class solar flare on the 15th February 2011 (SOL2011-02-25T01:56:00), that

occurred in NOAA active region (AR) 11158. This two-ribbon flare began at roughly ~01:44 UT and peaked at ~01:56 UT, was located near disk centre, and had an associated CME. It has been comprehensively studied by a number of researchers, since it was the first X-class event of Cycle 24, and since it was well observed not only by the SOT, but by numerous instruments, including SDO's Atmospheric Imaging Assembly (AIA), Extreme-Ultraviolet Variability Experiment (EVE), and Helioseismic and Magnetic Imager (HMI), the RHESSI spacecraft and the Nobeyama Radio Observatory (NRO; Nakajima et al. 1994).

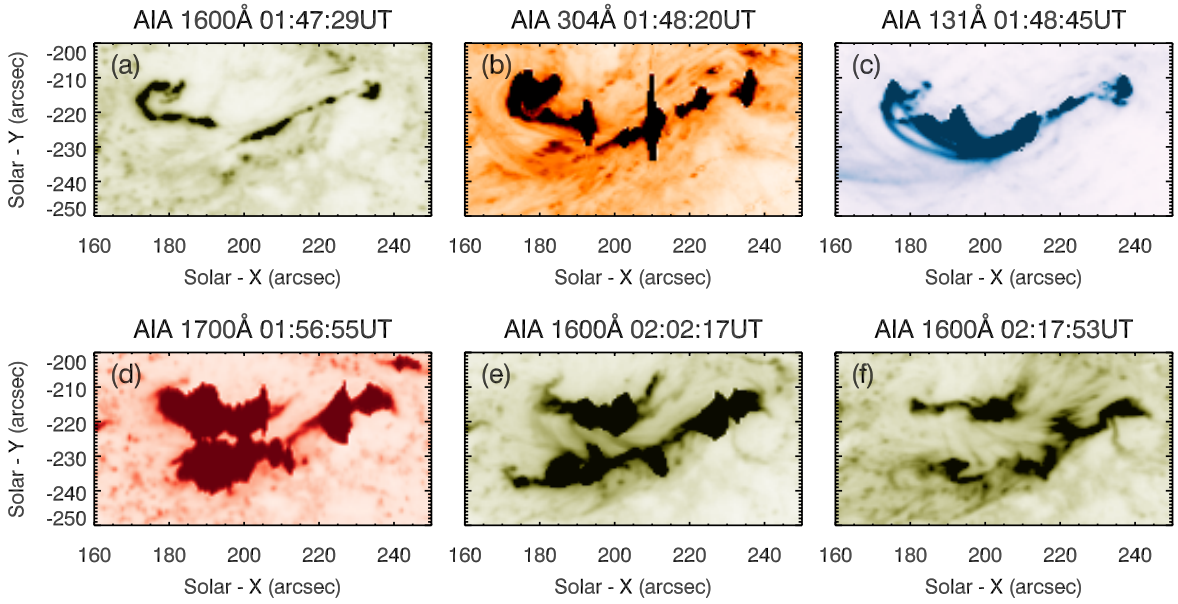

Figure 6.1: *A sequence of AIA images from flare impulsive phase (panels a-c), peak (panel d) and decay (panels e-f). The filter is indicated on each panel, and images are inverse scale. During the flare peak there is saturation and bleeding of the CCD, so only one image from the peak is shown, to illustrate the ribbon structure at that time.*

6.2.1 Flare Context

In addition to the X2.2 class event, the AR also produced numerous C-class and five M-class flares in the days prior to 2011-Feb-15 (Maurya et al. 2012; Tarr et al. 2013). This AR was a rotating sunspot group with a complicated structure that included penumbral fibrils with a twisted appearance, orphaned penumbrae, and light bridges.

Flare ribbons began to form at ~01:44 UT in the AIA images, with ribbons located north and south of the polarity inversion line (PIL). Figure 6.1 shows a sequence of AIA images at various times during the flare, illustrating the evolution of the ribbon morphology. The northern ribbon appeared as a hooked structure, which expanded north and west during the flare. The southern appeared more elongated, and expanded south and east. Due to AIA saturation and bleeding, it was not possible to observe the flare at the peak, but in a few images (such as Figure 6.1(d)) the structures are discernible. The intensity in most AIA filters had decayed to the pre-flare by around 02:30 UT. Figure 6.2 shows the RHESSI 3-6 keV, 6-12 keV, 25-50 keV, & 25-50 keV and 50-100 keV lightcurves, alongside the GOES 1-8Å lightcurve. Energies ≥ 25 keV are generally considered to be of non-thermal origin, so this event had a clear non-thermal signature. The flare impulsive phase showed several peaks before reaching maximum at ~01:56 UT, after which the 50-100 keV signal decayed over 2-3 minutes, and the others more gradually.

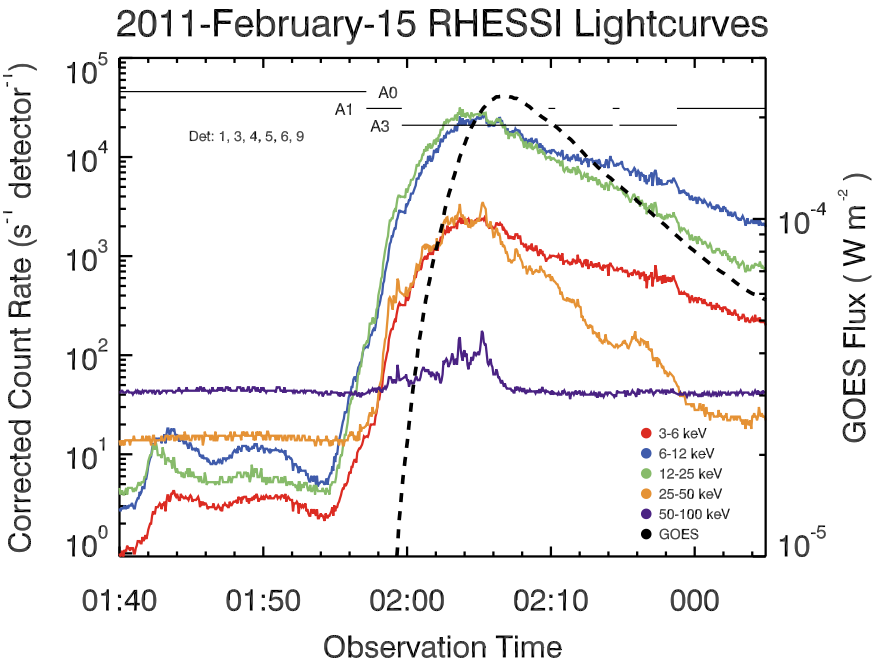

Figure 6.2: *Lightcurves of various energy channels from RHESSI. The colour is indicated in the legend. The 1-8Å GOES lightcurve is shown as a dashed line. The detectors used are listed on the top right of the image.*

Using HMI data Tarr et al. (2013) estimated the drop in magnetic free energy following the X-flare to be 1.68×10^{32} erg, which is consistent with the results of Milligan et al. (2014) who state that the total energy contained in non-thermal electrons was $> 2 \times 10^{31}$ erg. This could be interpreted as the energy deposited into the chromosphere by a beam of non-thermal electrons, over the ~ 10 minute duration of the event's impulsive phase.

Again using HMI data, Wang et al. (2012) showed that the horizontal photospheric magnetic field underwent a rapid and irreversible enhancement of 30% along the PIL during the flare. Co-spatial with the flare ribbons, and magnetic field enhancements, were compact non-thermal HXR footpoints sources observed by RHESSI. There was a motion of the RHESSI footpoint sources along the ribbon that was also observed by Kuroda et al. (2015). Combining RHESSI HXR observations with microwave (MW) data from NRP, Kuroda et al. (2015) showed that there were seven separate peaks in the HXR & MW lightcurves, that were associated predominately with two compact spatial sources. Initially these sources were aligned along the elongated southern ribbon with only weak emission from the northern ribbon near $\sim [180, -225]$". Between the second and third peak in the lightcurves (after ~01:52:11 UT) the strongest sources shifted location to near $\sim [190, -235]$" and $\sim [190, -225]$", one on either side of the PIL. This is roughly co-spatial with the most intense emission at flare peak (see Figure 6.1(d)). Of course, RHESSI's dynamic range means that only the strongest sources are imaged, so the absence of observed HXR footpoint sources elsewhere along the ribbon at later times (e.g near the intense emission at $\sim [230, -215]$") does not preclude the presence of HXRs in those locations. Figures 1 & 3 from Wang et al. (2012) and Kuroda et al. (2015) show the evolution of HXR sources.

Observations from EVE showed that the EUV free-bound Lyman, He I, and He II continua (which all showed clear recombination edges), and the underlying free-free continuum in the range 6.5-37 nm, were enhanced during the flare (Milligan et al. 2012). The free-bound continua exhibited a rapid rise phase, with a similar temporal profile to the HXR lightcurves. Unlike the free-bound continua, the free-free continua instead showed a temporal profile that more closely resembled SXR emission. Free-free emission was deemed to be coronal in origin.

A final noteworthy finding is that this flare produced two strong seismic sources in the photosphere (Kosovichev 2011; Zharkov et al. 2011). Curiously, the sunquakes were not co-spatial with the most intense parts of the flare ribbon, nor where they

co-spatial with the largest variations in magnetic field or Doppler velocity. Instead the sources were located at the extreme ends of each ribbon structure. Also, the eastern seismic source (the strongest) preceded the peak of the HXRs occurring early in the impulsive phase. This is contrary to one idea that sunquakes and WLF emission originate from the same location with similar energy (Donea et al. 2006). Zharkov et al. (2011) deduce that the cause of the sunquakes was in fact an erupting flux rope, with the sources appearing at the flux rope ends.

6.2.2 *Hinode*/SOT Observations

The *Hinode*/SOT BFI observed the flare on a trigger mode, and so missed the pre-flare and onset, but managed to capture most of the impulsive phase, the peak, and the initial decay in the red, green and blue continuum passbands (collectively referred to as RGB), and the Ca II H line passband. Level-0 data were downloaded from Hinode Science Data Centre Europe repository[1]. Images were 1024×1024 pixels in size, with on-board 2×2 pixel averaging and a resulting pixel scale of $.109 \times .109''$ pixel^{-1}. This gave a field of view of $111.575'' \times 111.575''$. Observation times for each filter are listed in Table 6.1. A filter wheel rotates between passbands in the sequence Ca II - R - G - B, giving a cadence between successive filters of ~ 3.2 s and a repeat cadence for each filter of $\sim 19 - 21$ s.

	Ca II H	**Red**	**Green**	**Blue**
Wavelength	(3968.5 ± 1.5)Å	(6684.0 ± 2)Å	(5550.5 ± 2)Å	(4504.5 ± 2)Å
Start Time	01:50:18.46 UT	01:50:21.66 UT	01:50:24.84 UT	01:50:28.03 UT
End Time	01:59:59.92 UT	01:59:42.36 UT	01:59:45.55 UT	01:59:48.74 UT
$\tau_{\text{exp.}}$	0.123085 s	0.051195 s	0.076991 s	0.061742 s

Table 6.1: *SOT/BFI Observations from the 2011-Feb-15th X-class flare.*

Data were calibrated to Level-1 using the standard SSW routine `fg_prep.pro`. This procedure subtracts the dark pedestal and dark current, corrects for flat field, and removes cosmic ray spikes. Pointing information is updated in the header files. For dark current subtraction a dark frame with the same exposure and binning is

[1] http://sdc.uio.no/sdc/

selected automatically by the software. Negative pixels and other bad data are set to zero. Similarly, an appropriate flat field is selected for the gain correction. Level-1 images were then divided by exposure times so that data is in units of DN s^{-1} $pixel^{-1}$. The mean exposure time for each filter is listed in the final row of Table 6.1.

Figure 6.3 shows a sequence of Ca II H line images from the flare impulsive phase and peak. While difficult to see due to the scaling of the colour table, the sunspot and pores are visible in these images as lighter patches, since the BFI filter samples the line wings, which are formed in the photosphere. Aside from a few saturated pixels, the flare ribbons and their evolution are clear, and share a similar morphology to the UV and EUV images from AIA. These images reveal details that were saturated in AIA image, namely the fine structure within each of the ribbons. As newly reconnected loops deposit energy in the chromosphere new locations brighten so that the ribbons appear with a intense, and narrow, leading edge. As the emission decays, the material appears as a more diffuse and dimmer 'wake'. At flare peak there are three locations where the intensity is particularly high. The middle of the northern ribbon near $\sim[165,-240]$", and the two ends of the southern ribbon near $\sim[165,-265]$" & $\sim[210,-240]$". Note that these images have not been aligned with SDO, and there is an offset of a few $\times 10$".

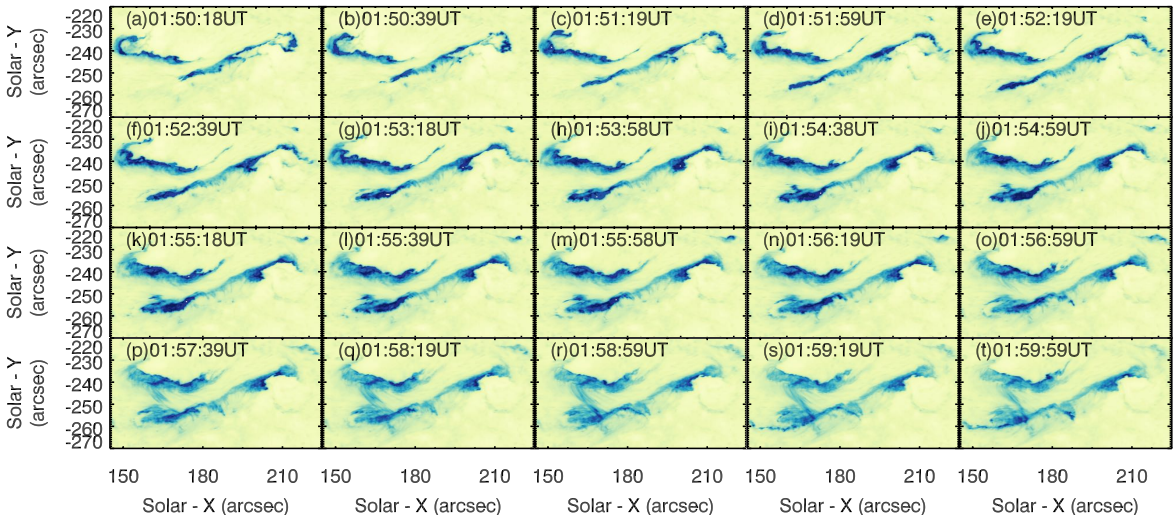

Figure 6.3: *Ca II H line images of the flare ribbons, showing a bright leading edge that leaves behind a more diffuse wake as the material cools.*

Figure 6.4 shows a red continuum image from flare peak, showing the full field of

view of the SOT. As will be discussed in § 6.3 the optical continuum flare sources do not immediately reveal themselves. This image does, however, show the complexity of the active region. There were a few large jumps of several tens of arcseconds in

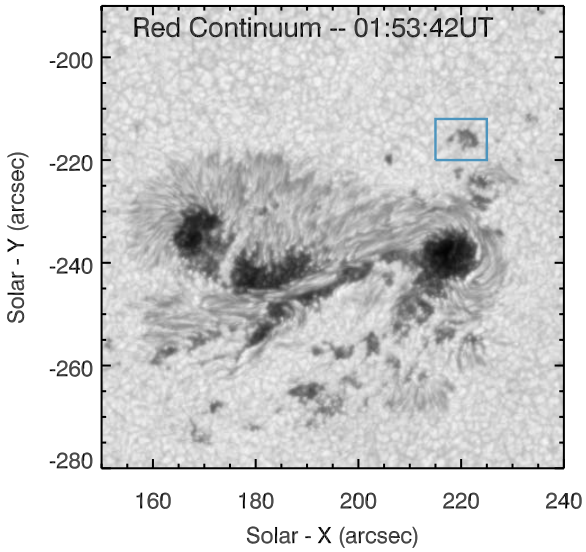

Figure 6.4: *A red continuum image from around the flare peak. WLF sources are present in this image, but are washed out by the background photosphere, and only visible in the intensity images when animated. The blue box outlines the pore used for co-alignment.*

the SOT pointing during the flare, as well some spacecraft jitter. The four filters were mostly aligned to each other but there was some small drifting between exposures. In order to analyse the same WL sources from all three filters, the data were aligned. This was achieved in two stages. First, the data were manually aligned to a reference image by overlaying contours of the small pore at $\sim [225, -215]$" (outlined by the blue box on Figure 6.4), and shifting the each individual image until it matched the reference. The reference image was frame 10 of the red continuum data (01:53:42 UT). Images were then cropped so that they all showed the same field of view, and each crudely co-aligned waveband set was cross-correlated using the *Hinode* `SSW` routine `fg_rigidalign.pro` to remove residual jitter. This procedure works by breaking down each data set into subsets of four images, internally cross-correlating each subset to the first frame in that subset, and then finally cross-correlating all of the subsets to each other. Visual inspection of the data set showed that they were

accurately aligned to within 1-2 pixels.

6.2.3 *Hinode*/SOT BFI Filters and Intensity Calibration

Intensity data from SOT is recorded in terms of counts, or Data Numbers (DN) so, as we did with IRIS data in Chapter 3, it is necessary to calibrate the data if we want intensity expressed as physical units of W cm^{-2} sr^{-1} $Å^{-1}$. For the 2011-Feb-15th flare this calibration was performed by Dr. Ted Tarbell (*private communication*), who provided the conversion factors for each passband that are listed in Table 6.2. The average disk centre intensity in physical units used to calibrate the SOT data was confirmed by me, and the procedure for calibration is described here.

Figure 6.5(a,b,c,d) shows the disk centre specific intensity in units of W cm^{-2} sr^{-1} $Å^{-1}$, in the wavelength range of the SOT red, green, blue, and Ca II H line filters. Also shown are the SOT transmission filters. The SOT response functions functions are not published, only the pre-flight transmission filters, so that the average disk centre intensity across each passband must be compared to disk centre observations from the SOT to ascertain the conversion factors from DN s^{-1} $pixel^{-1}$ to physical units.

The average disk centre intensities were obtained from the Fourier-Transform-Spectra (FTS) spectral atlas, produced by Brault & Neckel in 1987 at the Kitt Peak Observatory. This atlas was later made available via the Hamburg Observatory `ftp` site[2] (Neckel 1999). Disk centre intensity, and disk-averaged flux, at wavelengths in the range 3290 to 12510Å were observed using similar techniques to those detailed in Neckel & Labs (1984). In each panel of Figure 6.5 the average disk centre intensity observed by each SOT filter is written in the top left corner, found by integrating the solar atlas over each filter bandpass.

Disk centre SOT images from around the date of the flare were processed with `fg_prep.pro` and divided by exposure time to obtain DN s^{-1} $pixel^{-1}$. After excluding bad data, sunspots and plage, the images are averaged to obtain the mean disk centre count rate. Dividing the average disk centre intensity by the count rate yields conversion factors for each passband, which are listed in Table 6.2. Note that these conversion factors are valid only for dates around the time of these observations. Degradation of the instrument will change the spectral response and so this procedure must be repeated for any particular date in question.

[2] `ftp.hs.uni-hamburg.de/pub/outgoing/FTS-Atlas`

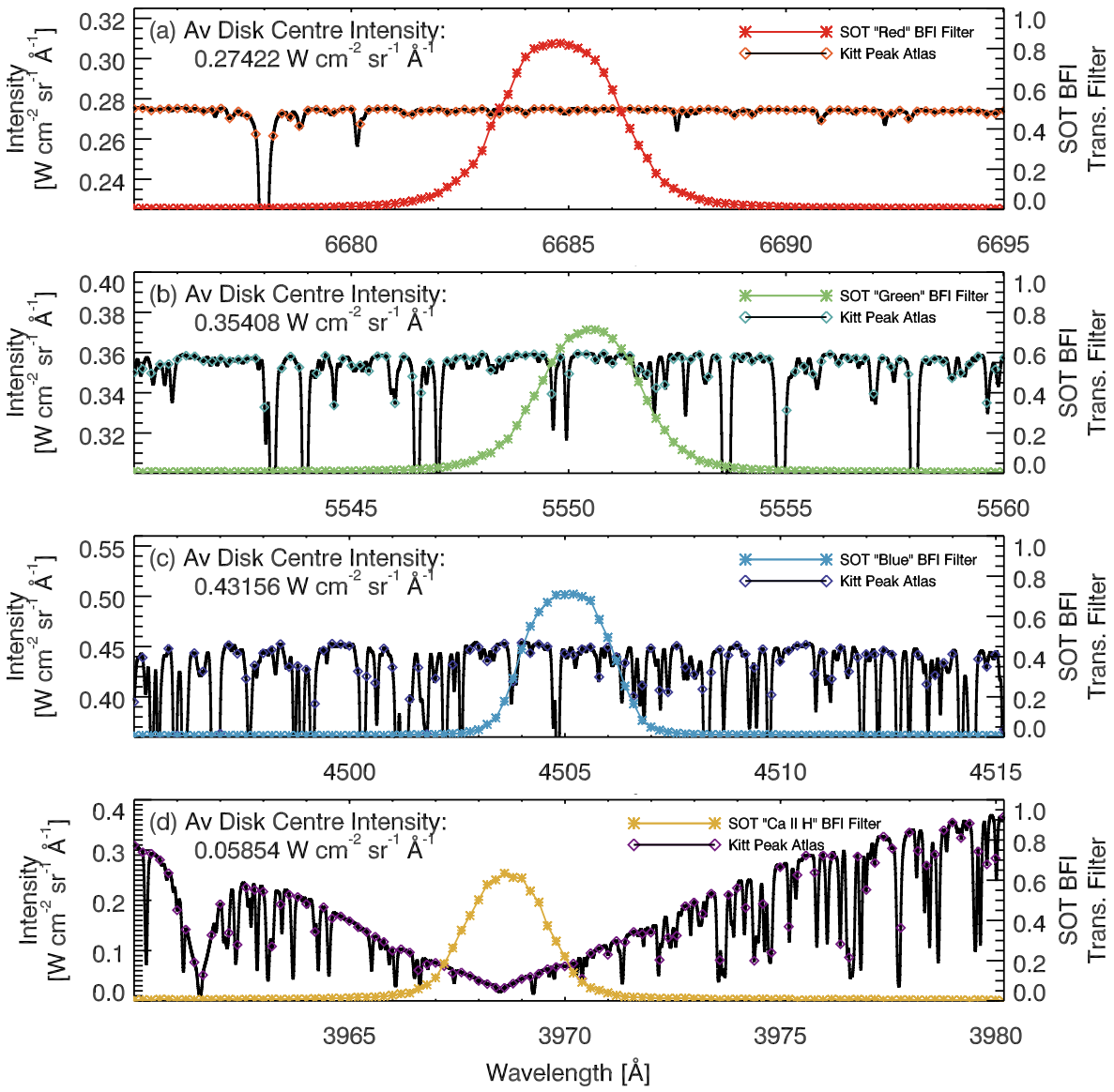

Figure 6.5: *The Hinode/SOT BFI transmission filters (coloured stars) for the red, green and blue continua are shown in panels (a-c), and the Ca II H line in panel (d). The Kitt Peak Observatory FTS disk centre solar atlas at the appropriate wavelengths are plotted alongside, where the diamonds are the wavelengths interpolated to the BFI filters. The average disk centre intensity is in the top left corner of each panel.*

It is worth pointing out that the red continuum filter observes the cleanest part of the continuum. The Ca II H line is shown as this filter was used to help establish the morphology of the flare ribbons in the near-optical/ultraviolet, providing context to the WL observations. During flares this wide absorption lines behaves similarly

Passband	Conversion Factors		
	Average Solar Intensity across BFI Filter W cm^{-2} sr^{-1} Å^{-1}	**Mean Count Rate** DN s^{-1} pixel^{-1}	**Conversion Factor**
Red Cont. (6684Å)	0.2742	36023.8	7.6122×10^{-6}
Green Cont. (5550.5Å)	0.3541	24236.6	1.4610×10^{-5}
Blue Cont. (4504.5Å)	0.4316	22558.1	1.9133×10^{-5}
Ca II H Line	0.0585	2177.5	2.6885×10^{-5}
G-band (4305Å)	0.2243	28531.0	7.8626×10^{-6}
CN Bandhead (3883Å)	0.1979	12023.7	1.6462×10^{-5}

Table 6.2: *Conversion factors from SOT countrate to physical units, for the 2011-Feb-15th solar flare.*

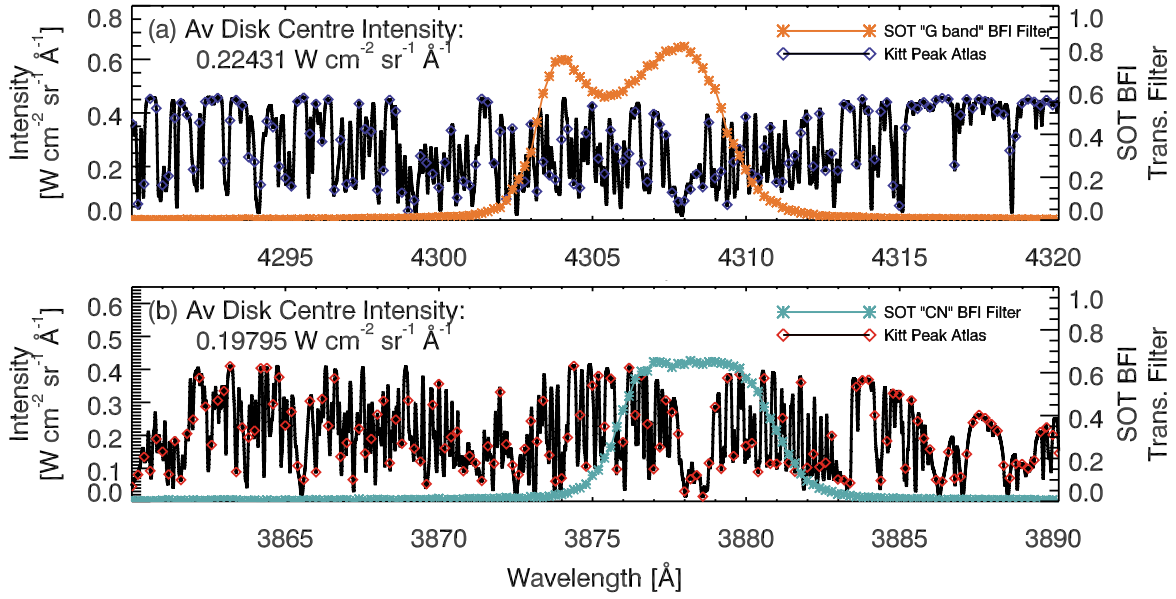

Figure 6.6: *Same as Figure 6.5, but for (a) the G-band and (b) the CN bandhead BFI filters.*

to the Mg II h & k lines, with the line centre going into emission in response to flare energy input. Images of the H line show a high contrast between flare and non-flaring sources.

Figure 6.6(a,b) shows average disk centre intensity and transmission filters for

the other two BFI filters. While observations were not made using these filters for this particular flare, it is important to comment on their suitability for flare continuum studies. It is obvious that the CN bandhead is not suitable because of the main contribution is from a strong absorption line. The G-band filter observations are somewhat more ambiguous. This filter has a double-peaked pre-flight shape, sampling a part of the continuum (albeit, a fairly noisy part) but also sampling the upper photospheric CH absorption line. Previous studies have used the G-band as a proxy for WLF emission (e.g Isobe et al. 2007; Wang 2009; Watanabe et al. 2010; Krucker et al. 2011), since this passband does contain contributions from the continuum, and was observed more frequently than the RGB filters. The flare contrast in the G-band appears to be larger than the RGB observations (from surveying G-band flare observations in the literature), which may be due to a strong response of the absorption line filling in or going into emission, in addition to the continuum response, during the flare. Wang (2009) compared flare observations of the G-band with the blue continuum, finding that the blue continuum had a contrast less than half that of the G-band. So, while a good proxy for a white light flare sources, care must be taken when interpreting flare observations from this filter because we can not be sure what is present. The ideal scenario would be to use the higher contrast of the G-band to more easily identify WL sources and then to use the RGB filters for a study of WLF energetics. Unfortunately, while it is rare for RGB flare observations, it is even more rare for combined flare G-band/RGB observations.

6.3 Finding White Light Flare Sources

Extracting the location of WLF sources poses a challenge due to the bright photospheric background. Figure 6.4 shows an image from near the peak of the flare, but while flare ribbons are the dominant feature in the EUV/UV and Ca II H line images, no flare sources are discernible at WL continuum wavelengths. The photosphere is bright, and variations due to granulation, and even within the sunspot, are comparable to the flare intensity at WL wavelengths. Viewing an animation of each of the RGB datasets *does* reveal two faint, wispy, ribbon-like sources that sweep quickly through the field of view, in the same locations as the larger Ca II H line ribbons. These are considerably thinner and less extended in comparison to other wavelengths.

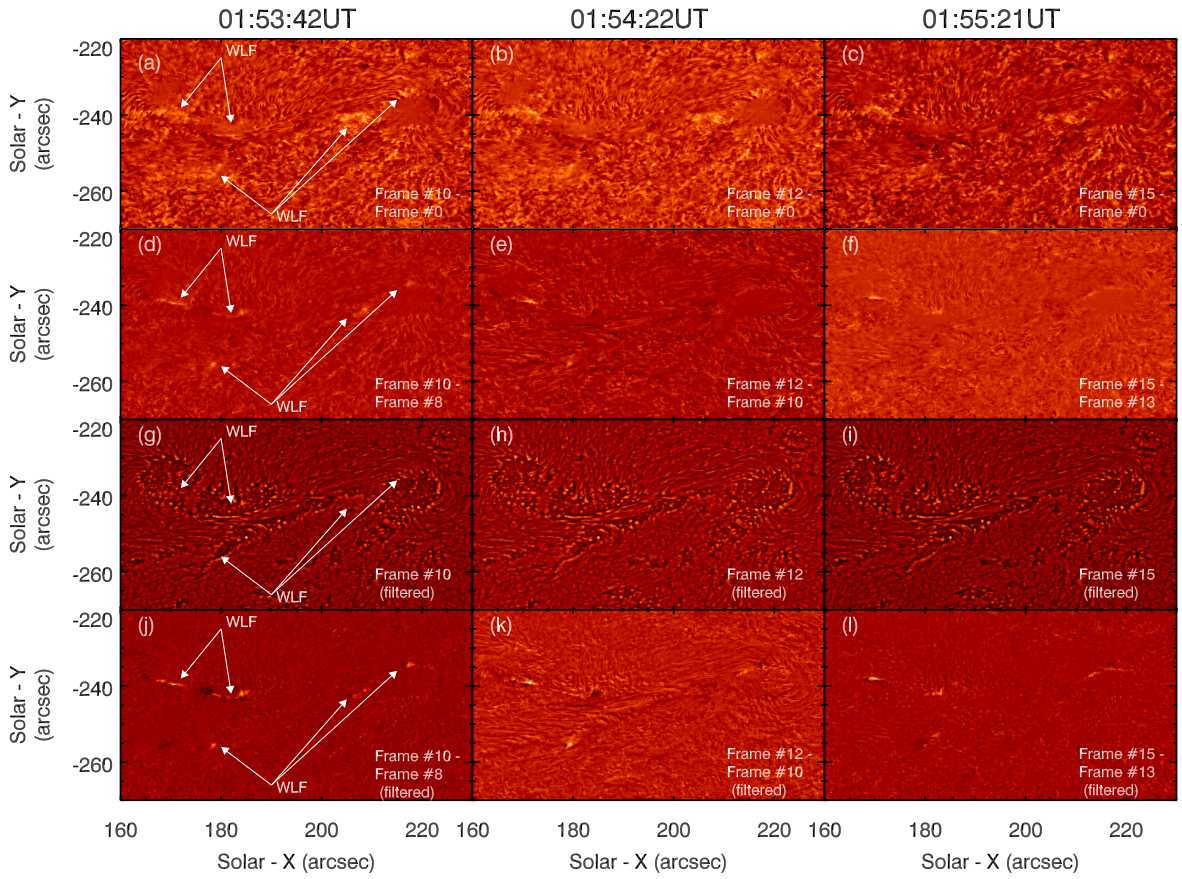

Figure 6.7: *Finding WLF sources using red continuum images. Each row is a different processing step, for the time indicated in each column. Row 1, panels (a-c), shows base differencing of unfiltered intensity images. Row 2, panels (d-f), shows a running $F_i - F_{i-2}$ differencing of unfiltered intensity images. Row 3, panels (g-i), shows the effects of using a log unsharp filter on the intensity images. Row 4, panels (j-l), shows a running $F_i - F_{i-2}$ differencing of the filtered intensity images. In each the first row, flare sources identified in panel (j) are indicated in the preceding processing steps to illustrate the benefits of the log unsharp filter.*

Difference imaging must be used to identify the transient and localised WLF sources. Figure 6.7(a-c) shows red continuum difference images at three times during the flare corresponding to frame numbers F_i, where $i = 10, 13, \& 15$. Initially, the images were base differenced, so that the images shown are $F_i - F_0$. In the absence of a pre-flare image the base frame, F_0, was the first image in the dataset (from 01:50:21 UT). Brighter sources represent an intensity increase between F_i and F_0, and darker sources represent an intensity decrease. In this way, newly brightened

flare sources appear bright. While bright sources were visible early in the flare (in the first few frames) the difference images became increasingly noisy due to granulation. Granulation in the background photosphere, combined with rotation and intensity variations in the sunspot umbra and penumbra, introduced a growing non-flaring signal to the difference images. By the time flare peak is approached it was difficult to pick out the motions due to flare ribbons from the background. In Figure 6.7(a) arrows point to a few WLF sources that were eventually identified from filtered images, but which are difficult to pick out from these base differenced images.

To mitigate these effects some other difference schemes were attempted, including averaging the data up the $(i-1)$-th frame in each instance ($F_i - < [F_0 : F_{i-1}] >$), and running differences. It was found that $F_i - F_{i-2}$ running differences were an effective compromise between removing background intensity variations whilst still identifying flare changes. An $F_i - F_{i-1}$ running difference produced similar results, but could occasionally result in an ambiguous detection if the ribbon had not moved a sufficient distance between consecutive frames. The $F_i - F_{i-2}$ running difference is shown in Figure 6.7(d-f), for the same times as in panels (a-c). Flare sources were much more easily distinguishable from the background. Again, in the first column arrows point to flare sources.

There is still some residual granulation noise and noise from the sunspot, so that a threshold could not be applied to leave only flare sources. In some frames the noise was sufficient that this noise still posed problems for identifying flare pixels. To further mitigate the effects of granulation the images were filtered before differencing was performed. A log-unsharp filter technique was used to create the maps shown in Figure 6.7(g-i). If L is the logarithm of the original intensity image, then the log-unsharp filter image is $L_{\rm fil} = L - L_{\rm smooth}$, where $L_{\rm smooth}$ is a 10 pixel boxcar smoothed (or unsharp) version of L. This enhances edges of features within each image, including granulation cell edges. Granulation variability was greater in cell centre than at the boundaries so that differencing the filter images, $L_{\rm fil}$, effectively suppressed background noise and revealed the flare sources much more clearly. These can be seen in Figure 6.7(j-l). A running $F_i - F_{i-2}$ difference was used.

Typically, bluer wavelengths show greater enhancement during the flare (e.g. Neidig 1989), but flare enhancements were more pronounced and readily identifiable in red continuum images. The reason for the red continuum being less noisy was not known, but the continuum is the cleanest in this filter which could be the explanation.

From the running difference of the filter images, groups of WLF pixels were identified, and boxes drawn around these pixel groups. Within each group the mean and standard deviation, σ, of the processed images were calculated. Pixels greater than the local mean plus n standard deviations were selected as flaring pixels, where n was allowed to take values $n = 1, 2, 3$, or 4. Upon visual comparison comparison to the difference images it was decided that 4σ threshold was too high as many of the of the flare pixels visible to the eye were not detected. A detection threshold of 2σ was adopted. New WLF sources were identified in most frames, but not all, and after ~01:58 UT.

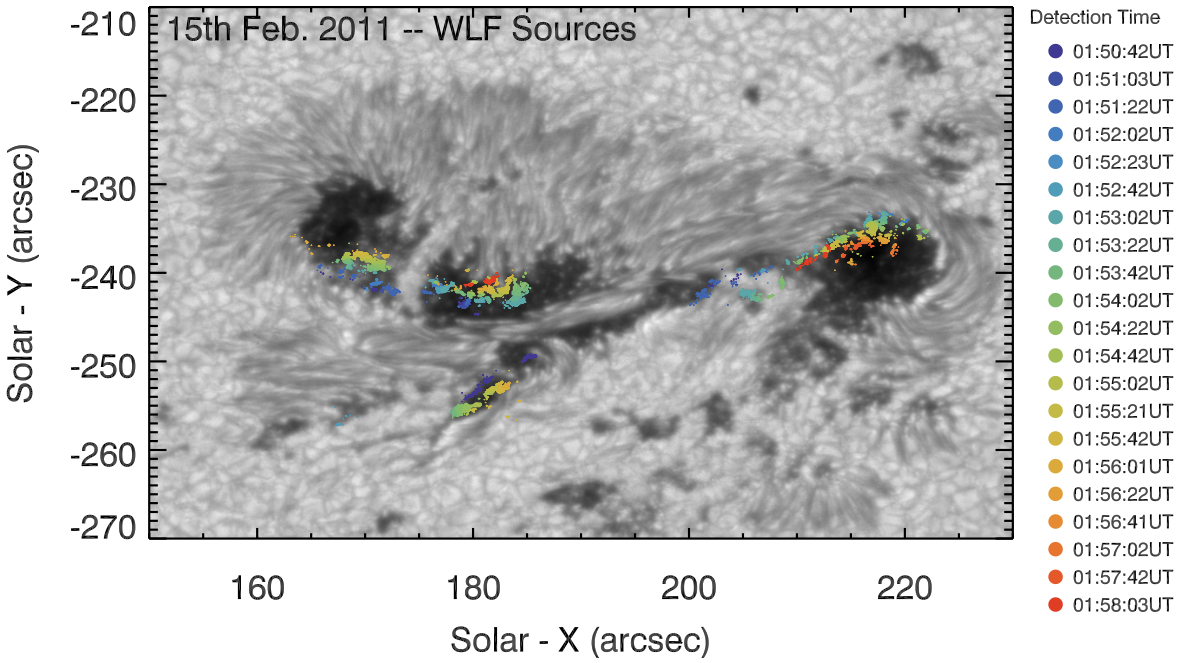

Figure 6.8: *A map of the WLF sources (color), overlaid on a continuum image (greyscale). Colour represents the time at which the sources were first detected ('switched on').*

WLF sources are overlaid as coloured contours on a background photosphere image in Figure 6.8. Colour represents the time that each footpoint source was first observed. The WL sources appear as both smaller footpoint sources as well as more extended ribbon-like features. They are co-spatial with the Ca II H line ribbons, but are thinner, more localised and generally associated with the strongest Ca II H line emission along the intense leading edge of the ribbon. Using the Ca II ribbons as a

guide the WLF sources were separated into either the eastern (ER) ribbon or western ribbon (WR).

The ER moved northwards, and was located between $x \sim 160$" and 190", above $y \sim -246$". Despite the Ca II H ribbon being continuous across that range (albeit with variations in intensity with spatial location), the WLF sources were largely confined to the umbra, and were not present in the lightbridge. Of course, this could be due to detection difficulties, since the lightbridge was substantially brighter than the umbra.

The WR moved south, further into the umbra, and showed enhancements co-spatial with either end of the western Ca II H ribbon, but WL sources did not appear in the middle section of this ribbon. The WR was split into two sections, with WR1 located in the western sunspot near $\sim [215, -240]$", and WR2 located in a small portion of umbra near $\sim [180, -255]$". WR2 was more difficult to observe, and less WLF pixels were detected in this location.

Selecting the WLF sources introduces a source of error, due to uncertainties in correctly identifying pixels as a WLF source. This originates not only from potential mis-identification of WFL pixels (such as flagging a bright source that appears to be flare-related but is simply normal background variation) or from misalignment of the images so that changes are not solar. If this error is noted as σ_{pixel} then an estimate of σ_{pixel} was found by shifting the mask of pixels flagged as being WLF sources, by 2 pixels in each (x,y) direction (the level to which a visual inspection confirmed the image alignment). The standard deviation on intensity resulting from these shifts were taken as the error on intensity.

6.4 WLF Lightcurves & Optical Power

The temporal evolution of WLF sources identified as newly brightened in frame F_i are shown in Figures 6.9 & 6.10, for the east and west ribbon respectively. Each panel of these figures shows the flare excess lightcurves of the RGB continuum filters, of the sources identified as being newly brightened in that frame, with intensity averaged over the sources. The flare excess is shown, which is the intensity minus the pre-flare intensity. With an absence of pre-flare observations, the intensity of Frame 0 is subtracted. Whilst not ideal for early observations, this is probably sufficient for sources that brighten later in the flare as the sources moved quickly over the field of

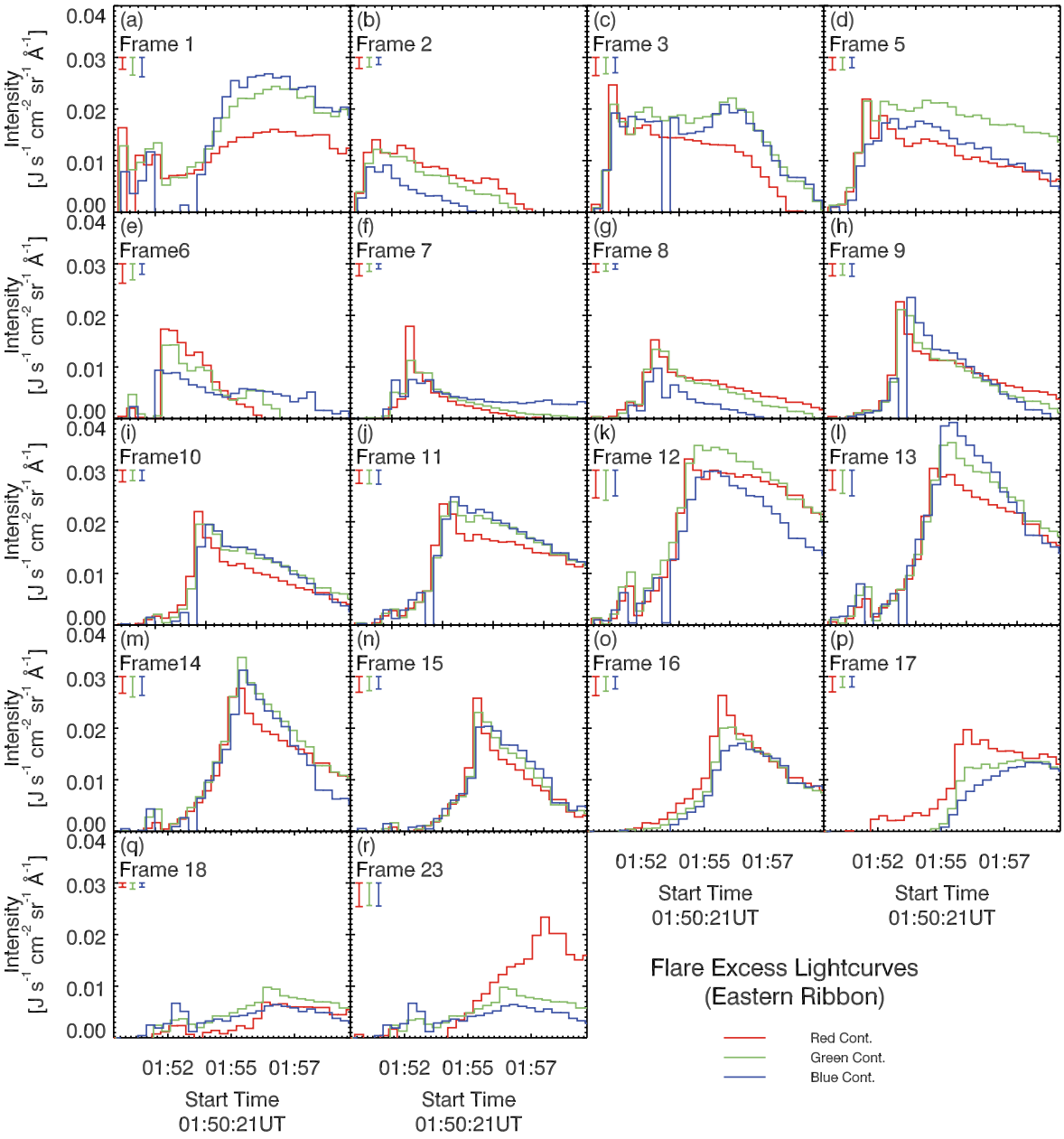

Figure 6.9: *Lightcurves of the flare excess, for sources in the eastern ribbon. Each panel shows the lightcurves of all sources identified as newly brightened in the frame number indicated. Typical error bar size is shown on each plot. In the absence of pre-flare images, the intensity of Frame* 0 *was subtracted.*

view, as energy was deposited into different atmospheric elements. Note that sudden drops in one continuum filter, present in a few of the flare excess lightcurves, are due to missing data in the original images. The size of the error bars are indicated in the

top right hand corner of each frame.

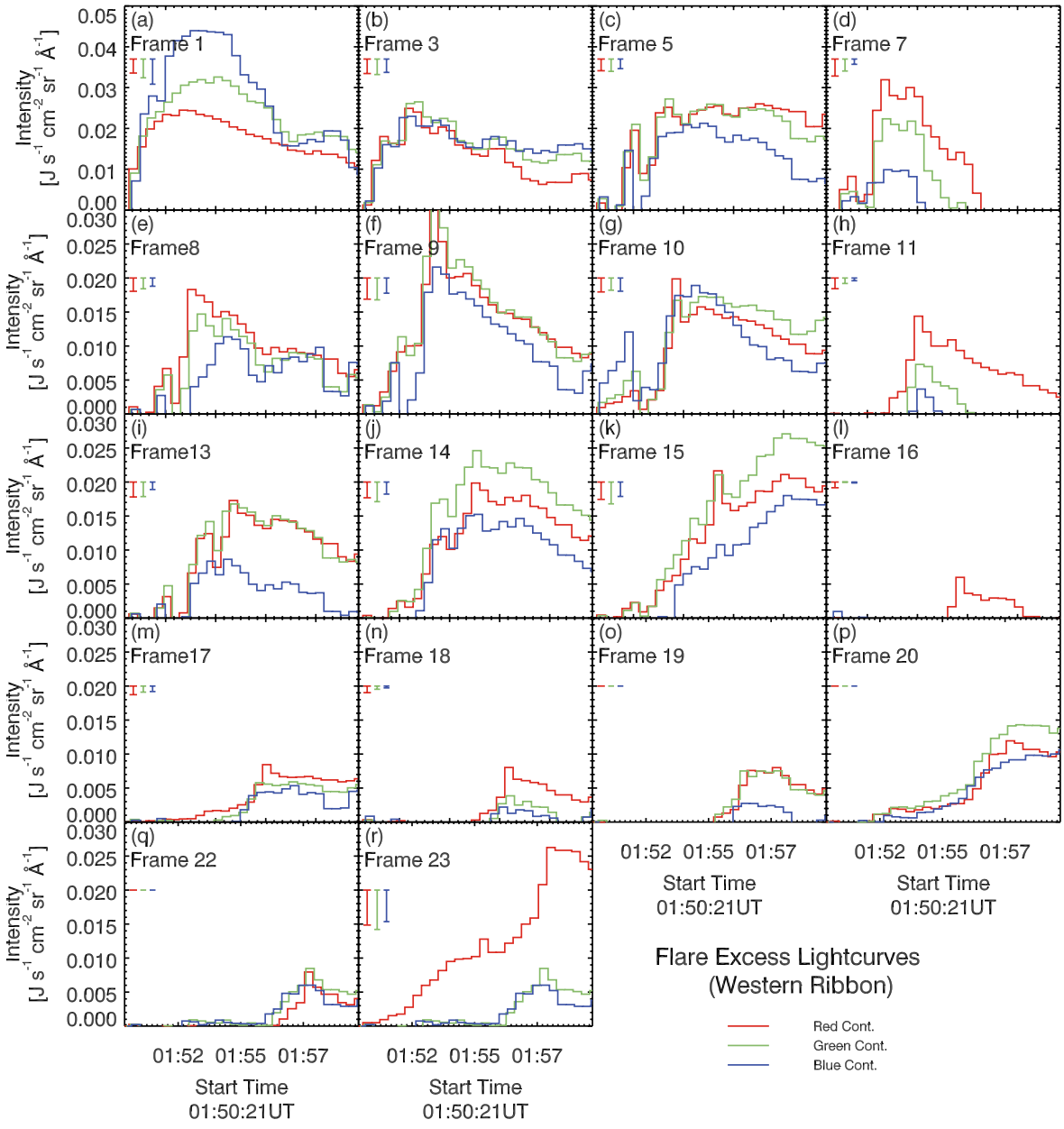

Figure 6.10: *Same as Figure 6.9 but for the western ribbon.*

Certain frames are somewhat ambiguous, particularly in the western ribbon, and for the first few frames where a good background measurement was not available. Frame 16 in the western ribbon (Figure 6.10(l) for example, where the red filter shows a signal, but the green and blue do not. For sources that are intense around the time of the HXR peak, however, there is a clear flare signal, with contrasts of a

few tens of percent observed. Typically, the three passbands show similar behaviour, rising simultaneously (within the ~ 20 s cadence of the observations). There is an impulsive peak lasting around 1-2 minutes followed by a longer decay, consistent with UV observations of flare heating and other WLF observations (e.g. Hudson 2007; Qiu et al. 2010; Matthews et al. 2003; Jess et al. 2008).

It is interesting to note that while similar temporal profiles are displayed, in some frames the peak of the red continuum precedes the peak of blue and green passbands. This may be due to SOT not observing the main peak of the event in each source since exposure times are short and the repeat cadence of each filter is ~ 20 s. This might also explain the rather low contrasts, and difficulty in observing WL sources, compared to the observation of a WLF by Jess et al. (2008), who noted a very high peak contrast of 300%. They observed that flare with a significantly higher cadence of 0.12 s using the Swedish Solar Telescope (SST). The lightcurve for that source was strongly peaked. Averaging over 9 s reduced the contrast considerably, so it is reasonable to expect that the 20 s cadence of SOT observations would further reduce the peak contrast. Surveying *Yohkoh* (Ogawara et al. 1991) observations of WLFs, Matthews et al. (2003) found that the peak contrast had a large range of values (over 28 events), from only a few percent up to 30%. The majority of WLF sources were located in the penumbra or on the boundary between the penumbra and photosphere, similar to the sources from the event reported here. Additionally, the observations here, and from Matthews et al. (2003) were all from the Paschen continuum (longward of the Balmer jump), and previous observations suggest that lower contrasts are present in this part of the spectrum, compared to wavelengths shortward of the Balmer jump, where contrasts of > 100% have been observed (e.g Neidig & Cliver 1983; Heinzel & Kleint 2014).

The background-subtracted intensity, $I_{f,\lambda}$, was used to measure the instantaneous power, $P_{f,\lambda}$ radiated by each WLF source, in each of the three WL passbands over the duration of observations. As before, the background for each pixel was taken to be the intensity of that pixel in the first frame of the dataset. Sources which brighten early in the flare might therefore be underestimated. Assuming isotropic emission then the power emitted in erg s^{-1} is $P_{f,\lambda} = 10^7 \pi I_{f,\lambda} A \Delta\lambda$, where $\Delta\lambda$ is the width of the passband, A is the area of each pixel in cm^{-2}, and the 10^7 factor is to convert from watts to erg s^{-1}.

Integrating over time returned the total energy emitted by the WLF sources and

summing the energy from each source gave the total energy emitted in each passband, over the nearly 10 minutes of observations. Energies were on the order of 10^{25} erg for each passband, and Table 6.3 lists the energy in each passband for the different thresholds set on pixel identification.

	Energy [erg]		
Detection Threshold	**Red**	**Green**	**Blue**
1σ Threshold	7.6×10^{25}	7.3×10^{25}	5.3×10^{25}
2σ Threshold	1.8×10^{25}	1.7×10^{25}	1.2×10^{25}
3σ Threshold	5.0×10^{24}	3.5×10^{24}	2.4×10^{24}

Table 6.3: *Energy emitted by each SOT passband. Each row shows the results assuming a different detection threshold. A WLF pixel must be greater than $n-\sigma$ above the mean in the difference images to be counted.*

SOT continua passbands are narrow ($\sim$ 4Å) in comparison to the full optical spectrum. Without assuming a shape to the spectrum (but assuming that it is continuum), the total WL energy can be estimated by scaling to the full optical range ($\sim$ 3000Å wide). This gives the total energy in WL as being on the order $\sim 10^{28}$ erg. Decay from the peak intensity takes several minutes and often extended beyond the observational period so that additional energy might have been emitted in WL that is not taken into account here. Similarly there may have been some WL sources which preceded the start of SOT observations.

6.5 Optically Thick WL Interpretation

In this section the WL is analysed under an assumption that it is entirely optically thick and, in the next section, it is analysed assuming that is entirely optically thin. For this analysis one set of representative flaring sources is selected for each ribbon. Sources identified as newly brightened in Frame 11 in the ER and Frame 9 in the WR were chosen (their lightcurves are shown in Figure 6.9(j) & Figure 6.10(f), respectively).

6.5.1 Source Temperature

A local temperature increase in the photosphere/upper photosphere would increase the H^- opacity, leading to the observed enhanced WL emission. While the source of this temperature enhancement is not addressed fully here, a potential source is backwarming of chromospheric Balmer continuum photons. A modest temperature increase of only 100 K was found to be adequate to produce a 10 % contrast at Paschen continuum wavelengths in the models of Machado et al. (1989).

To asses the viability of an optically thick photospheric origin the temperature of the source as derived form from the three SOT passbands was measured in two ways. First, the colour temperature was calculated using a filter ratio method. Then, the three SOT intensities were fit to a blackbody to obtain the effective temperature, T_{eff}.

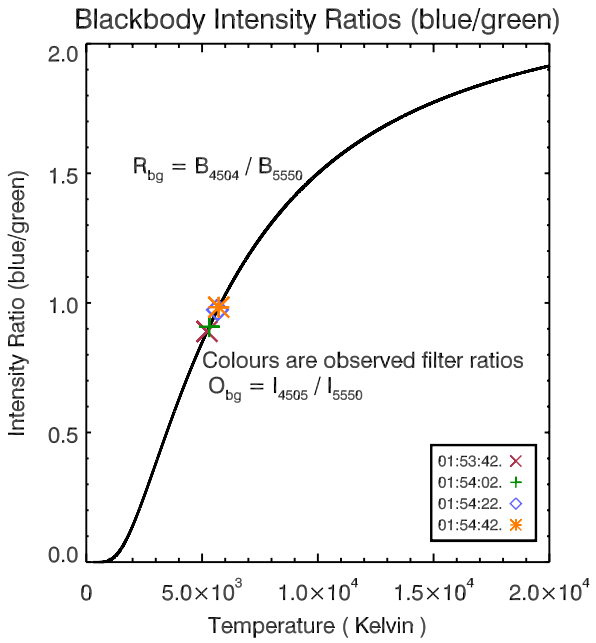

Figure 6.11: *The solid curve the ratio of blackbody intensity at 4504Å:5550Å as a function of temperature. Overlaid on this curve are observed filter ratios for one of the sources, with times indicated in the lower left corner. The temperature at which the observed ratio matches the model ratio is the colour temperature.*

From the Planck function, $B_\lambda(T_{\text{eff}})$, the emission that a blackbody would emit at $\lambda = [6684, 5550, 4504]$ Å was computed for temperatures $T_{\text{eff}} \in [0, 20,000]$ K. An expression for the Planck function is:

$$B_\lambda(T_{\rm eff}) = \frac{2hc^2}{\lambda^5}\frac{1}{\exp\left(\frac{hc}{\lambda k_{\rm b} T_{\rm eff}}\right)-1}. \tag{6.1}$$

If this emission were observed by SOT then strictly speaking the observation would be a convolution of the spectral response function of the filters with the blackbody intensity. However, the width of the filters is small and they are largely symmetric, so it is reasonable to assume that the intensity does not vary strongly across the passbands. This was confirmed by comparing the blackbody intensity at the wavelengths listed above with and without accounting for the SOT transmission filters. Differences were indeed negligible, and so filter effects were ignored. With three filters, two independent ratios were calculated:

$$R_{\rm BG} = \frac{B_{\rm B_{4504}}(T)}{B_{G_{5550}}(T)}, \tag{6.2}$$

$$R_{\rm BR} = \frac{B_{\rm B_{4504}}(T)}{B_{R_{6684}}(T)}. \tag{6.3}$$

Figure 6.11 illustrates the filter ratio technique. The curve is the model ratio of Blue to Green filter intensity, as a function of temperature (Eq 6.2). Overlaid on this curve are the observed filter ratios ($O_{\rm BG}$ & $O_{\rm BR}$) which are the same as Eqs 6.2 & 6.3, but for the observed intensity instead of blackbody intensity. The temperature at which they lie on the curve is the colour temperature of the observed emission. Recall that SOT images sequentially so that the ratios are not simultaneous, and can in fact be separated by $\sim 3-6$ s. An estimate of the error that this lack of simultaneity might introduce was made by assuming the intensity in each SOT filter varied linearly between successive exposures (i.e. between each image at $\sim 19-20$ s). This allowed a measure of the maximum variation in intensity over the 3-6 s offset between different filters. These were added in quadrature with the errors on the intensity. Using the upper and lower estimates of the filter ratios, the resulting error on the colour temperatures was found. The colour temperature error ended up being quite large, but the trend in the data can still be observed.

Figure 6.12(a,b) shows the colour temperature as a function of time for the source in the ER and WR respectively (using the pixels detected at the 2σ threshold). For each source the two ratios were consistent with each other, and the ER showed the expected behaviour of a reasonably stable pre-flare temperature, followed by a temperature increase of $T_c \sim 100-200$ K during the flare (note the 'low' background

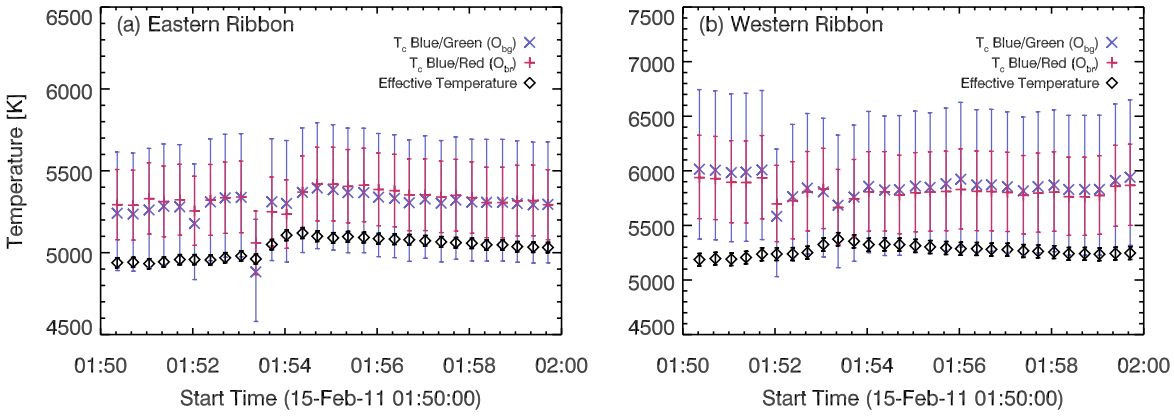

Figure 6.12: *Colour and effective temperatures (coloured symbols and black symbols respectively) for a source in (a) the eastern ribbon, and (b) the western ribbon.*

temperature is because these sources are within the penumbra). The western ribbon source, however, is more complicated. Initially the temperature is higher, before falling sharply. They they then show two rises, the second of which is in response to the flare (it occurs at the detection time in the difference images), and on the order 100 – 200 K. The reasons for the more complex profile is not known, but the western ribbon source was located on the boundary of the penumbra and umbra where some penumbral fibrils extended into the umbra. There was a large temperature gradient (in addition to the flare enhancement) in this region, and variation in the background intensity due to larger scale motions of the sunspot here, which could explain the sharp drop in T_c from $\sim$ 6000 K to $\sim$ 5600 K at $\sim$01:52 UT.

These figures also show the effects of fitting the three filter intensities to a blackbody function (black symbols), to find the best fit effective temperature. The errors on this temperature are the results of repeating the fitting with the upper and lower bounds on intensity. Both sources show a temperature offset from the colour temperature results, but the eastern ribbon is within the error bounds of colour temperature and both results show the same trends. For the western ribbon, however, only the later stages show the same trend as colour temperature and effective temperature. The western ribbon might not be emitting as a blackbody, or perhaps the blackbody emission might a component in combination with another source (such as free-bound emission). It might also be the case that given the large temperature gradient between the umbra and penumbra here, that a single temperature is a poor characterisation of the overall source.

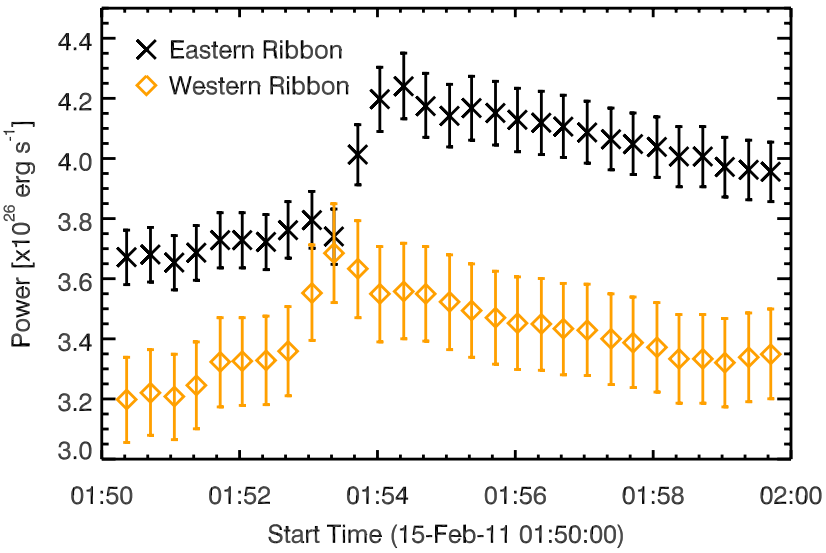

Figure 6.13: *Instantaneous power of the source, assuming an optically thick source with effective temperature, $T_{\rm eff}$. The black line shows the eastern ribbon, and the yellow the western ribbon.*

Kretzschmar (2011) performed a similar analysis with a blue and green passband, using full Sun fluxes. A significantly larger temperature than found here was reported, with a colour temperature of around 9000 K. Watanabe et al. (2013), however, found similar temperatures to those reported here, from fitting SOT intensities to a blackbody function. It is not known why the SOT derived temperatures differ so much from the results of Kretzschmar (2011), but it is worth noting that both this flare, and the flare of Watanabe et al. (2013), were not particularly strong WL emitters (as evidenced by the difficulty in identifying WL sources). Kretzschmar (2011) on the other hand used full-Sun fluxes, suggesting that the WLFs he observed could be much stronger, being observable over the full-Sun background.

6.5.2 Energetics of an Optically Thick Source

The Stefan Boltzmann's law, $F = \sigma T_{\rm eff}^4$ was used to estimate the total integrated flux emitted by a blackbody, assuming the $T_{\rm eff}$ derived from SOT intensity. The power is then simply $P = A\sigma T_{\rm eff}^4$, where A is the source area. For the two sources selected for investigation, Figure 6.13 shows the blackbody power emitted over the duration of the observations. The instantaneous power in each source $\sim 3-4\times10^{26}$ erg s^{-1}.

Comparing the *observed* power of these WL sources (Figure 6.14(a,b)) shows that

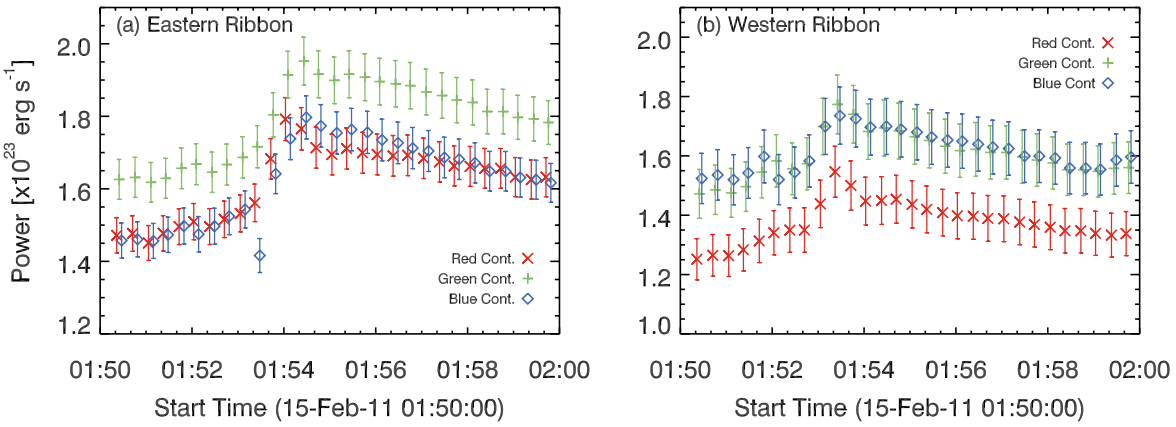

Figure 6.14: *Observed power from the source in (a) the eastern ribbon, and (b) the western ribbon. Colour represents each SOT continuum band.*

the power in each filter was on the order $\sim 10^{23}$ erg s^{-1}. Extending this observed power over the whole WL spectrum, then the expected power would, roughly, be on the order $\sim 1-2\times10^{26}$ erg s^{-1}. This is consistent with the estimate from blackbody fitting.

6.6 Optically Thin Interpretation

We can also analyse the flare under the assumption that the radiation is entirely optically thin free-bound continuum, with no contribution from backwarming or other sources. That is, flare energy deposition heats and ionises the chromosphere leading to an enhanced free-bound continuum. The observed intensity would be the photospheric background plus this enhancement. Adopting a simple model of a chromospheric slab of thickness L, uniform electron density n_e, and isothermal temperature T, the flare-excess continuum intensity, $I_{\lambda,\mathrm{fb}}$, that would be emitted can be approximated as the product of the emissivity, $j_{\lambda,\mathrm{fb}}$, and slab thickness, L. Aller (1963) presents a derivation of the emissivity $j_{\nu,\mathrm{fb}}$. Dividing Equation 4 – 159 from Aller (1963) by 4π, to obtain the emissivity measured in erg s^{-1} cm^{-3} sr^{-1} Hz^{-1}, gives:

$$j_{\nu,fb} = \frac{h n_i n_e T^{-3/2}}{4\pi n^3} \mathfrak{C} Z^4 g_{II} \exp\left\{\frac{-h}{k_b T}(\nu - \nu_n)\right\}, \tag{6.4}$$

where h is Planck's constant, n_i is the ion density (in this case, the density of H II), $\mathfrak{C}$ is a constant (defined below), $Z = 1$ is the atomic number, g_{II} is the Gaunt factor,

ν is the frequency at which we compute the emissivity, ν_n is the frequency of the transiton from level n to the continuum, and k_b is Boltzmann's constant. All variables are in c.g.s units. This expression assumes a Maxwellian velocity distribution. The constant $\mathfrak{C}$, is (from Aller 1963, Equation 4 – 158):

$$\mathfrak{C} = \left(\frac{h^2}{2\pi m_e k_b}\right)^{3/2} \frac{8\pi^2 e^2 R_{\rm freq}^2}{m_e c^3} \frac{2^4}{3\sqrt{3}\pi} = 3.260 \times 10^{-6}. \tag{6.5}$$

In Equation 6.5, e is the electron charge, m_e is the electron mass, c is the speed of light, and $R_{\rm freq}$ is Rydberg's constant in frequency units ($cR = R_{\rm freq}$ for R the Rydberg's constant in units of cm^{-1}). Inserting the other constants, assuming that $n_i = n_e$, and $g_{II} \sim 1$, and converting from frequency units to wavelength units, Equation 6.4 becomes

$$j_{\lambda,fb} = \frac{6.48 \times 10^{-14}}{4\pi\lambda^2} \frac{n_e^2 T^{-3/2}}{n^3} \exp\left\{\frac{h\nu_n}{k_b T} - \frac{hc}{k_b \lambda T}\right\}, \tag{6.6}$$

for λ measured in Å. Noting that

$$\frac{h\nu_n}{k_b T} = \frac{hR_{\rm freq} Z^2}{n^2 k_b T} = \frac{1.58 \times 10^5}{n^2 T}, \tag{6.7}$$

we can write the intensity $I_{\lambda,\rm fb} = j_{\lambda,\rm fb} L$ as:

$$I_{\lambda,\rm fb} = j_{\lambda,\rm fb} L = \frac{6.48 \times 10^{-14}}{4\pi\lambda^2} \frac{n_e^2 T^{-3/2}}{n^3} \exp\left\{\frac{1.58 \times 10^5}{n^2 T} - \frac{1.44 \times 10^8}{\lambda T}\right\} L. \tag{6.8}$$

In Eq 6.8, $I_{\lambda,\rm fb}$ is in units of erg s^{-1} cm^{-2} sr^{-1} Å^{-1}, and L is in units of cm. The principal quantum number $n = 3$ since all three SOT passbands are at Paschen continuum wavelengths.

6.6.1 Parameter Constraints

Equation 6.8 describes the intensity of free-bound radiation given the atmospheric properties T and n_e in a slab of thickness L, none of which are known. What is known is the flare enhancement (with the dominant photospheric background subtracted) in each of the SOT passbands. The electron density and slab thickness each appear only once in this expression, and so this combined parameter $n_e^2 L$ can be calculated for each observed value of $I_{\lambda,\rm fb}$, over a range of temperatures $T \in [4000, 3 \times 10^4]$ K. Observationally-derived values for each wavelength will be denoted $n_e^2 L|_{\lambda,\rm obs}$.

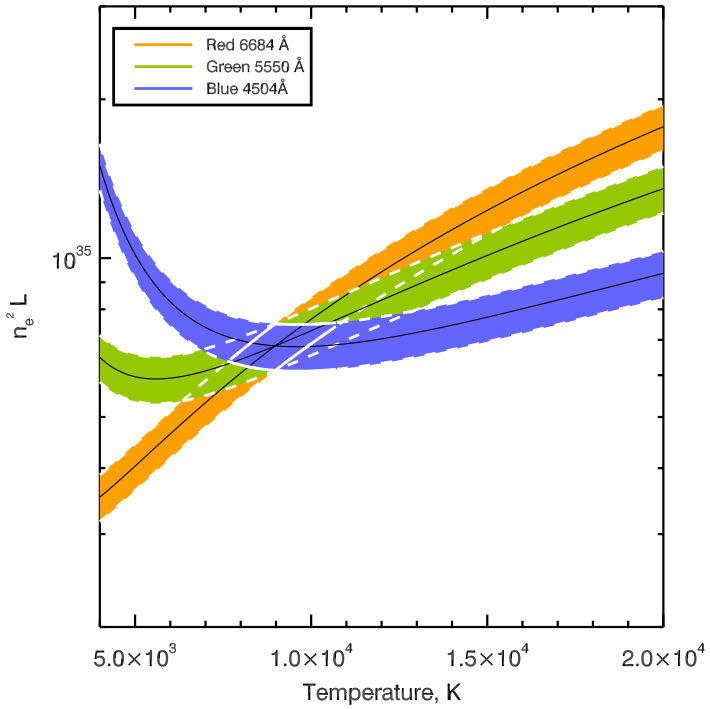

Figure 6.15: *An illustration of finding the temperature and $n_e^2 L|_{\lambda,\mathrm{obs}}$ constraints for the simple optically thin slab model. Colour represents the range of values for each filter, and the area of overlap is highlighted in white solid lines.*

Figure 6.15 shows the results of this for a time near the peak of the flare, where $n_e^2 L|_{\lambda,\mathrm{obs}}$ is plotted as a function of temperature. Each coloured band represents the range of values of $n_e^2 L|_{6684,\mathrm{obs}}$, $n_e^2 L|_{5550,\mathrm{obs}}$ and $n_e^2 L|_{4504,\mathrm{obs}}$ (red, green and blue colours, respectively), where the range is due to the error on each intensity value. A region of overlap exists centred on ~ 9000 K. This overlap provides a constraint on the value of temperature and $n_e^2 L$ for that time consistent with all three filters. This was performed for each of the frames in the two selected sources, where temperatures were typically in the range $\sim 5500 - 20,000$ K, but could go as high as $\sim 25,000$ K or as low as ~ 4500 K.

This method worked best at producing overlap regions when the flare-excess intensity was large, and sometimes early in the flare overlap regions were present. This could indicate that the WL emission at certain stages was not well described by this free-bound model, and H^- opacity still dominated. The most probable temperature was the value that had the closest overlap.

The upper and lower bounds on temperature permitted by this simple model and

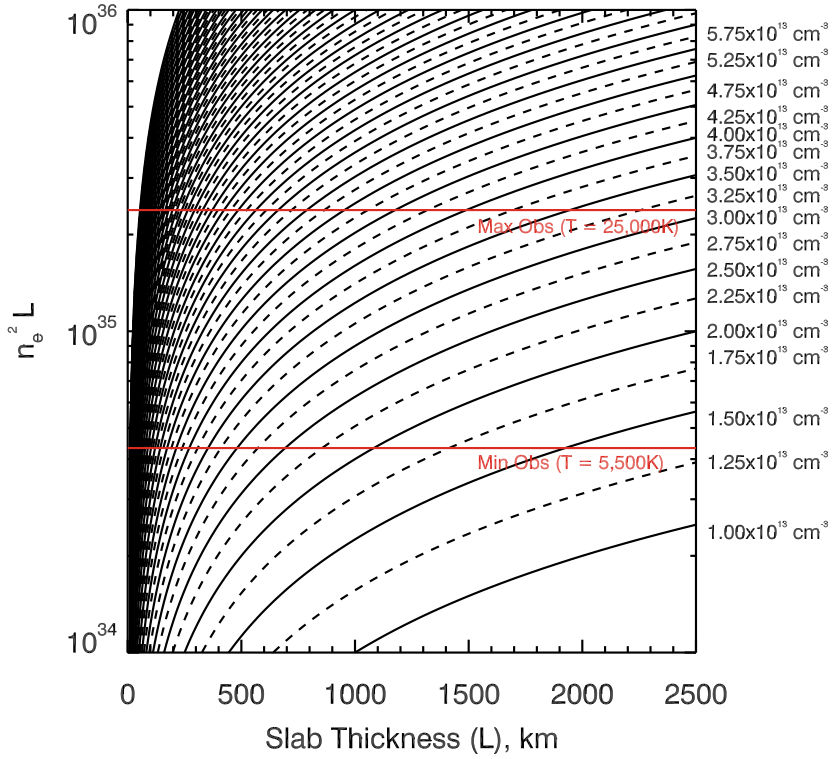

Figure 6.16: *Each curve is a model $n_e^2 L|_{\text{model}}$ for the density indicated on the right hand side. The red lines indicate the minimum and maximum values of the observed value of $n_e^2 L|_{\lambda,\text{obs}}$ that suitably describe the intensity of all three SOT passbands. It is likely that the slab is only a few hundred km thick, limiting $n_e \sim 3 - 6 \times 10^{13}$ cm^{-3}.*

observed intensity allow an estimation of the electron density in the chromospheric slab. Figure 6.16 shows model curves of $n_e^2 L|_{\text{model}}$ (calculated using a range of n_e and L values) as a function of slab thickness. The corresponding value of n_e for some of the curves is labelled (curves are separated by 0.25×10^{13} cm^{-3}). Overlaid on this figure are the minimum and maximum values of $n_e^2 L|_{\lambda,\text{obs}}$ given the bounds on temperature, which allows the range of valid values of n_e and L to be estimated. A limit on the electron density is $n_e \sim 10^{13-14}$ cm^{-3}, the actual value of which depends on slab thickness. It is more likely that the slab is in the lower range of thicknesses plotted, so that for a slab of thickness 500 km, $n_e \sim 2.75 - 6.25 \times 10^{13}$ cm^{-3}, whereas an even thinner slab must have a larger density on the order of $n_e \sim 10^{14}$ cm^{-3}. In the non-flaring chromosphere such densities are found in the deepest atmospheric layers. However, as demonstrated in previous chapters, flare simulations do result in electron density enhancements in the mid-upper chromosphere on the order of

$n_e \sim 10^{13-14}$ cm^{-3}. Additionally, electron densities of $> 10^{13}$ cm^{-3} were derived by Feldman & Doschek (1978) based on flare observations of the O IV intersystem lines, which form at $\sim 100,000$ K. This result is somewhat consistent with electron density and temperatures inferred here from continuum observations since one would expect lower n_e and higher T in the TR compared to the chromosphere.

6.6.2 Energetics of an Optically Thin Source

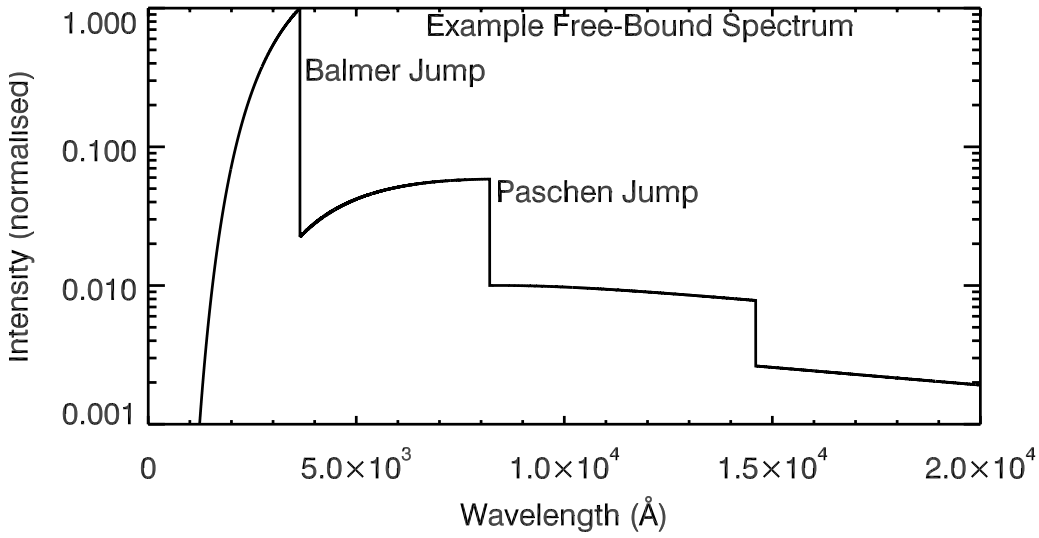

Figure 6.17: *An example of a H free-bound spectrum, for $T = 8500$ K and $n_e^2 L = 1 \times 10^{35}$. Intensity is normalised. The locations of the Balmer and Paschen edges are shown.*

Model free-bound continua were produced in the wavelength range $\lambda \in [0 - 16,000]$ Å using Eq 6.8, for each value of temperature within the overlap region. Each value of temperature had an upper and lower bound on $n_e^2 L|_{\lambda,\mathrm{obs}}$ constrained by the three SOT passbands. Figure 6.17 shows an example of a free-bound spectrum ($T = 8500$ K and intensity normalised) calculated using Eq. 6.8. Integrating these curves over wavelength at each time step, and multiplying by source area, gives the instantaneous power P_{fb}.

Power was calculated at each time step, with the range of allowed temperatures providing upper and lower limits on the value of P_{fb}. Typically, this was on the order of $P_{\mathrm{fb}} \sim 10^{27}$ erg s^{-1} at flare peak for each of the sources investigated. Figures 6.18 &

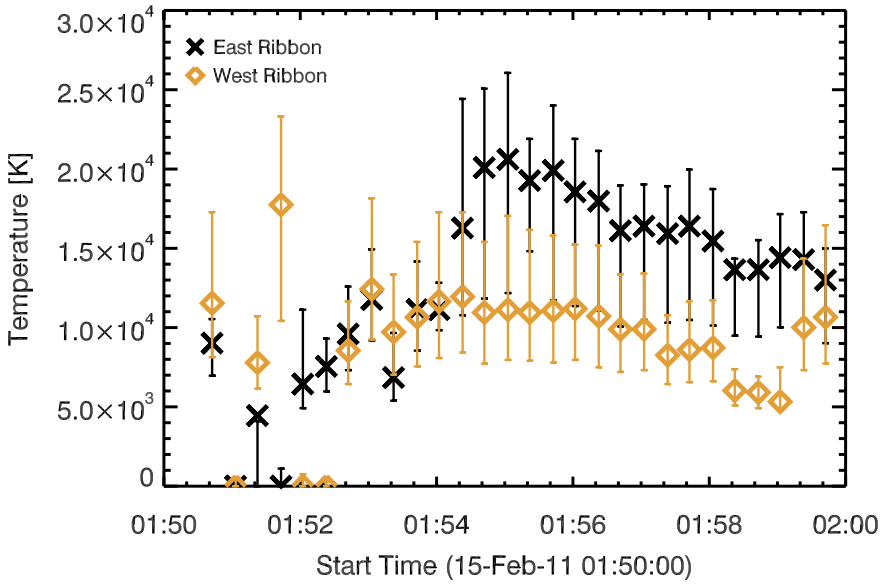

Figure 6.18: *Most probable temperature, with error bars showing the range of allowed temperature, for the selected sources (black crosses are the eastern ribbon and yellow diamonds are the western ribbon).*

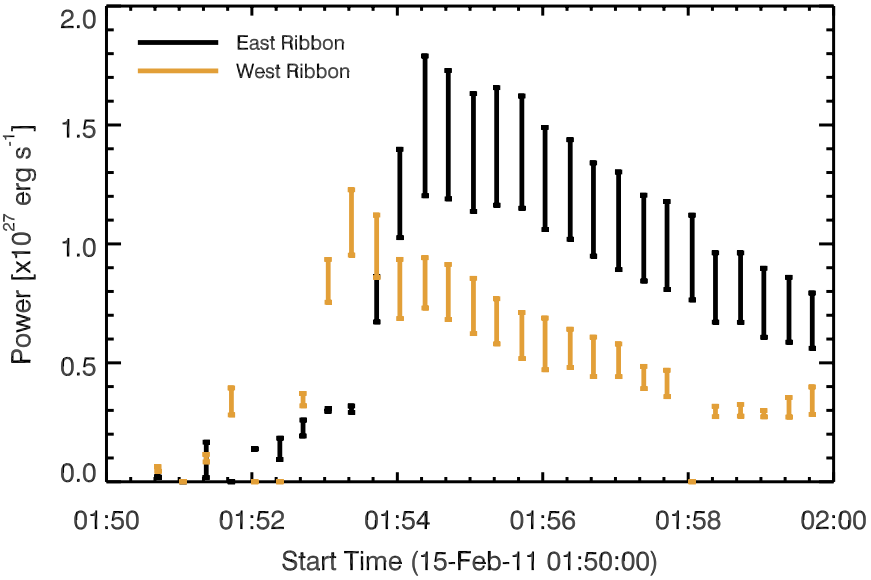

Figure 6.19: *The instantaneous power of the selected sources assuming an optically thin slab emitting free-bound radiation (integrated over the wavelength). Yellow lines are the western source, and black lines are the eastern source.*

6.19 shows the temperature and power for each of the sources investigated. As in

the optically thick modelling case, the eastern ribbon shows a clear rise to flare peak, albeit with a large spread of allowed temperature values, followed by a slow cooling time. The evolution of western source temperature is note so clear at early times but does exhibit a small rise between 01:53-01:54 UT before cooling.

6.7 Core-Halo Appearance of WLF sources

The previous two sections analysed the WLF emission assuming that it is formed by a single mechanism, however the actual origin may be more complex. A commonly cited possibility is that hydrogen free-bound radiation is emitted in the chromosphere following direct heating by electron beams. Some of this radiation then backwarms the lower atmosphere. The hotter lower atmosphere then re-radiates with an an enhanced H^- opacity. Thus at Paschen continuum wavelengths a contribution from free-bound and flare-enhanced blackbody radiation would be present.

An observational property of this model would be the core-halo structure of WLF emission, which has been noted by Neidig et al. (1993), Xu et al. (2006), and Isobe et al. (2007), amongst others. These authors report that there is often a brighter core emission produced in the chromosphere, surrounded by a weaker more diffuse halo resulting from backwarming into the photosphere. The emission of the core region would be a mix of hydrogen free-bound and H^- emission. Xu et al. (2006) found a time delay between the near infrared (NIR; the NIR emission showed similar morphology to the visible continuum and was used as a proxy) core emission and the halo of $\sim$ 2 minutes for one event, and $\sim$ 20 s in another, with cadences of 1 minute and 2 s respectively. This was attributed to the finite time taken to heat the chromosphere and photospheric components of the emission.

To ascertain if the 2011-Feb-15th flare had a core-halo structure the WLF sources identified using the $1\sigma, 2\sigma$ & 3σ thresholds were compared. The 3σ sources would represent the most intense WLF emission (the core), and 1σ would represent the weakest WLF emission (the halo). Figure 6.20(a) shows contours of a WLF source from the ER, where the core-halo structure does appear to be present. The pixels flagged as flaring using the 3σ threshold appear in the middle, surrounded by pixels with smaller contrast (flagged using the 1σ & 2σ thresholds). Figure 6.20(b) shows the same sources, but this time a difference image. Colour represents intensity so that the highest contrast emission is red and weaker contrast is blue (note that this

image has been masked to better highlight the flaring pixels). Again, it is clear that the strongest emission is in the middle of each source.

A caveat here is the size of the SOT/BFI point spread function. The SOT is a diffraction-limited telescope of 50cm diameter, which means the FWHM of the ideal PSF is $\sim 0.19'' - 0.28''$ depending on the wavelength of each filter (longer wavelength means broader FWHM). Tsuneta et al. (2008) and Suematsu et al. (2008) state that the SOT does operate near the diffraction limit. Wedemeyer-Böhm (2008) demonstrated that stray light can act to broaden the PSF, though only by ~ 1 % of the diffraction-limited case. The size of the core-halo structure observed is close to the diffraction limit and so some of this structure could be smearing of intensity due to the PSF.

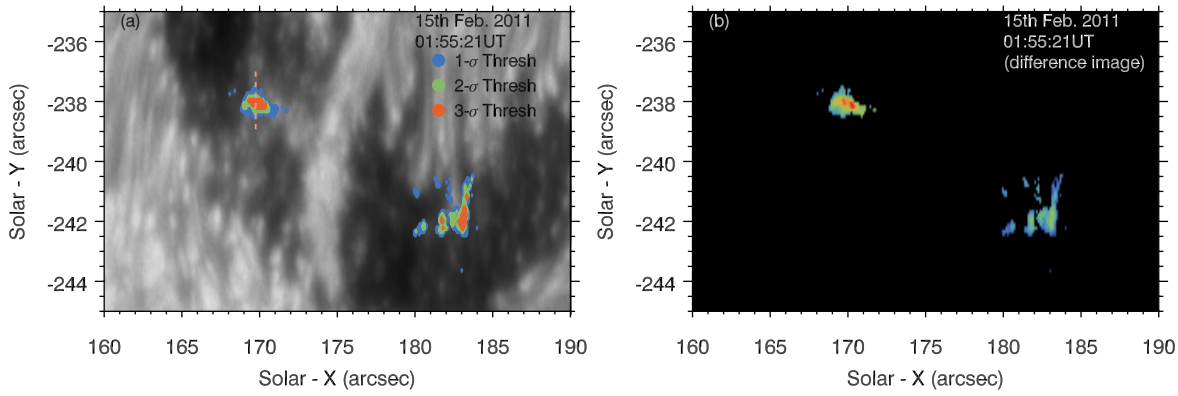

Figure 6.20: *Both panels show WLF sources detected at 01:55:21 UT. Panel (a) shows flare pixels flagged using the $1\sigma, 2\sigma$ & 3σ thresholds. The pink vertical line is the cut shown in Figure 6.21. Panel (b) shows a difference image of the same region, where colour represents intensity.*

Taking a vertical cut through one of the sources (the dashed line in Figure 6.20(a)), and plotting intensity along this cut at various times, any time differences between the core emission and halo emission can be determined. Figure 6.21 shows the background-subtracted intensity as a function of distance along the slit at three times. Results from this exercise are inconclusive. The peak intensity in panel (a) is in a narrow region, with extended weaker emission further along the slit. Panel (b), showing 20 s later, shows that this peak location has moved along the slit, but this could be due to ribbon motion rather than a time delay between core and halo components. Panel (c) shows two minutes after panel (a), where the intensity in the

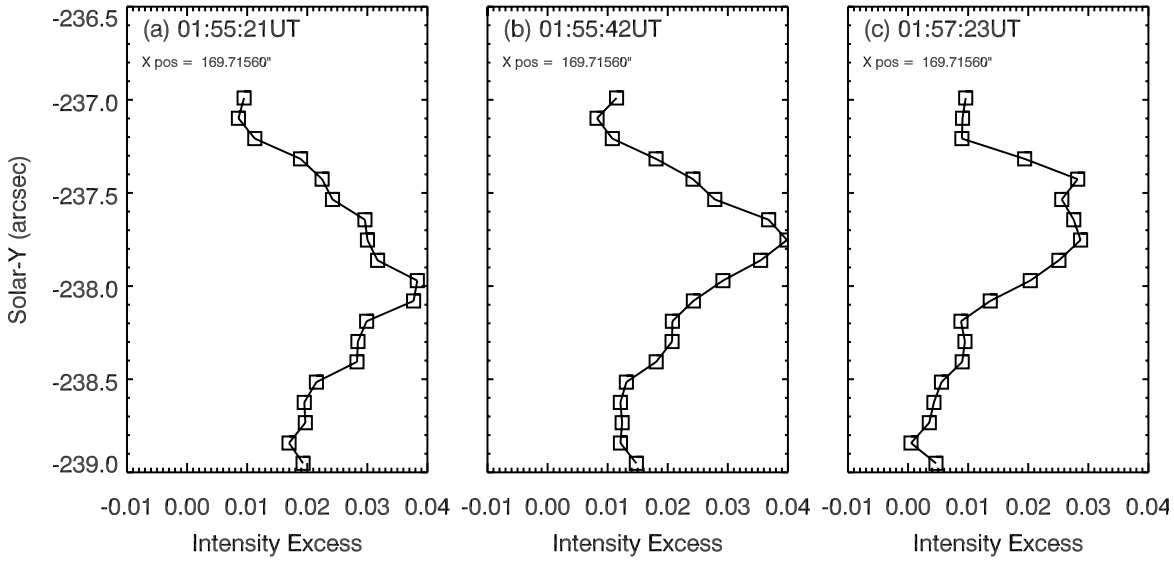

Figure 6.21: *Excess intensity as a function of position along the slit in 6.20(a), for three different times.*

'halo' component has actually reduced in most locations. The increase near the top of the slit is again likely to be due to ribbon motion (the leading edge of the ribbon travels north). With the cadence of this data it was not possible to identify the time delay observed by Xu et al. (2006).

This data does seem to exhibit the core-halo structure (albeit with no evidence of time delays), which could mean that a combination of emission mechanisms is at work in this flare. The absence of a time delay might be due to the cadence of the observations or ribbon movement which may smear out such effects. Alternatively the core-halo effect observed here might have another cause, or be exaggerated by the SOT PSF. Even if it is backwarming, it is not possible to ascertain the split of free-bound to H^- emission from this data alone; emission at Balmer continuum wavelengths would be required to estimate this.

6.8 Joint IRIS & *Hinode*/SOT WLF Observations: Initial Results

Joint observations of WLF enhancements to both Balmer and Paschen continuum wavelengths can aid in the determination of the emission mechanisms. Such observations would help to identify the existence of a Balmer jump indicative of a

recombination continuum. Estimates of the the Balmer recombination continuum based on wavelengths shortward of the Balmer jump can lead to estimates of the intensity of the Paschen recombination continuum. Comparing to observations then any excess emission above that expected from a recombination spectrum would be the result of some other mechanism (most likely H^-).

At NUV wavelengths the IRIS/SG covers several patches of quasi-continuum in addition to the Mg II h & k lines discussed previously. The exact wavelength ranges are variable and often, instead of the full range, several patches near 2814Å, 2826Å, & 2832Å are observed. Though this part of the continuum is line-blanketed with many photospheric absorption lines (that go strongly into emission during flares), Heinzel & Kleint (2014) demonstrated for the first time, using IRIS observations of the 2014-March-29 X-class flare, that narrow passbands free of emission lines can be extracted which allowed clear detection of Balmer continuum enhancements. This section describes the preliminary analysis of joint observations from IRIS and SOT.

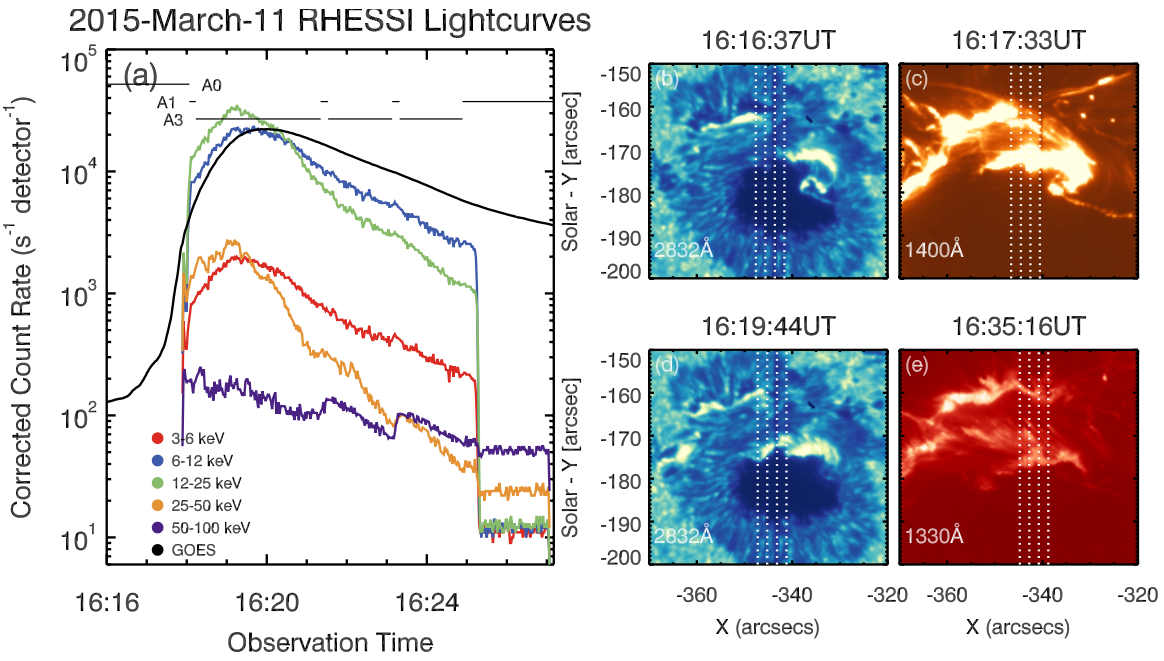

Figure 6.22: *Panel (a) shows the RHESSI and GOES lightcurves from the 2015-March-11th X-class flare. Panels (b-e) show four SJI images during the flare.*

The 2015-March-11th X-class solar flare was well observed by IRIS *and Hinode*/SOT, providing useful information about both Balmer and Paschen wavelengths.

Figure 6.22 shows an overview of the flare. RHESSI did not observe the full event but did catch the peak, with a strong HXR signal up to an energy of ~ 50 keV. The flare ribbons became apparent at ~16:16 UT, with the flare peaking near ~16:19 UT, and ending by ~16:25 UT.

6.8.1 IRIS Observations of the 2015-March-15th Flare

IRIS observed the full duration of the event, on a four-step coarse raster program, with a SG exposure time of ~ 4 s in the pre-flare, and ~ 2.2 s during the flare. The slit stepped by ~ 1.99" per exposure, catching a large section of the lower ribbon with a repeat cadence of ~ 20.75 s. The SJI observed using the 2832Å, 1400Å, & 1330Å filters. Note that the presence of strong emission lines in the 2832Å limits its use as a means to quantitatively investigate the continuum, but similarly to the G-band observations it can be used as a proxy for NUV continuum sources. The SG field of view was 8" × 128.09". The slit width was 0.33", and the y-scale was 0.3327" pixel^{-1} (on board summing reduced the spatial resolution). Spectral binning was also performed so that the wavelength pixel scale was 50.92 mÅ pixel^{-1}.

Figure 6.22(b-e) shows four SJI images during the flare, and the SG slit positions. There were two clear ribbons, but only the lower ribbon was cleanly observed by all the IRIS slit positions (albeit the initial stages were not caught). A small portion of the northern ribbon was observed by one slit position. The lower ribbon expanded south and east into the sunspot, appearing over the penumbra and umbra. The northern ribbon propagates north into the umbra. The 2832Å 'continuum' images showed that the ribbons had largely disappeared by ~16:25 UT, but the TR FUV passbands showed weaker, diffuse emission lasting until >16:35 UT.

The SG observed the NUV continuum over three wavelength ranges: ~ [2812.64 – 2816.27]Å (the 2814Å passband), ~ [2824.81 – 2828.43]Å (the 2826Å passband) and ~ [2831.33 – 2834.15]Å (the 2832Å passband). However, it was difficult to find a clean area of continuum in the 2832Å passband, so only the 2826Å and 2814Å have been considered for this preliminary investigation. Data were processed and calibrated as described in Chapter 3 § 3.2.1.

To isolate patches of continuum from line emission the spectra from all slit positions were visually inspected. Regions that were clear from strong lines were selected, ensuring that these were also clear from the line wings which were broadened during

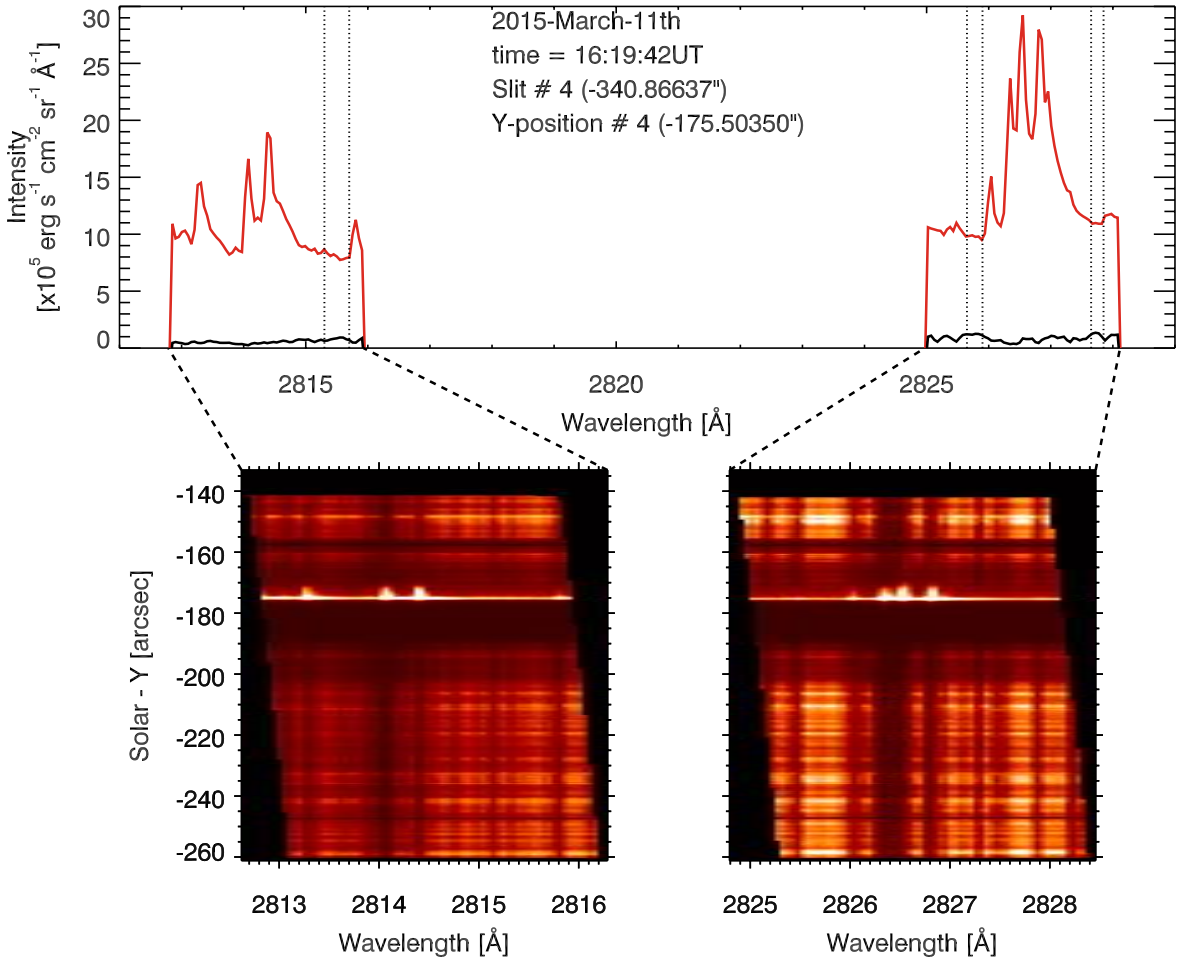

Figure 6.23: *The NUV continuum from a pixel in the lower ribbon, along slit number 4. The red line is from during the flare, and the black line is pre-flare. Dotted lines indicate the continuum regions. Full exposures for each continuum passband are shown also.*

the flare. Three regions were identified, one from the 2814 Å passband, and two from the 2826 Å passband. Those were: [2814.30 – 2814.70] Å, [2825.65 – 2825.90] Å, and [2827.65 – 2827.85] Å. Figure 6.23 shows a sample NUV continuum emission from a single pixel from slit position 4. The red line shows the flare spectrum, and black the pre-flare, with dotted lines indicating the continuum regions. Also shown on this figure are full exposures showing the spectrum along the slit. In these figures the bright line spanning the full wavelength range is the leading edge of the flare ribbon. Within each continuum region the mean intensity was measured at each time, and the contrast measured, $C = (I_f - I_0)/I_0$, where I_f is the flare intensity and I_0 the pre-

flare intensity. The pre-flare intensity was averaged over 30 minutes of observations before the flare. Flare sources were defined as those that had a contrast of at least 100%. Setting that threshold and plotting pixels that the pixels that qualified on a SJI showed that NUV continuum flare sources were co-spatial with the FUV ribbons (as would be expected).

6.8.2 *Hinode*/SOT Observations of the 2015-March-15th Flare

The *Hinode*/SOT observed on a flare trigger mode so, as with the 2011-Feb-15th flare, missed the initial onset most and of the decay phase of the event. Most of the impulsive phase, the peak, and the initial decay was observed, between 16:16:45 UT to 16:21:55 UT, using the RGB and Ca II H line filters. The cadence of each filter was ~ 19.2 s, with average exposure times of 0.0512 s, 0.0770 s and 0.0617 s, for the red, green and blue filters respectively. Note that some frames were missing, or were discarded as there were readout errors in the flare region, so that the cadence was occasionally larger than the nominal ~ 19.2 s. The field of view was $111.575'' \times 111.575''$, with pixel scale of 0.10896" pixel^{-1} (2×2 on-board binning), centred on the sunspot. The field of view of IRIS and SOT overlapped on the sunspot.

Passband	**Conversion Factors**		
	Average Solar Intensity across BFI Filter W cm^{-2} sr^{-1} Å^{-1}	**Mean Count Rate** DN s^{-1} pixel^{-1}	**Conversion Factor**
Red Cont. (6684Å)	0.2742	33824.0	8.1067×10^{-6}
Green Cont. (5550.5Å)	0.3541	20724.3	1.7086×10^{-5}
Blue Cont. (4504.5Å)	0.4316	18851.1	2.2895×10^{-5}

Table 6.4: *RGB Conversion factors from SOT countrate to physical units, for the 2015-March-11th solar flare.*

Images were aligned and processed as described in § 6.2.2 & § 6.2.3. Calibration from DN s^{-1} to J s^{-1} cm^{-2} sr^{-1} Å^{-1} was achieved by comparing disk centre images from dates near 2015-March-11th, to account for instrumental degradation since 2011-Feb-15th. The new conversion factors are listed in Table 6.4.

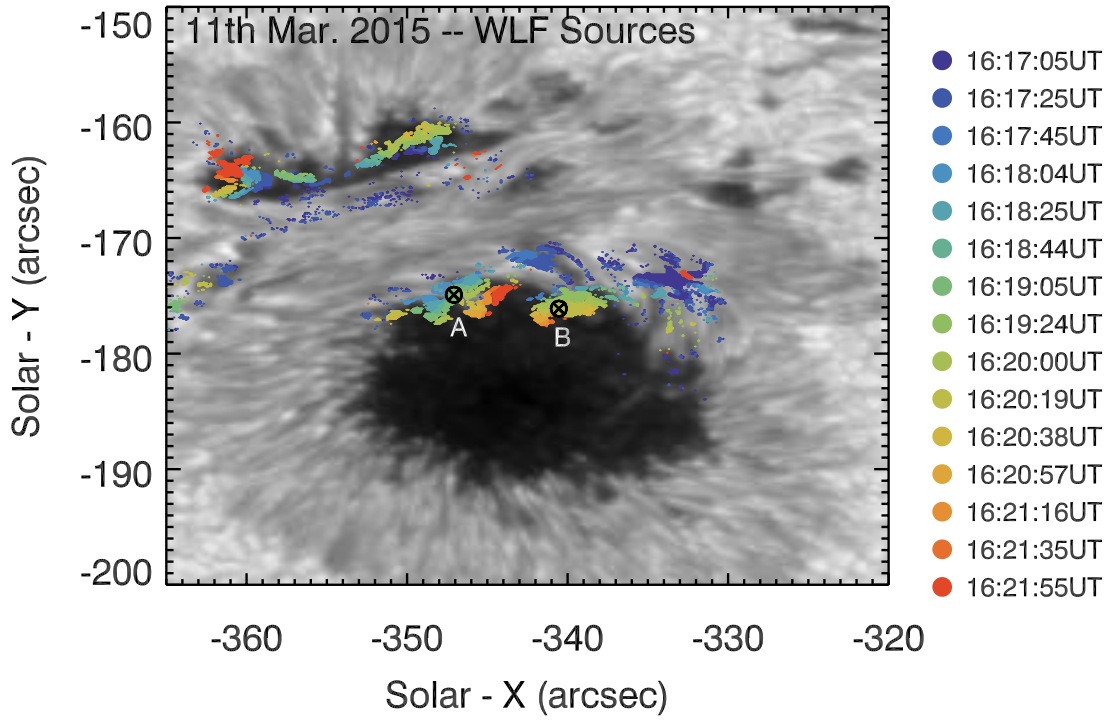

Figure 6.24: *WLF sources from the 2015-March-11th X-class solar flare. Colour represents detection time. Sources A & B are indicated.*

As with the 2011-Feb-15th observations it was non-trivial to identify these sources in each image so that the difference image techniques described in § 6.3 were again used to flag WLF sources. WL enhancements from the RGB movies were more apparent in this flare than their counterparts from the 2011-Feb-15th flare. Figure 6.24 shows the compact and spatially localised WLF sources, where colour represents the detection time. The lower sources forming on the western edge of the sunspot, and travelling south into the sunspot umbra as energy is deposited in new atmospheric elements. The upper sources travels northwards into the umbra adjacent to the main sunspot. New flare sources were identified up to the point that SOT observations ceased. Note that the SOT data had a pointing offset from IRIS. SOT maps were shifted to match the IRIS pointing.

6.8.3 Comparing NUV and Optical Continua

Two sources were selected, one from the the first slit position and one from the fourth slit position, at coordinates $\sim [-346.97, -174.52]$" ('source A') and $\sim [-340.79, -175.83]$"

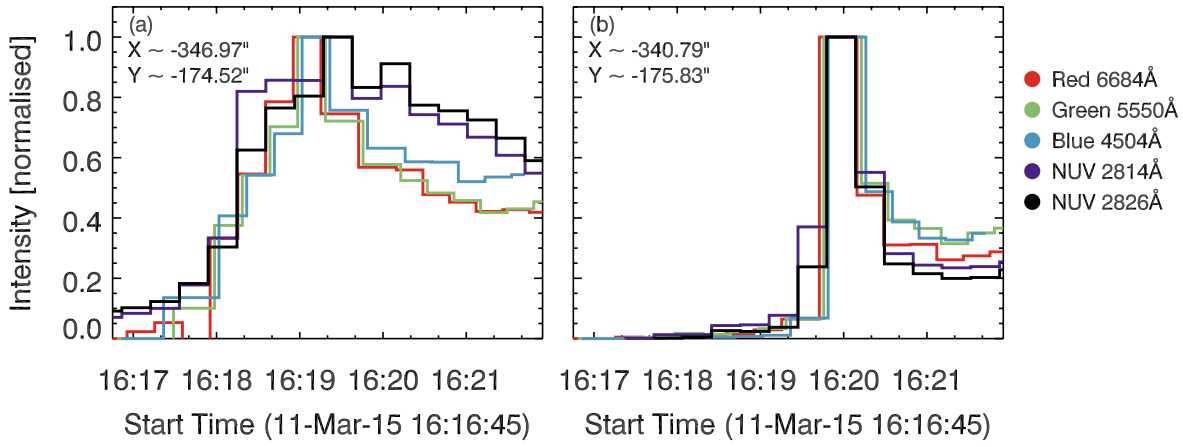

Figure 6.25: *Normalised lightcurves for source A (panel (a)), and source B (panel (b)). The WL lightcurves are the red, green and blue lines, the 2814Å continuum is the purple line, and the 2826Å continuum is the black line.*

('source B') respectively. The SOT pixel scale is smaller than that of IRIS so SOT data were averaged over 3×3 pixels. Source A was located in the penumbra while source B was located in the umbra. Figure 6.25(a,b) shows normalised lightcurves for each each source. Source B lightcurves shows that the WL and NUV continua peaked co-temporally. Note that the $\sim$ 3s time delay between the red, green and blue observations is simply due to the observation sequence. Source A lightcurves, however, show a time delay between the RGB and NUV observations of $\sim$ 20 s. This time delay might not be significant given the observational cadence of 20.75 s, and the SG exposure time of $\sim$ 2.2 s. Also, the co-alignment between SOT and IRIS was performed manually for this initial investigation work, so a small mis-alignment might be the explanation.

The contrast is shown as a function of time in Figure 6.26(a,b). WL contrasts are on the order of 10 – 20% for the penumbral source, and up to 50 – 60% for the umbral source. Contrast in the NUV is significantly higher, reaching 500 – 600% for source A, and in excess of 1000% for source B. To check if the larger NUV contrast is due to the existence of a Balmer jump the pre-flare and flare intensities were plotted a function of wavelength in Figures 6.27 & 6.28. In each of these figures the dotted line is the wavelength of the Balmer jump (3646Å), and several Blackbody functions are overlaid, with the temperatures indicated in each panel.

The pre-flare RGB intensity is taken as the intensity from the first frame since pre-

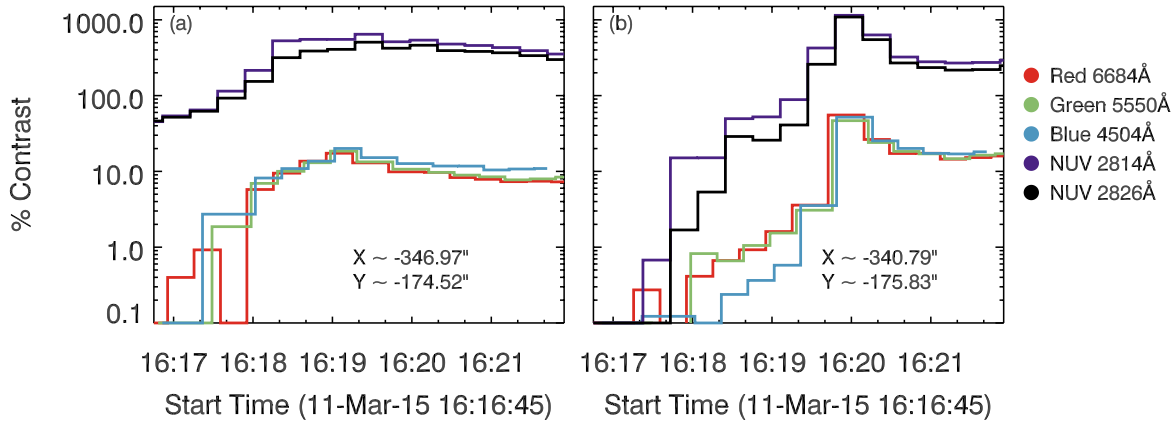

Figure 6.26: *The contrast of each passband during the 2015-March-15th flare. Colours and sources are the same as Figure 6.25.*

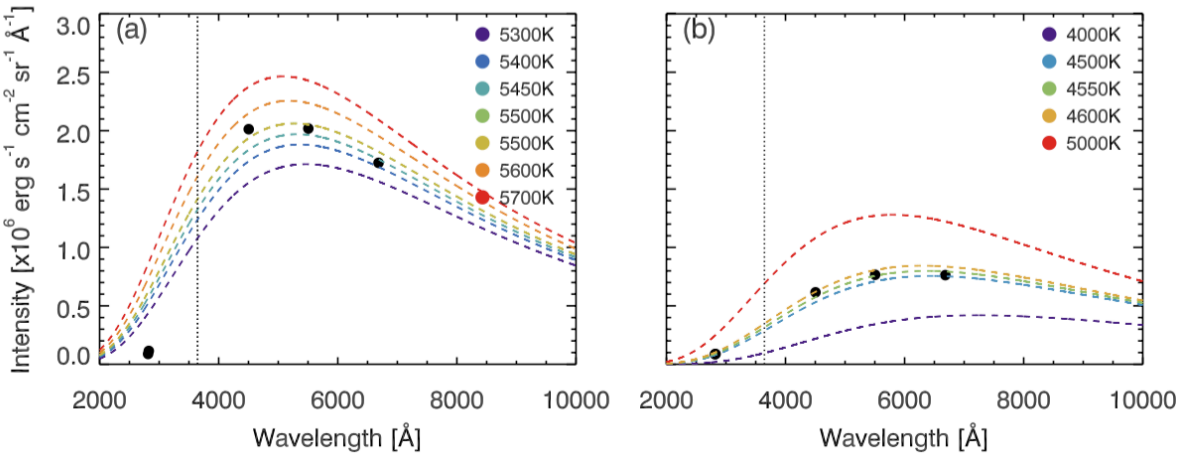

Figure 6.27: *Pre-flare continuum intensities from the 2015-March-11th flare. Panel (a) is source A, and panel (b) is source B. Blackbody curves are overlaid, with the temperature of each curve indicated on the right hand side of the panel. The dotted line is the wavelength corresponding to the Balmer jump.*

flare observations were not available. However, since this source became enhanced towards the end of the flare and was not affected in the early stages, the first frame is adequate as a pre-flare estimate. For the NUV wavelengths the pre-flare intensity was the average intensity over a period of 30 minutes before the flare. Figure 6.27(a,b) shows the pre-flare for source A & B respectively. Source B shows that all the continuum wavelengths are consistent with a blackbody of temperature ~ 4500 – 4600 K (recall that this source is in the umbra). Source A is not so clear. The Paschen

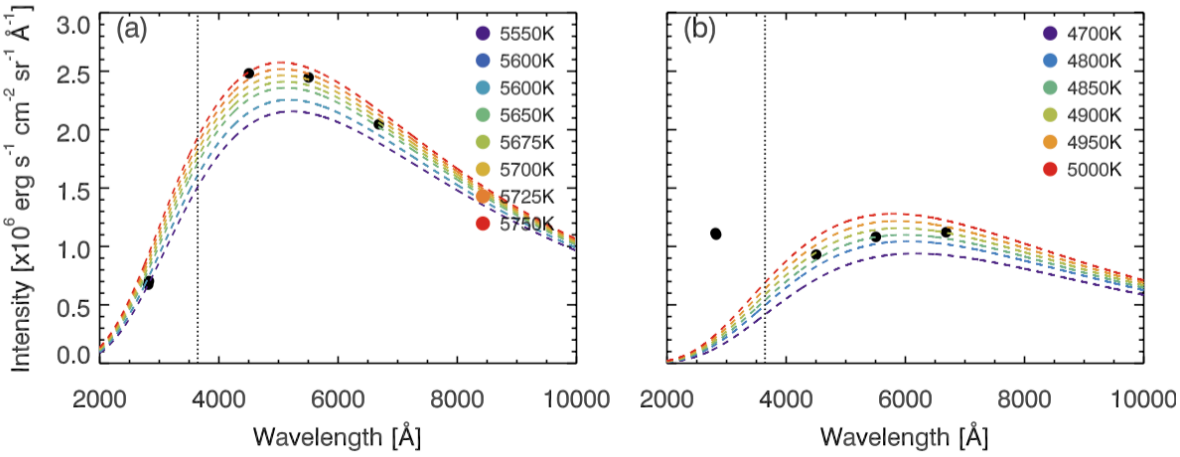

Figure 6.28: *Same as Figure 6.27 but at flare peak for each source.*

intensities (RGB) seem consistent with a blackbody of temperature $\sim 5400-5500$ K (with some spread), but the intensity of the Balmer continuum wavlengths (NUV) lie far below the blackbody curves. During the flare, shown in Figure 6.28, Source B (panel b) shows Paschen continuum intensities consistent with a blackbody curve of $T \sim 4850-4950$ K, an increase of $\Delta T \sim 350$ K over the pre-flare. The NUV intensities are substantially higher than a blackbody would produce. Assuming that intensity increases from the NUV wavelengths to the Balmer jump then this figure suggests the presence of a Balmer jump. A Balmer jump is a sign that Hydrogen free-bound spectrum is contributing to the flare intensity. This contribution would mean that the blackbody component, and the inferred temperature increase, during the flare is reduced. Curiously, source A (panel b) still lies below the blackbody curves. From the RGB intensities a blackbody temperature of $T \sim 5650-5750$ K is inferred, noting the larger spread compared to source B.

While the results from source A are ambiguous, source B certainly seems to suggest that two components are contributing to the continuum enhancement. Co-ordinated SOT & IRIS observations can hopefully allow estimates of the the split between free-bound to enhanced Blackbody.

6.9 RHD Modelling of the Contributions to Continuum Emission

In addition to the observations by Martínez Oliveros et al. (2012), Watanabe et al. (2013) analysed Hinode/SOT RGB data, finding that in their flare the WL sources originated from only a few hundred km above the photosphere (albeit based on the relative formation height of the red, green and blue emission to the Ca II H line emission and the assumption that Ca II H formed in a similar location during the flare as in the quiet Sun). These observations, and some evidence of a substantial photospheric contribution (e.g Hiei 1982) to WLF emission requires an explanation, as does the lack of Balmer jump in some of the historical broadband spectra (Fang & Ding 1995). It is interesting, therefore, to determine the relative contribution to the optical continuum in a solar flare from two RADYN simulations with different heating profiles: a standard non-thermal electron beam with strong (F11) heating, and Alfvén wave dissipation. RHD modelling of the WL continuum in solar flares have so far found that continuum enhancements are largely the result of H recombination radiation, emitted from the mid chromosphere where the optical depth is negligible, plus a small contribution from a backward photosphere (e.g Abbett & Hawley 1999; Allred et al. 2005, 2006). No study (to my knowledge) goes into detail regarding the relative contribution.

Note that Kowalski et al. (2015) modelled a stellar flare from an M-dwarf star using RADYN, in an attempt to reproduce the $T \sim 10,000$ K blackbody component plus Balmer continuum emission of stellar flare observations. They found that an optically *thick* Balmer and Paschen recombination continuum could explain the observations. This resulted from an extremely dense and narrow chromospheric condensation, which only appeared with a non-thermal energy flux of $F = 1{\times}10^{13}$ erg s^{-1} cm^{-2} (F13). More 'solar-like' heating (i.e. F11) could not produce the atmospheric conditions necessary. Kowalski et al. (2015) note that while the conclusion that heating is required at high density to reproduce stellar-flare observations, the F13 heating function is perhaps not physical and so work must be done to experiment with energy deposition models which are more realistic.

We present here the contribution to the optical continuum in a solar flare: the reference flare simulation from Chapter 4 (described in § 4.3.1) that has heating

by a non-thermal electron beam, and the the 'AW_Sim1' model from Chapter 5 (described in § 5.4) that has Alfvén wave heating, with parameters S11, $f = 10$ Hz, $k_{x,0} = 1 \times 10^{-5}$ cm^{-1}. Energy deposition in this latter simulation penetrated deep into the upper photosphere, with direct heating of the lower atmosphere.

6.9.1 Continuum Contribution Function

Using the RADYN flare atmospheres the Hydrogen continuum contribution functions were calculated. Equation 2.7 describes the line contribution function to the emergent intensity as a function of height. This can also describe the continuum contribution function, replacing the line source function with the height dependent continuum source function. Replacing $\chi_\nu S_\nu$ in Eq. 2.7 with j_ν, the emissivity, then the contribution function can be re-written as:

$$C_I(z) = \frac{j_\nu}{\mu} \exp\left(-\tau_\nu/\mu\right), \tag{6.9}$$

where as usual τ_ν is the optical depth (so that $\exp\left(-\tau_\nu/\mu\right)$ is the attenuation) and μ is the viewing angle.

The emissivity is the sum of various sources: Hydrogen bound-free ($j_{\mathrm{H,bf}}$), Hydrogen free-free ($j_{\mathrm{H,ff}}$), H^- bound-free ($j_{\mathrm{H^-,bf}}$), H^- free-free ($j_{\mathrm{H^-,ff}}$) and background metals (j_{metals}). Note that the ν subscript has been dropped for clarity but all terms are frequency and height dependent. Strictly, the emissivity from the Rayleigh and Thompson scattering terms should also be included, but these require having the average intensity $J(z)$, which is not computed by RADYN. For now these terms are omitted, but in the future it may be possible to estimate this term from RH. They are included on the figures that show opacity to illustrate their relative contribution.

The Hydrogen bound-free opacities were calculated in NLTE for the transitions computed in detail by RADYN, since their population densities are available ($\chi_{\mathrm{H,bf,det}}$), and assuming LTE for the upper level transitions, ($\chi_{\mathrm{H,bf,upp}}$). All other continuum components are assumed to be in LTE, with their emissivity calculated by $j_X(z) = \chi_X(z) B_\nu(z)$, for component X, where B_ν is the Planck function, and $\chi_X(z)$ the opacity. Expressions for the opacities and emissivities are listed in Appendix A.

Four wavelengths that RADYN samples and which are close to the SOT and IRIS continuum passbands were selected, and the evolution of their contribution function with time was compared between the two simulations. The selected wavelengths

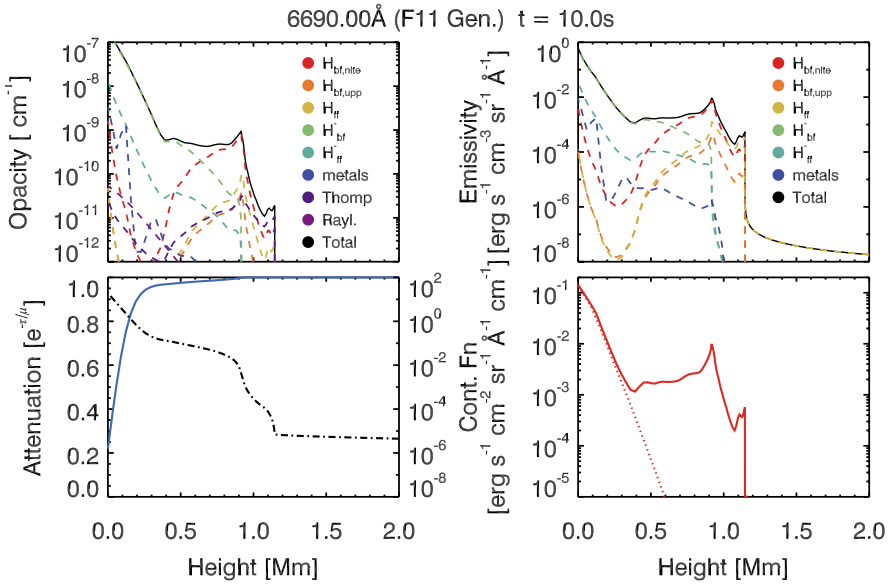

(a)

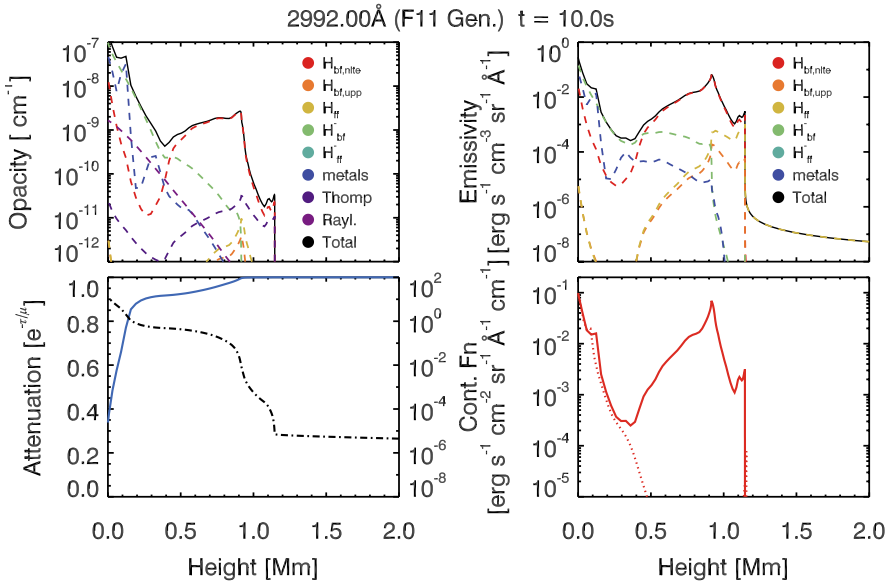

(b)

Figure 6.29: *Continuum contribution functions from an F11 electron beam simulation. (a) shows 6690Å, and (b) shows 2992Å. Each figure has four panels, showing clockwise from top left, the opacity sources, emissivity sources, contribution function, and attenuation (plus optical depth as a dot-dashed line). In bottom right panel the dotted line is the contribution function at $t = 0$. In each panel the colour indicates a source, as listed in the panel itself.*

were: 6690Å, 5790Å, 4300Å, and 2992Å. The behaviour of the three optical wavelengths was qualitatively the same, with differences in the magnitude of contribution function (and opacities) arising due to wavelength dependence of the cross sections.

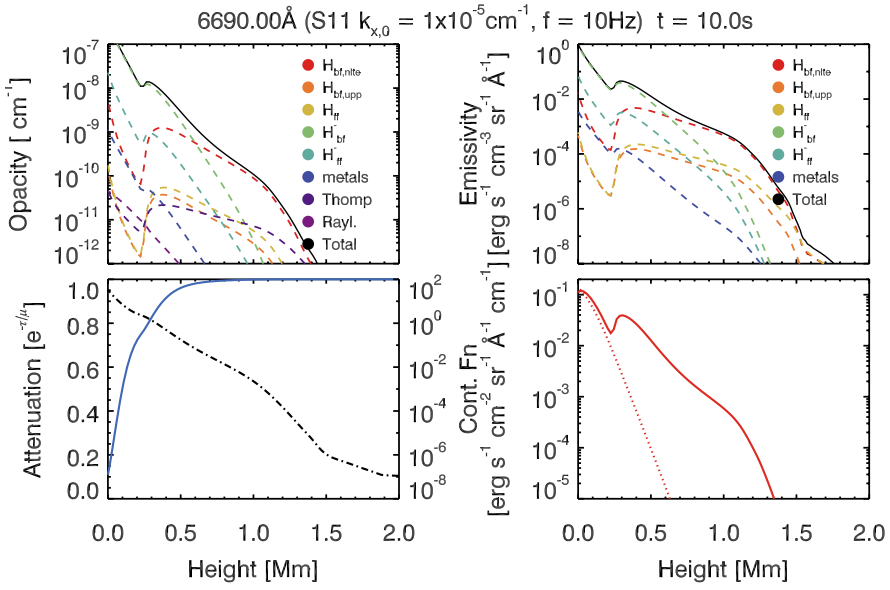

(a)

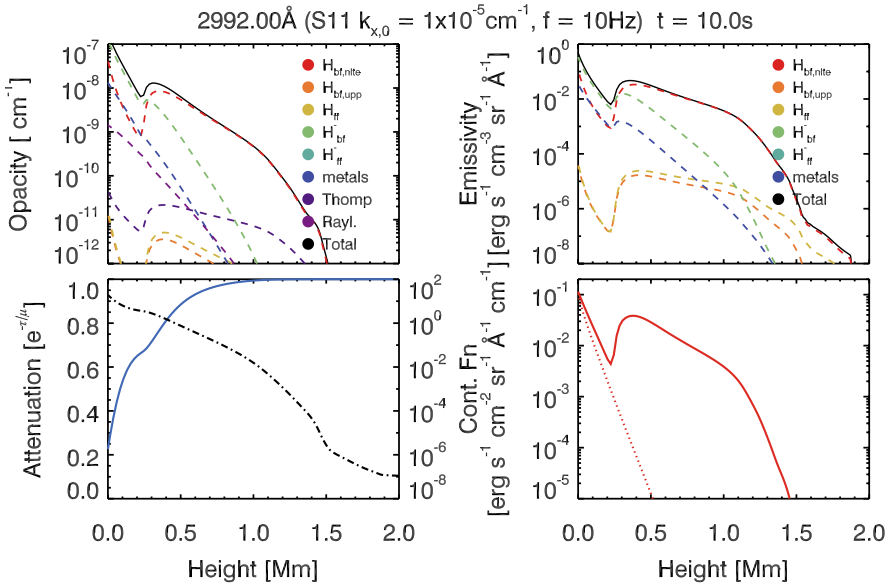

(b)

Figure 6.30: *Same as Figure 6.29, but for the Alfvén wave simulation.*

Figure 6.29(a) shows a breakdown of the contribution function into four panels,

for the 6690Å emission at $t = 10$ s in the electron beam simulation. The top left panel shows the sources of opacity, the top right shows the sources of emissivity, the bottom left shows the attenuation (blue solid line) and the optical depth (dot-dashed line), and the bottom right shows the contribution function (where the dotted line is the $t = 0$ case). In the F11 simulation the WL emission arose primarily from recombination radiation in the chromosphere, from around the height of energy deposition. The contribution function initially showed a peak around 1 Mm, where the optical depth was $\tau \sim 0.01 - 0.001$. There was an increased H^- opacity as a result of temperature increases from backwarming, which dominated the increased C_I between 0.5-0.65 Mm after which H_{bf} took over. While the increased H^- opacity played a role, the main contribution to the flare excess was recombination radiation. Over time, as the temperature in deeper layers increased, the H^- contribution increased more so that by the end of the heating phase of the simulation (20 s) there was an increased H^- opacity to depths of ~ 0.3 Mm.

Figure 6.29(b) shows the contribution function for the 2992Å emission at $t = 10$ s for the electron beam simulation. At this wavelength (blueward of the Balmer jump), the recombination radiation is much stronger than at WL wavelengths, and spreads over a larger height range. Increases to the H^- opacity are modest, and instead increases in the lower atmosphere around 0.5 Mm results from enhanced opacity of background metals. So, while at WL wavelengths there was a contribution from both recombination and H^-, there is only really a contribution from recombination radiation in the NUV (plus a small amount of H free-free emission at the top of the chromosphere).

This is contrasted with the Alfvén wave simulation, shown in Figure 6.30(a,b) for 6690Å and 2992Å respectively. In this simulation there is strong heating directly into the upper photosphere, which initially ($t < 1$ s) increases both H^- opacity and the H_{bf} opacity. There is a sharp increase in the contribution function at ~ 0.6 Mm, with a tail into the upper atmosphere, originating from recombination radiation. By $t = 1$ s the H^- opacity has increased down to 0.5 Mm, where it is now larger than the recombination radiation. In fact, between $0.5 - 0.6$ Mm, this is the dominant component of the contribution function (which peaks at these heights). Higher in the atmosphere, the tail of the contribution function is produced by recombination radiation, but this is a smaller component than the H^- opacity. Over the next few seconds the upper atmosphere remains fairly constant, whereas the enhanced

H^- opacity occurs at ever increasing depth, reaching ~ 0.3 Mm by the end of the simulation (10 s).

Again, the 2992Å emission shows different behaviour to the WL. At this wavelength the recombination radiation dominates over the H^-, so that even though there is an enhanced H^- opacity, it has little impact in the early stages of the flare. The peak of this recombination emission originates from deep in the atmosphere, (~ 0.5 Mm), and has a sizeable optical depth, but there is a long tail extending into the upper atmosphere so that the emission is mostly optically thin.

6.10 Summary and Conclusions

An analysis of the WL sources from the 2011-Feb-15th solar flare has been presented, using optical continuum data from the *Hinode*/SOT. WLF sources were identified using a running difference of log-unsharp filtered images, where pixels were flagged as being a flare source if they had an intensity at least $2-\sigma$ above the local mean in the difference image. Using this flare mask, flare sources were isolated. Data were calibrated to physical units, with the assistance of Dr. T. Tarbell, via a comparison between disk centre observations and the intensity from the Brault and Neckel spectral atlas averaged over the SOT filter response.

Detectable flare sources were largely confined to the penumbra and umbra of the sunspot, with sources crossing the penumbra/umbra boundary in certain locations. Sources within the photosphere were not detected, but it is recognised that this could be a contrast issue. Spatially compact, footpoint-like sources were identified, that mimicked the motion of the larger (and more easily identifiable) ribbons observed in the Ca II H line images, and AIA UV images. These sources moved rapidly through the field of view, moving away from the PIL. As viewed from above, the continuum enhancements seemed to be co-spatial with the brightest emission from the Ca II H line and UV ribbons. From these on-disk observations it is not possible to determine any vertical structure, so it is not suggested that the continuum emission and Ca II ribbons originate in the same volume, just that their 2D projection is co-spatial.

The flare intensity, luminosity and temperature were estimated under two idealised model assumptions of (1) blackbody emission from the photosphere (a result of enhanced H^- emission during the flare) and (2) hydrogen recombination radiation (resulting from over-ionisation and heating in an optically thin chromospheric slab).

Flare sources identified as being newly brightened in Frame 11 of the eastern ribbon, and newly brightened in Frame 8 of the western ribbon were analysed to show the typical temporal evolution of WLF sources.

In model (1) temperature increases of $\sim 100-200$ K were observed, with colour temperatures that were largely consistent with the effective temperature (though with an offset) in the eastern ribbon, but which showed some ambiguity in the western ribbon, which could be a result of strong temperature in-homogeneity at the penumbra/umbra boundary. Model (2) suggests a higher temperature in the emission region, ranging from $\sim [5500-25,000]$ K, peaking around $T \sim 20,000$ K. Additionally, the electron density was constrained to $n_e \sim 10^{13-14}$ cm^{-3}. Model (1) implied the instantaneous power emitted, by the newly brightened sources was on the order 10^{26} erg s^{-1}, compared to an instantaneous power emitted under the assumption of model (2) of the order 10^{27} erg s^{-1}. The observed radiated power in each filter was on the order $\sim 10^{23}$ erg s^{-1}, and extending to the full continuum (which is several 1000 Å wide) the observed energy would be approximately $\sim 10^{26}$ erg s^{-1}, which was consistent with the blackbody interpretation.

The viability of a combined model was assessed by studying the 'core-and-halo' structure of WL footpoints (e.g Xu et al. 2006; Isobe et al. 2007). Xu et al. (2006) remark that a chromospheric source that is directly heated (and over-ionised) will backwarm the lower atmosphere. The 'core' portion of WLF sources appears the brightest, surrounded by a diffuse 'halo' of weaker emission. This was suggested by observations of the 2011-Feb-15th flare.

With joint IRIS and SOT observations of flare it is possible to observe continuum enhancements in both the NUV and optical. WLF sources from the RGB continua and from NUV continua (near $\sim$ 2814Å and 2826Å) were identified and compared. Preliminary results show that the NUV contrasts are significantly higher than the WL contrasts reaching $\sim 500-600\%$ for the NUV compared to $\sim 50\%$ for the WL), supporting the historical observations of 'blue' WLFs when observed at lower wavelengths and suggesting the existence of a Balmer jump. In comparison the RGB contrasts were consistent between the three passbands, suggesting a relatively flat spectrum longward of the Balmer jump. This is similar to the observations of, for example, Hiei (1982). A temperature increase of $\sim 250-350$ K was inferred from overlaying blackbody functions of various temperatures against the observed intensities. In one selected source the NUV continuum intensity was ~ 5 times larger

than might be expected if it were to be described by a blackbody at temperature $\sim 4850 - 4950$ K (consistent with the WL observations), and was therefore more intense than the WL emission. In contrast, in the other source the NUV was weaker than the WL. Though not attempted here, these observations can be used to estimate the proportion of H^- versus recombination radiation that produces the WL continuum. This flare, and other flares with joint SOT and IRIS observations, will form the basis of a future planned study that aims to answer the outstanding questions of continuum formation.

Finally, the contribution function to the emergent continuum intensity was calculated for two flare simulations. One simulation was the reference non-thermal electron beam simulation, and the second was an Alfvén wave simulation. The electron beam simulation showed that blueward of the Balmer jump (at 2992Å) enhanced H^- opacity contributed negligibly to the WL emission, with the dominant source was recombination radiation from the chromosphere. Redward of the Balmer jump (at 6690Å), recombination radiation was, again, the dominant contributor to the intensity, but there was non-negligible H^- contribution to the WL continuum. The H^- opacity was increased down to 0.3 Mm as a result of backwarming, by the end of the simulation. In contrast, the Alfvén wave simulation showed that H^- was the dominant source of the WL emission redward of the Balmer jump, with a tail extending into the chromosphere produced by recombination radiation. Blueward of the Balmer jump, the dominant source was recombination radiation, but the direct heating at low depth meant that the recombination radiation was optically thick where it contributed the most to the WL continuum, with a tail that extended to the chromosphere (where it was optically thin).

These simulation results are interesting in illustrating that increased heating of the lower atmosphere is necessary to produce a dominant H^- contribution to the WL continuum during flares. These simulations should be combined with the observations from IRIS and SOT to try and determine the split of emission mechanisms in observed flares.

Chapter 7

Concluding Remarks and Future Work

This thesis has presented observations and modelling of the chromosphere during solar flares, focusing on new or rare observations in an effort to increase our understanding of the radiative and hydrodynamic response of the chromosphere to flare energy input. Chapter 3 discussed one of the first detailed investigations of the Mg II h & k lines during flares and Chapter 4 used RHD & RT modelling to understand the formation properties that led to the observed flare response. Chapter 5 described the implementation of Alfvén wave dissipation as an alternative flare energy transport mechanism, and gave a detailed comparison between simulations in which flare energy was transported by either Alfvén waves or by a non-thermal electron beam. Finally, Chapter 6 showed an analysis of optical continuum emission during a solar flare using RGB data from *Hinode*/SOT (a relatively rare observation). In addition to the optical continuum, some initial results using NUV continuum data were presented.

These results are summarised below in § 7.1, and ideas for further work to build upon these findings are presented in § 7.2.

7.1 Thesis Summary

Observations of the Mg II resonance lines during a flare were analysed to understand how these lines respond to flare energy input. During the flare the central reversal in the Mg II h & k lines vanished, though some profiles did appear flat-topped, and some had some more complex structure. Despite the absence of the reversal, analysis of the k/h intensity ratio suggests the lines remained optically thick. The spatial and

temporal evolution of Mg II during the flare showed spatially localised energy input at the outer edge of the ribbon (with variations on scales of $\sim$0.5″ or less). There was evidence of a slow onset of excitation before a main impulsive peak.

Following flare energy deposition, profiles appeared significantly more intense (the integrated intensity during the flare was approximately 25 times larger than the quiet Sun value and 8 times larger than the plage value), with line centroids that were redshifted with an equivalent velocity of $\sim$15-25 km s^{-1}. The profiles were very broad, increasing from $\sim 0.28 - 0.5$Å, an increase that was greater than could be explained by increased turbulence. It is likely that the lines were broadened due to so-called opacity broadening, with a broadening factor from 2.5-5.7. This suggests that flare heating was felt deep in the atmosphere, or that that line wings formed close in height to the line core. Asymmetries were present in the most intense pixels, which also showed the largest redshifts. It was speculated that these resulted from multiple optically thick line components, one shifted by mass flows and one stationary, formed deeper in the atmosphere.

Both the intensity and velocity enhancements showed an impulsive rise, but had different decay timescales. While both showed a sharp decreas from the peak within one timestep (43 s), the equivalent velocity then returned to the pre-flare within 3-4 minutes, whereas the line intensity took approximately 15 minutes to return to the background. This is likely because the lines remain broad, which increased the integrated intensity.

Numerical modelling of the Mg II spectrum during flares was performed to elucidate the line formation properties, and what the line response tells us about the flaring chromosphere. This analysis confirmed that the lines do remain optically thick during the flare, though mass motions in the upper atmosphere result in local density enhancements which produce an optically thin contributions to the emergent intensity. This is a weak component, but is responsible for some line asymmetry in the wings. The h & k lines form lower in the atmosphere during flares as a result of a reduction in the Mg II opacity when the heated upper chromosphere ionises Mg II to Mg III. Although formed lower, the lines are more intense than in the pre-flare due to flare heating at the line formation heights, and the subsequent increase in electron density at formation heights. The increase in electron density results in a stronger coupling of the h & k source functions to the local temperature. The k2

emission peaks and k3 line cores are formed closer in height than in the non-flaring atmosphere, and the line wings contain contributions from a large height range.

The simulated flare profiles qualitatively match the observed flare profiles, showing significant intensity enhancements (integrated intensities were between $\sim 60–100$ times the quiet Sun - recall that RADYN uses a radiative equilibrium atmosphere as the initial solution, which does not contain the chromospheric temperature rise), Doppler motions (where the whole line is shifted), line broadening, and line asymmetries. Simulations confirmed that blue wing asymmetries are from multiple components to the emission, and a simulation with larger flows showed larger asymmetries. A dense downflow redshifts the emission of the line core, but lower lying Mg II ions contribute a stationary component to the emergent intensity, which gives the overall profile a blue wing asymmetry. Since the opacity profile higher in the atmosphere is shifted to the red also, the line core photons are free to escape. The Doppler shift of the line core was well correlated to the atmospheric velocity. During the flare the intensity of the line core expressed as a radiation temperature was not that well correlated with the local temperature. The values of radiation temperature did mostly lie between $(0.5 – 1)\times$ the atmospheric temperature so do provide a rough estimate. The peak intensity was more correlated with the local temperature. Observational methods to identify the line centroid (quartiles and bisectors), and therefore the Doppler shift of the line, were applied to the synthetic spectra. This revealed that although observationally derived Doppler shifts largely agree with the direction of the true Doppler shift, and the magnitude at later stages, they miss the strong and rapid rise at the start of the downflow.

While the line is qualitatively similar there are two differences. First, the lines are not as broad as observed flare profiles. Increasing microturbulence did broaden the lines further, but mainly in the core. Instead, it is likely that the behaviour of the source function is responsible for the observed widths (opacity broadening). In the simulations the source function increases steeply between the wing formation height and the core, producing narrow profiles. To obtain the broad profiles that are observed then the gradient must be reduced. Either the line wings and core are formed geometrically closer than in simulations, or the lower chromosphere is hotter than in simulations so that the temperature gradient to the core formation height is reduced. Additionally, the lines are mostly not single peaked, and show reversals. Generally the profiles had shallow reversals, though some were single peaked or

showed a complex structure. Analysing the source functions showed that they were more coupled to the background temperature during the flare, but that the line core source function still decreased following a maximum before reaching the formation height.

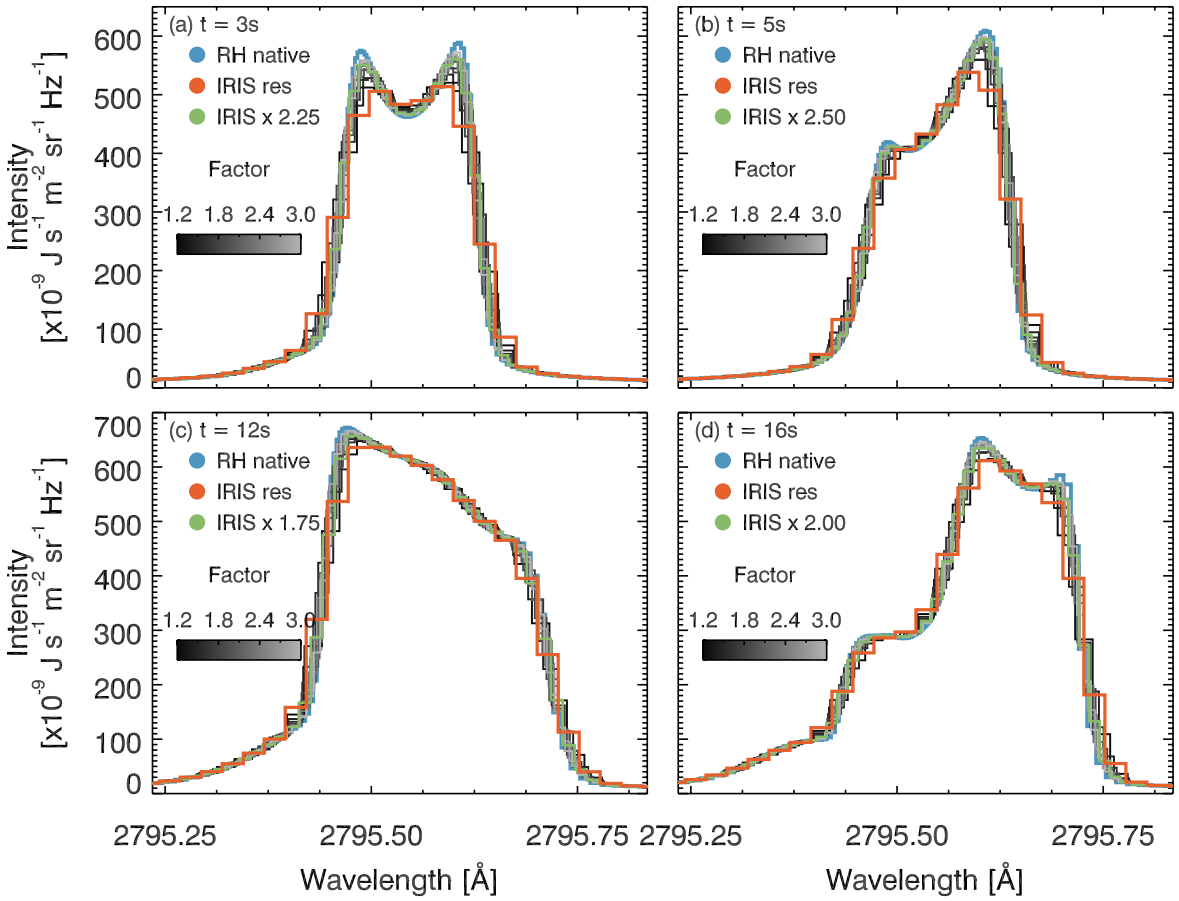

Figure 7.1: *Mg* II *k-line profiles from an RH flare simulation, convolved with various model instrumental responses. Grey profiles represent a factor* $(1.2-3)\times$ *improvement over the IRIS spectral resolution. Blue lines are the native RH resolution, red lines are the IRIS resolution, and green profiles are the required improvements over IRIS to recover some line core details.*

Features that are visible at the native resolution of RH can be lost when degraded to the IRIS spectral resolution. This can result in the central reversal disappearing, or some structure in the line core core being smeared out. To determine what resolution would be required to recover these features the RH spectra were convolved with an

iteratively varied model instrumental response. This was done assuming that the FWHM of the instrumental response was still a factor two greater than the pixel scale (as with IRIS). An increase in resolution of $(2.5-3)\times$ that of IRIS recovers both the structure and intensity of line core features. Features could, however, generally be recovered partially with a more modest increase in resolution of $(1.5-1.75)\times$. Figure 7.1 shows four examples of varying the instrumental response, illustrating that some of the detailed features of the RH simulations can be observed with instrumental resolution higher than that of IRIS. Grey profiles represent convolutions with instrumental response $(1.2-3)\times$ that of IRIS. The blue profiles are the native RH profiles, green profiles show what resolution is required to mostly recover the line profile, and red profiles are the profiles degraded to IRIS resolution.

The optical continuum emission from the 15-February-2011 solar flare was analysed, which also suggested flare heating low in the atmosphere. Continuum enhancements were identified using a combination of filtering and running difference methods, revealing spatially localised WLF kernels that appeared as a subset of the more extended UV ribbons. Images showed a brighter leading edge that rapidly progressed through the field of view, and the corresponding optical lightcurves showed a rapid impulsive rise followed by a longer decay lasting several minutes. The leading edge is likely the site of energy deposition into newly brightened sources.

The SOT data were calibrated to physical units using a comparison of synoptic data to a spectral atlas, which allowed the emission mechanism of the WLF to be investigated using two simple models. These models were of optically thick enhanced H^- emission originating from the photosphere, or hydrogen recombination radiation originating from an overionised slab in the chromosphere. In the latter case the emission was assumed to be optically thin. Assuming the photospheric origin then the data were found to be consistent with a blackbody with temperature enhancement of around $100-200$ K, whereas the chromospheric origin suggests temperatures ranging from $[5500-25,000]$ K with electron density $\sim 10^{13-14}$ cm^{-3}. The instantaneous power emitted from the blackbody model was on the order 10^{26} erg s^{-1}, whereas the recombination radiation model had an instantaneous power on the order 10^{27} erg s^{-1}. Of these, the blackbody model was the most consistent with the observed instantaneous power. The observations exhibited the core-and-halo structure, which might suggest that both mechanisms play a role.

Observations from the 2015-March-11th flare were also presented, which showed that while the Paschen continuum wavelengths were consistent with a blackbody during the flare, the Balmer continuum wavelengths were not. This suggests that both mechanisms contribute, with varying dominance in each part of the spectrum (consistent with the results of Kleint et al. 2016). This was explored further with RHD modelling, where the continuum contribution functions showed that the H^- opacity was increased more in Paschen continuum than the Balmer. However, in the electron beam simulation the H^- opacity increase was not the dominant contributor to the emergent intensity. It will be necessary to further analyse the 2015-March-11th flare, in order to estimate the Balmer recombination spectrum from the NUV observations from that determine the relative contribution of each mechanism to the Paschen continuum.

There is observational evidence that flare heating can be felt to great depth in the chromosphere and possibly deeper, which means a transport mechanism that can reach these depths is required. This can be direct heating, or a secondary flare effect (such as radiative backwarming). Direct heating can be challenging to explain within the framework of the standard flare model since there is not power carried by the highest energy electrons, so sufficient energy is not deposited in the lower atmosphere. This, and additional problems with the electron beam model (as discussed in Chapters 1 & 5), motivated the study of Alfvén waves as a flare energy transport mechanism by Emslie & Sturrock (1982); Fletcher & Hudson (2008); Russell & Fletcher (2013); Reep & Russell (2016). This mechanism was incorporated to the RADYN code allowing a radiation hydrodynamics simulations of Alfvén wave heating during flares. An overview of atmospheric heating was given for four representative simulations, showing that Alfvén waves can directly heat the lowest layers of the atmosphere, as well as in the mid-upper chromosphere, depending on the wave parameters.

A detailed comparison between an electron beam and Alfvén wave simulation was presented. While both mechanisms resulted in a strongly heated chromosphere with an overall similar evolution, there were differences in the temperature structure with height. Consequently, the electron density, pressure, and velocity structure also differed. In particular, the electron beam simulation produced the large temperature bubble in the mid-chromosphere, while the Alfvén wave simulation resulted in a

hotter upper chromosphere, and a warmer lower chromosphere.

Two chromospheric spectral lines were chosen for a comparison: the Mg II k-line and the Ca II 8542 Å line. The Ca II 8542 Å line was largely similar in each simulation, apart from a difference in the time taken to reach maximum intensity. The Mg II k-lines, however, did show differences. The electron beam simulation produced a profile that had a shallow central reversal and mostly symmetric k2 emission peaks. The Alfvén wave simulation produced a profile that was more asymmetric, with a k2r peak twice as intense as the the k2v peak, compared to the electron beam simulation in which the k2r and k2v components were approximately equal. Additionally, the central reversal became indiscernible from the k2v component so that the line could be mistakenly interpreted as single peaked with a redshift and blue wing asymmetry.

Since it is able to sufficiently heat the chromosphere, this energy transport mechanism should be taken seriously as either an alternative to the standard electron beam model, or as a significant component in a scenario in which both mechanisms transport flare energy. Chromospheric radiation should be able to discern between the competing mechanisms, and this should be a focus for further work using the Alfvén wave flare energy transport model.

7.2 Future Work

Further work is needed to understand the effects of different heating profiles have on Mg II line formation. In particular, determining whether increasing the temperature of the lower chromosphere will increase line width, to match the broad wings observed in flares. This will involve producing synthetic Mg II spectra from a large grid of flare models, collaborating with Dr J. Allred (NASA/GSFC) who has already produced this grid, as well performing experiments with model-independent heating. Energy can be deposited at specified heights and times in the `RADYN` simulation. Observing the effect of an artificially increased lower chromospheric temperature on the profile widths will help us understand the requirements of a flare heating model. For example, is a certain temperature (or temperature gradient) required between the wing and core formation heights to produce wider profiles?

Finding methods better at identifying the line core is also important, which might be easier when studying the Mg II subordinate lines. Pereira et al. (2015) found that the subordinate lines are in emission when lower chromospheric temperatures

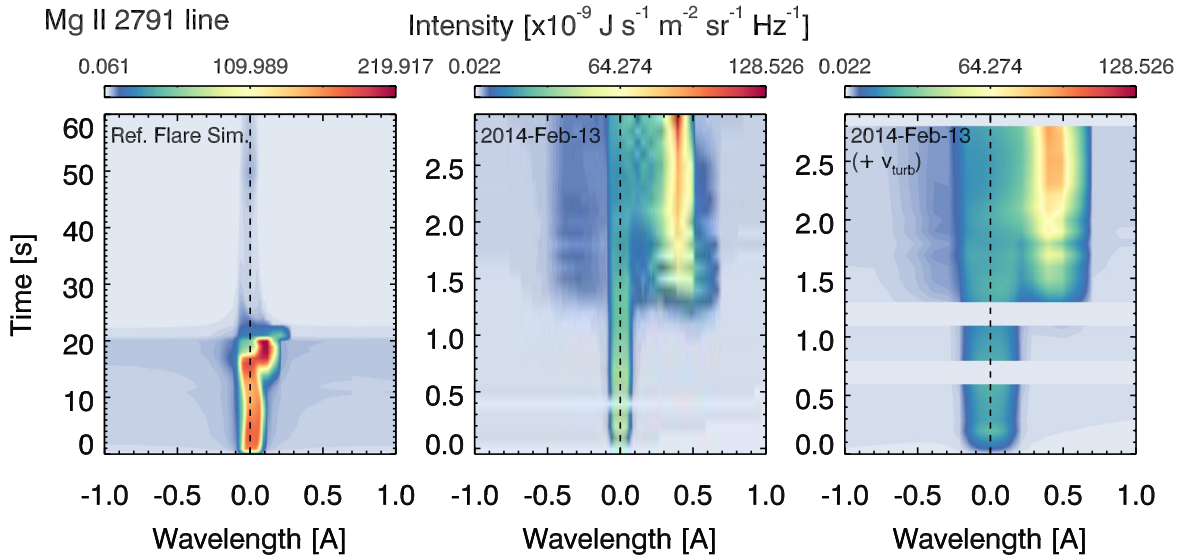

Figure 7.2: *Mg II 2791Å line profiles from the three simulations, plotted with wavelength along the x-axis and time. along the y-axis. Missing data is when the simulation did not converge. Colour represents intensity.*

are large in regions with sufficiently high electron density. However, a preliminary analysis of our simulations shows that the subordinate lines in flares are actually formed much higher, and not too distant from the resonance lines. They are still optically thick, but are without strong central reversals, and are generally narrower. Identifying the line core, or multiple components (which could be blended in the wider resonance lines) could be a simpler task with the subordinate lines. They appear to follow the same pattern as the resonance lines (compare Figure 7.2 with Figure 4.29), and so velocity differences between the subordinate and resonance lines could provide information regarding gradients in the chromosphere, and intensity differences could provide information about temperature gradients. These lines have already been synthesised for these flares, and will be analysed using similar techniques.

In addition to Mg II, IRIS observes the strong lines of C II & Si IV, as well as Fe II lines and O I. These lines form throughout the chromosphere and transition region, sampling different heights. An analysis which investigates the observed flare response of all of these lines, informed by flare modelling, will be valuable in gaining a fuller picture of the flaring chromospheric and TR. For example, do all of these lines show a consistent picture of atmospheric flows and asymmetry? The RH

simulations can solve for many atomic species at once, so a joined up approach is possible with the only penalty being computational time. Since the 2015-March-11th flare also has SOT continuum observations this event is an ideal candidate for such a study. A particular focus of continued analysis of this flare is to identify the relative contribution of continuum emission mechanisms, and how this might vary as a function of spatial location in the flare.

These efforts can be combined with further exploration of Alfvén wave heating in flares. The parameter space for AW simulations is large. Further work will focus on filling in the parameter space, including changing the magnetic field, and energy flux in addition to the frequency and wave number. Changing conditions during the flare (the density and temperature structure) in response to flare heating has a corresponding effect on the heating rate which varies in strength as a function of both height and time. Since the effectiveness of collisions varies strongly due to both temperature and density, future experiments should also consider varying the pre-flare atmosphere used (Dr J. Allred has a suite of initial atmospheres with a variety of coronal temperatures, loop lengths, and densities).

As discussed previously, accelerated electrons are definitely present in the flaring chromosphere. Two scenarios present themselves: Alfvén waves act alone to transport and dissipate flare energy, and secondary effects accelerate electrons locally, or Alfvén waves act as an additional mechanism in concert with electron beams. In the latter scenario waves could directly heat the lower atmosphere, and beams could heat the upper atmosphere producing the HXR sources. The first case has been tested so far (though note that no effort is made here to explain the local acceleration of electrons), but the second case warrants attention also. Experiments with tandem energy transport mechanisms open new questions, however, as the distribution of energy to each mechanism is not well constrained. Tying to observations will be key. Identifying flares that either do not have a strong HXR signature or in which the energy deposited by an electron beam (as derived from RHESSI observations) is not sufficient to account for observed radiative losses (e.g. Fletcher et al. 2013), will be useful in helping to ascertain if Alfvén waves can account for the radiation observed (either alone or in tandem with beams). Additionally, identifying differences in the lines profiles of continuum emission from locations co-spatial with HXR footpoints and those located elsewhere in the flare ribbons could elucidate this problem.

Waves have so far been simulated as being monochromatic, which are able to heat different parts of the atmosphere effectively depending on their parameters. It is more likely that a spectrum of waves would be produced by strong flare perturbations of the magnetic field. Continuing the collaboration with Dr. Alex Russell and Dr. Jeff Reep, it is hoped that a heating function that describes a spectrum of waves can eventually be incorporated into RADYN.

In RADYN simulations the competition between energy losses and energy input is key to determining the dynamics of the flaring atmosphere. Currently RADYN uses an optically thin radiative loss function to capture losses from transitions that are not treated by detailed radiative transfer. However, during flares some strong lines (such as C II, C III) might be optically thick, and so not radiate as intensely as the loss function implies. RH simulations of the dominant lines can predict their losses whilst allowing them to be optically thick, and indicate how large the deviation is from the optically thin assumptions. This is somewhat artificial as it will use RADYN atmospheres that were created assuming the optically thin radiative losses (the temperature and density structure would presumably be different if a more realistic loss function were included in the simulation), but the overall effect can be at least estimated using the RADYN snapshots. If there is a substantial deviation then the loss function should be modified to try and capture this.

Bibliography

Abbett, W. P. & Hawley, S. L. 1999, *The Astrophysical Journal*, 521, 906

Aboudarham, J. & Henoux, J. C. 1986, *Astronomy and Astrophysics*, 156, 73

Acton, L. W., Leibacher, J. W., et al. 1982, *The Astrophysical Journal*, 263, 409

Aller, L. H. 1963, Astrophysics. The atmospheres of the sun and stars, 2nd edn. (Ronald Press)

Allred, J. C., Hawley, S. L., et al. 2005, *The Astrophysical Journal*, 630, 573

Allred, J. C., Hawley, S. L., et al. 2006, *The Astrophysical Journal*, 644, 484

Allred, J. C., Kowalski, A. F., et al. 2015, *The Astrophysical Journal*, 809, 104

Antonucci, E. & Dennis, B. R. 1983, *Solar Physics*, 86, 67

Artzner, G., Bonnet, R. M., et al. 1977, *Space Science Instrumentation*, 3, 131

Aschwanden, M. J., Benz, A. O., et al. 1995, *The Astrophysical Journal*, 455, 347

Aschwanden, M. J., Brown, J. C., et al. 2002, *Solar Physics*, 210, 383

Asplund, M., Grevesse, N., et al. 2009, *Annual Review of Astronomy and Astrophysics*, 47, 481

Athay, R. G. & Skumanich, A. 1968, *Solar Physics*, 3, 181

Avrett, E. H. & Loeser, R. 2008, *The Astrophysical Journal, Supplement*, 175, 229

Avrett, E. H., Machado, M. E., et al. 1986, in The lower atmosphere of solar flares, p. 216 - 281, ed. D. F. Neidig, 216–281

Ayres, T. R. & Linsky, J. L. 1976, *The Astrophysical Journal*, 205, 874

Bartoe, J.-D. F., Brueckner, G. E., et al. 1977, *Applied Optics*, 16, 879

Battaglia, M., Kontar, E. P., et al. 2012, *The Astrophysical Journal*, 752, 4

Berlicki, A. 2007, in Astronomical Society of the Pacific Conference Series, Vol. 368, The Physics of Chromospheric Plasmas, ed. P. Heinzel, I. Dorotovič, & R. J. Rutten, Heinzel

Bian, N. H., Watters, J. M., et al. 2016, *The Astrophysical Journal*, 833, 76

Bonnet, R. M., Lemaire, P., et al. 1978, *The Astrophysical Journal*, 221, 1032

Boyer, R., Sotirovsky, P., et al. 1985, *Solar Physics*, 98, 255

Bradshaw, S. J. & Mason, H. E. 2003, *Astronomy and Astrophysics*, 401, 699

Brosius, J. W., Landi, E., et al. 2002, *The Astrophysical Journal*, 574, 453

Brosius, J. W. & Phillips, K. J. H. 2004, *The Astrophysical Journal*, 613, 580

Brosius, J. W. & White, S. M. 2006, *The Astrophysical Journal, Letters*, 641, L69

Brown, J. C. 1971, *Solar Physics*, 18, 489

Brown, J. C. 1972, *Solar Physics*, 26, 441

Brown, J. C. 1973, *Solar Physics*, 28, 151

Brown, J. C., Karlicky, M., et al. 1990, *The Astrophysical Journal, Supplement*, 73, 343

Brown, J. C. & Melrose, D. B. 1977, *Solar Physics*, 52, 117

Brown, J. C., Turkmani, R., et al. 2009, *Astronomy and Astrophysics*, 508, 993

Bruhweiler, F. C., Morgan, T. H., et al. 1982, *The Astrophysical Journal*, 262, 675

Canfield, R. C., Gunkler, T. A., et al. 1984, *The Astrophysical Journal*, 282, 296

Canfield, R. C., Metcalf, T. R., et al. 1987, *Nature*, 326, 165

Carlsson, M. 1998, in Lecture Notes in Physics, Berlin Springer Verlag, Vol. 507, Space Solar Physics: Theoretical and Observational Issues in the Context of the SOHO Mission, ed. J. C. Vial, K. Bocchialini, & P. Boumier, 163

Carlsson, M., Leenaarts, J., et al. 2015, *The Astrophysical Journal, Letters*, 809, L30

Carlsson, M. & Stein, R. F. 1994, in Chromospheric Dynamics, ed. M. Carlsson, 47

Carlsson, M. & Stein, R. F. 1995, *The Astrophysical Journal, Letters*, 440, L29

Carlsson, M. & Stein, R. F. 1997, *The Astrophysical Journal, Letters*, 481, 500

Carlsson, M. & Stein, R. F. 1999, in American Institute of Physics Conference Series, Vol. 471, American Institute of Physics Conference Series, ed. S. T. Suess, G. A. Gary, & S. F. Nerney, 23–28

Carlsson, M. & Stein, R. F. 2002, *The Astrophysical Journal*, 572, 626

Carrington, R. C. 1859, *Monthly Notices of the Royal Astronomical Society*, 20, 13

Caspi, A., Krucker, S., et al. 2014, *The Astrophysical Journal*, 781, 43

Chen, Q. R. & Ding, M. D. 2005, *The Astrophysical Journal*, 618, 537

Cheng, J. X., Kerr, G., et al. 2012, *The Astrophysical Journal*, 744, 48

Cliver, E. W. 2006, *Advances in Space Research*, 38, 119

Cliver, E. W. & Dietrich, W. F. 2013, *Journal of Space Weather and Space Climate*, 3, A31

Cowling, T. G. 1956, *Monthly Notices of the Royal Astronomical Society*, 116, 114

Culhane, J. L., Phillips, A. T., et al. 1994, *Solar Physics*, 153, 307

De Pontieu, B., Martens, P. C. H., et al. 2001, *The Astrophysical Journal*, 558, 859

De Pontieu, B., Title, A. M., et al. 2014, *Solar Physics*, 289, 2733

Dennis, B. R. & Pernak, R. L. 2009, *The Astrophysical Journal*, 698, 2131

Dere, K. P., Landi, E., et al. 1997, *Astronomy and Astrophysics, Supplement*, 125

Dickson, E. C. M. & Kontar, E. P. 2013, *Solar Physics*, 284, 405

Ding, M. D., Fang, C., et al. 1995, *Solar Physics*, 158, 81

Donati-Falchi, A., Smaldone, L. A., et al. 1984, *Astronomy and Astrophysics*, 131, 256

Donea, A.-C., Besliu-Ionescu, D., et al. 2006, *Solar Physics*, 239, 113

Dorfi, E. A. & Drury, L. O. 1987, *Journal of Computational Physics*, 69, 175

Doschek, G. A. & Feldman, U. 1977, *The Astrophysical Journal, Supplement*, 35, 471

Doschek, G. A. & Feldman, U. 2010, *Journal of Physics B Atomic Molecular Physics*, 43, 232001

Doschek, G. A., Feldman, U., et al. 1980, *The Astrophysical Journal*, 239, 725

Doschek, G. A., Mariska, J. T., et al. 1996, *The Astrophysical Journal*, 459, 823

Emslie, A. G. 1978, *The Astrophysical Journal*, 224, 241

Emslie, A. G., Dennis, B. R., et al. 2012, *The Astrophysical Journal*, 759, 71

Emslie, A. G. & Sturrock, P. A. 1982, *Solar Physics*, 80, 99

Fang, C. & Ding, M. D. 1995, *Astronomy and Astrophysics, Supplement*, 110, 99

Feldman, U. & Doschek, G. A. 1977, *The Astrophysical Journal, Letters*, 212, L147

Feldman, U. & Doschek, G. A. 1978, *Astronomy and Astrophysics*, 65, 215

Feldman, U., Doschek, G. A., et al. 1988, *Journal of the Optical Society of America B Optical Physics*, 5, 2237

Fisher, G. H. 1989, *The Astrophysical Journal*, 346, 1019

Fisher, G. H., Canfield, R. C., et al. 1985a, *The Astrophysical Journal*, 289, 434

Fisher, G. H., Canfield, R. C., et al. 1985b, *The Astrophysical Journal*, 289, 425

Fisher, G. H., Canfield, R. C., et al. 1985c, *The Astrophysical Journal*, 289, 414

Fletcher, L., Dennis, B. R., et al. 2011, *Space Science Reviews*, 159, 19

Fletcher, L., Hannah, I. G., et al. 2013, *The Astrophysical Journal*, 771, 104

Fletcher, L., Hannah, I. G., et al. 2007, *The Astrophysical Journal*, 656, 1187

Fletcher, L. & Hudson, H. S. 2002, *Solar Physics*, 210, 307

Fletcher, L. & Hudson, H. S. 2008, *The Astrophysical Journal*, 675, 1645

Fontenla, J. M., Avrett, E. H., et al. 1993, *The Astrophysical Journal*, 406, 319

Foukal, P. 1990, Solar astrophysics (Wiley-Interscience)

Foukal, P., Fröhlich, C., et al. 2006, *Nature*, 443, 161

Freeland, S. L. & Handy, B. N. 1998, *Solar Physics*, 182, 497

Gan, W. Q., Rieger, E., et al. 1993, *The Astrophysical Journal*, 416, 886

Geiss, J. & Bürgi, A. 1986, *Astronomy and Astrophysics*, 159, 1

Geltman, S. 1962, *The Astrophysical Journal*, 136, 935

Gouttebroze, P. 1977, *Astronomy and Astrophysics*, 54, 203

Gouttebroze, P. 1989, *The Astrophysical Journal*, 337, 536

Graham, D. R. & Cauzzi, G. 2015, *The Astrophysical Journal, Letters*, 807, L22

Graham, D. R., Zangrilli, L., et al. 2016, *In Prep*

Gray, D. F. 1976, The observation and analysis of stellar photospheres, 1st edn. (Wiley-Interscience)

Gray, D. F. 1992, The observation and analysis of stellar photospheres., 2nd edn. (Cambridge University Press)

Gudiksen, B. V., Carlsson, M., et al. 2011, *Astronomy and Astrophysics*, 531, A154

Gustafsson, B. 1973, *Uppsala Astron. Obs. Ann.*, 5

Hacar, A., Alves, J., et al. 2016, *Astronomy and Astrophysics*, 591, A104

Haerendel, G. 2012, *The Astrophysical Journal*, 749, 166

Hannah, I. G., Hudson, H. S., et al. 2011, *Space Science Reviews*, 159, 263

Harra, L. K., Matthews, S. A., et al. 2014, *The Astrophysical Journal*, 792, 93

Hasan, S. S., Kalkofen, W., et al. 2000, *The Astrophysical Journal, Letters*, 535, L67

Hawley, S. L. & Fisher, G. H. 1994, *The Astrophysical Journal*, 426, 387

Heinzel, P., Karlicky, M., et al. 1994, *Solar Physics*, 152, 393

Heinzel, P. & Kleint, L. 2014, *The Astrophysical Journal, Letters*, 794, L23

Heinzel, P., Schmieder, B., et al. 2015, *The Astrophysical Journal, Letters*, 800, L13

Heinzel, P., Schmieder, B., et al. 1992, *Solar Physics*, 139, 81

Hiei, E. 1982, *Solar Physics*, 80, 113

Hill, F., Martens, P., et al. 2009, *Earth Moon and Planets*, 104, 315

Hodgson, R. 1859, *Monthly Notices of the Royal Astronomical Society*, 20, 15

Holman, G. D. 2012, *The Astrophysical Journal*, 745, 52

Holman, G. D., Aschwanden, M. J., et al. 2011, *Space Science Reviews*, 159, 107

Holman, G. D., Sui, L., et al. 2003, *The Astrophysical Journal, Letters*, 595, L97

Hoyng, P., Knight, J. W., et al. 1978, *Solar Physics*, 58, 139

Hoyng, P., van Beek, H. F., et al. 1976, *Solar Physics*, 48, 197

Hubený, I. 1982, *Journal of Quantitiative Spectroscopy and Radiative Transfer*, 27, 593

Hubeny, I. 2001, in Astronomical Society of the Pacific Conference Series, Vol. 247, Spectroscopic Challenges of Photoionized Plasmas, ed. G. Ferland & D. W. Savin, 197

Hubeny, I. & Mihalas, D. 2014, Theory of Stellar Atmospheres (Princeton University Press)

Hudson, H. S. 1972, *Solar Physics*, 24, 414

Hudson, H. S. 2007, in Astronomical Society of the Pacific Conference Series, Vol. 368, The Physics of Chromospheric Plasmas, ed. P. Heinzel, I. Dorotovič, & R. J. Rutten, 365

Hudson, H. S., Wolfson, C. J., et al. 2006, *Solar Physics*, 234, 79

Hurford, G. J., Schmahl, E. J., et al. 2002, *Solar Physics*, 210, 61

Isobe, H., Kubo, M., et al. 2007, *Publications of the ASJ*, 59, S807

Jefferies, J. T. & Thomas, R. N. 1960, *The Astrophysical Journal*, 131, 695

Jess, D. B., Mathioudakis, M., et al. 2008, *The Astrophysical Journal, Letters*, 688, L119

Kane, S. R., Hurley, K., et al. 1998, *The Astrophysical Journal*, 500, 1003

Karlicky, M. 1990, *Solar Physics*, 130, 347

Karlicky, M. & Henoux, J.-C. 1992, *Astronomy and Astrophysics*, 264, 679

Karlický, M. & Kontar, E. P. 2012, *Astronomy and Astrophysics*, 544, A148

Kašparová, J., Varady, M., et al. 2009, *Astronomy and Astrophysics*, 499, 923

Kerr, G. S. & Fletcher, L. 2014, *The Astrophysical Journal*, 783, 98

Kerr, G. S., Fletcher, L., et al. 2016, *The Astrophysical Journal*, 827, 101

Kerr, G. S., Simões, P. J. A., et al. 2015, *Astronomy and Astrophysics*, 582, A50

Khodachenko, M. L., Arber, T. D., et al. 2004, *Astronomy and Astrophysics*, 422, 1073

Kimball, D. 1960, *Geophysical Institute, University of Alaska*, Tech Report.

Kiplinger, A. L., Dennis, B. R., et al. 1983, *The Astrophysical Journal, Letters*, 265, L99

Kleint, L., Heinzel, P., et al. 2016, *The Astrophysical Journal*, 816, 88

Kneer, F., Mattig, W., et al. 1981, *Solar Physics*, 69, 289

Knight, J. W. & Sturrock, P. A. 1977, *The Astrophysical Journal*, 218, 306

Kohl, J. L. & Parkinson, W. H. 1976, *The Astrophysical Journal*, 205, 599

Kontar, E. P., Brown, J. C., et al. 2011, *Space Science Reviews*, 159, 301

Kontar, E. P., Hannah, I. G., et al. 2010, *The Astrophysical Journal*, 717, 250

Kontar, E. P., Hannah, I. G., et al. 2008, *Astronomy and Astrophysics*, 489, L57

Kosovichev, A. G. 2011, *The Astrophysical Journal, Letters*, 734, L15

Kowalski, A. F., Allred, J. C., et al. 2016, *ArXiv e-prints*

Kowalski, A. F., Hawley, S. L., et al. 2015, *Solar Physics*, 290, 3487

Kowalski, A. F., Hawley, S. L., et al. 2012, *Solar Physics*, 277, 21

Kretzschmar, M. 2011, *Astronomy and Astrophysics*, 530, A84

Krucker, S., Hudson, H. S., et al. 2011, *The Astrophysical Journal*, 739, 96

Krucker, S., Saint-Hilaire, P., et al. 2015, *The Astrophysical Journal*, 802, 19

Kuridze, D., Mathioudakis, M., et al. 2015, *The Astrophysical Journal*, 813, 125

Kuridze, D., Morton, R. J., et al. 2012, *The Astrophysical Journal*, 750, 51

Kuroda, N., Wang, H., et al. 2015, *The Astrophysical Journal*, 807, 124

Landi, E., Young, P. R., et al. 2013, *The Astrophysical Journal*, 763, 86

Leake, J. E., Arber, T. D., et al. 2005, *Astronomy and Astrophysics*, 442, 1091

Lee, K. W., Büchner, J., et al. 2008, *Astronomy and Astrophysics*, 478, 889

Leenaarts, J., a, T. M. D., et al. 2013a, *The Astrophysical Journal*, 772, 89

Leenaarts, J. & Carlsson, M. 2009, in Astronomical Society of the Pacific Conference Series, Vol. 415, The Second Hinode Science Meeting: Beyond Discovery-Toward Understanding, ed. B. Lites, M. Cheung, T. Magara, J. Mariska, & K. Reeves, 87

Leenaarts, J., Pereira, T., et al. 2012, *Astronomy and Astrophysics*, 543, A109

Leenaarts, J., Pereira, T. M. D., et al. 2013b, *The Astrophysical Journal*, 772, 90

Lemaire, P., Choucq-Bruston, M., et al. 1984, *Solar Physics*, 90, 63

Lemaire, P. & Gouttebroze, P. 1983, *Astronomy and Astrophysics*, 125, 241

Lemaire, P., Gouttebroze, P., et al. 1981, *Astronomy and Astrophysics*, 103, 160

Lemaire, P. & Skumanich, A. 1973, *Astronomy and Astrophysics*, 22, 61

Lemen, J. R., Title, A. M., et al. 2012, *Solar Physics*, 275, 17

Lin, H.-H. & Carlsson, M. 2015, *The Astrophysical Journal*, 813, 34

Lin, R. P., Dennis, B. R., et al. 2002, *Solar Physics*, 210, 3

Lin, R. P. & Hudson, H. S. 1976, *Solar Physics*, 50, 153

Linsky, J. L. & Avrett, E. H. 1970, *Publications of the ASP*, 82, 169

Linsky, J. L., Hunten, D. M., et al. 1979, *The Astrophysical Journal, Supplement*, 41, 481

Lites, B. W. & Hansen, E. R. 1977, *Solar Physics*, 55, 347

Liu, W., Heinzel, P., et al. 2015, *Solar Physics*, 290, 3525

Machado, M. E., Avrett, E. H., et al. 1986, in The lower atmosphere of solar flares, p. 483 - 488, ed. D. F. Neidig, 483–488

Machado, M. E., Avrett, E. H., et al. 1980, *The Astrophysical Journal*, 242, 336

Machado, M. E., Emslie, A. G., et al. 1989, *Solar Physics*, 124, 303

Machado, M. E., Emslie, A. G., et al. 1978, *Solar Physics*, 58, 363

Machado, M. E. & Linsky, J. L. 1975, *Solar Physics*, 42, 395

Machado, M. E. & Rust, D. M. 1974, *Solar Physics*, 38, 499

Magain, P. 1986, *Astronomy and Astrophysics*, 163, 135

Markwardt, C. B. 2009, in Astronomical Society of the Pacific Conference Series, Vol. 411, Astronomical Data Analysis Software and Systems XVIII, ed. D. A. Bohlender, D. Durand, & P. Dowler, 251

Martin, S. F. 1979, *Solar Physics*, 64, 165

Martínez Oliveros, J.-C., Hudson, H. S., et al. 2012, *The Astrophysical Journal, Letters*, 753, L26

Matthews, S. A., Harra, L. K., et al. 2015, *The Astrophysical Journal*, 812, 35

Matthews, S. A., van Driel-Gesztelyi, L., et al. 2003, *Astronomy and Astrophysics*, 409, 1107

Maurya, R. A., Vemareddy, P., et al. 2012, *The Astrophysical Journal*, 747, 134

McClements, K. G. & Fletcher, L. 2009, *The Astrophysical Journal*, 693, 1494

McClintock, W. E., Rottman, G. J., et al. 2005, *Solar Physics*, 230, 225

McIntosh, S. W., de Pontieu, B., et al. 2011, *Nature*, 475, 477

McKim Malville, J., Tandberg-Hanssen, E., et al. 1968, *The Astronomical Journal Supplement*, 73, 69

Melrose, D. B. 1990, *Solar Physics*, 130, 3

Melrose, D. B. & Wheatland, M. S. 2013, *Solar Physics*, 288, 223

Melrose, D. B. & Wheatland, M. S. 2014, *Solar Physics*, 289, 881

Metcalf, T. R., Alexander, D., et al. 2003, *The Astrophysical Journal*, 595, 483

Metcalf, T. R., Canfield, R. C., et al. 1990, *The Astrophysical Journal*, 365, 391

Mihalas, D. 1978, Stellar atmospheres, 2nd edn. (W. H. Freeman and Co.)

Milkey, R. W. & Mihalas, D. 1973, *The Astrophysical Journal*, 185, 709

Milkey, R. W. & Mihalas, D. 1974, *The Astrophysical Journal*, 192, 769

Milkey, R. W., Shine, R. A., et al. 1975, *The Astrophysical Journal*, 202, 250

Milligan, R. O. 2015, *Solar Physics*, 290, 3399

Milligan, R. O., Chamberlin, P. C., et al. 2012, *The Astrophysical Journal, Letters*, 748, L14

Milligan, R. O. & Dennis, B. R. 2009, *The Astrophysical Journal*, 699, 968

Milligan, R. O., Gallagher, P. T., et al. 2006a, *The Astrophysical Journal, Letters*, 638, L117

Milligan, R. O., Gallagher, P. T., et al. 2006b, *The Astrophysical Journal, Letters*, 642, L169

Milligan, R. O., Kerr, G. S., et al. 2014, *The Astrophysical Journal*, 793, 70

Morrill, J. S., Dere, K. P., et al. 2001, *The Astrophysical Journal*, 557, 854

Nakajima, H., Nishio, M., et al. 1994, *IEEE Proceedings*, 82, 705

Neckel, H. 1999, *Solar Physics*, 184, 421

Neckel, H. & Labs, D. 1984, *Solar Physics*, 90, 205

Neidig, D. F. 1983, *Solar Physics*, 85, 285

Neidig, D. F. 1989, *Solar Physics*, 121, 261

Neidig, D. F. & Cliver, E. W. 1983, *Solar Physics*, 88, 275

Neidig, D. F., Kiplinger, A. L., et al. 1993, *The Astrophysical Journal*, 406, 306

Neidig, D. F. & Wiborg, Jr., P. H. 1984, *Solar Physics*, 92, 217

Noyes, R. W. & Hall, D. N. B. 1972, in Bulletin of the AAS, Vol. 4, Bulletin of the American Astronomical Society, 389

Ogawara, Y., Takano, T., et al. 1991, *Solar Physics*, 136, 1

Penn, M., Krucker, S., et al. 2016, *The Astrophysical Journal, Letters*, 819, L30

Pereira, T. M. D., Carlsson, M., et al. 2015, *The Astrophysical Journal*, 806, 14

Pereira, T. M. D., Leenaarts, J., et al. 2013, *The Astrophysical Journal*, 778, 143

Pesnell, W. D., Thompson, B. J., et al. 2012, *Solar Physics*, 275, 3

Pick, M. & Vilmer, N. 2008, *Astronomy and Astrophysics Reviews*, 16, 1

Priest, E. R. 1982, Solar magneto-hydrodynamics (Dordrecht, Holland ; Boston : D. Reidel Pub. Co. ; Hingham,)

Priest, E. R. & Forbes, T. G. 2002, *Astronomy and Astrophysics Reviews*, 10, 313

Qiu, J., Lee, J., et al. 2002, *The Astrophysical Journal*, 565, 1335

Qiu, J., Liu, W., et al. 2010, *The Astrophysical Journal*, 725, 319

Rathore, B. & Carlsson, M. 2015, *The Astrophysical Journal*, 811, 80

Rathore, B., Carlsson, M., et al. 2015, *The Astrophysical Journal*, 811, 81

Reep, J. W. & Russell, A. J. B. 2016, *The Astrophysical Journal, Letters*, 818, L20

Reid, H. A. S. & Ratcliffe, H. 2014, *Research in Astronomy and Astrophysics*, 14, 773

Ricchiazzi, P. J. & Canfield, R. C. 1983, *The Astrophysical Journal*, 272, 739

Rubio da Costa, F., Kleint, L., et al. 2016, *ArXiv e-prints*

Russell, A. J. B. & Fletcher, L. 2013, *The Astrophysical Journal*, 765, 81

Rutten, R. J. & Uitenbroek, H. 1991, *Solar Physics*, 134, 15

Ryan, D. F., Chamberlin, P. C., et al. 2013, *The Astrophysical Journal*, 778, 68

Rybicki, G. B. & Hummer, D. G. 1991, *Astronomy and Astrophysics*, 245, 171

Rybicki, G. B. & Hummer, D. G. 1992, *Astronomy and Astrophysics*, 262, 209

Sabine, E. 1852, *Phil. Trans. R. Soc. London*, 142, 103

Samain, D. & Lemaire, P. 1985, *Astrophysics and Space Science*, 115, 227

Schmahl, E. J., Pernak, R. L., et al. 2007, *Solar Physics*, 240, 241

Schmieder, B., Forbes, T. G., et al. 1987, *The Astrophysical Journal*, 317, 956

Schmieder, B., Heinzel, P., et al. 1995, *Solar Physics*, 156, 337

Schmit, D., Bryans, P., et al. 2015, *The Astrophysical Journal*, 811, 127

Schunk, R. & Nagy, A. 2009, Ionospheres, 2nd edn. (Cambridge University Press)

Schwartz, R. A., Csillaghy, A., et al. 2002, *Solar Physics*, 210, 165

Seaton, M. J. 1960, *Reports on Progress in Physics*, 23, 313

Shea, M. A. & Smart, D. F. 2006, *Advances in Space Research*, 38, 313

Shimizu, T., Nagata, S., et al. 2008, *Solar Physics*, 249, 221

Shine, R. A. & Linsky, J. L. 1972, *Solar Physics*, 25, 357

Shine, R. A., Milkey, R. W., et al. 1975, *The Astrophysical Journal*, 199, 724

Solanki, S. K. 2003, *Astronomy and Astrophysics Reviews*, 11, 153

Staath, E. & Lemaire, P. 1995, *Astronomy and Astrophysics*, 295, 517

Stewart, B. 1861, *Phil. Trans. R. Soc. London*, 151, 423

Stilley, J. L. & Callaway, J. 1970, *The Astrophysical Journal*, 160, 245

Su, Y., Veronig, A. M., et al. 2013, *Nature Physics*, 9, 489

Sudol, J. J. & Harvey, J. W. 2005, *The Astrophysical Journal*, 635, 647

Suematsu, Y., Tsuneta, S., et al. 2008, *Solar Physics*, 249, 197

Sweet, P. A. 1969, *Annual Review of Astronomy and Astrophysics*, 7, 149

Sylwester, B. & Sylwester, J. 2000, *Solar Physics*, 194, 305

Tarr, L., Longcope, D., et al. 2013, *The Astrophysical Journal*, 770, 4

Tsiropoula, G., Tziotziou, K., et al. 2012, *Space Science Reviews*, 169, 181

Tsuneta, S., Ichimoto, K., et al. 2008, *Solar Physics*, 249, 167

Tsurutani, B. T., Gonzalez, W. D., et al. 2003, *Journal of Geophysical Research (Space Physics)*, 108, 1268

Tu, J. & Song, P. 2013, *The Astrophysical Journal*, 777, 53

Uitenbroek, H. 1989, *Astronomy and Astrophysics*, 213, 360

Uitenbroek, H. 2000, *The Astrophysical Journal*, 536, 481

Uitenbroek, H. 2001, *The Astrophysical Journal*, 557, 389

Uitenbroek, H. 2002, *The Astrophysical Journal*, 565, 1312

Švestka, Z. 1966, *Space Science Reviews*, 5, 388

van Driel-Gesztelyi, L. & Green, L. M. 2015, *Living Reviews in Solar Physics*, 12

Varady, M., Karlický, M., et al. 2014, *Astronomy and Astrophysics*, 563, A51

Varady, M., Kasparova, J., et al. 2010, *IEEE Transactions on Plasma Science*, 38, 2249

Vernazza, J. E., Avrett, E. H., et al. 1976, *The Astrophysical Journal, Supplement*, 30, 1

Vernazza, J. E., Avrett, E. H., et al. 1981, *The Astrophysical Journal, Supplement*, 45, 635

Veronig, A., Temmer, M., et al. 2002, *Astronomy and Astrophysics*, 382, 1070

Wang, H.-M. 2009, *Research in Astronomy and Astrophysics*, 9, 127

Wang, S., Liu, C., et al. 2012, *The Astrophysical Journal, Letters*, 745, L17

Watanabe, K., Krucker, S., et al. 2010, *The Astrophysical Journal*, 715, 651

Watanabe, K., Shimizu, T., et al. 2013, *The Astrophysical Journal*, 776, 123

Webb, D. F. & Howard, T. A. 2012, *Living Reviews in Solar Physics*, 9, 3

Wedemeyer, S., Bastian, T., et al. 2016, *Space Science Reviews*, 200, 1

Wedemeyer-Böhm, S. 2008, *Astronomy and Astrophysics*, 487, 399

Woods, T. N., Kopp, G., et al. 2006, *Journal of Geophysical Research (Space Physics)*, 111

Xu, Y., Cao, W., et al. 2006, *The Astrophysical Journal*, 641, 1210

Xu, Y., Cao, W., et al. 2004, *The Astrophysical Journal, Letters*, 607, L131

Yokoyama, T., Akita, K., et al. 2001, *The Astrophysical Journal, Letters*, 546, L69

Zarro, D. M., Canfield, R. C., et al. 1988, *The Astrophysical Journal*, 324, 582

Zharkov, S., Green, L. M., et al. 2011, *The Astrophysical Journal, Letters*, 741, L35

Zirin, H. 1988, Astrophysics of the sun (Cambridge University Press)

Zweibel, E. G. & Haber, D. A. 1983, *The Astrophysical Journal*, 264, 648

Appendix A

Hydrogen Continuum Opacities and Emissivities Used to Compute C_I

The opacities and emissivities used to calculate the contribution function to the emergent continuum intensity. In the following all units are in c.g.s unless otherwise noted.

A.1 Hydrogen Bound-Free

H_{bf} Absorption Cross-Sections:
The bound-free absorption cross-section for hydrogen energy level i, in cm^{-2}, is given by Mihalas (1978) Eq. 4 – 114 as:

$$\alpha_i(\nu) = \frac{64}{3\sqrt{3}} \frac{\pi^4 m_e e^{10}}{ch^6} \frac{1}{\nu^3} \frac{1}{i^5} g_{\mathrm{II(i,}\nu)} = 2.815 \times 10^{29} \frac{1}{\nu^3} \frac{1}{i^5} g_{\mathrm{II(i,}\nu)} \tag{A.1}$$

where m_e is the electron mass, c is the speed of light, h is Planck's constant, e is the electron charge, ν is the frequency, and $g_{\mathrm{II}}(i,\nu)$ is the bound-free Gaunt Factor. An algorithm for calculating the bound-free Gaunt factors was taken from `hydrogen.c` in the (publicly available) `RH` source code. This algorithm was based on expressions from Seaton (1960).

H_{bf} Opacity and Emissivity (NLTE):
For hydrogen transitions treated in detail by `RADYN` the NLTE bound-free opacity and emissivity were calculated. For the upper levels the LTE expressions were used

instead. The opacity (or absorption coefficient) per cm^{-3} is found by multiplying the absorption cross-section by the number density of hydrogen atoms in level i and summing over all the levels that are able to absorb light at ν. From the second term in Mihalas (1978) Eq. 7 – 1 the NLTE bound-free opacity is:

$$\chi_{\mathrm{H,bf,det}}(\nu) = \sum_i \left(n_i - n_i^* exp\left\{ -\frac{h\nu}{k_b T} \right\} \right) \alpha_i(\nu), \tag{A.2}$$

where k_b is Boltzmann's constant, and T is temperature. The term n_i^* is the population density of level i in LTE computed using the actual ion density: $n_i^* = n_p(n_i/n_p)^*$. Equation A.2 includes a correction for stimulated emission. The emissivity is then, from the second term in Mihalas (1978) Eq. 7 – 2:

$$j_{\mathrm{H,bf,det}}(\nu) = \frac{2h\nu^3}{c^2} \sum_i n_i^* \alpha_i(\nu) \exp\left\{ -\frac{h\nu}{k_b T} \right\}, \tag{A.3}$$

$\mathrm{H_{bf}$ Opacity and Emissivity (LTE):
Hydrogen upper levels $i = 6, 7, 8$ were included in LTE. The opacity is given by the second term in Mihalas (1978) Eq. 7 – 3:

$$\chi_{\mathrm{H,bf,upp}}(\nu) = \left(1 - \exp\left\{ -\frac{h\nu}{k_b T} \right\} \right) \sum_i n_i^* \alpha_i(\nu). \tag{A.4}$$

The emissivity is then:

$$j_{\mathrm{H,bf,upp}}(\nu) = \chi_{\mathrm{H,bf,upp}}(\nu) * B(\nu). \tag{A.5}$$

where $B(\nu)$ is the Planck function.

Computing n_i^*:
Following Mihalas (1978) and Aller (1963), an expression for n_i^* can be obtained from the Saha ionisation equation. Mihalas (1978) Eq. 5 – 14 states an expression for the population i of an ion j:

$$n_{i,0}^* = n_{0,1} n_e \frac{g_{i,0}}{g_{0,1}} \frac{1}{2} \frac{h^2}{2\pi mk} T^{-3/2} \exp\left\{ \frac{(E_{I,0} - E_{i,0})}{k_b T} \right\}. \tag{A.6}$$

In this expression $n_{i,0}$ refers to neutral hydrogen population density of state i, $n_{0,1}$ is the population density of singly ionised hydrogen (hereafter n_p), $E_{I,0}$ is the ionisation potential in eV from hydrogen ground state and $E_{i,0}$ is the potential from level i. The

statistical weights are for level i ($g_{i,0} = 2n^2$) and for the proton ($g_{0,1} = 1$). Note that with the potentials in units eV, k_b must be measured in eV also ($k_b = 8.6171 \times 10^{-5}$ eV). Equation A.6 reduces to:

$$n^*_{i,0} = 4.1416 \times 10^{-16} i^2 n_p n_e T^{-3/2} \exp\left\{\frac{157825}{iT}\right\}. \tag{A.7}$$

A.2 Hydrogen Free-Free

H_{ff} Absorption Cross-Sections:
For a Maxwellian velocity distribution the hydrogen free-free absorption cross-section is, from Mihalas (1978) Eq. 4 – 122, is:

$$\alpha(\nu, T) = \frac{4e^6}{3ch}\left(\frac{2\pi}{3k_b m_e^3}\right)^{1/2} T^{-1/2}\nu^{-3} g_{\rm III}, \tag{A.8}$$

where $g_{\rm III}$ is the free-free Gaunt factor. The free-free Gaunt factor is stated by Gray (1992) Eq. 8.10 as:

$$g_{\rm III} = 1 + 0.3546(\lambda R)^{(-1/3)}\left(\frac{\lambda k_b T}{hc} + \frac{1}{2}\right), \tag{A.9}$$

where R is Rydberg's constant. Inserting values for the constants, and converting R into Å^{-1} equation A.9 becomes:

$$g_{\rm III} = 1 + 3.3512\lambda^{(-1/3)}\left(6.95 \times 10^{-9}\lambda T + \frac{1}{2}\right). \tag{A.10}$$

H_{ff} Opacity and Emissivity:
Multiplying Eq. A.8 by electron and proton densities and correcting for stimulated emission gives the opacity:

$$\chi_{\rm H,ff}(\nu) = 3.692 \times 10^8 \nu^{-3} T^{-1/2} n_e n_p \left(1 - \exp\left\{\frac{-h\nu}{k_b T}\right\}\right) g_{\rm III}. \tag{A.11}$$

The emissivity is then simply:

$$j_{\rm H,ff}(\nu) = \chi_{\rm H,ff}(\nu) B_\nu. \tag{A.12}$$

A.3 H^- Bound-Free

The H^- ion contributes significant opacity, but the absorption cross-sections are very tricky to measure, so that there is not a nice analytical expression. Instead values of the cross-section have been calculated as a function of wavelength. The values of $\alpha_{H^-,bf}$ from Table 3 in Geltman (1962) were interpolated to provide the cross-sections at the wavelengths of interest. Then, the H^- opacity is given, from Vernazza et al. (1976) Eq. 13, as:

$$\chi_{H^-,bf}(\nu) = \alpha_{H^-,bf} n_{H^-} \left(1 - \exp\left\{-\frac{h\nu}{k_b T}\right\}\right), \tag{A.13}$$

where n_{H^-} is the number density of H^- ions:

$$n_{H^-} = 1.0354 \times 10^{-16} n_e n_{HI} T^{-3/2} \exp\left\{\frac{8762}{T}\right\}. \tag{A.14}$$

Assuming LTE the H^- bound-free emissivity is:

$$j_{H^-,bf}(\nu) = \chi_{H^-,bf}(\nu) B_\nu. \tag{A.15}$$

n_{HI} is the neutral hydrogen number density.

A.4 H^- Free-Free

Stilley & Callaway (1970) computed the free-free absorption cross sections for H^- as a function of wavelength, to which Gray (1976) fit polynomials. From those cross-sections Gray (1976) wrote the H^- opacity as:

$$\chi_{H^-,ff}(\nu) = n_e n_{HI} k_b T \; 10^{(f_0 + f_1 \log\theta + f_2 \log^2\theta)}, \tag{A.16}$$

where $\theta = 5040/T$, and the polynomial fits are:

$$f_0 = -31.63602 + 0.48725 \log\lambda + 0.296586 \log^2\lambda - 0.0193562 \log^3\lambda, \tag{A.17}$$

$$f_1 = 15.3126 - 9.33651 \log\lambda + 2.000242 \log^2\lambda - 0.1422568 \log^3\lambda, \tag{A.18}$$

$$f_2 = -2.6117 - 3.22259 \log\lambda - 1.082785 \log^2\lambda + 0.1072635 \log^3\lambda. \tag{A.19}$$

The H^- free-free emissivity is:

$$j_{H^-,ff}(\nu) = \chi_{H^-,ff}(\nu) B_\nu. \tag{A.20}$$